

6th Croatian-Hungarian and 17th Hungarian geomathematical congress

Geomathematics - from theory to practice

Editors:

Marko Cvetković, Kristina Novak Zelenika and János Geiger

ISBN 978-953-95130-8-3

Opatija, 21-23 May, 2014

Impressum

Publisher: Croatian Geological Society, 2014

For publisher: Josip Halamić, president of the Croatian Geological Society

Editors: Marko Cvetković, Kristina Novak Zelenika and János Geiger

Circulation: 50 copies

Copy and distribution: Denona d.o.o., Zagreb

ISBN 978-953-95130-8-3

Note

The content of proceedings has not been passed English proof reading by native speaker, and that is why solely the authors are responsible for the quality of language usage.

Organizers

Croatian Geological Society (Hrvatsko geološko društvo)

<http://www.geologija.hr>

Geomathematical Section (Geomatemički odsjek)

<http://www.geologija.hr/geomat.php>



Hungarian Geological Society (Magyarhoni Földtani Társulat)

<http://www.foldtan.hu/>

Geomathematical Section (Geomatematikai Szakosztály)

<https://www.smartportal.hu/>



Under the auspices



RGNF

**Faculty of Mining, Geology and Petroleum Engineering
(Rudarsko-geološko-naftni fakultet)**

<http://www.rgn.hr>

Committees

Organizing Committee

Dr. Kristina Novak Zelenika (chairman, INA)

Dr. Marko Cvetković (vice-chairman, Univ. Zagreb, HR)

Prof. Dr. Janos Geiger (vice-chairman, Univ. Szeged, HU)

Andrea Wagenhoffer (Univ. Szeged, HU)

Karolina Novak (INA, HR)

Scientific Committee

Prof. Dr. Janos Geiger (chairman, HU)

Prof. Dr. Josipa Velić (vice-chairman, Univ. Zagreb, HR)

Prof. Dr. Tomislav Malvić (vice-chairman, HR)

Prof. Dr. Jasenka Sremac (Univ. Zagreb, HR)

Janina Horvath (Univ. Szeged, HU)

Honorary Committee

Prof. Dr. Josip Halamić (president, Croatian Geol. Soc.)

Prof. Dr. Janos Haas (president, Hungarian Geol. Soc.)

CONTENT

Janos Geiger: Characterization of millimeter-scale petrophysical heterogeneity of some Upper Pannonian (s.l.) clastic rocks by using medical CT and conventional core analysis	13
Marko Cvetković, Josipa Velić and Filip Vukičević: Selection of the most successful neural network algorithm for the purpose of subsurface velocity modelling, example from the Sava Depression, Croatia	21
Željka Tutek and Miljenko Lapaine: Forward intersection and its accuracy	29
Tomislav Malvić and Kristina Novak Zelenika: Why we use Simpson and trapezoidal rule for hydrocarbon reservoir volume calculation?	37
Danijel Ivanišević, Josip Halamić and Zoran Peh: Discrimination and interpretation of natural and anthropogenic soil contamination using principal component analysis	45
István Gábor Hatvani, József Kovács, Adrienne Clement and János Korponai: Determining alternative stable states in the Keszthely bay – Kis-Balaton system with the aid of stochastic modelling	53
István Nemes: Throwing oily dices, uncertainty in HCIIP	61
Andrea Wágenhoffer: 3D facies analysis with combination of 3D sequential simulation and well-log shape application	69
Janina Horváth: Identification of clastic sedimentary facies based on cluster process and Indicator Kriging	77
Noémi Jakab: Statistical characters of realizations derived from stochastic simulations based on CT images	83
Angelika Sóla: High-resolution facies modelling to locate by-passed oil: a case history from Algyó Field	91

János Blahó: Road from using seismic attribute to inventing special approach of facies modelling	97
Gábor Szatmári: Optimization of sampling configuration by spatial simulated annealing for mapping soil variables	105
István Gábor Hatvani and Zoltán Kern: Spatiotemporal patterns of East Antarctic stable isotope records	113
Viktor Volford: 3d facies analysis based on well data with different geostatistical and sedimentological approache	121
Márta Kis, Katalin Gribovszki, Márta Kiszely and András Koppán: Analysis of an earthquake based on extensometric and seismological measurements of has and MFGI observatories	129
Gyula Mentés, Ildikó Eper-Pápai, Márta Kis and András Koppán: Analysis of long-term extensometric data of Sopron and Budapest geodynamical observatories	135
Zalán Tobak, Boudewijn van Leeuwen, László Henits and József Szatmári: Satellite-based inland excess water flood detection	139
András Koppán, Márta Kis, P. Kovács, L. Merényi and G. Vadász: Observatory gravimeter calibration results with magnetic correction	145
Karolina Novak and Ivan Zelenika: Carbon capture and storage possibility, case study Ivanić Field	151
Omar Sliman: The impact of sedimentary facies characteristics on the petrophysical reservoir properties: Lower Cretaceous Nubian formation, South East Sirt Basin, Libya	159
Judit Horváth, Péter Koroncz and Ferenc Fedor: Petrophysical and hydrodynamical investigation of unconsolidated rocks – measurement vs. empirical estimation	167

Boudewijn van Leeuwen, Zalán Tobak, Zsuzsana Ladányi and Viktoria Blanka: **Satellite based soil moisture estimates for agricultural drought** **175**

Ivana Mesić and Gordana Medunić: **Declustering of field's data located on northern margin of the Bjelovar Subdepression** **183**

FOREWORD

As all good things get to be repeated, this is not an exception. This, now a very traditional congress, is getting to be held for the second time in Croatia. This is only due to the longevity of the thematic - geomathematics and geosciences, and to the very successful cooperation between the Hungarian and Croatian geomathematical sections which resulted in the continuing the congress tradition and quality.

This volume contains the full overview of 24 oral and poster presentations. The topics range from theoretical approaches through reservoir modeling and methods used in nuclear remediation as well as the most recent innovations of geoinformational investigations. Authors listed range from employees of major oil industries of Croatia and Hungary (INA - Industrije nafte, Croatia, MOL Hungarian Oil and Gas Public Limited Company), representatives of the Libyan Petroleum Institute, as well as Universities (University of Zagreb, University of Szeged, Eötvös Lóránd University of Budapest), National Geological Surveys, and the Eötvös Lóránd Geophysical Institute, Hungary.

In the 2014 the applied articles covered a wide range of topics – from the theoretical aspect of mathematics to the ones that mainly regarded the application of such methods on a very specific set of problems.

We hope that this congress, along with all the works presented will give birth to some new ideas and new collaborations.

We hope to meet you the next year in Hungary!

In Zagreb and Szeged, May 2014

The Editors

Marko Cvetković, Kristina Novak Zelenika and János Geiger

REVIEWED PAPERS

Characterization of millimeter-scale petrophysical heterogeneity of some Upper Pannonian (s.l.) clastic rocks by using medical computerized tomography (CT) and conventional core analysis

János GEIGER

University of Szeged, Department of Geology and Paleontology, H-6723 Szeged, Egyetem u.2.

e-mail: matska@geo.u-szeged.hu

The main purpose of this study is to model the mm-scale petrophysical heterogeneity of core samples by using medical computerized tomography (CT) and conventional petrophysical core measurements. Ten core samples with different sedimentary structures were measured under medical CT, and upscaled to 1x1x1 mm of voxel volume. The identified rock types were assigned by Hounsfield Units in the corresponding CT data bricks. To characterize their 3D porosity and permeability, a set of 590 conventional core measurements coming from the same stratigraphical position as the CT-measured samples, were selected. A statistical workflow helped to define significant petrophysical subsets for each rock types of the CT-samples. A function distributed the petrophysical values of these subsets, voxel-by-voxel, in the CT volume.

On the basis of the spatial continuity of the porosity and permeability data bricks, potential flow paths could be defined in each sedimentary structure. In addition, model type vertical sequences of point-bar, crevasse channel and flood plain facies could be built up from these petrophysical data bricks. The validation showed that these models are as good as the background petrophysical data base.

Key words: CT measurements, sedimentary structures, lattice data, small-scale petrophysical heterogeneity

1. INTRODUCTION

Computerized tomography (CT) provides non-destructive three-dimensional visualization and characterization, by creating images that map the variation of X-ray attenuation within objects, which relate closely to density. Density transitions usually correspond to boundaries between materials or phases. That is why these data are often straightforward and intuitive for the geologist and engineers to interpret.

In reservoir engineering, several authors presented CT studies aimed to analyze core-flood and displacement efficiency during miscible and immiscible displacement experiments (e.g. Frenshan and Jelen, 1986) and to visualize mud invasion (e.g. Kuru et al., 1998). Some studies were addressed to the use of CT-derived multiphase saturation data for steady or unsteady state relative permeability determination (e.g. Frenshan and Jelen, 1986). Porosity and saturation profiles were also calculated during steady state relative permeability tests. Honarpour and Mahmood (1986) summarized methods to determine fluid saturations during multiphase core-flood experiments.

One of the best outlooks of recent CT-applications was provided by Mees et al., (2003). Some meso-scaled geostatistical study of CT data bricks showed how to interpret the representative elementary volume (REV, e.g. Vogel and Brown, 2003) and how to study cyclic sedimentation (e.g. Geiger et al., 2008).

The main goal of this study is to develop such representative model sequences which present generalized mm-scale porosity and permeability properties for the delta plain rock bodies of the sub-basins of the Great Hungarian Plain.

2. CT PRINCIPALS

X-ray computer tomography based on the attenuation of X- or gamma rays emitted from an X-ray tube. The attenuation of a thin, well-collimated beam of X-ray follows the Beer's law. The linear attenuation coefficient depends on both the effective atomic number and the density of the object (Curry et al., 1990). The result is a numerical map consisting of all the attenuation coefficients corresponding to each volume element (voxel). The values expressed as non-dimensional CT number (Hounsfield Units or HUs), according to the following relation:

$$CT = 1000 \frac{\mu - \mu_w}{\mu_{tw}} \quad (1)$$

Fixed values of this scale take (-1000) for the air, and 0 for the water. The greater is the value of μ , the higher is the corresponding HU. The degree of attenuation is conventionally expressed in Hounsfield Units being normalized by the attenuation coefficient of pure water.

3. METHODS

In this study, the general workflow consisted of three main steps: (1) Definition of rock types in the elementary bricks; (2) Derivation porosity, horizontal and vertical permeability for elementary CT-bricks and filling-up CT-bricks with petrophysics; (3) Composition of sequences by vertical combinations of elementary CT-brick units and volumetric upscaling of these models.

Definition of rock types in the elementary CT bricks.

The main purpose of this preliminary step was to identify the main sedimentary rock types building up the samples. The cylinder geometry of the samples gave possibility to face beam hardening, which can significantly modify the CT numbers. To avoid this effect, only the central parts of the images were kept for further processing (**Figure 1**).

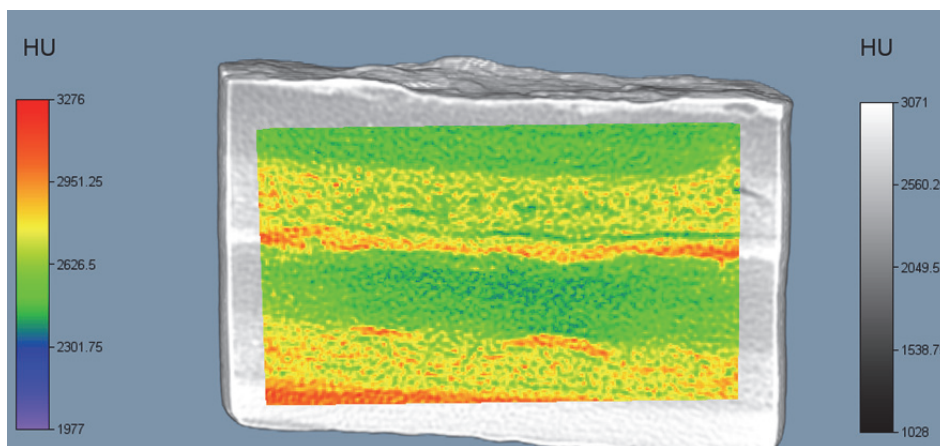


Figure 1: Hard beaming showing bright edges, and definition of a smaller volume for further analysis. Note: the height of the samples is 5.5 cm.

All the geometries (sedimentary structures) suggested by the CT-voxels were identified with their core-counterparts. In this way the rock types of these structures could be identified. Their CT-numbers, more exactly the minimum and maximum CT numbers (Hounsfield Units) were recognized by a volume rendering system and by statistical analysis the voxel-values (**Figure 2**).

Derivation porosity, horizontal and vertical permeability for elementary CT-bricks and filling-up CT-bricks with petrophysics

To characterize the model-level porosity and permeability distribution of a sample, a set of 590 conventional core measurements were selected. They

were obtained from the same stratigraphical position as the CT-measured samples. A statistical workflow based on k-means clustering, hypothesis tests and discriminant analysis made possible to define significant petrophysical subsets for each rock types of the CT-samples.

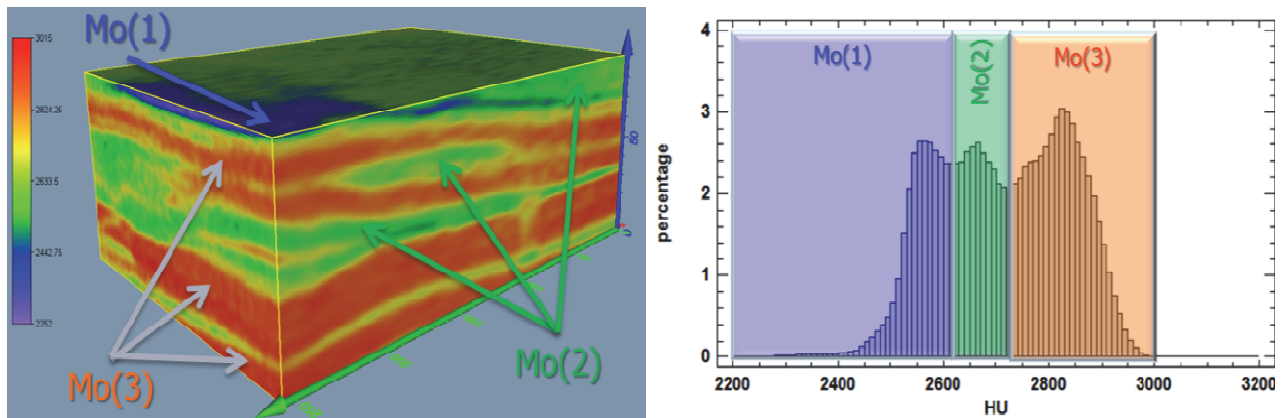


Figure 2: 3D HU-bricks of flaser bedding (left) and the corresponding probability distribution of HUs (right). Mo: mode.

For a given rock types the minimum and maximum porosity, horizontal and vertical permeability, coming from the statistical work flow, were assigned to the minimum and maximum Hounsfield Units measured in the corresponding CT-volume. A function distributed the petrophysical values of these subsets, voxel-by-voxel, in the CT volume. In this way the resolutions of the petrophysical and CT data bricks were the same (1x1x1 mm).

Composition of sequences by vertical combinations of elementary CT-brick units and volumetric upscaling of these models

In this step, some characteristic vertical model sequences of Újfalu Formation (Upper Pannonian, s.l., Hungary) were selected. Their vertical compositions were defined by Markov-analysis of the ‘real’ lithological successions of this formation. The basic idea was to represent each of the model-member by a CT brick of which sedimentary structures and lithological composition had already been known from the above outlined steps. In addition, after mapping the corresponding porosity and permeability data to the CT-voxel, their small-scale model petrophysics could also be suggested. The workflow of this step is shown in **Figure 3**.

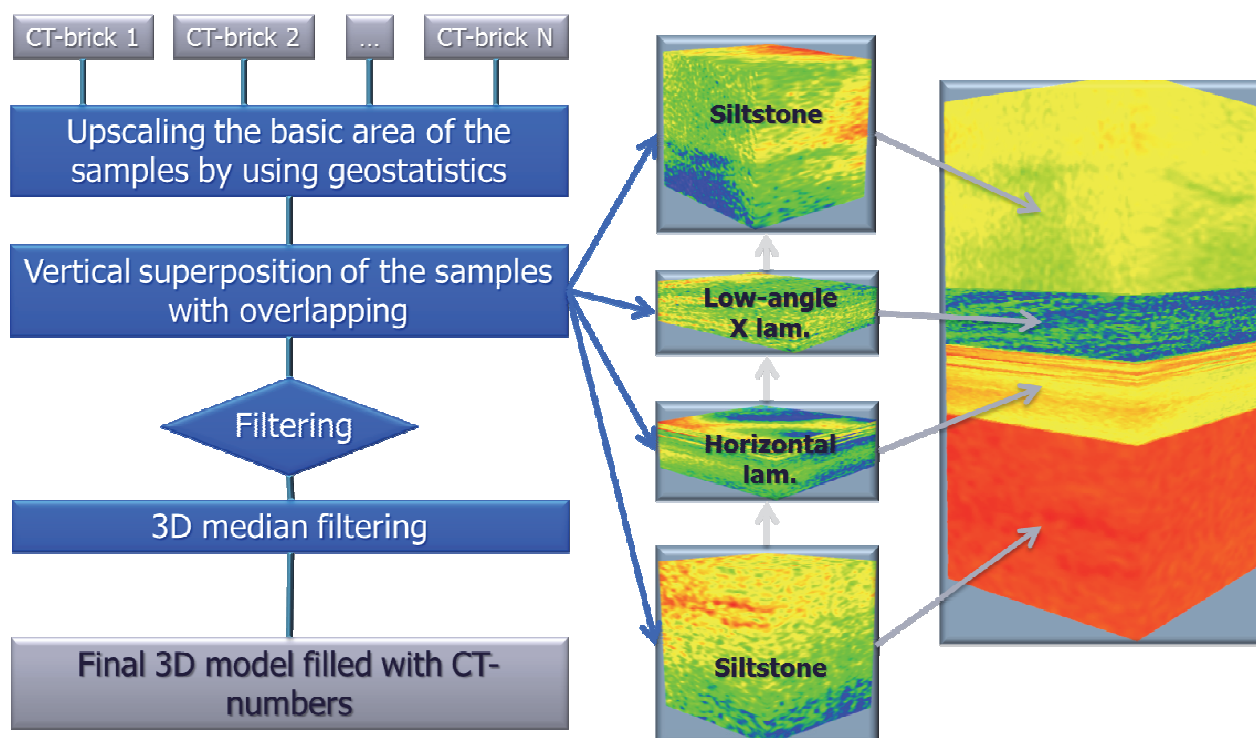


Figure 3: Workflow for construction of model sequences from CT-bricks

4. RESULTS AND DISCUSSION

Altogether 9 samples were selected: (1) Sand-silt alternation; (2) Massive sandstone; (3) Bioturbation, (4) Flaser bedding, (5) Laminated siltstone; (6) Laminated sandy and silty bands; (7) Trough cross-lamination; (8) Fluid escape structures; (9) Low angle cross-lamination. Their stratigraphical position (~ 1750-1820 m below the sea level) suggested the lithification stage of sandstone diagenesis.

In their CT bricks four significant rock types could be identified in terms of HU: (1) Coarse sandstone, (2) Fine sandstone, (3) Coarse siltstone, (4) Fine siltstone and clay marl. The corresponding HU-intervals were (1) <2500, (2) 2500-2700, (3) 2700-2900, (4) >2900.

Using the statistical worksheet, four significantly different porosity intervals could be derived for these rock types (**Table 1**). The model-type porosity bricks were calculated voxel-by-voxel by using a simple function which, for a particular rock type, distributed the figures of the corresponding porosity interval in the function of the HU data. The resolutions of both the HU and the petrophysical data bricks were 1x1x1 mm (**Figure 4**).

Table 1: Porosity intervals for the four rock-types

ROCK TYPES	PORmin	PORmax
COARSE SDST	0.2542	0.3399
FINE SDST	0.2310	0.3470
COARSE SLST	0.2059	0.3218
FINE SLST	0.0245	0.2283

In these high resolution petrophysical data bricks several calculations were done to visualize the inflow and outflow regions (Laplacian second derivative), to suggest some possible way for the within-brick flow-paths, and to reveal the range of influence for both HU and petrophysical characters (**Figure 4, 5, and 6**)

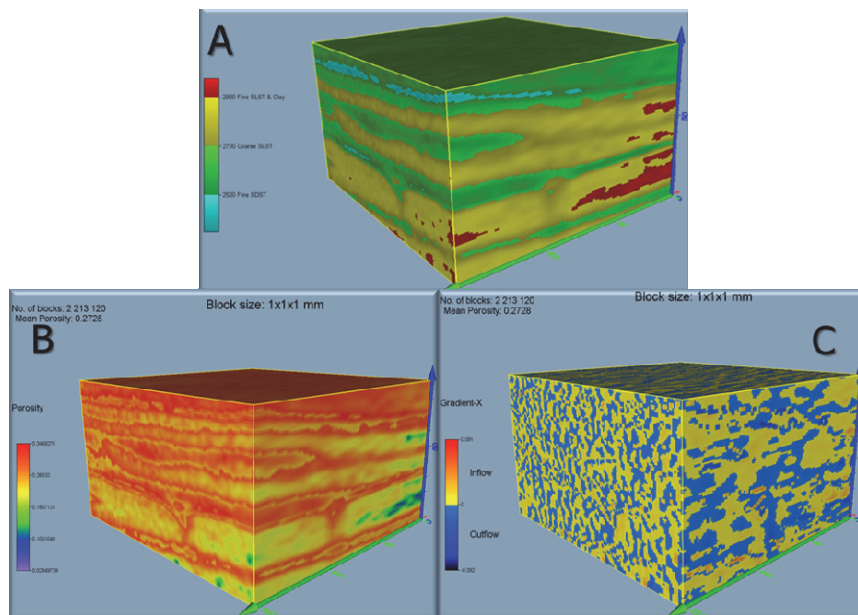


Figure 4: Rock types of the flaser bedding (A), its 3D porosity voxel (B) and regions of inflows and outflows within the porosity brick (C)

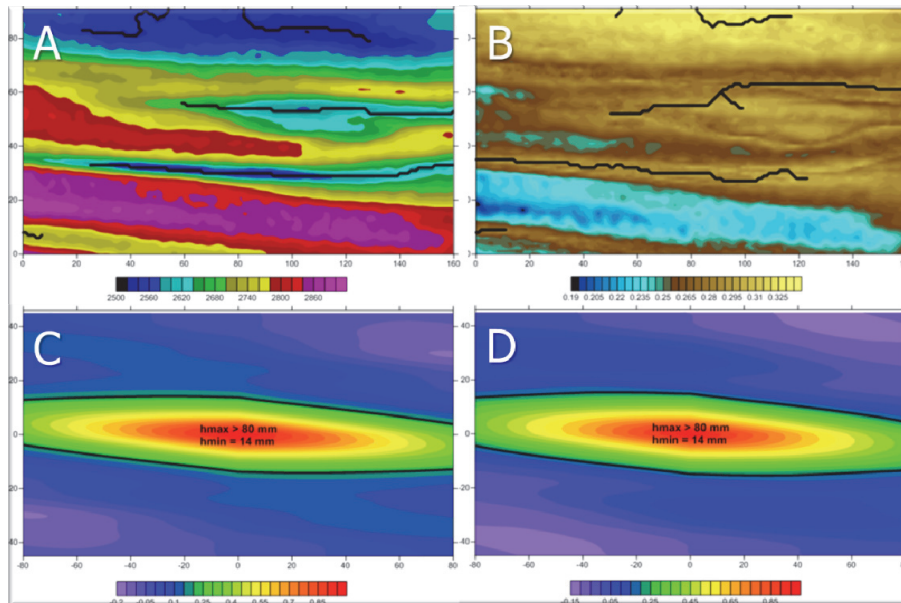


Figure 5: Flow paths (A and B) and range of influences (C and D) in (x,z) plane of flaser bedding. A and C: HUs, B and D: Porosity

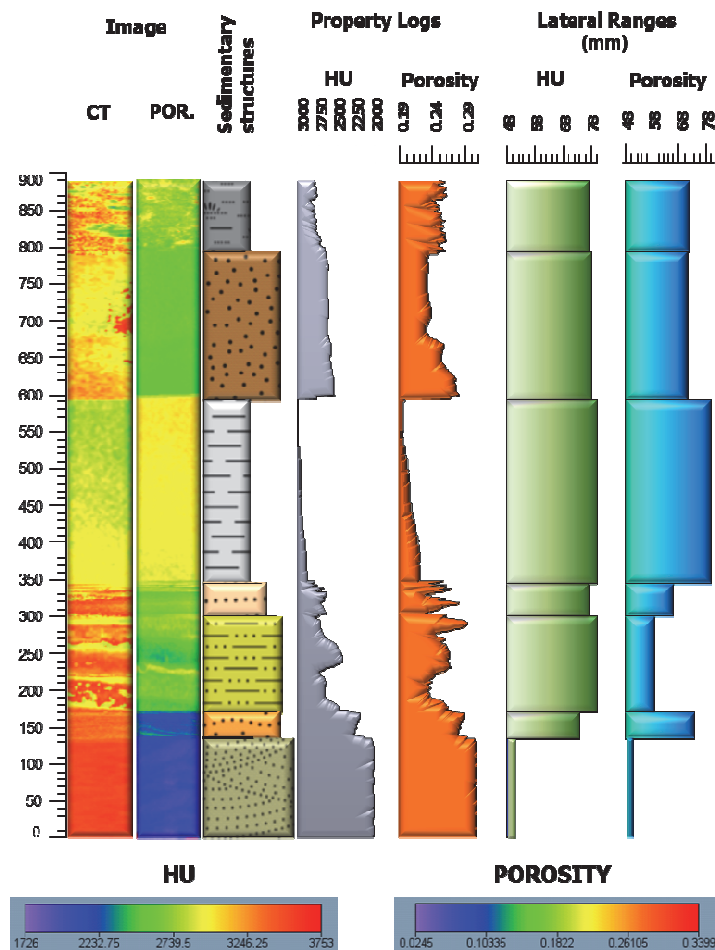


Figure 6: Vertical model sequence of a point bar compiled from CT images. It shows the mm-scale textural and porosity trends along with the sedimentary structures and the lateral extendibility (ranges) of HUs and porosity.

These model 'sequences' can be used suggest that mm-scale of textural and petrophysical heterogeneity, which otherwise cannot be measured continuously. The ranges of influences of both textural and petrophysical properties for each sample may be used to point out those distances which belong to the lateral extendibility of core properties. So they may show valuable data for capacity improving procedures.

5. REFERENCES

- CURRY, T.S., DOWDEY, J.E., &MURRY JR., R.C., (1990): Christensen's Physics of Diagnostic Radiology, 4th edition. Lea and Febiger, Philadelphia.
- FRENSHAN, P.B. & JELEN, J. (1986): Displacement of heavy oil visualized by CAT scan. -In: Proceedings of the 37th Annual Technical Meeting of the Petroleum Society of CIM, Calgary, 8-11 June, 605-620.
- GEIGER, J., HUNYADFALVI, Z. & BOGNER, P. (2008): Analysis of small-scale heterogeneity in clastic rocks by using computerized X-ray tomography (CT). Engineering Geology, 103, 3-4, 112-118.
- HONARPOUR, M. & MAHMOOD, S.M. (1988): Relative-Permeability Measurements: An Overview. Journal of Petroleum Technology, 40, 8, 963-966. SPE-18565-PA.
- KURU, E., DEMIRAL, B., AKIN, S., KEREM, M. & CAGATAY,B. (1998):. An integrated study of drilling-fluid shaly rock interactions: a key to solve wellboreinstability problems. Oil Gas European Magazine, , 25-29.
- MEES, F., SWENNEN, R., VAN GEET, M, JACOBS, P. 2003: Application of X-ray Computed Tomography in the Geosciences. Geological Society Special Publication Geological Society of London, UK, no. 115.,250 p.
- VOGEL, J. R. & BROWN, G. O. (2003): Geostatistics and the representative elementary volume of 81gamma ray tomography attenuation in rock cores. In MEES et al (eds.): Application of X-ray Computed Tomography in the Geosciences. Geological Society Special Publication, 115, 81-95.

SELECTION OF THE MOST SUCCESSFUL NEURAL NETWORK ALGORITHM FOR THE PURPOSE OF SUBSURFACE VELOCITY MODELING, EXAMPLE FROM SAVA DEPRESSION, CROATIA

Marko CVETKOVIĆ¹, Josipa VELIĆ¹ and Filip VUKIČEVIĆ²

¹University of Zagreb, Faculty of Mining, Geology and Petroleum Engineering, Pierottijeva 6,
10000 Zagreb, Croatia; e-mail: marko.cvetkovic@rgn.hr

²Strme Stube 2, 22000 Šibenik, Croatia

An accurate time to depth conversion between seismic and well data (velocity modeling) is often a challenge in those hydrocarbon fields which were developed in the second part of the 20th century due to the quantity and quality of well logs. The problem is also apparent in the regional explorations where well data are scarce or spatially far apart. In this study, several neural network types were tested for the purpose of solving the time to depth relations in field with relatively dense well network, selected in the NW part of the Sava Depression, Croatia. A distinctive lithological boundary was determined within wells and its surface was interpreted from 3D seismic cube. Input data for the learning process were grid points with seismic two way time (TWT) expressed in ms and the absolute depth (Z) of the lithological borders determined from the well in part of grid points. Maps of selected borders were generated by neural prediction of time to depth relations of TWT values for each grid point. The validation of the approach was tested by comparing the values of surfaces generated by neural networks with ones by kriging and with values from wells which were subtracted from the dataset for learning. Multi-layer neural networks proved to be the most successful with the task of solving the time to depth relationships.

Keywords: *Neural networks, velocity modeling, 3D seismic, Sava Depression, Croatia.*

1. INTRODUCTION

Subsurface mapping in the domain of petroleum geology uses several inputs for obtaining maps with sufficient detail level for the task at hand, e.g. regional exploration for hydrocarbon accumulations with relatively low detail requirements or field development which requires high detail maps. End result of mapping procedure is the combination of well and seismic data. However, these two datasets are not in the same domain, well data represents depth in meters while seismic represents it in time (ms). Defining a valid relation of these two data sources is often a challenge, especially in areas and within fields which were explored in the early second part of the 20th century.

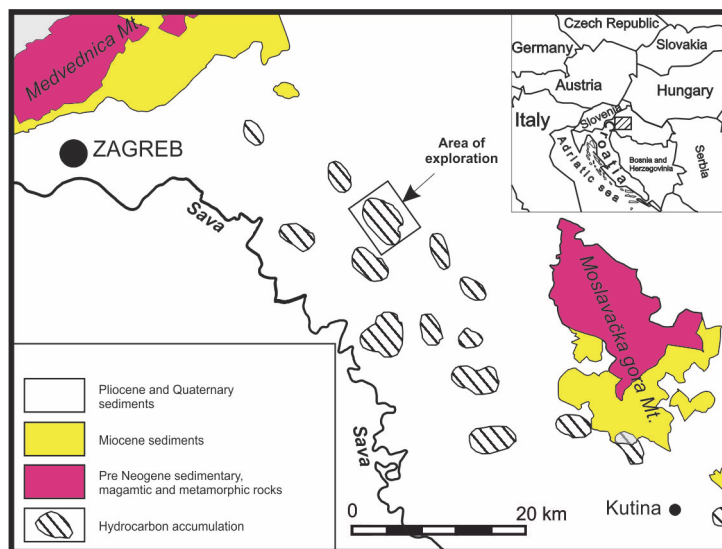


Figure 1: Location of the area of exploration (modified after Velić et al., 2011)

Well log data acquired in that time period lacked logs that are used for establishing time to depth relations (TDR) and often only consisted of conventional electric logs and determined E-log markers and borders. The second problem is the spatial distribution of the TDR or solving the TDR in the inter-well area. For all of these purposes, artificial neural networks (ANN) were used. An example is shown for solving the TDR for the deepest, least explored, E-log border Tg. Area of exploration is within an oil and gas field covered by a seismic 3D cube, located in the Sava Depression (**Figure 1**). Selection of the appropriate type of the ANN algorithm and network properties is crucial for obtaining TDR relations.

2. BASIC GEOLOGY SETTINGS

The ANN analysis will be limited only to the border of Neogene and Quaternary sediments and older pre-Neogene magmatic and metamorphic rocks. Neogene-Quaternary strata consists of heterogeneous lithology with frequent lateral changes (Malvić and Velić, 2011), thus making the TDR extremely complex. Middle Miocene Badenian and Sarmatian sediments are represented by coarse clastics, carbonates and marls while Upper Miocene intervals consist mainly of marls and sandstones with sporadic occurrences of breccias and biogenic limestones in the oldest parts of Pannonian. Youngest clastic interval of Pliocene, Pleistocene and Holocene age consists of poorly consolidated sands and clays, lignite and gravel in the youngest part. Thickness variation of the aforementioned interval is high due to the type of sedimentation and tectonic influence (Cvetković, 2013) and can have a high impact on the solving of the TDR.

3. ARTIFICIAL NEURAL NETWORKS

The basic architecture of neural networks consists of neurons that are organized into layers. A neuron is a basic element of a network that is mathematically presented as a point in space toward which signals are transmitted from surrounding neurons or inputs.

The value of a signal on the activity of a neuron is determined by a weight factor multiplied by a corresponding input signal. Total input signal is determined as a summation of all products of weight factor multiplied by the corresponding input signal given by

$$u_i = \sum_{j=1}^n (w_{ji} \cdot input_j) \quad (1)$$

where n represents the number of inputs for the neuron i . If the total input signal has a value more than the sensitivity threshold of a neuron, then it will

have an output of maximum intensity. Alternatively, a neuron is inactive and has no output. Value of the output is given by

$$output_i = F(u_i \cdot t_i) \quad (2)$$

where F represents the activation function and t_i , the targeted output value of neuron i . One can find a more detailed description of neural networks basics and methods in McCulloch and Pitts (1943), Rosenblatt (1958), and Anderson and Rosenfeld (1988).

For this analysis, several neural networks were used for comparison - multilayer perceptron (MLP) network and radial basis function (RBF) network. The MLP network is based on a backpropagation algorithm that has one or more hidden layers. The MLP is more successfully applied in classification and prediction problems (Rumelhart et al. 1986) and is the most often used neural network in solving geological problems. The RBF network is also a commonly used neural network but is more successfully and frequently applied in solving classification problems than in solving prediction problems. Neural networks have been successfully applied in petroleum geology problems such as determining reservoir properties (e.g., lithology and porosity) from well logs (Bhatt, 2002) and well-log correlation (Luthi and Bryant, 1997). In the Croatian part of the Pannonian Basin, only a few petroleum geology research projects have been performed. In these studies, clastic facies were determined from well logs (Malvić, 2006; Cvetković et al., 2009; Cvetković 2013) and porosity was predicted based on well and seismic data (Malvić and Prskalo, 2007).

4. METHODOLOGY

For the purpose of solving TDR relationship in the oil and gas field, a distinctive boundary between Neogene sediments and pre-Neogene magmatic and metamorphic rocks was selected. It's distinctive appearance on seismic and well logs (**Figure 2**) made it a good starting point for the research. Firstly the well log border Tg spatial coordinates were obtained. These consisted of well head northing and easting along with true vertical depth subsea (TVDSS).

Later, the Tg boundary was interpreted within the 3D cube for every 10th inline and xline from which the surface of the boundary was mapped with values in two way time (TWT) in ms.

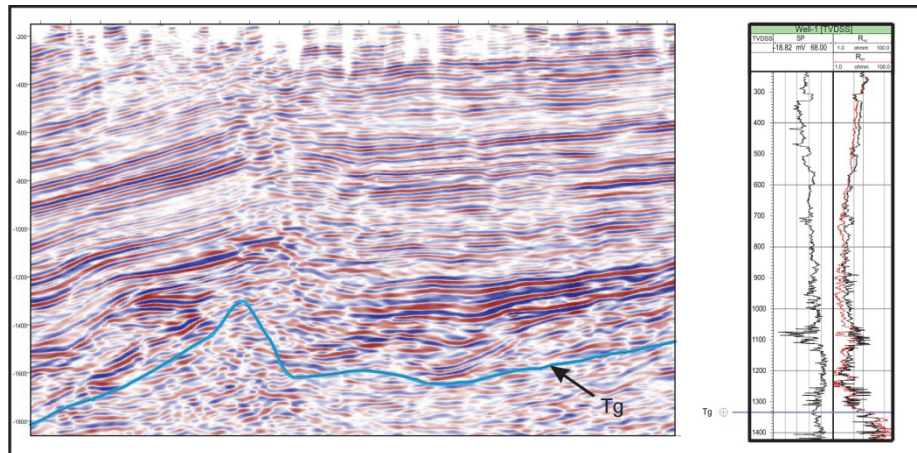


Figure 2: Distinctive appearance of the Tg boundary on seismic profiles and well logs (SP left curve; R₁₆ (black) and R₆₄ red right curves).

Dataset for training the neural networks consisted of four values of which three were defined as input and one as output variables (**Table 1**). A total of 36 values were used for ANN training process as this was the number of wells that drilled trough the Tg boundary.

Table 1: Data formatting for ANN analysis with an example

	Input variables			Output variable
Well	Northing (m)	Easting (m)	TWT (ms)	Depth (m)
Well 1	6378754,46	5065115,01	-1024,22	-1334,06

5. RESULTS

Several neural RBF and MLP networks with different properties (number of hidden layers, in the case of MPL, and with different number of neurons within hidden layers), were trained on the dataset. In general, MLP neural networks gave better results in training and selection which resulted in low error values (< 5%) while their RBF counterparts gave an average training error of 10% or more which can be at the depth of 2000 m an error of 400 m. Thus, only MLP neural networks were considered for the task of solving the TDR. Network with best properties was selected

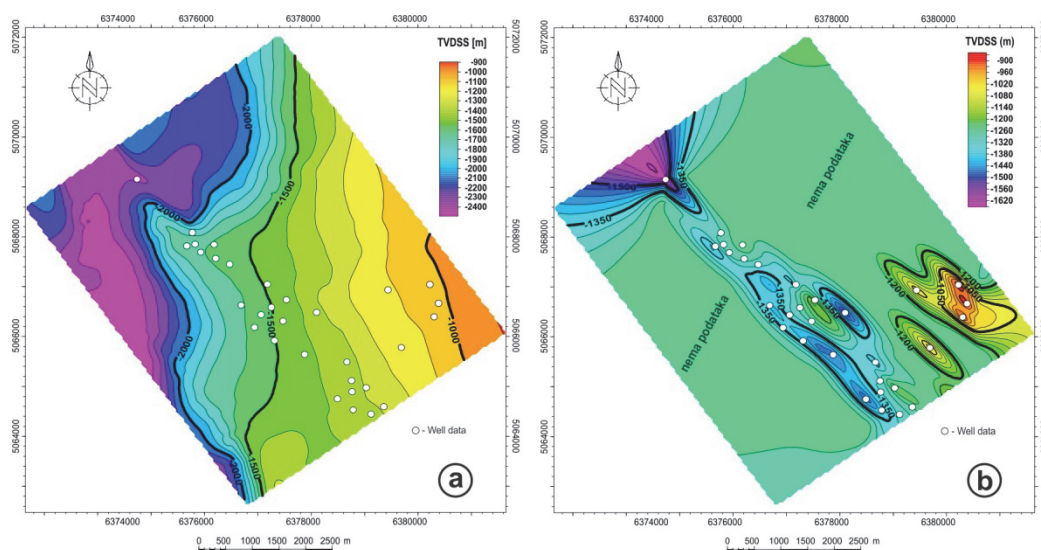


Figure 3: a – map of E-log border Tg derived from neural network TDR analysis and seismic interpretation; b – map of E-log border Tg mapped by ordinary kriging of well tops values

Trained neural network was used to predict the depth in meters from the TWT value of every node on the surface which was derived from seismic interpretation of the E-log border Tg. The surface showed high detail throughout the exploration area (**Figure 3a**). A much different structure on the resulting map (**Figure 3a**) was observed in comparison when only well data was used for mapping (**Figure 3b**, Malvić and Jović, 2012). Later, showed lots of uplifted structures which in fact resulted from small number of input wells which were placed unevenly across the field area.

6. CONCLUSIONS

For the purpose of solving TDR, MLP neural networks proved to be more successful than their RBF counterparts. Architecture of the RBF neural network with the presented task gave much larger training errors and the end result was high offset between TWT and depth values which cannot occur in the lithology that is observed within the selected oil and gas field. On the other hand, MLP neural networks showed much smaller training error and were successful in solving the TDR throughout the investigated area of the field. The

end result was the possibility of more precise mapping of the area outside well coverage. Using of the neural networks for solving the TDR gave not only the distribution of velocities in a single verticle, but for a spatial distribution throughout the whole field area.

7. ACKNOWLEDGEMENTS

This work is part of a research project “Stratigraphical and geomathematical researches of petroleum geological systems in Croatia” (project no. 195-1951293-0237), financed by the Ministry of Science, Education and Sports of the Republic of Croatia and geological research project entitled “Development of geomathematical methods for analysis of Neogene depositional environments in the Croatian part of Pannonian Basin System” financially supported by the University of Zagreb in programme “Supporting of researching 2” in the 2013. Authors would also like to thank Schlumberger supplying academic licenses for Petrel to the Faculty of Mining, Geology and Petroleum Engineering in Zagreb.

8. LITERATURE

- ANDERSON, J.A., ROSENFELD, E. (1988): Neurocomputing: Foundations of Research. MIT Press, Cambridge, 729 p.
- BHATT, A. (2002): Reservoir properties from well logs using neural networks: doctoral dissertation, NTNU, Trondheim, 151 p.
- CVETKOVIĆ, M. (2013): Naftnogeološki potencijal i litostratigrafska razradba trećega neogensko-kvartarnoga megaciklusa u Savskoj depresiji [Lithostratigraphic units of the third Neogene-Quaternary megacycle in the Sava Depression and their petroleum potential]. –PhD Thesis, University of Zagreb, Faculty of Mining, Geology and Petroleum Engineering, Zagreb, 175.
- CVETKOVIĆ, M., VELIĆ, J., MALVIĆ, T. (2009): Application of neural networks in petroleum reservoir lithology and saturation prediction. *Geologia Croatica*, 62, 2, 115-121.
- JACOBS, R.A. (1988): Increased rates of convergence through learning rate adaptation. *Neural Networks*, 1, 295-307.

LUTHI, S.M., BRYANT, I.D. (1997) Well-log correlation using a back-propagation neural network. *Math. Geol.*, 29, 3,, 413-425.

MALVIĆ, T (2006) Clastic facies prediction using neural network (case study from Okoli field). *Nafta*, 57, 10, 415-431.

MALVIĆ, T. & JOVIĆ, G. (2012): Thickness maps of Neogene and Quaternary sediments in the Kloštar Field (Sava Depression, Croatia). *Journal of Maps*, 8, 3, 260-266.

MALVIĆ, T & PRSKALO, S (2007): Some benefits of the neural approach in porosity prediction (Case study from Beničanci field). *Nafta*, 58, 9, 455-467.

MALVIĆ, T & VELIĆ, J. (2011): Neogene Tectonics in Croatian Part of the Pannonian Basin and Reflectance in Hydrocarbon Accumulations. -In: SCHATTNER, U. (ed.): *New Frontiers in Tectonic Research - At the Midst of Plate Convergence*, InTech, Rijeka, 2011, 215-238.

McCULLOCH, W.S., PITTS, W. (1943): A logical calculus of ideas immanent in nervous activity. *B. Math. Biol.*, 5, 4, 115-133.

ROSENBLATT, F. (1958): The perceptron: A probabilistic model for information storage and organization in the brain. *Psychol. Rev.*, 65, 6, 386-408.

RUMELHART D.E., HINTON, G.E., WILLIAMS, R.J. (1986): Learning internal representations by error propagation. -In: RUMELHART, D.E., McCLELLAND, J.L. (ed.) *Parallel Distributed Processing*, Vol.1. MIT Press, Cambridge, 381-362.

VELIĆ, J., MALVIĆ, T., CVETKOVIĆ, M. (2011): Palinspastic reconstruction of synsedimentary tectonics of Neogene and Quaternary sediments in the Kloštar Field (Sava Depression, Pannonian Basin, Croatia). *Zeitschrift der Deutschen Gesellschaft für Geowissenschaften*, 162, 2, 193-203.

FORWARD INTERSECTION AND ITS ACCURACY

Željka TUTEK, Miljenko LAPAINE

University of Zagreb, Faculty of Geodesy, Kaciceva 26, 10000 Zagreb, Croatia,

zeljkat@geof.hr, mlapaine@geof.hr

Consider two known points, A and B , and assume that angles, α and β , between line segment AB and lines to the unknown point T , are measured. The position of the point T is determined as the intersection of lines AT and BT , a technique often used in surveying and land navigation. It is usually said that the accuracy increases when the angle between the lines is approaching 90 degrees.

In this paper it will be shown that the highest accuracy is not achieved at the intersection of lines at a right angle. The new formula for estimating the accuracy of forward intersection, where instead of angles α and β the rectangular coordinates of the point T are used, is derived. Finally, the accuracy distribution of forward intersection is visualized as a surface in 3D and contour plot in the plane.

Key words: *forward intersection, accuracy estimation, visualization of the accuracy distribution*

1. INTRODUCTION

Point positioning is the determination of the coordinates of a point on land, at sea, or in space with respect to a coordinate system. Intersection as a trigonometric point determination method is used nowadays primarily when targets are not easily accessible, while formerly it was exclusively used for geodetic triangulation. The forward intersection technique in surveying and civil engineering uses measuring devices, such as total station, in known triangulation positions to observe the positions which cannot be physically occupied because of very long distance, swamp terrain, risk of sinking ground; or some other reason. In land navigation planar forward intersection, known as map-and-compass method and the straightedge method, is used to locate distant or inaccessible points or objects such as enemy targets and danger areas.

1.1. Definition of forward intersection

Forward intersection consists of following: we assume that two points, A and B , are given and that angles, α and β , between line segment AB and lines to the unknown point T , are measured. The position of the point T is then determined as the intersection of lines AT and BT (**Figure 1**).

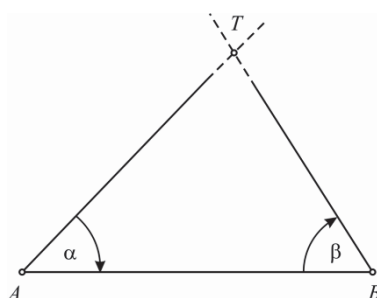


Figure 1: Forward intersection

The formula by which one can determine the position of the intersection of the observed lines can be found in almost every textbook of elementary surveying and practical or engineering geodesy (eg. Kostić, Svečnikov 1932, Macarol 1968, Cvetković 1970, Mihailović 1981, Janković 1981, Kahmen and Faig 1988). Less attention in the literature is devoted to the accuracy estimation of the so obtained intersection. Some of the approaches are flawed, and some end up with wrong conclusions.

1.2. Accuracy of forward intersection

From **Figure 2** it is easy to see that the coordinates of the point T can be calculated by the following formulas (**Formula 1**):

$$y = \frac{c}{\operatorname{ctg}\alpha + \operatorname{ctg}\beta}, \quad x = y \operatorname{ctg}\alpha = \frac{c \operatorname{ctg}\alpha}{\operatorname{ctg}\alpha + \operatorname{ctg}\beta}. \quad (1)$$

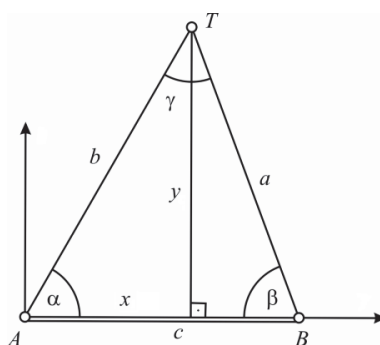


Figure 2. Forward intersection (Mihailović, 1981)

If we assume that c , the distance between the points A and B , is completely accurate then the position of point T will depend only on the accuracy of the angles α and β . Squared mean errors m_x and m_y of the coordinates of point T will be:

$$m_x^2 = \left(\frac{\partial x}{\partial \alpha}\right)^2 m_\alpha^2 + \left(\frac{\partial x}{\partial \beta}\right)^2 m_\beta^2, \quad m_y^2 = \left(\frac{\partial y}{\partial \alpha}\right)^2 m_\alpha^2 + \left(\frac{\partial y}{\partial \beta}\right)^2 m_\beta^2, \quad (2)$$

where

$$\begin{aligned} \frac{\partial x}{\partial \alpha} &= \frac{-c \operatorname{ctg} \beta}{(\operatorname{ctg} \alpha + \operatorname{ctg} \beta)^2} \frac{1}{\sin^2 \alpha} = -c \frac{\sin \beta \cos \beta}{\sin^2 \gamma} \\ \frac{\partial x}{\partial \beta} &= \frac{c \operatorname{ctg} \alpha}{(\operatorname{ctg} \alpha + \operatorname{ctg} \beta)^2} \frac{1}{\sin^2 \beta} = c \frac{\sin \alpha \cos \alpha}{\sin^2 \gamma} \\ \frac{\partial y}{\partial \alpha} &= \frac{c}{(\operatorname{ctg} \alpha + \operatorname{ctg} \beta)^2} \frac{1}{\sin^2 \alpha} = c \frac{\sin^2 \beta}{\sin^2 \gamma} \\ \frac{\partial y}{\partial \beta} &= \frac{c}{(\operatorname{ctg} \alpha + \operatorname{ctg} \beta)^2} \frac{1}{\sin^2 \beta} = c \frac{\sin^2 \alpha}{\sin^2 \gamma}, \end{aligned} \quad (3)$$

because of $\operatorname{ctg} \alpha + \operatorname{ctg} \beta = \frac{\sin(\alpha + \beta)}{\sin \alpha \sin \beta} = \frac{\sin \gamma}{\sin \alpha \sin \beta}$

and with notation $\gamma = 180^\circ - (\alpha + \beta)$.

If we substitute (3) in (2) we get

$$m_x^2 = c^2 \frac{\sin^2 \beta \cos^2 \beta m_\alpha^2 + \sin^2 \alpha \cos^2 \alpha m_\beta^2}{\sin^4 \gamma}, \quad m_y^2 = c^2 \frac{\sin^4 \beta m_\alpha^2 + \sin^4 \alpha m_\beta^2}{\sin^4 \gamma}$$

and thence

$$M^2 = m_x^2 + m_y^2 = c^2 \frac{\sin^2 \beta m_\alpha^2 + \sin^2 \alpha m_\beta^2}{\sin^4 \gamma}, \quad M = c \frac{\sqrt{\sin^2 \beta m_\alpha^2 + \sin^2 \alpha m_\beta^2}}{\sin^2 \gamma}.$$

2. DISTRIBUTION OF THE ACCURACY FOR FORWARD INTERSECTION POINT POSITIONING

The assumption of $m_\alpha = m_\beta$ is common practice and we get simplified formula

$$M = c \frac{\sqrt{\sin^2 \beta + \sin^2 \alpha}}{\sin^2 \gamma} m_\alpha. \quad (4)$$

The equation (4) defines a parameterized surface with two parameters α and β . This raises several questions. What can we say about the surface? Can we visualize it somehow? Can we represent it with isolines $z = \text{const.}$ in the xy – plane?

The coordinates of the point T (see **Figure 2**) are as follows:

$$x = b \cos \alpha, \quad y = b \sin \alpha \quad \text{where} \quad b = c \frac{\sin \beta}{\sin(\alpha + \beta)}.$$

For angles $\alpha, \beta \in \left(0, \frac{\pi}{2}\right)$ we derive the following relationships

$$\tan \alpha = \frac{y}{x}, \quad \tan \beta = \frac{y}{c-x}, \quad \sin^2 \alpha = \frac{y^2}{x^2 + y^2}, \quad \sin^2 \beta = \frac{y^2}{(c-x)^2 + y^2},$$

$$\alpha + \beta = \arctan \frac{y}{x} + \arctan \frac{y}{c-x} = \arctan \frac{\frac{y}{x} + \frac{y}{c-x}}{1 - \frac{y}{x} \frac{y}{c-x}} = \arcsin \frac{\frac{cy}{x(c-x) - y^2}}{\sqrt{1 + \left(\frac{cy}{x(c-x) - y^2}\right)^2}}$$

$$\sin^2(\alpha + \beta) = \frac{\left(\frac{cy}{x(c-x) - y^2}\right)^2}{1 + \left(\frac{cy}{x(c-x) - y^2}\right)^2} = \frac{c^2 y^2}{[x(c-x) - y^2]^2 + c^2 y^2}.$$

It can be easily shown that the last relation holds for all angles $\alpha, \beta \in (0, \pi)$ for which $\alpha + \beta < \pi$. And so we get the expression for z as function of rectangular coordinates of the point T

$$z = cm_\alpha \frac{\sqrt{\sin^2 \alpha + \sin^2 \beta}}{\sin^2(\alpha + \beta)} = cm_\alpha \left\{ \left[\frac{x(c-x) - y^2}{cy} \right]^2 + 1 \right\} \sqrt{\frac{y^2}{x^2 + y^2} + \frac{y^2}{(c-x)^2 + y^2}}$$

that allows us to visualize the distribution of the accuracy for forward intersection point positioning (**Figures 3 and 4**).

3. OPTIMUM FORWARD INTERSECTION POINT

Furthermore, if $\alpha = \beta$ then $\alpha = \beta = 90^\circ - \frac{\gamma}{2}$ and the **Formula 4** may be written

as
$$M = c\sqrt{2} \frac{\cos \frac{\gamma}{2}}{\sin^2 \gamma} m_\alpha.$$

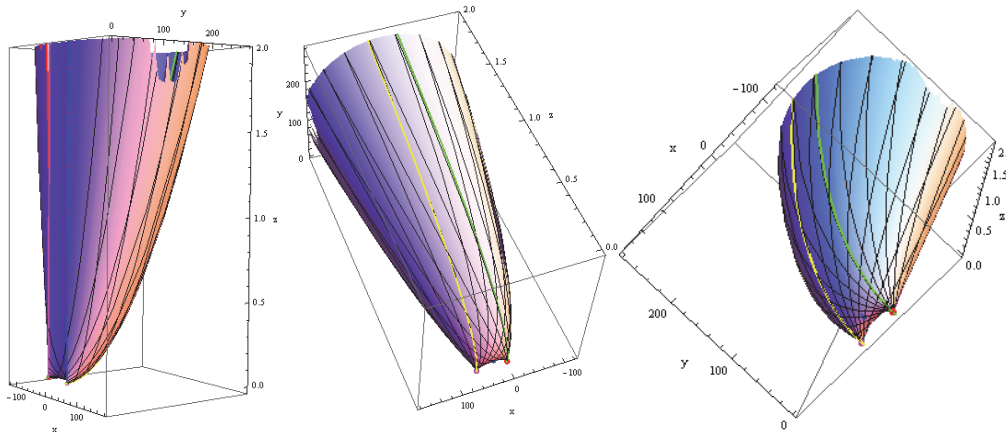


Figure 3. Accuracy distribution as a surface in 3D

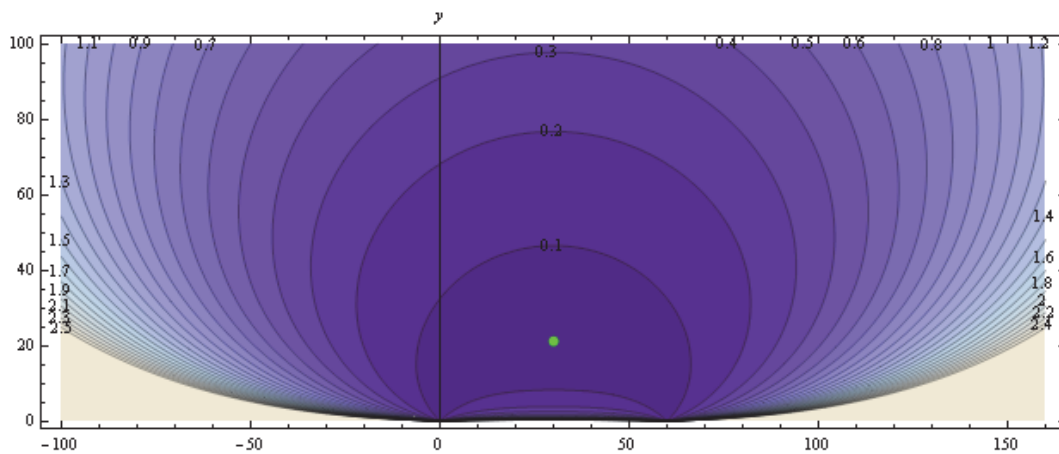


Figure 4. Contour lines for accuracy distribution

In order to find the minimum of the function $M = M(\gamma), \gamma \in (0^\circ, 180^\circ)$ its derivative must be equal to zero:

$$\frac{dM}{d\gamma} = 0.$$

Last equation for γ is equivalent to $\sin \frac{\gamma}{2} \sin \gamma + 4 \cos \frac{\gamma}{2} \cos \gamma = 0$

and the solution is: $\tan \frac{\gamma}{2} = \sqrt{2}$

$$\text{i.e. } \gamma = 109^\circ 28', \alpha = \beta = 35^\circ 16'. \quad (5)$$

In order to complete the proof it is needed to show that the critical point has the property $\alpha = \beta$. We remark that function $M = M(\alpha, \beta)$ is not defined for $\sin(\alpha + \beta) = 0$. It is a positive function and therefore it is enough to find extreme values of function

$$M^2 = M^2(\alpha, \beta) = c^2 \frac{\sin^2 \beta + \sin^2 \alpha}{\sin^4(\alpha + \beta)} m_\alpha^2.$$

Its partial derivatives are shown in **Formula 6** and **Formula 7**.

$$\frac{\partial M^2}{\partial \alpha} = \frac{c^2 m_\alpha^2}{\sin^5(\alpha + \beta)} [\sin 2\alpha \sin(\alpha + \beta) - 4(\sin^2 \alpha + \sin^2 \beta) \cos(\alpha + \beta)] = 0 \quad (6)$$

$$\frac{\partial M^2}{\partial \beta} = \frac{c^2 m_\alpha^2}{\sin^5(\alpha + \beta)} [\sin 2\beta \sin(\alpha + \beta) - 4(\sin^2 \alpha + \sin^2 \beta) \cos(\alpha + \beta)] = 0. \quad (7)$$

By subtracting equation (7) from (6) we get the equation

$$\frac{c^2 m_\alpha^2}{\sin^4(\alpha + \beta)} (\sin 2\alpha - \sin 2\beta) = 0 \text{ from which follows } \cos(\alpha + \beta) \sin(\alpha - \beta) = 0.$$

There are two cases:

a) $\cos(\alpha + \beta) = 0$

In this case $\sin(\alpha + \beta) = 1$ or $\sin(\alpha + \beta) = -1$. According to the equations (6) or (7) it implies that $\sin 2\alpha = 0$ and $\sin 2\beta = 0$ and for forward intersection that has no sense.

b) $\sin(\alpha - \beta) = 0$

Then $\alpha = \beta$ or their difference is a multiple of 180° . The second possibility has no sense for forward intersection. We conclude that the critical point of function M^2 has the property (**Formula 8**):

$$\alpha = \beta. \quad (8)$$

Taking into account (8), it is clear that the equations (6) and (7) are identical. After some further manipulations we obtain

$$\sin^2 \alpha (3 \sin^2 \alpha - 1) = 0.$$

Solutions $\alpha = 0^\circ$ or a multiple of 180° have no sense for forward intersection.

It follows that
$$\sin \alpha = \pm \frac{\sqrt{3}}{3}.$$

For angle $\alpha \in (0^\circ, 180^\circ)$ sine value is positive and so

$$\sin \alpha = \sin \beta = \frac{\sqrt{3}}{3}, \quad \sin \gamma = \sin(\alpha + \beta) = \sin 2\alpha = \frac{2\sqrt{2}}{3}.$$

The three triangle angles are $\alpha = \beta = 35^\circ 16'$, $\gamma = 109^\circ 28'$.

This is consistent with the previous result (**Equation 5**). In this critical point the extreme value is

$$M^2 = \frac{27}{32} c^2 m_\alpha^2, \quad \text{i.e.} \quad M = \frac{3\sqrt{3}}{4\sqrt{2}} cm_\alpha.$$

The last unanswered question is that if the computed value is really a minimum of function M . In order to answer, we should apply the second derivate test at the critical point.

At the critical point the second derivatives have these values:

$$\frac{\partial^2 M^2}{\partial \alpha^2} = \frac{\partial^2 M^2}{\partial \beta^2} = \frac{189}{64} c^2 m_\alpha^2, \quad \frac{\partial^2 M^2}{\partial \alpha \partial \beta} = \frac{\partial^2 M^2}{\partial \beta \partial \alpha} = \frac{135}{64} c^2 m_\alpha^2.$$

$$\text{Since } \frac{\partial^2 M^2}{\partial \alpha^2} > 0 \text{ and } \frac{\partial^2 M^2}{\partial \alpha^2} \frac{\partial^2 M^2}{\partial \beta^2} - \frac{\partial^2 M^2}{\partial \alpha \partial \beta} \frac{\partial^2 M^2}{\partial \beta \partial \alpha} > 0,$$

we conclude that at the critical point the function M has a minimum i.e.

$$M_{\min} = \frac{3\sqrt{3}}{4\sqrt{2}} cm_\alpha \approx 0,91856 cm_\alpha.$$

For $\alpha = \beta = 45^\circ$, $\gamma = 90^\circ$: $M = cm_\alpha > M_{\min}$ (**Figure 5**).

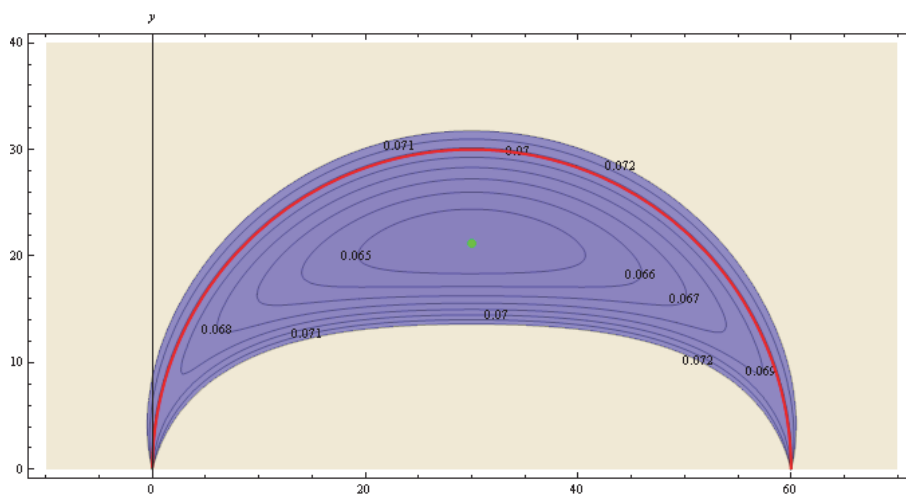


Figure 5. Optimum forward intersection point

4. INSTEAD OF CONCLUSION

In this paper we derive a new formula for estimating the accuracy of forward intersection where instead of angles α and β the rectangular coordinates of the point T are used.

It would be interesting to explore:

- accuracy of point positioning by forward intersection in cases when the observed lines are defined with two points, instead of one point and one angle as has been seen here,
- relationships between the accuracy estimations for a point determined by two different methods: forward intersection and arc section.

5. REFERENCES

- CVETKOVIĆ, Č. (1970): Primena geodezije u inženjerstvu (Application of Geodesy in Engineering), Građevinska knjiga, Beograd
- JANKOVIĆ, M. (1981): Inženjerska geodezija II (Engineering Geodesy II), 2. dopunjeno izdanje, Sveučilišna naklada Liber, Zagreb
- KAHMEN H., FAIG W. (1988): Surveying, Walter de Guyter, Berlin
- KOSTIĆ, A. L., SVEČNIKOV, N. S. (1932): Geodezija (Geodesy), Trigonometrijska, poligona i linijska mreža, Beograd, 26–30
- MACAROL, S. (1968): Praktična geodezija (Practical Geodesy), 2. izdanje, Tehnička knjiga, Zagreb
- MIHAILOVIĆ, K. (1981): Geodezija II (Geodesy II), I deo, Građevinska knjiga, Beograd, 10–12, 268–272

WHY WE USE SIMPSON AND TRAPEZOIDAL RULE FOR HYDROCARBON RESERVOIR VOLUME CALCULATION?

Tomislav MALVIĆ^{1,2}, Kristina NOVAK ZELENKA²

¹University of Zagreb, Faculty of Mining, Geology and Petroleum Engineering, Pierottijeva 6,
10000 Zagreb, HR, tomislav.malvic@ina.hr,

²INA Plc., Šubićeva 29, 10000 Zagreb, HR, kristina.novakzelenika@ina.hr

The calculation of hydrocarbon reservoir volume using solid is numerical integration problem. It is solved by numerical integration of function $f(x)$, i.e. integrand, continuous in interval $a \leq x \leq b$. It includes approximation of $f(x)$ with polynomial functions, like trapezoidal of Simpson formulas. Smaller calculation error can be reached by using Simpson rule based onto Lagrange polynomial. These two rules are regularly used for reservoir volume calculation, where trap anticline is approximated by frustum right circular cone. The error can be decreased with lowering equidistance between integrated areas.

Key words: *reservoir, volume, Sampson rule, trapezoidal rule.*

1. INTRODUCTION

An approximate value of the integral $\int_a^b f(x) dx$ can be calculated by (a) numerical formulas and (b) mechanical integrators like the planimeter. However, in both cases approximations are necessities. For example, measured data has only certain accuracy. Interpolation, visualization etc. are also approximation methods that could not reach higher accuracy then measurements itself. Often, subsurface structures are irregular and cannot be integrated by exclusively usage of elementary integral functions. It is why there are several methods of approximate integration, using planimeter for areal calculation and Simpson or trapezoidal rules for summation of integrals.

2. PRISMOIDAL FORMULA

The prismoidal formula is expression for volume calculation of any solid as prismoids and prismatoids. They can be suitably decomposed into prisms or related solids as pyramids and frustum of pyramids. In the following text terms (Nelson, ed., 1998) *prismatoid, prismoid, prism and frustum of pyramid* are explained. **Prismatoid** is a polyhedron with vertices that all lie in one or other

of two parallel planes. The two faces of the prismatoid lying in these planes are its bases. They do not necessarily both have the same number of sides. **Prismoid** is a prismatoid in which: (a) both bases have an equal number of sides, and (b) the lateral faces are quadrilaterals (either trapeziums or parallelograms). **Prism** is a special case of a prismoid in which the bases are identical. **Frustum of pyramid** is a prismoid in which the bases are (geometrically) similar. Volume of any regular frustum is:

$$V = \frac{1}{3} (A_1 + A_2 + \sqrt{A_1 A_2}) h \quad (\text{Eq. 2.1})$$

2.1. Frustum of a regular pyramid

Frustum of a regular pyramid is a portion of right regular pyramid included between the base and a section parallel to the base (**Figure 2.1**).

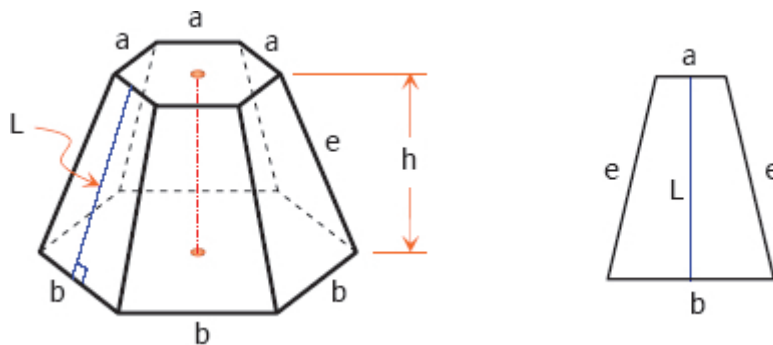


Figure 2.1: Frustum of regular pyramid (from web 1)

Elements of a frustum of regular pyramid (web 1) are: a = upper base edge; b = lower base edge; e = lateral edge; h = altitude; L = slant height; A_1 = area of lower base; A_2 = area of upper base; n = number of lower base edges. Properties of a frustum of regular pyramid (**Figure 2.1**) are: (a) the slant height of a frustum of a regular pyramid is the altitude of the face; (b) the lateral edges of a frustum of a regular pyramid are equal, and the faces are equal isosceles trapezoids; (c) the bases of a frustum of a regular pyramid are similar regular polygons. If these polygons become equal, the frustum will become prism.

Volume is defined as: $V = \frac{1}{3} (A_1 + A_2 + \sqrt{A_1 A_2}) h \quad (\text{Eq. 2.2})$

Lateral area as: $A_L = \frac{1}{2} n(a + b)L \quad (\text{Eq. 2.3})$

The relationship between L , b , a , e is: $(b - a)^2 + 4L^2 = 4e^2 \quad (\text{Eq. 2.4})$

2.2. Frustum of a right circular cone

That is that portion of right circular cone included between the base and a section parallel to the base not passing through the vertex.

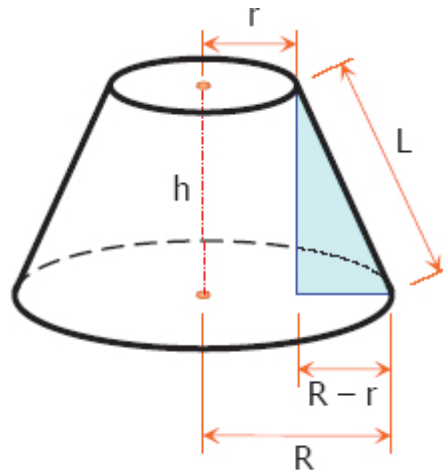


Figure 2.2.: Frustum of a right circular cone (web 1)

Properties (web 1) of frustum of right circular cone (**Figure 2.2**) are: (a) the altitude of a frustum of a right circular cone is the perpendicular distance between the two bases. It is denoted by 'h'; (b) all elements 'L' of a frustum of a right circular cone are equal.

Area of lower base is: $A_1 = \pi R^2$ (Eq. 2.5)

Area of upper base: $A_2 = \pi r^2$ (Eq. 2.6)

If 'C' and 'c' are the circumference of lower and upper bases the lateral area is: $A_L = \frac{1}{2}(C + c)L$ (Eq. 2.7)

Substitutions $C = 2\pi R$ and $c = 2\pi r$ giving $A_L = \pi(R + r)L$ (Eq. 2.8)

The relationship between L, R, h, and r is: $(R - r)^2 + h^2 = L^2$ (Eq. 2.9)

Volume of frustum of right circular cone:
 $V = \frac{1}{3}\pi(R^2 + r^2 + Rr)h$ (Eq.2.10)

3. APPLICATION OF PRISMOIDAL FORMULA

The prismoidal formula that could be applied for any prismatoid solid is:

$$V = \frac{h}{6}(A_1 + 4A_2 + A_3)$$
 (Eq. 3.1)

Where are:

A_1, A_3 - areas of the bases which distance apart with 'h';

A_2 - area of the cross-section parallel and halfway between end planes.

This formula is direct consequence of application of **Theorem 1** for integration of prismatoid areas (e.g., **Figure 2.2**) with polynomial of degree 3 or less:

$$\int_a^b f(x)dx = \frac{b-a}{6} \left[f(a) + f\left(\frac{a+b}{2}\right) + f(b) \right]$$

(Theorem 1)

Where are:

$f(a)$ - value of integrand when 'x=a',

$f(b)$ - value of integrand when 'x=b',

$f\left(\frac{a+b}{2}\right)$ - value of integrand when x is halfway between 'a' and 'b'.

The prismoidal formula gives exact volume of any solid bounded by quadric surface and two parallel planes. However, **for solids that don't satisfy the specified conditions, the prismoidal formula gives an approximation to the volume.** However, it can be used with a fair degree of accuracy for almost any solid whose surface does not have sudden extensive breaks and irregularities (e.g., **Figure 3.2**). In addition, the highly irregular surface may be divided into portions for which the formula holds. Both these properties made such approach widely used in earth sciences, especially petroleum geology, for subsurface volume calculation, i.e. mostly for the approximately anticline hydrocarbon reservoir volume estimation (e.g., **Figure 3.2**).

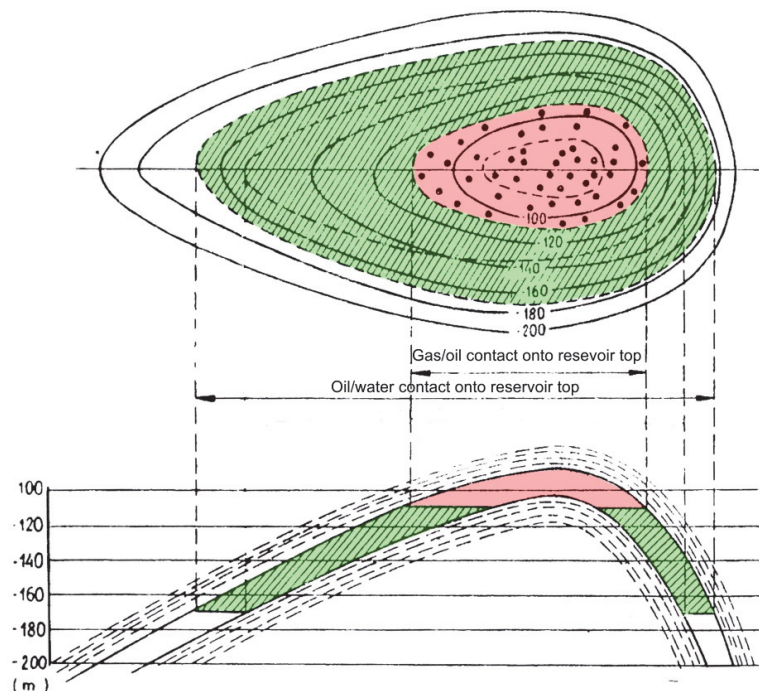


Figure 3.2: Example of brachianticline (Malvić and Velić, 2008; taken from Brod and Jeremenko, 1957) with different margin dips

4. TRAPEZOIDAL RULE

The often modification of general prismoidal formula is named trapezoid rule. It is described by e.g. Atkinson (1989) or Rahman and Schmeisser (1990). It can be applied for approximation of the value of the definite integral $\int_a^b f(x)dx$ for 2D problem, like it is shown for curve (**Figure 4.1**) or solid faces (**Figure 2.1**) and for 3D problem like frustum of pyramid.

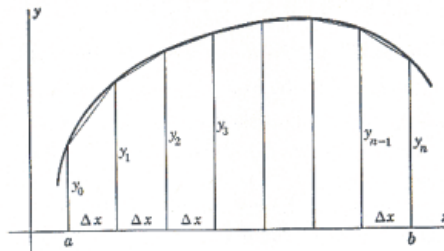


Figure 4.1: Example of definite integral calculated using trapezoids

The integral is divided for 'X=a to b' into 'n' equal step subintervals (trapezoids) of same length ' $\Delta x=(b-a)/n$ ', which cut the ordinate at ' $y_0, y_1...y_n$ ' (**Figure 4.1**). Note that Δx do not be equal. The sum of trapezoids is approximation of the area under the curve.

$$A(\text{trapezoids}) = \frac{1}{2}(y_0 + y_1)\Delta x + \dots + \frac{1}{2}(y_{n-1} + y_n)\Delta x = \Delta x\left(\frac{1}{2}y_0 + y_1 + \dots + y_{n-1} + \frac{1}{2}y_n\right) \quad (\text{Eq. 4.1})$$

The accuracy depends upon the number of trapezoids and the shape of the function $f(x)$. Integral of the trapezoidal rule (e.g., Kevo, 1986) is:

$$\int_a^b f(x)dx \cong \frac{h}{2} [f(a) + 2\sum_{i=1}^{n-1} f(x_i) + f(b)] \quad (\text{Eq. 4.2})$$

The number of integration intervals is ' $n=(b-a)/h$ '. The error of function break is proportional with ' h^2 ', and error of successive summation is approx. ' $1/h$ '. It means that for each particular case there is **optimal values 'h' and 'n'** (number of intervals) where approximation error is the lowest.

5. SIMPSON RULE

The Simpson rule is another special case of the prismoidal formula described by e.g. Atkinson (1989) where the value of integrand is defined as polynomial of degree 3 or less, where the area of integration is given by:

$$A = \frac{b-a}{6} [y_a + 4y_{\frac{a+b}{2}} + y_b] \quad (\text{Eq. 5.1})$$

If $f(x)$ is polynomial of 4th or more degree then and approximation of area is given with area under parabola:

$$y = Ax^2 + Bx + C \quad (\text{Eq. 5.2})$$

The Simpson formula is more precise than trapezoidal due to approximation (interpolation) function is polynomial of higher degree. When such function, e.g., Lagrange, is applied for some equidistance 'h' the formula is:

$$\int_{-h}^h f(x)dx = \frac{h}{3} (y_{-1} + 4y_0 + y_{+1}) \quad (\text{Eq. 5.3})$$

If the number of integration interval even ('n=2m') for 'x₀=a, x₁... x_n=x_{2m}=b' the expression can be extended into:

$$\int_a^b f(x)dx = \frac{h}{3} [(y_a + 4y_1 + y_2) + (y_2 + 4y_3 + y_4) + \dots + (y_{n-2} + 4y_{n-1} + y_b)] \quad (\text{Eq. 5.4})$$

$$\int_a^b f(x)dx = \frac{h}{3} (y_a + \sum_{i=1}^m (4y_{2i-1} + 2y_{2i}) + y_{2m}) \quad (\text{Eq. 5.5})$$

The error of break is proportional with 'h⁴', and error of successive summation is approx. '1/h'. The optimal number of integral intervals is n=2m=2^k. It is often successive increased like 2^{k+1}, 2^{k+2}, 2^{k+3} etc. (e.g. Kevo, 1986), until the absolute error between two successive results is not less than error tolerance. It means that for each particular case there is **optimal values 'h' and 'n'** (number of intervals) where is approximation error the lowest. The number of integration intervals is 'n=(b-a)/h'.

6. RESERVOIR VOLUME CALCULATION

The Simpson rule is regularly applied for reservoir volume calculation, when the structure is or closely regular anticline, i.e., could be approximated with frustum of right circular cone. Such approximation can be weak in case of very irregular or faulted anticline, and especially of folded monocline, and it is why these are simultaneously calculated by both Simpson and trapezoidal equation. If the difference of results is not more than 20%, the Simpson volume can be accepted and mapping equidistance is proper selected. An example is shown (**Figure 6.1**) of complex structure which is monocline with irregular anticline as part of it.

$$V_t = h \left(\frac{a_0}{2} + a_1 + a_2 + a_3 + a_4 + \frac{a_5}{2} \right) \quad (\text{Eq. 6.5})$$

The trapezoidal volume was 11,368,000 m³. The difference between volumes had been about 15% what is significant, but acceptable. Generally, when the structure is very far from dome or regular anticline, the approximation error is large.

7. CONCLUSIONS

There is crucial need that engineers included in reservoir volume calculation know basics of theory that lead to practical results. It is why this paper is given as short booklet with basic mathematical formulas and especially geometrical solids that are acceptable numerical and geometrical approximations in such calculations.

8. ACKNOWLEDGMENT

This researching had been part of project “Development of geomathematical methods for analysis of Neogene depositional environments in the Croatian part of the Pannonian Basin System”. The project was approved from University of Zagreb in program “Support to researching II” for 2013.

9. REFERENCES

1. ATKINSON, K. E. (1989): An introduction to Numerical Analysis. 2nd ed., John Wiley and Sons, 712 p., New York.
2. BROD, I. O. & JEREMENKO, N. A. (1957): Osnovi geologije nafte i gasa. Izdanje treće, Gostoptehizdat, 480 p., Moskva.
3. KEVO, M. (1986): Numerička integracija (Numerical integration – Slovenian, issue in Serbian). Moj mikro, 2, 7, 25-28.
4. Nelson, D. (editor) (1998): The Penguin dictionary of Mathematics. 2nd edition, Penguin Books Ltd., 461 p., London.
5. MALVIĆ, T. & VELIĆ, J. (2008): Geologija ležišta fluida (Geology of reservoir's fluids – in Croatian). University of Zagreb, Faculty of Mining, Geology and Petroleum Engineering, scripts, 139 p.
6. RAHMAN, Q. I. & SCHMEISSER, G. (1990): Characterization of the speed of convergence of the trapezoidal rule. Numerische Mathematik, 57, 1, 123-138.

Internet sources:

web 1: <http://www.mathalino.com/reviewer/solid-mensuration-solid-geometry/frustum-regular-pyramid>

web 2: <http://www.mathpages.com/home/kmath189/kmath189.htm>

web 3:

http://www1.uis.no/Fag/Learningspace_kurs/PetBachelor/webpage/tech%5CReservoir%5CMBE%5CResEvaluationDriveMech.pdf

ASSESSING NATURAL AND ANTHROPOGENIC IMPACT ON SOIL CHEMISTRY USING PRINCIPAL COMPONENT ANALYSIS FOR COMPOSITIONAL DATA

Danijel IVANIŠEVIĆ^{1,*}, Josip HALAMIĆ¹, Zoran PEH¹

¹Croatian Geological Survey, Sachsova 2, 10000 Zagreb, Croatia

*corresponding author, divanisevic@hgi-cgs.hr

For the purpose of this study, two surface soil samples (0-5 and 5-10 cm) were collected on each of the 36 regular grid locations around the fertiliser plant in Kutina, Croatia. Samples were analysed on chemical composition and statistically processed using principal component analysis. Concentrations of chemical elements are a typical example of compositional data. Such data form simplex space which has different properties than Euclidean space. Accordingly, data have to be properly transformed so that standard statistical methods can be safely applied. In this paper, efficiency of log and isometric log-ratio transformation in principal component analysis was tested. It was shown how compositional data methodology can improve the results of analysis and provide new possibilities in interpretation and determination of the associations of chemical elements and observations.

Keywords: *compositional data, principal component analysis.*

1. INTRODUCTION

Geochemical data are a typical example of compositional data. They consist of positive values and sum up to a constant k , usually 100 (if data are expressed in percentages) or 1,000,000 (if data are expressed in parts per million). Moreover, such data are related in a way that an increment (or decrement) of one variable must result in a decrement (or increment) of at least one other variable. According to these facts, such data form constrained sample space which is actually a subspace of the Euclidean space in which variables can range from $-\infty$ to $+\infty$. Thereby, standard statistical methods based on the Euclidean geometry are not applicable for compositional data (Pawlowsky-Glahn & Egozcue, 2006). To transform data from their own natural sample space (simplex space) to the Euclidean sample space, and therefore to apply standard statistical methods (e.g. principal component analysis; PCA), a proper transformation has to be applied. The main objective of this study is to show advantages of the log-ratio transformations over log-transformations in the PCA of the geochemical data from an environmental study.

2. STUDY AREA DESCRIPTION

Study area comprises the city of Kutina and surroundings. Kutina is situated in the lowlands of the central Croatia, on the southern flanks of the Mt Moslavačka and north of the Lonjsko polje depression. Area of the 40% is covered with forest and 50% with agricultural land. Climate is moderately continental (Rabljenović et al., 2007).

Details about the geology of the investigated area were given by e.g. Crnko (1998; 2014-in print) and Jurak et al. (2006). Quaternary rocks characterise the greatest part. Interstratified inland loess, lake and pond sediments and alluvial sediments form Pleistocene deposits. Holocene deposits are composed of deluvial-proluvial, proluvial and alluvial, organic-pond and flood plain sediments, derived from Mt Moslavačka and surrounding hills. Description of the Mt Moslavačka geology can be found in e.g. Jurković (2003).

Most of the soil of the investigated area is hydromorphic, predominantly pseudogley. Pseudogley is related to the surface water regime and is characterised by wet and dry periods (Jones et al., 2005).

The main sources of the anthropogenic contamination in the investigated area are the fertiliser plant and agriculture. (Rabljenović et al., 2007). The fertiliser plant processes phosphate ore from Khouribga, Morocco (Franković et al., 2013).

In general, the sampling grid was regular. On each sample site, top (0-5 cm) and bottom (5-10 cm) part of the top soil horizon were sampled.

3. APPLIED STATISTICAL ANALYSIS

Statistical analysis was performed using *R*, open source software for statistical computing.

3.1. Centred log-ratio and isometric log-ratio transformation

The *clr*-transformation (Aitchison, 1986) transforms vectors of compositions from simplex space to the Euclidean space. Sum of the values of such vectors is 0 and accordingly, they lie on the hyperplane which goes through the origin of \mathbb{R}^D . A covariance matrix of this kind of transformed data is singular so determinant is 0. This is a problem for using some methods, i.e. a PCA which rely on the full rank matrices. Expression for the *clr*-transformation is:

$$y = (y_1, \dots, y_D) = \left(\ln \frac{x_1}{\sqrt[D]{\prod_{i=1}^D x_i}}, \dots, \ln \frac{x_D}{\sqrt[D]{\prod_{i=1}^D x_i}} \right), \text{ for } i = 1, \dots, D. \quad (1)$$

The *ilr*-transformation results with coordinates in the $D - 1$ -dimensional Euclidean space. It is based on the choice of an orthonormal basis which is on the same hyperplane formed by the *clr*-transformation. There are infinite choices for such orthonormal basis. One of them was proposed by Egozcue et al. (2003):

$$v_i = \sqrt{\frac{i}{i+1}} \left(\frac{1}{i}, \dots, \frac{1}{i}, -1, 0, \dots, 0 \right) \text{ for } i = 1, \dots, D - 1. \quad (2)$$

The *ilr*-transformation with respect to the chosen base (**Eq.2.**) is then:

$$z_i = \sqrt{\frac{i}{i+1}} \ln \sqrt{\frac{\prod_{j=1}^i x_j}{x_{i+1}}} \text{ for } i = 1, \dots, D - 1. \quad (3)$$

Opposite from the *clr*-transformed data, the *ilr*-transformed data doesn't result with a singular matrix, and still, there is a relation between *clr*- and *ilr*-transformed data (see Egozcue et. al, 2003). Using **Eq.1.** and **Eq.3.** this relation can be expressed in matrix form as:

$$y = Vz \text{ and } z = V'y, \quad (4)$$

where $V = (v_1, \dots, v_{D-1})$ is the $D \times (D - 1)$ matrix with an orthonormal basis vectors from **Eq.2..**

3.2. Principal component analysis

The PCA is a multivariate statistical method used to reduce the dimensionality of the data set (see e.g. McKillup & Darby Dyar, 2010). It provides a way to find principal directions which capture the most variation of the data. In other words, performing the PCA, one searches for coherent subsets of correlated variables that are relatively independent of one another (Tabachnik & Fidell, 2007). First PC (PC1) captures the most variation and is related to the first subset, second PC (PC2) captures less variation and is related to the second subset, and so on. The number of components is less than or equal to the number of variables, but usually the first two or three PCs capture the majority of the total variation of the data set.

Every data set forms sample space defined by its coordinate axes. The PCs are found by rotation of the coordinate axes until the covariance matrix of the data set becomes diagonal (non-diagonal elements are 0). This means that new variables are uncorrelated (McKillup & Darby Dyar, 2010). Eigenvectors are vectors that define directions of the new axes and eigenvalues are their associated values which describe the variance along the new axes. Eigenvalues stand for the diagonal elements of the matrix formed after rotation. The eigenvector with the associated highest eigenvalue stands for the direction with the highest variation. The eigenvector with the second highest eigenvalue is orthogonal to the first one and captures the next highest variation, and so on.

If A is an $n \times n$ matrix (i.e. the covariance matrix; n is the number of variables), the eigenvalues (λ) of A are found by solving the characteristic polynomial:

$$\det(A - \lambda I) = 0, \quad (5)$$

where I is the $n \times n$ identity matrix (i.e. diagonal elements are 1s and off-diagonal elements are 0s). The eigenvectors are defined by the equation:

$$Ax = \lambda x, \quad (6)$$

where x is the eigenvector of A with the associated eigenvalue λ . From the **Eq.6.** it can be seen that there are infinite solutions for x . This is because x is only the direction vector. After all the eigenvectors had been calculated, they were normalised in a way that x was the length of 1 (unit vector), i.e. $xx^T = 1$.

If the eigenvectors of A are written as columns of the matrix Φ , and the associated eigenvalues in the form of a diagonal matrix Λ , **Eq.6.** can be written as:

$$A\Phi = \Lambda\Phi, \quad (7)$$

The eigenvectors are orthogonal and normalised so that:

$$\Phi\Phi^T = \Phi^T\Phi = I. \quad (8)$$

From the **Eq.7.** and **Eq.8.** it follows:

$$A = \Phi\Lambda\Phi^T, \quad (9)$$

and

$$\Phi A \Phi^T = \Lambda. \quad (10)$$

Eq.9. is the standard value decomposition (SVD) equation for the covariance (i.e. $n \times n$) matrix A and it is based on a theorem from linear algebra. The Φ matrix can be seen as the set of vectors of a linear transformation which transforms data points from their original system to the PCs system, and Λ is actually a correlation matrix of new variables in the PCs system (off-diagonal elements are 0, i.e. there is no correlation between the new variables). The PCA transformation is done with the equation:

$$A^* = (A - 1T(A)^T)\Phi, \quad (11)$$

where A^* is a matrix with the new variables in the PCs system, and $T(A)^T$ is the location estimator. For the classical PCA, the location estimator is an arithmetic mean vector. The 1 denotes a vector of $1s$.

3.2.1. PCA for *ilr* transformed data

The PCA transformation for *ilr*-transformed data is equivalent to the transformation **Eq.11.** and is defined as:

$$Z^* = (Z - 1T(Z)^T)\Phi_Z, \quad (12)$$

where $Z_{n \times D-1}$ is the original *ilr*-data matrix, Φ_Z (loadings) results from SVD of the covariance matrix of Z and Z^* is a matrix with the principal components scores. These scores are no longer interpretable, hence they have to be back-transformed to the *clr*-space (Filzmoser et al., 2009) with the equation similar to the **Eq.4.:**

$$Y^* = Z^*V^T, \quad (13)$$

while a matrix with loadings is transformed from the *ilr*- to the *clr*- space with the equation:

$$\Phi Y = V\Phi_Z. \quad (14)$$

3.3. The biplot

The biplot (Gabriel, 1971) is a 2D graphical display of the PCA results. It consists of an origin (data set centre), rays (variables) and points (samples). Length of the ray is proportional to the variability of the associated variable with respect to the full composition. Length of the link connecting rays is proportional to the variability of the associated pair of variables. Cosines between rays provide the information about a correlation between variables.

4. RESULTS AND DISCUSSION

Figure 1 shows biplots of the first two PCs after classical PCA (**A**) and PCA for compositional data (**B**). Observations are represented with numbers, and variables with rays.

Centre of the each confidence ellipse is a mean vector of the observations scores of the associated soil layer. Ellipses are of a radius 0.5, which means that there is a 50% probability for any value drawn from the distribution of the specific layer, to fall into the surface defined by the ellipse. Such small radius was used only for the presentation purposes to highlight the differences between layers, as discrimination of groups based on their differences is one of the properties of PCA (Reimann et al., 2008). Apparently, the PCA of both *log*-transformed and *ilr*-transformed data managed to discriminate between soil layers. The Euclidean distance between the centres of the confidence ellipses is larger for the *ilr*-transformed data (0.85 compared to 0.39). Moreover, both methods produced PCs with different orientations so that the observations pattern on the each biplot is different.

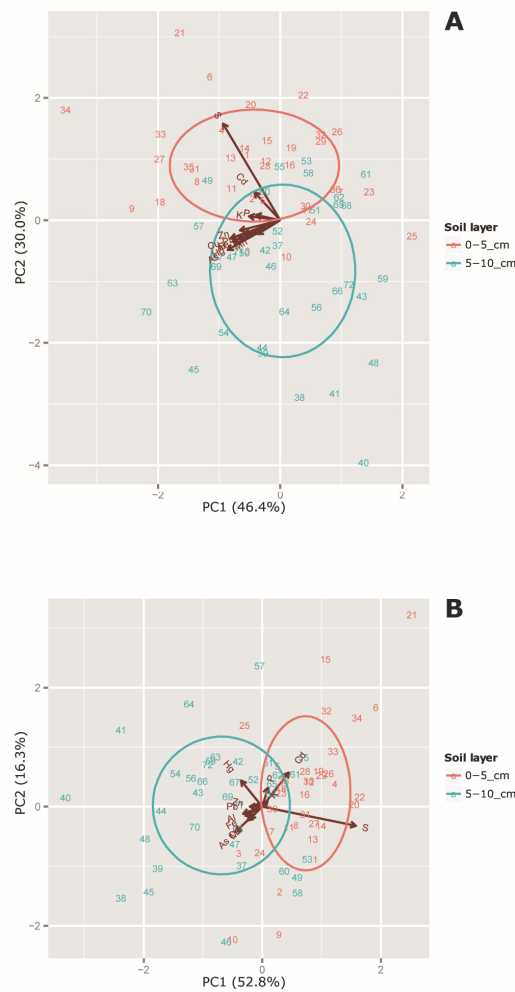


Figure 1: Biplots of classical PCA (**A**) and PCA for compositional data (**B**). Ellipses of normal distribution are of a radius 0.5

Even though the total explained variability is higher for PCA of *log*-transformed values (**Figure 1A**), rays representing loadings show the effect of closure (Buccianti et al., 2006; Reimann et al., 2008; Pawlowsky-Glahn & Buccianti, 2013). Rays after PCA of *ilr*-transformed values (**Figure 1B**) look more open, and therefore more interpretable. Grouping of rays, i.e. associations of elements, their directions and corresponding loadings on PC1 and PC2 are easily recognised.

Sulphur, cadmium, phosphorous and potassium have positive PC1 loadings. Such association of elements is a probable consequence of the anthropogenic contamination

with S, Cd, P and K. The source of airborne H₂S above Kutina is primarily the fertiliser plant and only to a small extent traffic and households heating (Rabljenović et al., 2007). The major source of Cd in soil is from the atmospheric dust and P-fertilisers (Kabata-Pendias & Mukherjee, 2007). P and K are the two of the three main constituents of commercial fertilisers (Montgomery, 2011). Contamination with P and K should be taken with reserve due to their lower variability when compared to Cd. Such lower variability possibly point out that the anthropogenic P and K are more likely to be consumed by plants than Cd. Specifically, plants don't have metabolic requirements for Cd, but it should be noted that its uptake by plants depends on a number of different parameters (Kabata-Pendias & Mukherjee, 2007). Finally, S has negative and Cd, P and K have positive PC2 loadings which is probably due to the different sources of these elements. Mercury has positive PC2 loadings, just like Cd, P and K which suggests that Hg probably originated from fertiliser. Alloway (2013) stated that elevated concentrations of Hg occur in P fertilisers, and are derived from phosphate source rock and sulphuric acid used in processing of phosphate source rock. Lead and Zinc form another cluster on the biplot and can be interpreted as the city runoff (Aloupi & Angelidis, 2001). Aluminium, iron, arsenic and manganese are more or less associated together, probably indicating the association of clay minerals, Fe- and Mn-oxides and As of a natural origin. Concentrations of Al are usually natural (Salminen, 2005) and inherited from source rocks (Kabata-Pendias & Mukherjee, 2007). According to Kabata-Pendias & Mukherjee (2007), Mn and Fe are highly correlated in various environmental cycles. It is because of their similar chemistry, i.e. they both participate in redox reactions in soil (Salminen, 2005). Because As is well correlated with Al, Mn and Fe, it can be assumed that it is of a natural origin. This is in accordance with studies about As in the Pannonian basin system, published by e.g. Varsányi & Kovács (2006), Ujević et al. (2010) and Rowland et al. (2011).

5. CONCLUSIONS

Although both methods achieved to discriminate between soil layers, the Euclidean distance between the centres of the groups (soil layers) showed that the PCA for compositional data achieved better results than classical PCA. Moreover, a graphical display is highly affected by the compositional nature of geochemical data, so the results of classical PCA can be considered questionable. These problems vanish when *ilr*-transformation is applied and the data set appears to open when *ilr*-transformed.

PCA for compositional data well managed to segregate the different associations of elements. Positive PC1 loadings stand for the agricultural contamination with Cd, and to a lesser extent with P and K, and the contamination with S following from the deposition of the atmospheric H₂S released by the fertiliser plant. PC2 loadings differentiated these contamination sources and added Hg to the agricultural contamination. Pb and Zn had negative PC1 loadings and formed isolated cluster representing city runoff. Association of Al, Fe, Mn and As had negative values of the first two PCs, representing natural concentrations.

Interpretation of chemical elements associations in this study should be considered as preliminary. To study associations in more detail, and processes responsible for specific associations, PCA should be performed separately for the each soil layer, or two-group discriminant function analysis (DFA) should be employed instead.

6. REFERENCES

- AITCHISON, J. (1986): *The Statistical Analysis of Compositional Data*. Monographs on Statistics and Applied Probability. -Chapman & Hall, London, 416 p.
- ALLOWAY, B. J. (2013): *Heavy Metals in Soils. Trace Metals and Metalloids in Soils and their Bioavailability*. -Springer, Dordrecht, 613 p.
- ALOUPI, M. & ANGELIDIS, M.O. (2001): Geochemistry of natural and anthropogenic metals in the coastal sediments of the island of Lesbos, Aegean Sea. *Environmental Pollution*, 113, 211-219.
- BUCCIANTI, A., MATEU-FIGUERAS, G. & PAWLOWSKY-GLAHN, V. (eds.): *Compositional Data Analysis in the Geosciences: From Theory to Practice*, Geological Society, London, 212 p.
- CRNKO, J. (1998): *Vodič geološke ekskurzije na Moslavačku goru* [Croatian Geological Society Excursion Guide Book for Moslavačka Gora – in Croatian]. – Hrvatsko geološko društvo, Zagreb, 85 p.
- CRNKO, J. (2014-in print): *Osnovna geološka karta Republike Hrvatske 1:100.000, List Kutina L33-94* [Basic geological map of the Republic of Croatia 1:100.000, Sheet Kutina – in Croatian]. –Fond stručne dokumentacije Hrvatskog geološkog instituta, Zagreb.
- CRNKO, J. (2014): *Osnovna geološka karta Republike Hrvatske 1:100.000, Tumač za list Kutina L33-94* [Basic geological map of the Republic of Croatia 1:100.000, explanation for sheet Kutina – in Croatian]. –Fond stručne dokumentacije Hrvatskog geološkog instituta, Zagreb.
- EGOZCUE, J. J., PAWLOWSKY-GLAHN, V., MATEU-FIGUERAS, G., & BARCELÓ-VIDAL, C. (2003): Isometric logratio transformations for compositional data analysis. *Mathematical Geology*, 35, 279-300.
- FILZMOSER, P., HRON, K., REIMANN, C. (2009): Principal component analysis for compositional data with outliers. *Environmetrics*, 20, 6, 621-632.
- FRANKOVIĆ MIHELJ, N., UKRAINCZYK, N., LEAKOVIĆ, S. & ŠIPUŠIĆ J. (2013): Waste Phosphogypsum – Toward Sustainable Reuse in Calcium Sulfoaluminate Cement Based Building Materials. *Chemical & Biochemical Engineering Quarterly*, 27, 219-226.
- GABRIEL, K. R. (1971): The biplot graphic display of matrices with application to principal component analysis. *Biometrika* 58, 3, 453-467.
- JONES, A., MONTANARELLA, L. & JONES, R. (2005): *Soil atlas of Europe*. - European Soil Bureau Network, European Commission, Luxembourg, 128 p.
- JURAK, V., PFAFF, S., HORVAT, K. & KRKLEC, N. (2006): *Provjera hipoteze o homogenosti geotehničkih sredina na lokaciji 'Čađare' u Kutini* [Verification of the hypothesis regarding the homogeneity of geotechnical mediums at the 'Soot factory / Čađara' location in Kutina – in Croatian]. *Rudarsko-geološko-naftni zbornik*, 18, 29–41.
- JURKOVIĆ, I. (2003): *Metalogenija južne Tisije – Moslavačka gora, Psunj, Papuk, Krndija* [Metallogenesis of the southern Tisia – Mt Moslavačka, Mt Psunj, Mt Papuk and Mt Krndija – in Croatian]. *Rudarsko-geološko-naftni zbornik*, 15, 1–17.

- KABATA-PENDIAS, A. & MUKHERJEE, A.B. (2007): Trace elements from soil to human. -Springer, Berlin, 550 p.
- McKILLUP, S. & DARBY DYAR, M. (2010): Geostatistics Explained: Introductory Guide for Earth Scientists. -Cambridge University Press, Cambridge, 396 p.
- MONTGOMERY, C. W. (2011): Environmental geology. -McGraw-Hill, New York, 511 p.
- PAWLOWSKY-GLAHN, V. & BUCCIANTI, A. (2011): Compositional Data Analysis. Theory and Applications. -John Wiley & Sons, Chichester, 400 p.
- PAWLOWSKY-GLAHN, V. & EGOZCUE, J. J. (2006): Compositional data and their analysis: an introduction. -In: BUCCIANTI, A., MATEU-FIGUERAS, G. & PAWLOWSKY-GLAHN, V. (eds.): Compositional Data Analysis in the Geosciences: From Theory to Practice. -Geological Society, London, 212 p.
- R Core Team (2014). R: A Language and Environment for Statistical Computing. -R Foundation for Statistical Computing, Vienna. Retrieved from <http://www.R-project.org> (Last Accessed: 2014-12-04).
- RABLJENOVIĆ, D., JENDRIČKO, J., DEANOVIĆ, M., MOMČILOVIĆ, Đ. & VUČETIĆ, J. (2007): Izvješće o stanju okoliša grada Kutine [Environmental status report of the city of Kutina – In Croatian]. -Grad Kutina, Kutina, 88 p.
- REIMANN, C., FILZMOSER, P., GARRETT, R. G. & DUTTER, R. (2011): Statistical data analysis explained – Applied environmental statistics with R. - John Wiley & Sons, West Sussex, 343 p.
- ROWLAND, H., OMOREGIE, E., MILLOT, R., JIMENEZ, C., MERTENS, J., BACIU, C., HUG, S. J. & BERG, M. (2011): Geochemistry and arsenic mobilisation in groundwaters of the Pannonian Basin (Hungary and Romania). Applied Geochemistry, 26, 1-17.
- SALMINEN, R., BATISTA, M. J., BIDOVEC, M., DEMETRIADES, A., DE VIVO, B., DE VOS, W., DURIS, M., GILUCIS, A., GREGORAUSKIENE, V., HALAMIĆ, J., HEITZMANN, P., LIMA, A., JORDAN, G., KLAVER, G., KLEIN, P., LIS, J., LOCUTURA, J., MARSINA, K., MAZREKU, A., O'CONNOR, P. J., OLSSON, S. Å., OTTESEN, R.-T., PETERSELL, V., PLANT, J. A., REEDER, S., SALPETEUR, I., SANDSTRÖM, H., SIEWERS, U., STEENFELT, A. & TARVAINEN, T. (2005): Geochemical Atlas of Europe. -Geological Survey of Finland, Espoo, 526 p.
- TABACHNICK, B. & FIDELL, L. S. (2007): Using Multivariate Statistics. -Pearson Education, Boston, 980 p.
- UJEVIĆ, M., DUIĆ, Ž., CASIOT, C., SIPOS, L., SANTO, V., DADIĆ, Ž., HALAMIĆ, J. (2010): Occurrence and geochemistry of arsenic in the groundwater of Eastern Croatia. -Applied Geochemistry, 25, 1017-1029.
- VARSÁNYI, I. & KOVÁCS, L. O. (2006): Arsenic, iron and organic matter in sediments and groundwater in the Pannonian Basin, Hungary. -Applied Geochemistry, 21, 949-963.

DETERMINING ALTERNATIVE STABLE STATES IN THE KESZTHELY BAY – KIS-BALATON SYSTEM WITH THE AID OF STOCHASTIC MODELING

István GÁBOR HATVANI^{a,*}, Adrienne CLEMENT^c, József KOVÁCS^b, János KORPONAI^{d,e}

^aInstitute for Geological and Geochemical Research, Research Center for Astronomy and Earth Sciences, Hungarian Academy of Sciences, H-1112 Budapest, Budaörsi út 45.,

^bEötvös Loránd University, Department of Physical and Applied Geology, H-1117 Budapest, Pázmány Péter stny. 1/C

^cBudapest University of Technology and Economics, Department of Sanitary and Environmental Engineering, H-1111 Budapest, Műegyetem rakpart 3

^dWest Transdanubian Water Authority, Department Kis-Balaton, H-8360 Keszthely, Csík Ferenc stny. 1., Hungary

^eUniversity of West Hungary, Department of Chemistry and Environmental Sciences, H-9700 Szombathely, Károly Gáspár tér 4., Hungary

*hatvaniig@gmail.com

Lakes are sensitive to environmental changes and anthropogenic effects, and Lake Balaton, the largest shallow lake in Central Europe, is no exception. To protect it against elevated nutrient loads, the Kis-Balaton Water Protection System (KBWPS) was constructed as a mitigation wetland at the mouth of the largest tributary of the lake.

This work aims to demonstrate the applicability of various multivariate statistical methods in water quality management with an emphasis put on determining the new stable state, ecological equilibrium between the former hypertrophic basin (Keszthely Bay) of Lake Balaton and the establishment of the KBWPS. Cluster and principal component analyses were conducted on 19 weekly measured (1981-2009) time series coming from 14 sampling sites. The results have explicitly proven that the new stable state of the system has been achieved: (i) trophic processes moved upstream from Lake Balaton and (ii) both the internal and external loads decreased.

Keywords: *alternative stable state, cluster analysis, eutrophication, Lake Balaton, principal component analysis*

1. INTRODUCTION

Conserving the water quality of Lake Balaton, the largest shallow freshwater lake in Central Europe (watershed approx. 5181 km²) is one of the primary goals in Hungarian water management. The lake's largest tributary, the River Zala, supplies almost 50% of the lake's total water- and 35-40% of its nutrient input (Hatvani et al., 2014). The River Zala enters the lake at its westernmost

and smallest basin, Keszthely Basin (87 km²) therefore adversely affecting its water quality.

In the nineteenth century the water level of the lake was modified artificially. In this way the river had completely separated from the former wetland areas of Kis-Balaton Wetland (KBW) and the Lower Zala Valley. Since KBW stopped functioning as a filter, the waters of the River Zala entered Lake Balaton without having been naturally filtered. This, along with accelerated anthropogenic activity in the catchment, resulted in a significant increase in external nutrient loads and a deterioration of Lake Balaton's water quality, most explicitly in Keszthely Bay.

To handle these negative trends (e.g. phosphorus (P) precipitation at the Zalaegerszeg waste water treatment plant, or a dramatic decreasing of fertilizers) in the lake's and especially in Keszthely Bay, measures for nutrient control were taken., The Kis-Balaton Water Protection System (KBWPS) was also set up in two constructional phases on the remains of the former Kis-Balaton Wetland. Phase I was finished in 1985 and resulted in an eutrophic pond. Phase II was addressed to form a classic wetland (it was partially finished in 1992; Hatvani et al., 2009; **Figure 1**).

It has been known, that all ecosystems, being exposed to gradual changes, tend to respond to these modifications in a damped (buffered) way. However, when these external effects are sudden – as in the case of Keszthely Bay - the system may shift to an alternative stable state in an accelerated way (Scheffer et al., 1993). Therefore, supporting the resilience of such disturbed system should be a primary goal.

In the case of the study area, mainly Keszthely Bay, the question was raised; did any change occur in the stable state of its ecosystem?

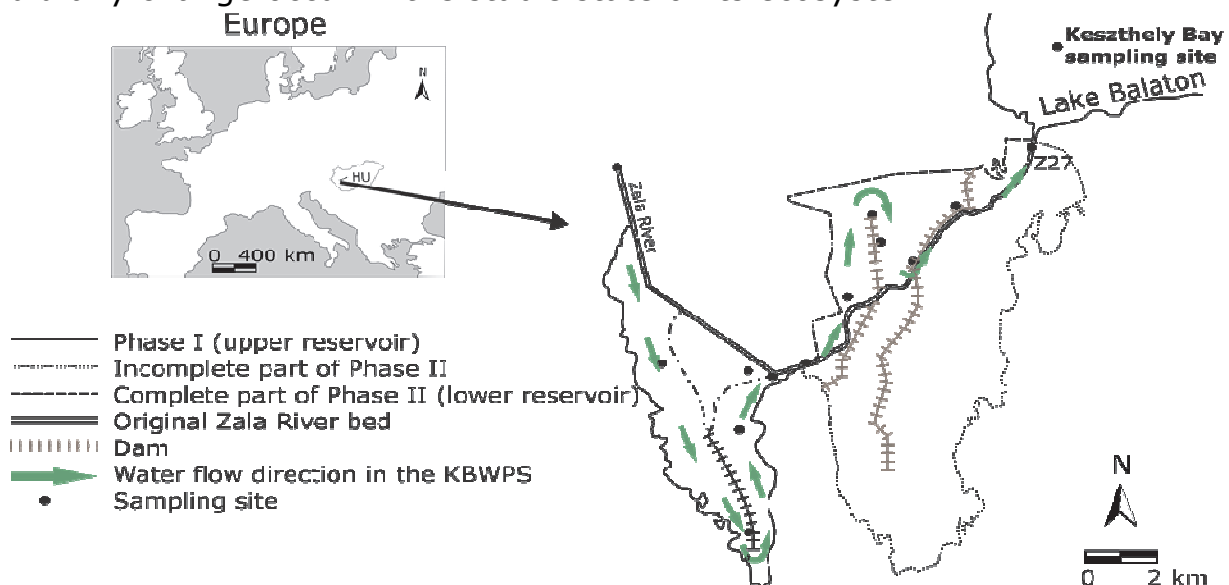


Figure 1: Location of the study area and the analyzed sampling sites

2. MATERIALS AND METHODS

The time series of 19 weekly measured physical, chemical and biological water quality parameters were assessed from 14 monitoring stations. Thirteen of which came from the KBWPS (1994-2009) and one represented Keszthely Bay (1981-1992 & 1994-2009).

In this study the followings were used: principal component analysis (used for manually rarefied bi-weekly data; Kovács et al., 2012a; Rogerson, 2001), hierarchical cluster analysis (using Ward’s method, and squared Euclidean distance) and Wilks’ lambda statistics (Wilks, 1932) to determine which parameter influences the cluster groups the most (Hatvani et al., 2011). For verification, discriminant analysis was used.

3. RESULTS AND DISCUSSIONS

3.1 BEHAVIOR OF KESZTHELY BAY DEPENDING ON RUNOFF

After clustering the sampling sites (SS) of the KBWPS and Keszthely Bay (Kszt) for each year it became obvious that in years with high runoff Kszt becomes similar to the sites of Phase II, while it forms a separate groups from all the other SSs of the system in the low runoff years¹ (**Figure 2**). These were the years when phosphorus forms had the greatest influence on the formation of the cluster groups - as indicated by the Wilks’ lambda results - because of their decreased loads. Therefore, the adverse decrease of nutrients responsible for Keszthely Bay forming a cluster group alone in the low runoff years (Hatvani et al., 2014).

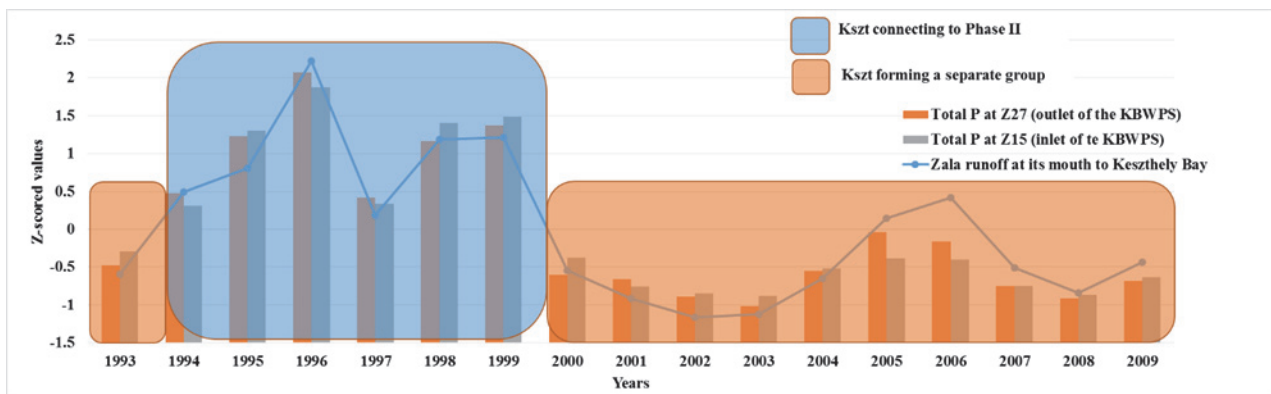


Figure 2: Behavior of Keszthely Bay depending on runoff

¹It is considered a low runoff year when the output of Z27 is less than three times the volume of Keszthely Bay (87 km³) in a year; while if it is more than three times the volume, it is considered a high runoff year (Kovács et al., 2012b)

3.2 STOCHASTIC RELATIONSHIPS BETWEEN THE KBWPS AND KESZTHELY BAY

PCA was conducted separately on the two time periods pre-determined by runoff (1993-1999 & 2000-2009). Out of the obtained principal components only the first was accounted for. It explained ~30% of the variance. It is not unusual to have such “low” explanatory power in water quality datasets (e.g. Kovács et al., 2012a), since the system is continuously changing and rapid influences may occur effecting the different parameters to a different extent. In other scientific fields, however, such as glaciology/sedimentology much higher values may exist (e.g Kern et al., 2011). The two Phases and even Keszthely Bay behaved differently in respect to their stochastic characteristics. Phase I stayed somewhat the same, with the parameters related to eutrophication dominating its waters. However, in Phase II a clear change was witnessed after 2000. In the low runoff years eutrophication processes take a determining role next to the inorganic parameters.

However, at Keszthely Bay no significant change was observed, the inorganic parameters were most influential after 1992, the initiation of the KBWPS regardless of the volume of runoff entering the bay. Moreover its stochastic characteristics stayed similar to the ones of Phase II in that particular period of time (Hatvani et al., 2014). Therefore, the question was raised, did any change occur at Keszthely Bay before 1992?

The answer is yes. PCA was applied to the bi-weekly measured data for the time intervals 1981-1984 – prior to the inundation of Phase I – and 1985-1992. The first two principal components explained about 50% of the variance. It became obvious that during 1981-1992, the parameters in close relation to the eutrophication processes continuously lost their influencing role².

Prior to the construction of the KBWPS (1992) the processes in the bay were co-influenced by parameters related to eutrophication, resembling the eutrophic Phase I as it happened some years later (**Table 1**).

Table 1. Factor loadings of selected important parameters regarding the new stable state at Keszthely Bay: A) 1981-1984; and B) 1985-1992. (after Hatvani et al., 2014)

Principal component (loadings) / Parameter	1981-1984 A)		1985-1992 B)	
	1 st PC	2 nd PC	1 st PC	2 nd PC
COD _{ps}	-0.88	-0.134	-0.533	-0.672
BOI ₅	-0.73	-0.024	-0.337	-0.551
Chl-a	-0.94	-0.105	-0.73	-0.438
TSS	-0.216	-0.406	-0.003	0.012
NO ₂ -N	-0.73	0	0.22	-0.563
SRP	-0.368	0.202	-0.092	-0.555
TN	-0.85	-0.027	-0.283	-0.657

² Parameters with loadings outside the ±0.7 interval.

In the beginning, the parameters closely related to eutrophication – which was present alongside the other chemical parameters - continuously disappeared from the group of components, which determine the background processes at Kszt. These have happened because of (i) the water quality ameliorating measures of that time and (ii) the fact that Phase I of the KBWPS now serves as the location of intensive planktonic eutrophication.

4. CONCLUSIONS

The statistical evaluation presented in this research confirms and supports the observation that nutrients have less effect on the background processes – the stochastic relationships pointed out by PCA - of Kszt nowadays than in the past. From the management point of view this is an important conclusion, although it is obvious that besides the inundation of the KBWPS, additional measures have contributed to decreasing the external nutrient loads to the bay and eventually to its oligotrophication processes. With PCA and CA it has been demonstrated that the construction of the KBWPS has facilitated the establishment of an ecological integrity between the reservoirs and Keszthely Bay, resulting in a new, alternative stable (independent) state (Scheffer et al., 1993). This equilibrium can still be influenced by external effects (Scheffer et al., 2001), in this case runoff and external loads entering the system, although only to a moderate degree, and then not in such an immediate way. It can be described by:

- (i) a decreased inter-annual variability, which does not cause significant growth in macrophyte cover because of sediment resuspension and winds (Istvánovics et al., 2008). (Here it should be remarked that, although there have not been direct measurements, the public have reported the increase of submerged macrophytes in the shoreline);
- (ii) decreased external nutrient loads
- (iii) a decrease in internal nutrient loads
 - a. the rapid immobilization of mobile P in the sediment (Istvánovics & Somlyódy, 2001),
 - b. among many others, sediment containing high amounts of P is covered by new layers, thus remobilization is unlikely.
- (iv) low - or no - discharge from the KBWPS in dry years, especially in summer months . This is one reason why Kszt “behaves” differently in these situations. On the contrary, the background processes in the wetland area of the KBWPS seem to be highly influenced by runoff.

The KBWPS works as a buffer, lessening the impacts of extreme flow, and as consequence, possible extreme load events. It also retains the nutrients from entering the load-sensitive Keszthely Bay by providing a place for intensive planktonic eutrophication. These processes are therefore moved upstream to

Phase I. This facilitates the oligotrophication of Keszthely Bay. The identification of these key changes in the system was the result of the interaction of the parameters, and could not have been made using solely univariate methods. The beneficial effect of the KBWPS on the oligotrophication of Lake Balaton has been proved in this work from the perspective of concentration and stochastic relationships as well.

5. ACKNOWLEDGMENTS

The work of I.G. Hatvani was supported by the European Union and the State of Hungary, co-financed by the European Social Fund in the framework of TÁMOP 4.2.4. A/1-11-1-2012-0001 'National Excellence Program'. In addition, we would like to give thanks for the support of the “Lendület” program of the Hungarian Academy of Sciences (LP2012-27/2012). This is contribution No. 08 of 2ka Palæoclimatology Research Group.

6. REFERENCES

- HATVANI, I. G., KOVÁCS, J., KORPONAI, J. & KOVÁCSNÉ, SZ. I. (2009): A Kis-Balaton Vízvédelmi Rendszer (KBVR) hosszú távú fizikai, kémiai és biológiai paramétereinek elemzése [Analysis of long term physical, chemical and biological data series of the Kis-Balaton Water Protection System – in Hungarian]. *Hidrológiai Közlöny*, 89, 6, 15-18.
- HATVANI, I. G., KOVÁCS, J., KOVÁCSNÉ, SZ. I., JAKUSCH, P. & KORPONAI, J. (2011): Analysis of long-term water quality changes in the Kis-Balaton Water Protection System with time series-, cluster analysis and Wilks' lambda distribution. *Ecological Engineering*, 37, 4, 629-635.
- HATVANI, I.G., CLEMENT, A., KOVÁCS, J., KOVÁCSNÉ, SZ.I. & KORPONAI, J. (2014): Assessing water-quality data: the relationship between the water quality amelioration of Lake Balaton and the construction of its mitigation wetland. *Journal of Great Lakes Research*, 40 (1)
- ISTVÁNOVICS, V. & SOMLYÓDI, L. (2001): Factors influencing lake recovery from eutrophication - the case of Basin 1 of Lake Balaton. *Water Research* 35, 729-735.
- ISTVÁNOVICS, V., HONTI, M., KOVÁCS, Á. & OSZTOICS, A. (2008): Distribution of submerged macrophytes along environmental gradients in large, shallow Lake Balaton (Hungary). *Aquatic Botany* 88, 317-330.
- KERN, Z., SZELES, E., HORVATINCIC, N., FORIZS, I., BOCIC, N. & NAGY, B. (2012): Glaciochemical investigations of the ice deposit of Vukusic Ice Cave, Velebit Mountain, Croatia *CRYOSPHERE* 5, 5, 485-494.
- KOVÁCS, J., TANOS, P., KORPONAI, J., KOVÁCSNÉ, SZ. I., GONDÁR, K., GONDÁR-SŐREGI, K. & HATVANI, I. G. (2012a): Analysis of Water Quality

Data for Scientist. -In: VOUDOURIS, K., VOUTSA, D. (eds.): Water Quality Monitoring and Assessment, InTech Open Access Publisher, Rijeka, pp. 65-94.

ROGERSON, P.A. (2001): Statistical methods for geography. SAGE Publications, London, UK, 304p.

SCHEFFER, M., CARPENTER, S., JONATHAN, A.F., FOLKE, C. & WALKER, B. (2001): Nature 413, 591-596.

SCHEFFER, M., HOSPER, S.H., MEIJER, M-L., MOSS, B. & JEPPESEN, E. (1993): Alternative equilibria in shallow lakes. Trends in Ecology & Evolution 8, 275-279.

WILKS, S.S. (1932): Certain generalizations in the analysis of variance. Biometrika 24, 471-494.

THROWING OILY DICES, UNCERTAINTY IN HCIIP

István NEMES

MOL Plc., H-1117, Budapest, Október huszonharmadika str. 18., Fehérház 3rd floor, 330.

isnemes@mol.hu

Uncertainty and sensitivity analysis becomes a more-and-more significant part in the workflow of reservoir modelling. Its main goal is to give a more accurate picture about the HCIIP and reserves. This paper focuses partly on the process of these practical investigations, and partly on the theoretical background of this issue. The aim is to reveal the significance of proper input data, accurate exploration of the inner structure of the dataset, and the importance of the geological set up.

The main steps of the uncertainty analysis are demonstrated by some Hungarian and foreign HC reservoirs. This paper covers the assumed geological scenarios, the applied methods and software, as well as the presentation techniques. Conclusions are given on the methods and goals of uncertainty analysis by emphasising empirical aspects, tips and hints, and avoidable pitfalls.

Key words: *uncertainty, sensitivity, REP, Irap RMS*

1. INTRODUCTION

The title of this paper refers to the fact, that every aspect of subsurface modelling and engineering shall be handled with care. It should also be taken into account that no data can be acquainted with 100% accuracy. As a result of this inaccuracy, the dices being thrown are very slippery, i.e. oily. There are a lot of chances of misunderstanding, misinterpreting the used dataset, and getting false, misleading results.

On the other hand, neglecting these investigations in reservoir studies' volumetric calculations is recklessness. In fact by neglecting the inherent and inevitable uncertainties of gathered information, one would get unfoundedly narrow range of HCIIP, and likely over- or underestimations.

As the title says, this paper focuses on the HCIIP's uncertainty deriving from the geological settings, measurements, surveys, interpretations, which culminate in 3D static i.e. geological models of the reservoir.

2. ORIGINS OF UNCERTAINTY

Heisenberg’s Principle of Uncertainty: „...the act of observation affects the particle being observed...” (Hawking 1988). Obviously models of HC reservoirs are not on the scale of quantum, but this quote expresses quite well that the recognition of natural systems has its limits, therefore its uncertainty.

The uncertainties originate from several sources (Caers 2011), as it is illustrated in **Figure 1**. There are three main sources of uncertainties in geological modelling (**Figure 1**); they have effects on each other and can influence each other’s significance. E.g.: the more data exist from seismic surveys, the less uncertainty is imposed onto the scenarios; the more wells are drilled and sampled/logged, the less uncertainty shall remain in the inter-well space.

Scenario uncertainty expresses geological concept(s) that may possibly be true based on available data. (E.g.: whether a fault seals or not, it results in a smaller or larger area of the reservoir.)

Data uncertainty describes the goodness, reliability of data sets. Soft and hard data are usually available for model-building processes. For example, porosity could be overestimated due to a positively biased well pattern.

The third member of this trio can be the spatial uncertainty that could be located between the two described above. (If the less hard data are available, the more spatial uncertainty the model has to deal with.)

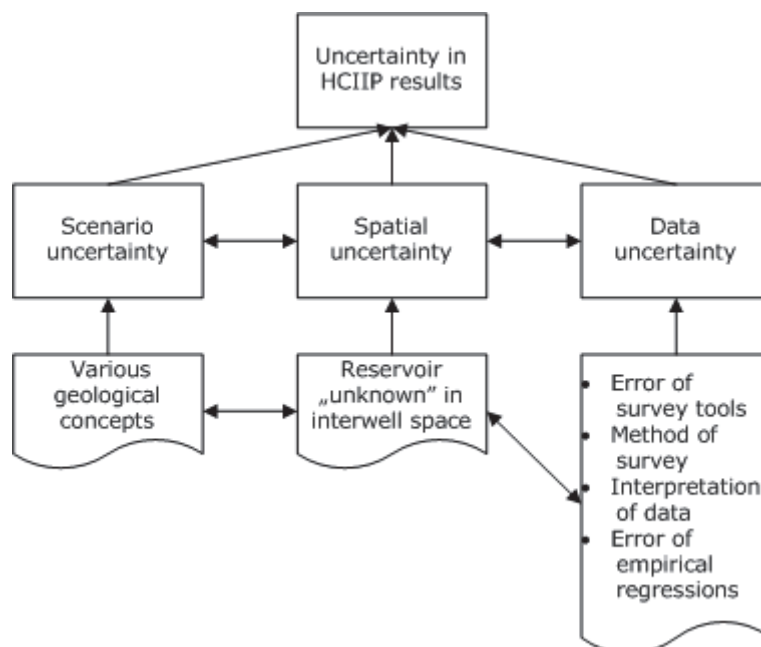


Figure 1: Schematic figure of the origins of uncertainty

A common and extremely important feature of these uncertainties is that they accumulate throughout the modelling process from survey through

interpretations. Also, they can affect both 3D static and dynamic modelling all the way to NPV calculations. This is why their ranges and significance have to be accounted for.

3. FROM INPUT DATA TO VALID RANGES OF HCIIP

A simplified, straightforward workflow chart of setting up a geological model with an aim of extended uncertainty and sensitivity analysis is illustrated in **Figure 2**. The equation indicated under the workflow represents the basic method of defining in-place volumes.

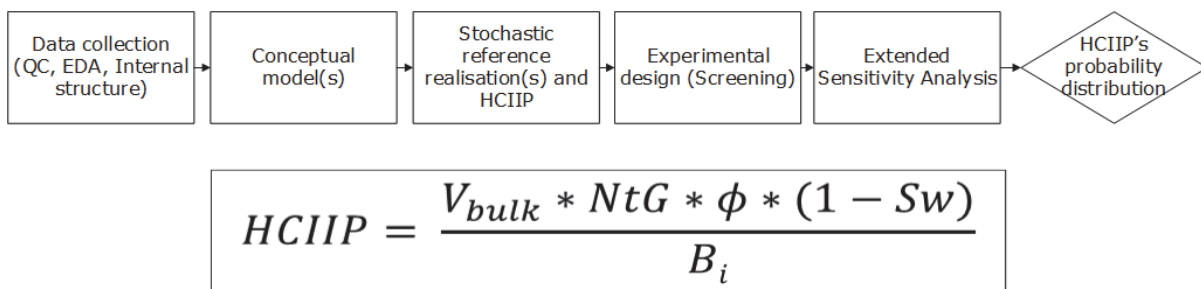


Figure 2: A common workflow for static modelling

3.1. DATA COLLECTION

The first and very important step of any modelling job is to gather all available data and existing documents, analogues. The collected dataset has to be quality checked because according to the ever-green rule of thumb: „garbage in, garbage out“, no reliable results can be achieved from inaccurate input parameters. A plausible example of this step can be described on the basis of a special green-field (Project A), and a simple brown-field (Project B) HC reservoir’s model.

The brown-field model (Project B) emphasizes the importance of the familiarity with the dataset. It is a gas-bearing, clastic reservoir with high porosity and permeability. The high correlation coefficient between porosity and permeability makes possible to decrease the computing time and increase the accuracy of the model. It should be kept in mind that these two parameters have to be correlated throughout the 3D modelling workflow, as well as during UA.

3.2. CONCEPTUAL MODELS (SCENARIOS)

In several cases, especially in green-field projects, the geological settings cannot be known accurately, due to the lack of sufficient amount of data and/or production history. It makes unreasonable to set up one and only one concept on the reservoir’s geology. In these cases, all of the conceivable ideas (constrained by data) have to be accounted for.

The major challenge of Project A was that the PVT model indicated two reservoirs. These BHSs were collected from an open-hole section of >100 m penetrating at least two reservoir sections. It was not certain, which fluid originated from the larger and which from the definitely smaller reservoir. This problem forced the modellers to deal with both scenarios and define a relatively wide range of HCIIP results.

3.3. REFERENCE MODEL

In the input workflow, all the non-investigated parameters of a 3D model are gathered from the reference model. The reference model contains the best set-up the modeller can achieve by using the most reliable data. In practice, a number of stochastic realizations are run to acquire a range of stochastic uncertainty, i.e.: the results of equally-probable realizations constrained by the input parameters.

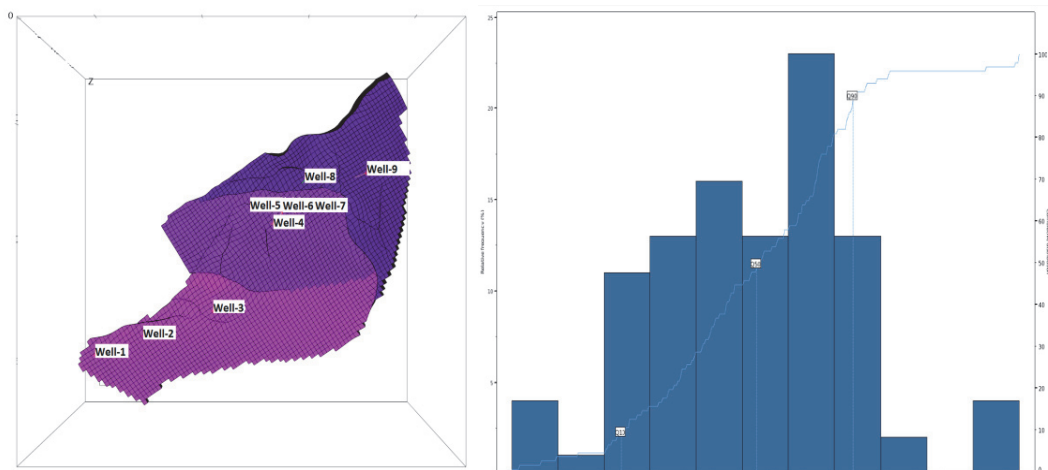


Figure 3: An example of 3D static model with three different fault regions.

The P50 (median) realization or one being close to the median is used as the reference model for uncertainty analysis.

3.4. Design of experiment (DOE)

The design of the experiment has to be planned and the probability ranges of studied parameters must also be determined in order to optimize computing time and number of necessary realisations.

A practical answer can be obtained by the ‘One-by-one’ sampling method (screening). It has a limited number of runs and can generate useful information on the significance of different parameters (Williams et al. 2004). The number of variations is illustrated in **Figure 4** by using the discrete sampling methods of Roxar Irap RMS 2012 software packages’ uncertainty module.

Comparison of different discrete sampling methods

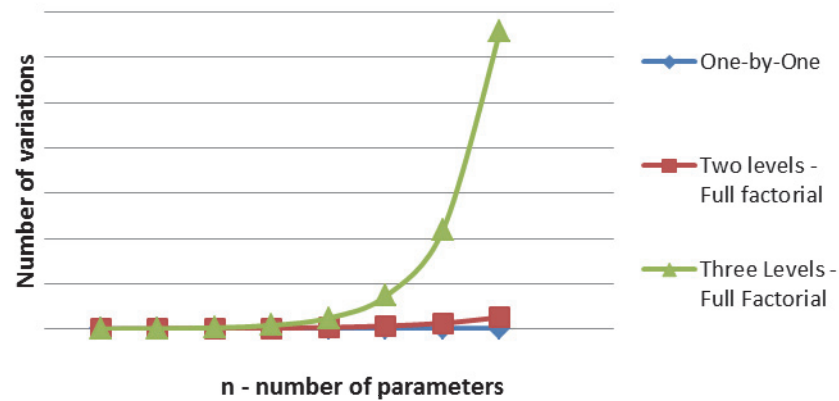


Figure 4: Different sampling methods of Roxar Irap RMS 2012 (discrete input cases)

The most useful output of screening is a True Response Tornado Diagram, which reflects the influence of input parameters, and thus makes it possible to choose the most important ones to be included in detailed UA&SA.

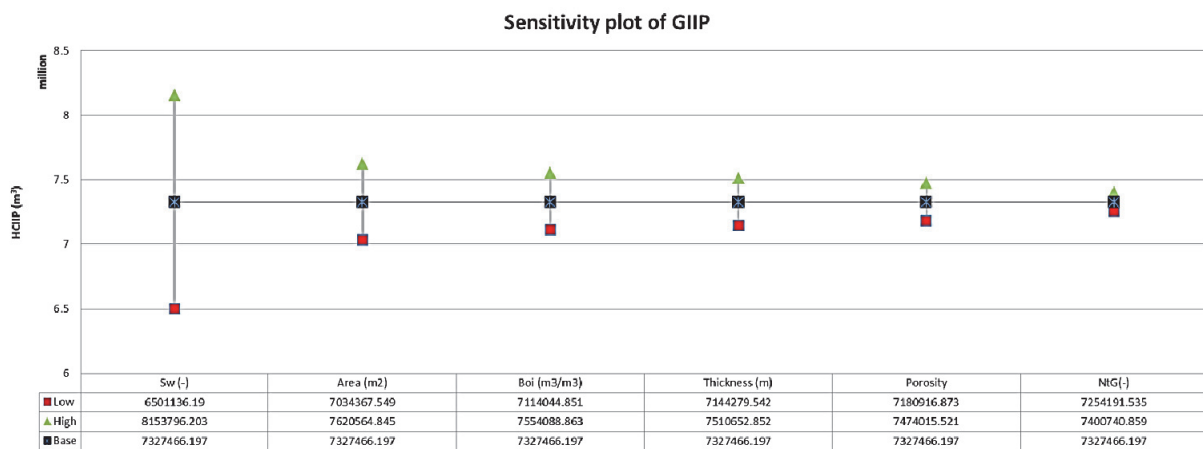


Figure 5: True Response Tornado Chart of screening method (hypothetical values)

Based on this method in Project C (gas reservoir), the HCIIP is most sensitive to Sw_i, area, and Bi.

4. EXTENDED UA&SA AND RESULTS

In another project (Project D), seven parameters were investigated during an extended UA&SA, using Roxar Irap RMS 2012, Microsoft Excel 2010 and REP 5.25. A collage of the most significant input parameters is shown in **Figure 6**.

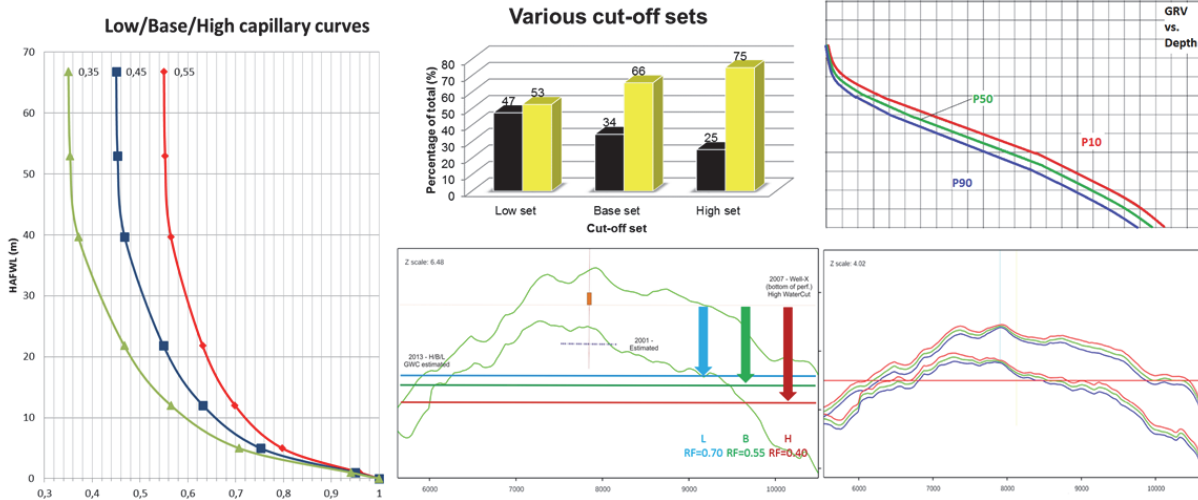


Figure 6: An overview of the most significant uncertainty ranges of input parameters in Project D

The results derived from an extensive UA&SA of a 3D static model can be presented in numerous ways. Some of the most important ones are shown in **Table 1** and **Figure 7**.

Table 1: The most important statistical descriptive parameters of the probability distribution of HCIIP (based on Neumann et al., 2012)

	Reference case	Uncertainty analysis								
	Reference case	Mean	P90	P50	P10	Std. dev	CV	P10/P90	P90-P50 diff. (%)	P10-P50 diff. (%)
	MMm ³	MMm ³	MMm ³	MMm ³	MMm ³	MMm ³	%	-	%	%
GIIP	7.3275	7.3319	6.3344	7.3244	8.3593	0.7666	10%	1.32	-14%	+14%

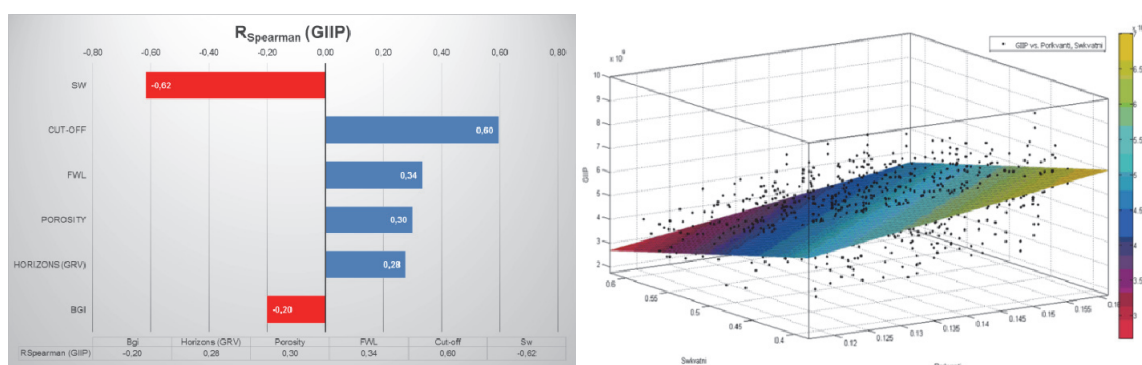


Figure 7: A relative tornado diagram (Spearman correlation) and a response surface reflecting the results of UA&SA

5. CONCLUSION

- UA&SA has to be an essential part of any stochastic 2D (isovol), 3D or 4D volumetric calculations.
- The results of UA&SA emphasize the fact that only ranges of HCIIP can be defined, not a single value.
- These methods have to be used with care. Their misunderstanding them is risky. Omitting their utilization may lead to an even higher risk.
- Response surfaces, HCIIP distributions, input parameter distributions can be employed during dynamic modelling as well (Travis et al. 2008).
- Amended with HM, the range of HCIIP can be narrowed and filtering of scenarios becomes possible.
- The results can be applied for economic, e.g. NPV calculations, and can form a base for future decisions.

6. NOMENCLATURE AND ABBREVIATIONS

<i>BHS</i>	bottom hole-sample (fluid)	<i>NtG</i>	net-to-gross, -
<i>B_i</i>	initial formation volume factor, m ³ /sm ³	<i>PVT</i>	pressure-volume-temperature
<i>DOE</i>	design of experiment	<i>QC</i>	quality check
<i>EDA</i>	exploratory data analysis	<i>RF</i>	recovery factor, -
<i>GRV</i>	gross rock volume, m ³	<i>SA</i>	sensitivity analysis
<i>HAFWL</i>	height above free water level, m	<i>S_{wi}</i>	initial water saturation, -
<i>HCIIP</i>	hydrocarbon-initially-in-place	<i>UA</i>	uncertainty analysis
<i>HM</i>	history match	<i>V_{bulk}</i>	bulk rock volume, m ³
<i>NPV</i>	net present value	<i>Φ</i>	porosity, -

7. REFERENCES

- CAERS, J. (2011): Modeling uncertainty in the Earth Sciences. – Wiley-Blackwell, UK, 249 p.
- HAWKING, S. (1988): A Brief History of Time. – Bantam Dell Publishing Group, UK, 256 p.
- NEUMANN B., K., HEGSTAD, K. B., BRATLI, E., OSMUNDSEN, K., I. (2012): Uncertainty Study on In-Place Volumes in Statoil. Ninth International Geostatistics Congress, Oslo, Norway.

TRAVIS, C. B., KYMBAT, D., GREG, R. K. (2008): Application of Brown-Field Experimental Design Techniques to a Super Giant Carbonate Reservoir. SPE 115422.

WILLIAMS, G., J., J., MANSFIELD, M., MACDONALD, D., G., BUSH, M., D. (2004): Top-Down Reservoir Modelling. SPE 89974.

3D FACIES ANALYSIS WITH COMBINATION OF 3D SEQUENTIAL SIMULATION AND WELL-LOG SHAPE APPLICATION

Andrea WÁGENHOFFER

University of Szeged, Dept. of Geology and Paleontology,
wagenhofferandrea@gmail.com

The purpose of this work was to study the macro-scale rock characteristics and the three-dimensional depositional geometry of a Lower Pannonian (s.str) turbidite reservoir rock body by a joint application of classic and stochastic sedimentological analysis. The porosity values were the inputs to 3D sequential Gaussian simulation. The first step consisted of the exploratory data analysis along with normal score transformation. The second step was a detailed 3D variography and the third one was the generation of one-hundred stochastic realizations. The median type estimation were derived from these realizations. The width of symmetrical probabilities intervals were used to express the degree of uncertainty. The direction of lateral movement of the depositional system was characterized by the spatial distribution of (1) sandstone/non-sandstone ratios calculated from quantitative well-log interpretation and (2) number of characteristic well-log-shapes identified in wells. Where the channels shifted, the clay units and well-logs shapes number are high. The vertical sequences of log-shapes (electric facies) were in harmony with the results of 3D stochastic approaches.

KEYWORDS: *3D variography, 3D stochastic simulation, uncertainty spatial distribution, well-logs shape*

1. INTRODUCTION

The goal of this study is to demonstrate an approach for the identification of three dimensional depositional geometry of a Lower Pannonian (s.str) turbidity reservoirs rock body using combination of 3D Sequential Gaussian Simulation and well log shape analysis. The study area is located in the middle part of Hungary. Large amount of information has been available for this rock body: corrected and interpreted well-logging data, preliminary stratigraphic and lithological descriptions, and detailed core analyses. Based on these data, the deposition system has been determined as deep-water turbidity system.

Reading and Richards (1994) classified the deep water basin margin depositional systems into 12 classes (mud-rich, mud-sand-rich, sand-rich and gravel-rich “point-source submarine fans”, “multiple-source submarine ramps and “linear-source slope apron”), on the basis of grain size and feeder system. Previous study of this rock body has introduced numerical models of

stratigraphy, lithology, porosity and permeability for this rock body (Horváth, Wágenhoffer, Geiger 2012).

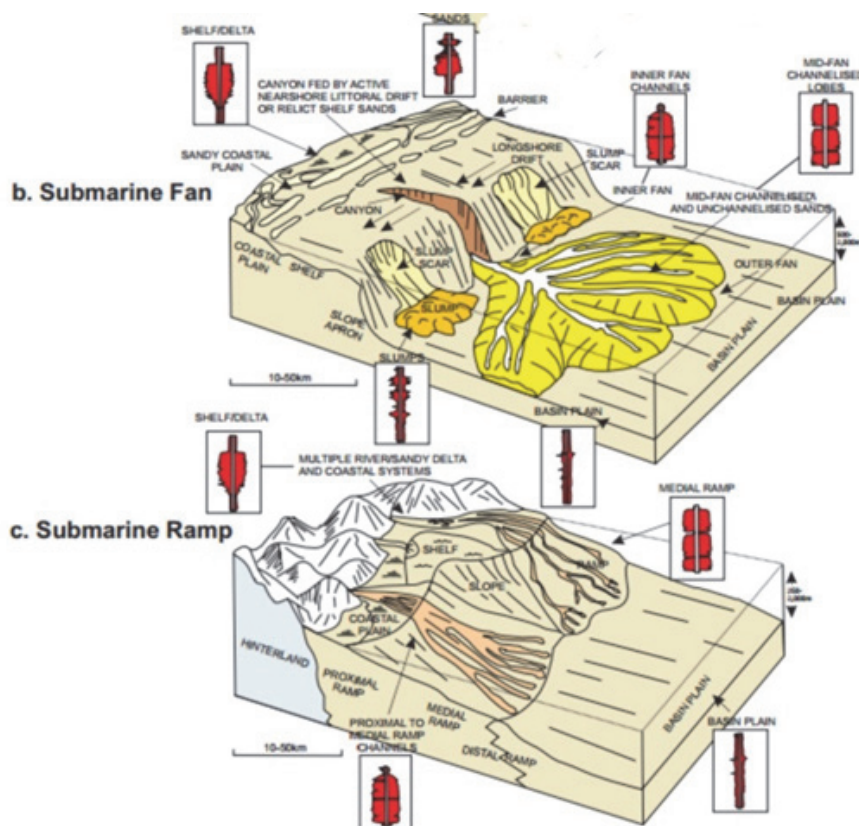


Figure 1 Theoretical models of submarine fan and ramp system (after Reading, Richards 1994)

In this study the phasize was given to sandstone-packages, and the authors suggested the existence of sand-rich submarine fan or sand rich ramp. Within the rock body depositional processed was supposed near the interfingering of upperfan and midfan region, in a suprafan lobe (**Figure 1**).

2. METHODS

2.1. BASIC DATA SET

The geophysical dataset consisted of gamma ray (GR), resistivity (RN) and spontaneous potential (SP) logs. Porosity, shale volume, permeability and lithological categories have been calculated from them.

2.2. 3D SEQUENTIAL SIMULATION

The sequential Gaussian simulation was used for modelling the regional uncertainty of porosity. Within the SGeSM-frame, the first step was the data pre-processing (including evaluation of distribution function and normal score transformation). It was followed by a detailed 3D variography. Search ellipsoid was identified by six parameters: three ranges and three angles: azimuth, dip and rake. Then Sequential Gaussian Simulation generated 100 equally

probable 3D realizations. After the back transformation, the 3D Md-type estimation and the 3D cube of a symmetric probability interval with 0.05 of total width was created.

2.3. WELL-LOG SHAPES AND SANDSTONE/NON-SANDSTONE RATIOS

As it has been proved, vertical depositional sequences of different depositional environments can result in different shapes of well logs (e.g. Rieder, 1999). In this study SP (Spontaneous Potential) and GR (Gamma Ray) logs were used to analyse log responses. Three categories could be identified: cylindrical shape, cylindrical/bell-shape and irregular trends (sawtooth-shape, symmetrical shape, funnel shape) (**Figure 2**).

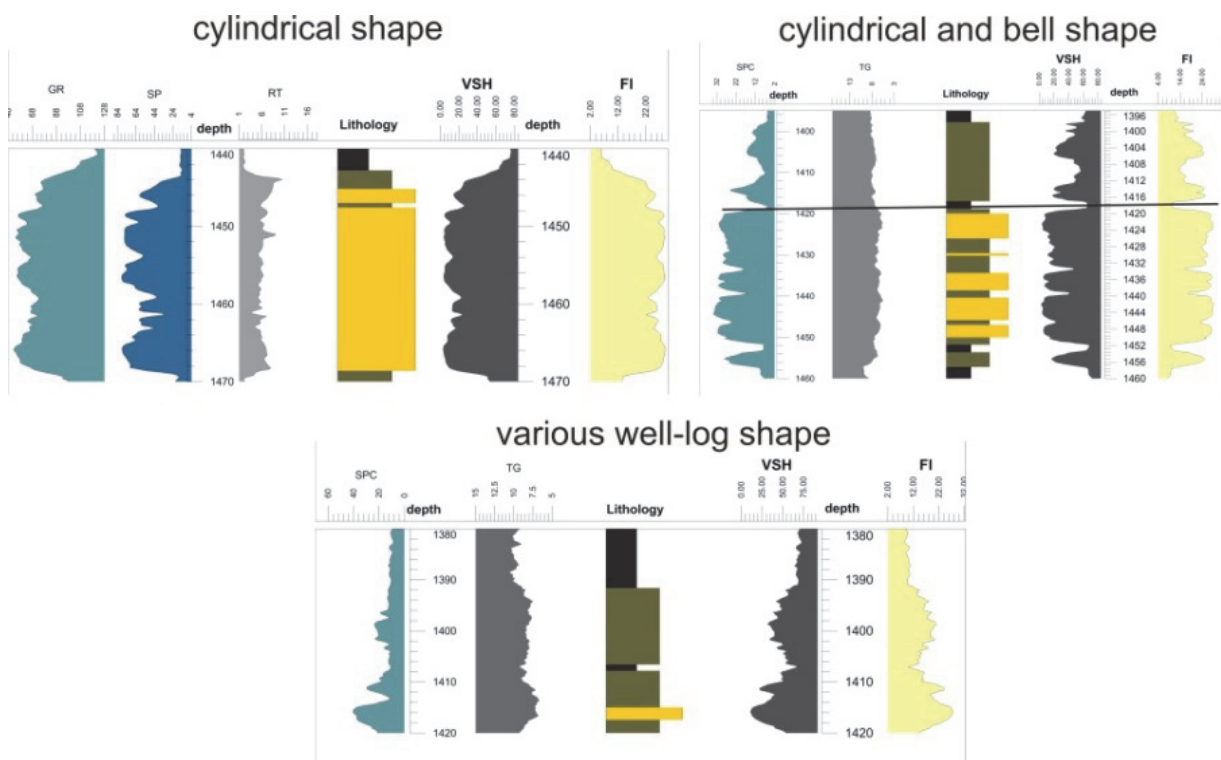


Figure 2 Typical well-log shapes on the study area

The cylindrical shapes represented channel-fills with clean-sand content. The second type had a characteristic form between the cylindrical and bell shapes. Its lithological content was between poor sandstones and siltstones. Finally, the third one was a mixture of the sawtooth, funnel and symmetrical shapes. This indicated channel-mouth bar.

The direction of lateral movement of the depositional system was characterized by the spatial distribution of sandstone/non-sandstone ratios calculated from quantitative well-log interpretation.

3. RESULTS

In the 3D Md-type estimation of porosity all values were smaller than 30%. The highest porosity values belonged to the north-eastern and northern part of the area (**Figure 3 (A)**). The results of the symmetrical probability interval suggested that they could be characterized medium and low levels of uncertainty (in this uncertainty model). The pixels of high uncertainty did not concentrated within the rock body (**Figure 3 (B)**).

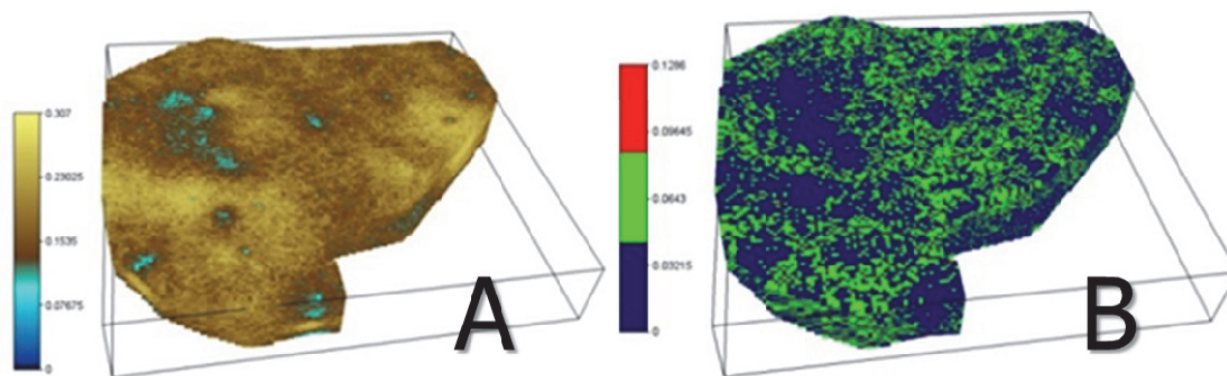


Figure 3 Result of 3D SGS: (A) Md-type estimation of porosity; (B) model of uncertainty of porosity

In the 3D stochastic models a so called stratigraphical coordinate system was used. In this system longitude and latitude is the same as in the geographical system, but the vertical coordinate is measured from the top of the rock body studied. In this way the 3D model is a kind of geocube. In fact the upper plan surface of the rock body, if it is connected to bottom surface of massive clay-marl succession, express the almost flat terrain of the deposition. In this case, the top of the geocube coincided with the bottom of the upper massive clay marl sequence. This geocube was sectioned by surfaces being parallel to the top and the vertical distance between any two surfaces was 1 m (**Figure 4**). Between 0 and 37 m (below the top), a well-developed channel could be recognized within the NE part. Another one appeared within the SW region. Within the middle region of this rock body a bar-like unit could be identified (**Figure 4**). These results were proved by the spatial distribution of well-log shapes (**Figure 5**).

Figure 5 shows that the cylindrical shapes were characteristics within those areas where the geocube suggested channel. The appearance of the second type of log-shapes above the cylindrical ones expressed the periodical abandonment of the channel processes. The third type of log shapes (mixture of sawtooth, funnel and symmetrical types) overlaid the former series and probably represented bar-type evolutions.

and the well-log shape was cylindrical. In this interpretation the net sand thickness larger than 20 m was the indication of channels.

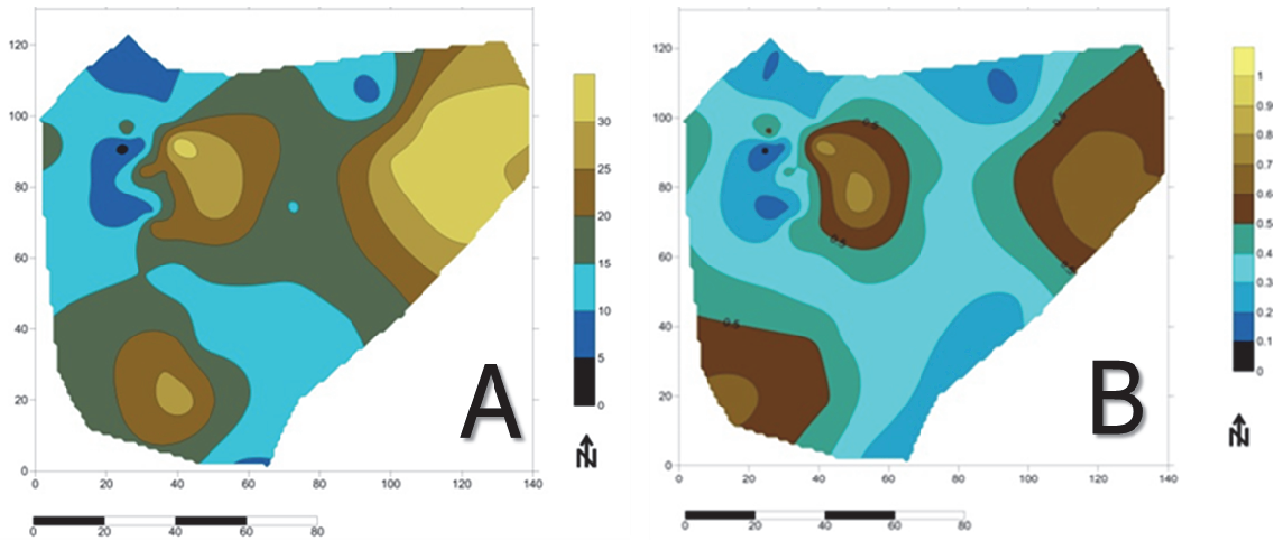


Figure 6 (A) Net sand thickness; (B) Sandstone/non-sandstone ratio

Figure 6 (B) shows the spatial distribution of sandstone/non-sandstone ratio. The highest sandstone ratio values were the indicators of channels and bars. The smaller sandstone ratio and porosity values defined those regions which were far from the sand laden currents.

4. DISCUSSION

Within the studied area having been defined as sandrich fan or ramp, two typical depositional facies were recognized: (1) channel and (2) channel-mouth bar. The analysis of well-log shapes and map of sandstone/non-sandstone ratio supported the result of 3D sequential simulation. The net sand and sand ratio maps suggested both the main sediment transport directions (N-NE) and the channels and channel-mouth bar continuous geometries.

5. ACKNOWLEDGMENT

The author would like to thank MOL Plc. for providing the data used in this study and to express her gratitude to János Geiger (from Dept.of Geology and Paleontology, University of Szeged, Hungary) for his useful suggestions.

6. REFERENCES

- GEIGER, J. (2012): Some thoughts on the pre- and postprocessing in sequential Gaussian simulation and their effects on reservoir characterization. In: GEIGER, J., PÁL-MOLNÁR, E. MALVIC, T. (Eds): New horizons in central European geomathematics, geostatistics and geoinformatics, GeoLitera Publ., Szeged, 17-35.
- GEIGER, J. (2006): Szekvenciális gaussi szimuláció az övzátonytestek kisléptékű heterogenitásának modellezésében. Földtani Közlöny, 136/4, 527-546.
- HORVÁTH, J. WÁGENHOFFER, A., GEIGER, J. (2012): "Analyses of reservoirs in Kisújszállás, Fegyvernek, Nagykörű fields" in Development of 'knowledge base' of general reservoir properties for EOR and IOR methodologies in Panonian (s.l.) clastic CH-reservoirs. Research Report.
- ISAAK, E. & SRIVASTAVA, M. (1987): Applied Geostatistics, Oxford University Press p.512
- MUTTI E. (1977): Distinctive thin-bedded turbidite facies and related depositional environments in the Eocene Hecho Group (South-central Pyrenees, Spain) Sedimentology (1977) 24, 107-131
- READING, H. G. & RICHARDS M. (1994): Turbidite System in Deep-Water Basin Margins Classified by Grain Size and Feeder System AAPG Bulletin, 78, 792-822.
- RIDER, M.H. (1999): Geologic interpretation of well logs Whittles Publishing Services. p.428

DEPOSITIONAL FACIES ANALYSIS IN CLASTIC SEDIMENTARY ENVIRONMENTS BASED ON NEURAL NETWORK CLUSTERING AND PROBABILISTIC EXTENSION

Janina HORVÁTH

Department of Geology and Palaeontology, University of Szeged,
H-6722, Szeged, Egyetem u. 2-6. Hungary
th.janina@geo.u-szeged.hu

In this study, two data clustering methods, an unsupervised neural network algorithm (UNN) and a k-means clustering are used to recognise different, subsurface, clastic depositional facies. Two case studies coming from different clastic sedimentary environments demonstrate the workflow. The first of them is Szőreg-1 reservoir of the Algyő field, SE Hungary, represents a delta plain environment. The second one shows a deep water turbidity system in Sava Depression, N Croatia. In the workflow the main emphasize is given on (1) the lateral estimation of the point like qualitative information of cluster members by indicator kriging (IK); (2) the way of interpretation of the geometry presented by IK; (3) comparison the efficiency of UNN and k-means clustering on the basis of the results provided by the previous two points.

Key words: *indicator kriging, sedimentary body geometry, variance analysis, Algyő field, Sava Depression*

1. INTRODUCTION

In the past few decades huge numbers of papers have introduced different multivariate statistical methods and workflows to identify subsurface facies analysis (e.g. Delfiner et al., 1987 tried to identify lithological units with discretion of log values based on discriminant factor analysis; Wolff and Pelissier-Combescure, 1982 and Serra, 1986 applied principal component analysis for separation of lithological unites.). Most of them have relied on the clustering the objects (samples) in the sample (or parameter) space (e.g. Gedeon et al. (2003) used clustering to identify lithofacies from well log data). However, only few (if any) have tried to use these classifying methods under the surface with combination of lateral extension of the cluster members. In fact, this approach can be expected to have significant uncertainty since the scattered lateral distribution of the sample points (wells). This study is aimed to contribute this issue by addressing three main points: (1) the lateral estimation of the point like qualitative information of cluster members by indicator kriging (IK); (2) the way of interpretation of the geometry presented by IK; (3) comparison the efficiency of UNN and k-means clustering on the basis of the results provided by the previous two points.

2. THEORETICAL CONSIDERATIONS

2.1 PROBABILISTIC EXTENSION OF QUALITATIVE INFORMATION BY IK

IK has been designed to estimate uncertainty at unknown points (e.g. at grid points, Journel 1983, 1986). For reaching this goal it uses a discretized form of the global probability distribution derived from the sample points. The procedure uses several cut-offs for this discretization. According to the spatial correlation structure measured between cut-offs this method estimates the probability distribution functions at any unsampled locations. These estimates (i.e. probability distributions) can change when the number of input samples change. That is why they are called conditional (i.e. conditioned to the actual number of data) probability distribution (e.g. Deutsch & Journel 1998, Olea 1999). In the frame of GSLIB this technique can be used for both continuous and discrete variable (Deutsch & Journel 1998). The later on is fits exactly to task of extending the clustering results into geographical space. It is, since clustering of any objects in the geographical space (let it be either UNN or k-means clustering) results in disjunctive sets of spatial points). Their “gridding” process means lateral estimation of the cluster memberships as qualitative objects at each grid node over a domain. This estimation can be than after the definition of as many indicator variables as the number of clusters. The implementation of IK in GSLIB calculates probability for each input category (i.e. for each cluster membership) at every grid nodes. Note, at any particular grid node, the sum of these probabilities must be 1. It is quite obvious that a particular grid node should be assigned to that cluster memberships which has the largest estimated probability (e.g. Bierkens and Burrough 1993). This type of interpretation can visualized through e.g. a post map. Another choice within the frame of GSLIB is a map showing the change of probability belonging to a particular cluster membership. It is necessary to find a reasonable probability-contour which can outline the shape of a supposed physiographic unit well.

2.2 IDENTIFICATION OF DEPOSITION FACIES BASED ON GEOMETRY

It has been proved, that different depositional environment can be characterized by special (though, not necessarily different) rock-body morphology (e.g. Moore 1949; Pettijohn et al. 1972). These geometries of depositional facies are the basis of seismic stratigraphy and multiple point simulations, as well. Following this way of thought, in this work the rock body geometry expressed by probability contours are interpreted in the terms of depositional facies.

2.3 EFFICIENCY OF APPLIED CLUSTER PROCESS

Both UNN and k-means clustering breaks the observations into groups that are internally homogeneous as possible and as different as possible from each other. The Kohonen neural network represents a non-linear separation technique, while the k-means clustering is based on the Euclidean distance between the object in the attribute (parameter) space. This later approach is regarded to be the most similar classical clustering (Ultsch, 1995; Murtagh and Hernandez, 1995). Warren (1994) and Ultsch (1995) dealt with their comparison using statistical tests and found that K-means sometimes failed to find any reasonable clusters.

In this study the comparison of these two methods relies on the results of variance analysis. Miller and Khan (1962) showed that, in case on normal distribution, the total variance was the sum of the within group and between group variances (WGV and BGV, correspondingly). Clustering seeks to minimize within-group variance (WGV) and maximize between-group variance (BGW). It can rarely reach a substantial difference between them. The within cluster variance refers to the spread of objects around the mean and the between-cluster variance is a measure of spreading of the cluster centroids.

The difference between WGV and BGV can express the suitability of cluster results. The relatively low WGV and larger BGW mean that cluster analysis has a number of heterogeneous groups with homogeneous contents.

3. STUDY AREAS

Szóreg-1 is one of the largest reservoirs of the Algyó Filed, S-Hungary. The average gross thickness is about 35m, but locally the reservoir can be up to 50m thick. Some earlier works (Geiger 2003, Sebők-Szilágyi and Geiger 2012) have proved its deltaic plain origin. In this reservoir, UNN was applied in two depositional sub-environments: (1) emerging distributary mouth bar and (2) prograded bifurcation channels. Their corresponding stratigraphical positions are 34–35 m and 24–27 m below the top argillaceous marl of the rock body. Their 3D geometry and geostatistical characters have already been reported (e.g. Geiger, 2003; Sebők-Szilágyi, Geiger, 2012). The input variables of their NN-analysis were porosity, hydraulic conductivity and sand content values. They were come from the high resolution quantitative geophysical interpretations.

The second case study was about the Sava Field, Northern Croatia. The entire sedimentary sequence belongs to the Neogene and Quaternary periods. Generally, the Middle and partially Upper Miocene sedimentation was highly influenced by the palaeo-relief of the pre-Neogene basement. The analysed two sequences were built up by Upper Miocene marls, siltstones and sandstones. The latter two lithotypes had been deposited by periodic turbidity

currents over the entire depression (e.g., Šimon, 1980). These turbidity flows were active in lacustrine environments during the Pannonian and Pontian ages (e.g., Vrbanac, 1996). The data used in this work were originated from the high resolution (0.2 m) petrophysical interpretations of the available well logs. The variability of thickness was very high in both reservoirs. So, the vertical thickness changed between 1-21 m. That is why the basic scale was 1m and not the whole thickness of the reservoirs. Between any two cutting surfaces, the petrophysical data (coming from well-log interpretation), of the 1.0 m thick vertical intervals were given by the average of the datum falling to these intervals. This data set was the input for UNN which contains the following petrophysical parameters porosity, water saturation, shale volume and a categorical variable, which was a code to describe the lithotypes. This code took values between 0-10 according to the shale alternation in the sandy deposit.

4. RESULTS AND DISCUSSION

In the case of Algyő Field, six NN-facies were defined: (1) interdistributary bays; (2) outer bars facing to still water sedimentation; (3) The marginal parts of distributary mouth bars having been developed as the results of channel and bay interactions, (4) main body of the distributary mouth bars with 6.5-7 km width and kidney-shape geometry; (5) marginal part of the involved channels and (6) bifurcation channels with dendroid geometry. This channel pattern characterized about 5km length and around 500m width channel network.

The identified facies showed two main phase of the depositional history of Szőreg-1 reservoir (Geiger 2003). In the first phase discrete major and minor mouth bars formed. During the second one bars prograded and bifurcating channel cut into their rock body.

In the case of Sava Field, four NN-facies were defined. (1) Massive marls with low porosity represent a still water sedimentation. (2) Low-density turbidity currents resulted in sandstones interbedded by siltstones and marls. They were accumulated between bifurcating channels of fan system. (3) Thin sandstones and interbedded siltstones of low-density turbidities were regarded to belong to lob-type deposits. (4) Massive sandstone was probably deposited at the axes of turbidity channels of a sand rich turbidity fan (Horváth, 2014). It has been proved they are equivalents to those of Vrbanac's former works (Vrbanac, 1996; Vrbanac et al., 2010, Horváth 2014).

The sedimentary environment was identified according to the characterized depositional facieses. In general, it is suggested to be a the mid-fan area of a sand-rich submarine fan system. The processes of facies migration suggest that this submarine fan system prograded from NW to SE. During the progradation the lobated sediments shifted laterally too.

From selected 1-2m thick intervals of the reservoirs three physiographic units were characterised: (1) channel with elongated and bifurcated shape in the direction of main progradation; it is maximum 1200-1300m long and 750m wide. (2) lobated deposit with radial pattern which is about 700m in the major axis (NW-SE) and in the perpendicular direction it is maximum 500m wide; (3) elongated channel without distribution which represents the proximal part of suprafan area and it has about 2000m long axis from NW to SE, maximum 800m breadth.

The comparison of data separation by Kohonen neural network and k-means algorithm pointed out, that (1) UNN is able to recognize cluster as facieses even in such situation where k-means clustering techniques fail to find any reasonable depositional units; (2) one of the advantage of using NN in facies analysis is that its cluster-forming ‘capacity’ is self-regulated, that is why is more efficient than in the cases of ‘classic’ clustering.

5. REFERENCES

- BIERKENS, M. F. P. and P. A. BURROUGH (1993) The Indicator Approach to Categorical Soil Data. I. Theory. *Journal of Soil Science*, 44, 361-368.
- DELFINER, P.; PEYRET, O.; SERRA, O. (1987): Automatic determination of lithology from well logs by statistical analysis. *SPE Formation Evaluation*, Vol. 2, pp. 303-310
- DEUTSCH, C.,V. & JOURNEL, A., G. (1998): *GSLIB Geostatistical Software Library and USER'S GUIDE*. Oxford University Press. p.369
- GEDEON, T. D.; WOND, P. M.; TAMHANE, D.; LIN, T. (2003): Extending the use of linguistic petrographical descriptions to characterise core porosity. In: NIKRAVESH, M.; ZADEH, L. A.; AMINZADEH, F. (2003): *Soft computing and intelligent data analysis in oil exploration*, Elsevier (Developments in Petroleum Science, Vol. 51), p.755
- GEIGER, J. (2003): A pannóniaiújfalui (törteli) formációbanlevőAlgyő-delta fejlődéstörténete – I.: Az Algyő-delta alkörnyezeteinek 3d modellezése (Depositional history of the PannonianAlgyő-delta (Újfalu Formation). Part one: 3D modeling of the sub-environments of Algyő-delta) - *FöldtaniKözlöny*, Vol. 133, no. 1, pp. 91-112
- HORVÁTH, J. (2013): Characterization of clastic sedimentary environments by clustering algorithm and several statistical approaches; two case studies (South-Eastern Hungary, Northern Croatia) - (Selected studies of the 2012 Croatian-Hungarian Geomathematical Convent, Mórahalom), Edited by Geiger, J., Pál-Molnár, E., Malvić, T.; pp. 71-85; *GeoLitera Publishing House Institute of Geosciences*, ISBN: 978-963-306-235-7
- JOURNEL, A. G. (1983): Nonparametric estimation of spatial distributions, *Mathematical Geology*, Vol.15, no.3, pp.445-468

- JOURNEL, A. G. (1986) Constrained Interpolation and Qualitative Information - the Soft Kriging Approach. *Mathematical Geology*, 18, 269-305
- LORR M. (1983): Cluster analysis for social scientists, The Jossey-Bass Social and Behavioral Science Series, San Francisco, Jossey Bass, p. 233
- MILLER, R.L, KHAN, J.S. (1962) Statistical analysis in the geological sciences. John Wiley and Sons Inc. pp. 164-144
- MOOR, R. C. (1949): Meaning of facies. In "Sedimentary facies in Geologic History", *Geol. Soc. Am. Mem. No. 39*, pp. 1-34
- MURTAGH, F.; HERNÁNDEZ-PAJARES, M. (1995): The Kohonen self-organizing feature map method: an assessment", *Journal of Classification*, Vol. 12, pp. 165-190
- OLEA, R., A. (1999): Geostatistics for engineers and geoscientists. Kluwer Academic Publisher. p.303.
- PETTIJOHN, F. J., P. E. POTTER, R. SIEVER (1972): Sand and sandstone, Springer-Verlag, New York, p 618.
- SEBŐK-SZILÁGYI, SZ., GEIGER, J. (2012): Sedimentological study of the Szőreg-1 reservoir (Algyő Field, Hungary): a combination of traditional and 3D sedimentological approaches, *Geologia Croatica*, Vol. 65, no. 1, pp. 77-90
- SERRA, O. (1986): Fundamentals of well-log interpretation. *Developments in Petroleum Science*, 15a,b. Elsevier, Amsterdam, p. 684
- ŠIMON, J. (1980): Prilog stratigrafiji u taložnom sustavu pješčanih rezervoara Sava-grupe naslaga mlađeg tercijara u Panonskom bazenu sjeverne Hrvatske. (Contribution to stratigraphy of sandstone reservoirs depositional system in the Sava Group sediments in Late Tertiary of Pannonian Basin in the Northern Croatia - in Croatian) PhD Thesis, University of Zagreb, Faculty of Mining, Geology and Petroleum Engineering, Zagreb p. 66
- ULTSCH, A. (1995): Self Organizing Neural Networks perform different from statistical K-means clustering. In *Proc. GfKI*, Basel, Swiss
- VRBANAC, B. (1996): Paleostrukturalne i sedimentološke analize gornjopanonskih naslaga formacije Ivanić Grad u Savskoj depresiji (Palaeostructural and sedimentological analyses of Late Pannonian sediments of Ivanić Grad formation in the Sava depression). PhD dissertation, Faculty of Natural Sciences, University of Zagreb, p. 303
- VRBANAC, B., VELIĆ, J., MALVIĆ, T. (2010): Sedimentation of deep-water turbidites in the SW part of the Pannonian Basin. *Geologica Carpathica*, Vol. 61, no.1, pp. 55-69
- WARREN, S. S. (1994): Neural Networks and Statistical Models, 19th Annual SAS Users Group International conference, April 1994, USA
- WOLFF, M. and PELISSIER-COMBESURE, J. (1982): FACIOLOG: automatic electro-facies determination, SPWLA Annual Logging Symposium, pp. FF, 6-9

STATISTICAL CHARACTERS OF REALIZATIONS DERIVED FROM STOCHASTIC SIMULATIONS BASED ON CT IMAGES

Noémi JAKAB

Department of Geology and Paleontology, University of Szeged, H-6722, Szeged, Egyetem u. 2-6. Hungary;
j.noemi@geo.u-szeged.hu

In this paper the local and regional spaces of uncertainty are analysed when using different stochastic simulation algorithms to assess the spatial uncertainty. The exhaustive data set used for the investigations originates from the CT image of a core-sized sedimentary structure. From this data set 100 random points were chosen and the modelling and simulation were based on these data. The stochastic simulations were performed on five different grid resolutions and the aim was to study the effect of the different grid resolutions and different simulation algorithms on the reproduction of spatial characteristics as well as their effect on the stability of the estimation, which was evaluated on the basis of variance decomposition.

Key words: *stochastic simulation, uncertainty, variance decomposition*

1. INTRODUCTION

The aim of this study is to study and compare the differences between the outputs of three types of stochastic simulation algorithms, and to analyse the effect of the different grid resolutions on the reproduction of spatial characteristics, as well as their effect on the stability of the estimation. In this work we are following a train of thought introduced by an earlier paper (Geiger et al., 2010) by applying variance decomposition on the pooled grid averages to subdivide the grid variances to a within-group and a between-group component to characterize the local and regional uncertainties.

2. METHODS

The analyses were carried out on a CT image originating from a core sized sedimentary structure. The image (**Figure 1**) and the corresponding background data set consisted of 16,000 measured Hounsfield unit values arranged on a regularly spaced 125 x 128 grid. From this exhaustive data set a random set of 100 locations was chosen and all geostatistical analyses were conducted on this subset, which will be referred to as the sample set.

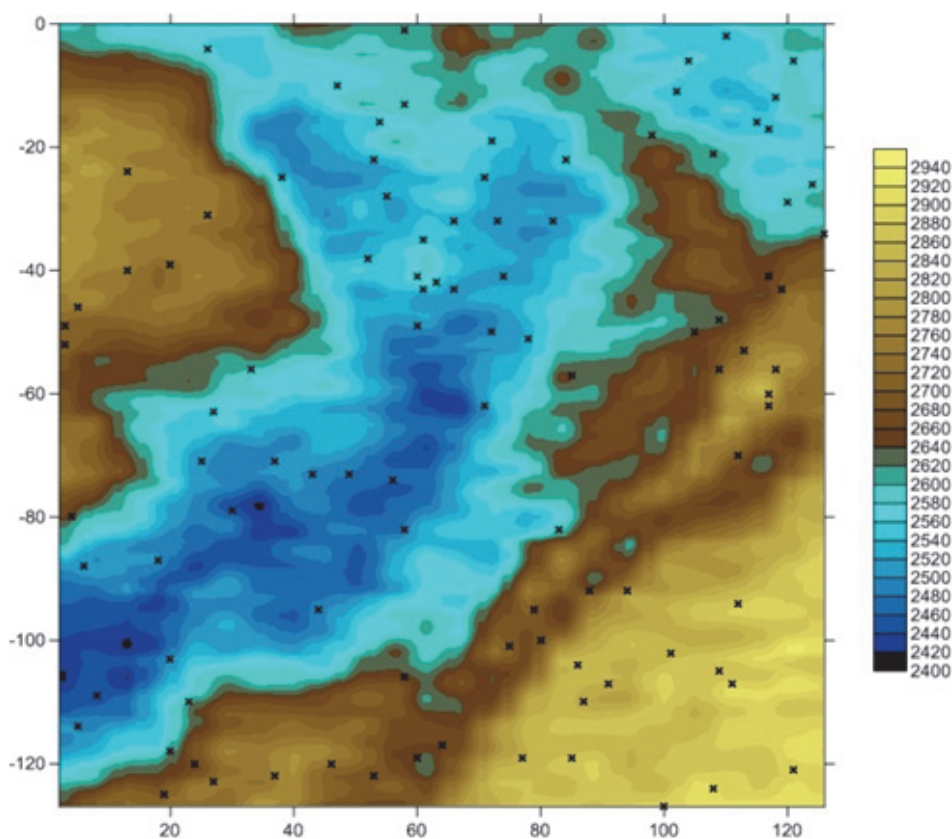


Figure 1: *The CT image of the exhaustive data set*

The first step in the workflow was the comparison of the distributions of the exhaustive and the sample set to check whether the sample set can be regarded representative of the background distribution. This was done by examining the frequency histograms and quantile plots of the two distributions. The next step was to perform stochastic simulations based on the sample set. Three types of simulation algorithms were utilized in this work: sequential indicator simulation, sequential Gaussian simulation, and P-field simulation. All simulations were executed in the GSLib framework, additionally in the case of P-field simulation a modified GSLib executable (Ying, 2000) was used. All three simulation types were performed on the following five different grid resolutions: 0.5×0.5 , 1×1 , 1.5×1.5 , 2×2 and 2.5×2.5 with 100 output realizations for each.

For the evaluation of the different simulation methods we examined the statistical characters of the output realizations and applied variance decomposition (Miller and Kahn, 1962) on the increasing number of realizations to assess the stability of our estimations. According to this work, the total variance of the simulation system depends on two things. The first is the variability around the grid average, while the second is the variances being characteristic around the node averages. In the terms of One-Way ANOVA they are called between-group (BGV) and within-group (WGV) variances. In this

approach the WGV reflects the local stability or uncertainty of the estimation, while the BGV expresses the lateral variability of the analysed property.

3.RESULTS

3.1. COMPARISON OF THE EXHAUSTIVE AND THE SAMPLE SET

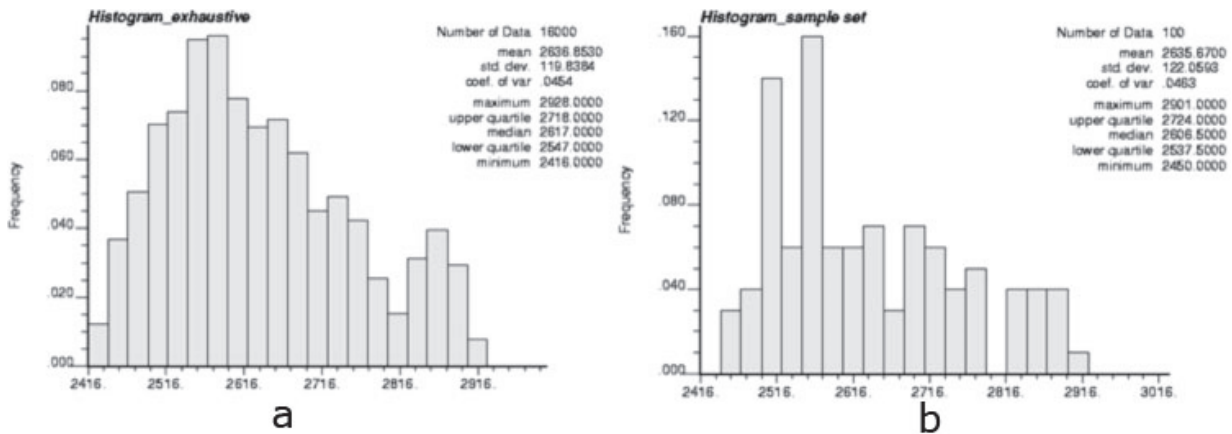


Figure 4: Frequency histograms (a: exhaustive set, b: sample set)

As we can see on **Figure 2** the exhaustive set can be characterized by a skewed bimodal distribution with the first mode around 2550 HU and the second one around 2850 HU. The distribution of the sample set was able to capture the features of the background distribution only partially: the minimum and the maximum of the values showed a narrower spread, the interval between 2796 and 2806 HU was completely missing, and the general shape of the distribution also showed some differences. However, according to the outputs of the conducted Kolmogorov-Smirnov test there was not a statistically significant difference between the two distributions at the 95.0% confidence level. This result suggested that the selected sample set is adequate for the modelling process, although the exact reproduction of the background distribution statistics could not be expected.

3.2. OUTPUTS OF THE STOCHASTIC SIMULATIONS

3.2.1. SEQUENTIAL GAUSSIAN SIMULATION

Figure 3-a depicts the frequency histogram of the 100 pooled realizations of SGS for the 1 x 1 grid resolution. The histogram implies that the SGS algorithm was able to capture the statistical features of the sample set quite well, although the exact reproduction of the mode was not achieved.

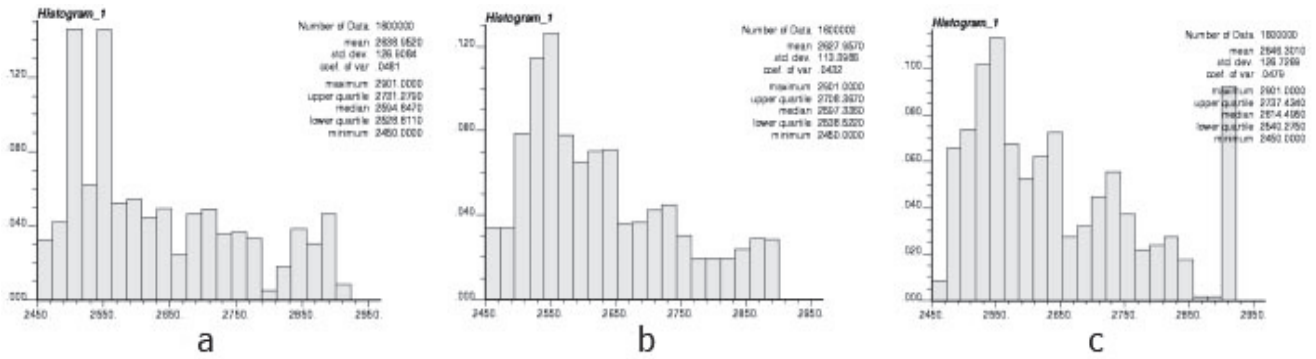


Figure 5: Frequency histograms of the 100 output realizations for 1 x 1 grid resolution (a: SGS, b: SIS, c: P-field simulation)

Examination of the QQ plots demonstrated that decreasing the grid resolution resulted in better reproduction of the sample statistics in the case of SGS. The E-type map derived from the 100 realizations for the 1 x 1 resolution (**Figure 4-a**) suggested that while the SGS algorithm reproduces a globally plausible picture of the exhaustive data set, it was not capable of representing the inner heterogeneities of the studied morphology.

3.2.2. SEQUENTIAL INDICATOR SIMULATION

The histogram of the 100 realizations of the SIS on 1 x 1 grid resolution (**Figure 3-b**) show a greater difference when compared to the sample set. The SIS algorithm generated a different shaped distribution with one distinct mode, while the tails of the distribution seemed to be less detailed.

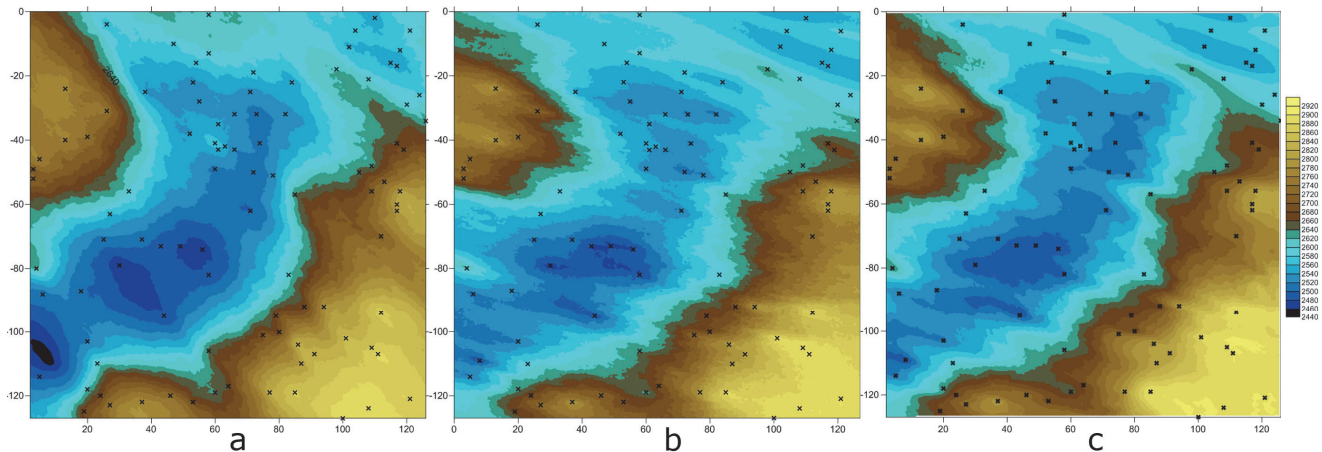


Figure 6: E-type maps for 1 x 1 grid resolution (a: SGS, b: SIS, c: P-field simulation)

According to the QQ plots lower values of the distribution were stable at all grid resolutions, while the fit of the higher values fluctuated as the resolution changed. These observations implied that the 1 x 1 grid resolution provided the best fit for SIS.

The E-type maps approximated the reality reasonably well, but they also provided a slightly different picture than the SGS E-type maps. In this case the

local heterogeneities of the middle part of the image were more pronounced (**Figure 4-b**). It is also interesting to note the SIS fails to reproduce the high valued salient in the upper right area of **Figure 1** (which the SGS and the P-field simulation were capable of), instead the algorithm only estimates an isolated high without extending it to the marginal high valued areas.

3.2.3. P-field SIMULATION

The P-field algorithm outputs were fairly similar to the SIS outputs, because the input data (indicator thresholds and corresponding variograms) were essentially the same. The algorithm also managed to reproduce the target statistics only partially with a slightly different mode and some artificial fluctuations at the high valued tail of the distribution (**Figure 3-c**). These fluctuations also appear on every QQ plot belonging to the different grid resolutions. Studying the QQ plots suggested that in the case of P-field simulation the most suitable grid resolution for this morphology was the 1.5 x 1.5 resolution. The E-type maps belonging to the 1 x 1 resolution of this algorithm (**Figure 4-c**) also seemed to reproduce the studied morphology quite well. In the aspect of local heterogeneities these maps seemed to provide a transition between the SGS and SIS E-type maps: local heterogeneities were recognizable but they were not as explicit as on the SIS E-type maps.

3.3. VARIANCE DECOMPOSITION

The sequences of grid averages for all three simulation algorithms can be seen on **Figure 5**, which shows the convergences of the sequences with increasing number of pooled realizations. Variance decomposition implied that the limit values are strongly related to the grid resolution: the higher the resolution the smaller the limit value. The speed of the convergence was different in each case: when using SIS the estimation started to become stable at around 57 realizations, while the SGS algorithm required only 50 realizations to reach stability. The SIS and SGS showed similar fluctuating characteristics while the P-field algorithm exhibited the most consistent behaviour, mild fluctuations were present until the number of pooled realizations reached 40, and after this point the sequences became extremely smooth.

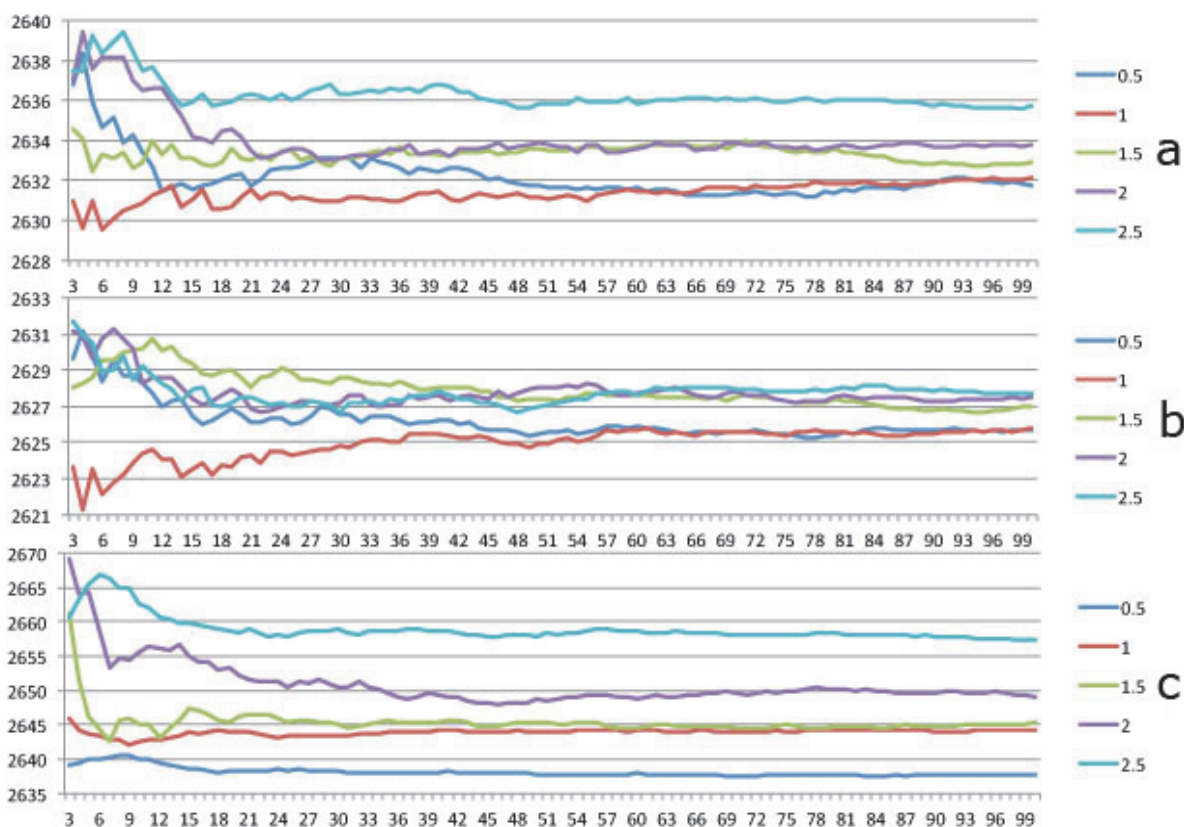


Figure 7: Pooled grid averages for the different resolutions (a: SGS, b: SIS, c: P-field simulation)

Looking at the WGV and BGV sequences tells us some important information. The first one is that the limits for the different grid resolutions were very close to each other within each simulation algorithm. The second one is that the sequences showed a favourable picture: according to the results, in the case of this particular morphology, all five grid resolutions of all three simulation algorithms were suitable in the sense that their between group variances were greater than the within group variances, starting from three pooled realizations. According to **Table 1**, which shows the ratios of BGV/BGV+WGV limits, SIS had the lowest ratio while P-field simulation had the highest with 77.6% of the variance originating from the geological background.

Table 1: Approximate limit values of the WGV and BGV sequences

	SGS	SIS	P-field
Average limit for WGV sequence	4250	5500	3600
Average limit for BGV sequence	11800	7600	12500
BGV/(BGV+WGV)	0.735	0.58	0.776

4. CONCLUSION

After the implementation of the demonstrated approach several conclusions can be drawn. At the present stage of this work it seems that all simulation algorithms have their advantages and disadvantages as well, and it would be questionable to highlight one grid resolution of one algorithm as the best. SGS algorithm yielded the closest reproduction of the target statistics, but it failed to capture the local heterogeneities of the studied morphology, and also required the highest number of pooled realizations to provide stable estimation. In the case of SGS the smallest grid resolution proved to be the most suitable.

SIS and P-field simulation outputs showed less resemblance to the target statistics, and they were rather similar to each other due to the same input data. However, there were some differences between the two, for example the observed artificial fluctuations at the high valued tail of the distribution belonging to the P-field realizations. Also, on one hand SIS reproduced local heterogeneities more effectively than P-field simulation did. On the other hand, the P-field algorithm required a smaller number of pooled realizations to reach convergence, and also it was a generally less CPU demanding procedure. These features may be of high importance when the reduction of computational time is necessary. For SIS the 1 x 1 grid resolution, while for the P-field simulation the 1.5 x 1.5 resolution proved to reproduce the background distribution the best.

Variance decomposition showed that all three simulation algorithms were suitable for the estimation in the case of this particular morphology, because they all provided higher BGV than WGV, meaning that the total variance of the E-type grid could rather be drawn back to the underlying geology than the instability of the estimation method. For further differentiation between the simulation algorithms our future plans are to analyse the Shannon entropy belonging to the pooled realizations of the simulation outputs.

5. REFERENCES

- GEIGER, J. & MALVIC, T. & HORVÁTH, J. & NOVAK ZELENIKA, K. (2010): Statistical characters of realizations derived from sequential indicator simulation: 16th Annual Conference of the International Association for Mathematical Geosciences, Budapest, Proceedings.
- MILLER, R.L. & KAHN, J.S. (1962): Statistical analysis in the geological sciences, John Wiley and Sons Inc. pp.164-144.
- YING, Z. (2000): Iksim: A fast algorithm for indicator kriging and simulation in the presence of inequality constraints, hard and soft data, Computer and Geosciences, v. 20, p. 605-608.

HIGH-RESOLUTION FACIES MODELING TO LOCATE BY-PASSED OIL: A CASE HISTORY FROM ALGYÓ FIELD

Angelika SÓLA

MOL Plc. H-1117 Budapest, Októberhuszonharmadika u. 18.

ASola@mol.hu

One of the most important tasks of Hungarian hydrocarbon production is investigating by-passed oil bodies through mining in order to enhance exploitation. One of our target areas to achieve this goal is Algyó Field, where the reservoirs belong to a delta system. In this system, the spatial distribution of different kinds of facies determines the directions of fluid flow and potential locations of traps. A reliable and high-resolution reservoir model was necessary to understand the movements of fluids (shifting of the oil body). In implementing this work, we constructed a facies distribution map, which we combined with seismic data and gross thickness map. The result is a facies map that helps to determine by-passed oil and to trace targets for production.

Keywords: *Algyó field, delta plain, facies map, by-passed oil*

1. INTRODUCTION

In mature oil fields, the high resolution mapping of the reservoir heterogeneity is an efficient tool to find by-passed oil bodies. Such a detailed reservoir geological model highlighting on the connectivity of different sand bodies within and among the different initial depositional environment is inevitable to prolong the life-cycle of the reservoir/field by tapping these oil bodies. This paper is about how to build such a detailed facies model on the example of Csongrád-Dél series in Algyó Field.

2. METHOD

The sandstone reservoirs of the Algyó Field are products of a Neogene, progradational delta system (Révész, 1980). We studied three distinct deposits (individual hydrodynamic systems), named Csonrád-Dél-1, -2, -3. focussing primarily on determination of the depositional environments from well log response analyses.

This method in our modelling is not an unprecedented one. It was published by Krueger (1968) who categorized different well log responses (GR, SP, RT)

integrating them with core analysis and, categorized them on the basis of their geometric forms. Through this he was able to determine depositional environments. The method was upgraded by Serra in 1985. In our case a few core samples were available so the main data sources were well logs. In addition the gross thickness map and the seismic attribute map were utilized to distinguish individual depositional environments (**Figure 1**).

Each well intersecting Csongrád-Dél deposits got a number from 1 to 13 indicating the dominating facies (swamp, channel, mouth bar etc.). With this we could check the spatial distribution of facies (**Figure 1**).

From these a contour map of facies could have been drawn (**Figure 2**) which was used in reservoir modelling. During drawing it was important to investigate recent delta systems.

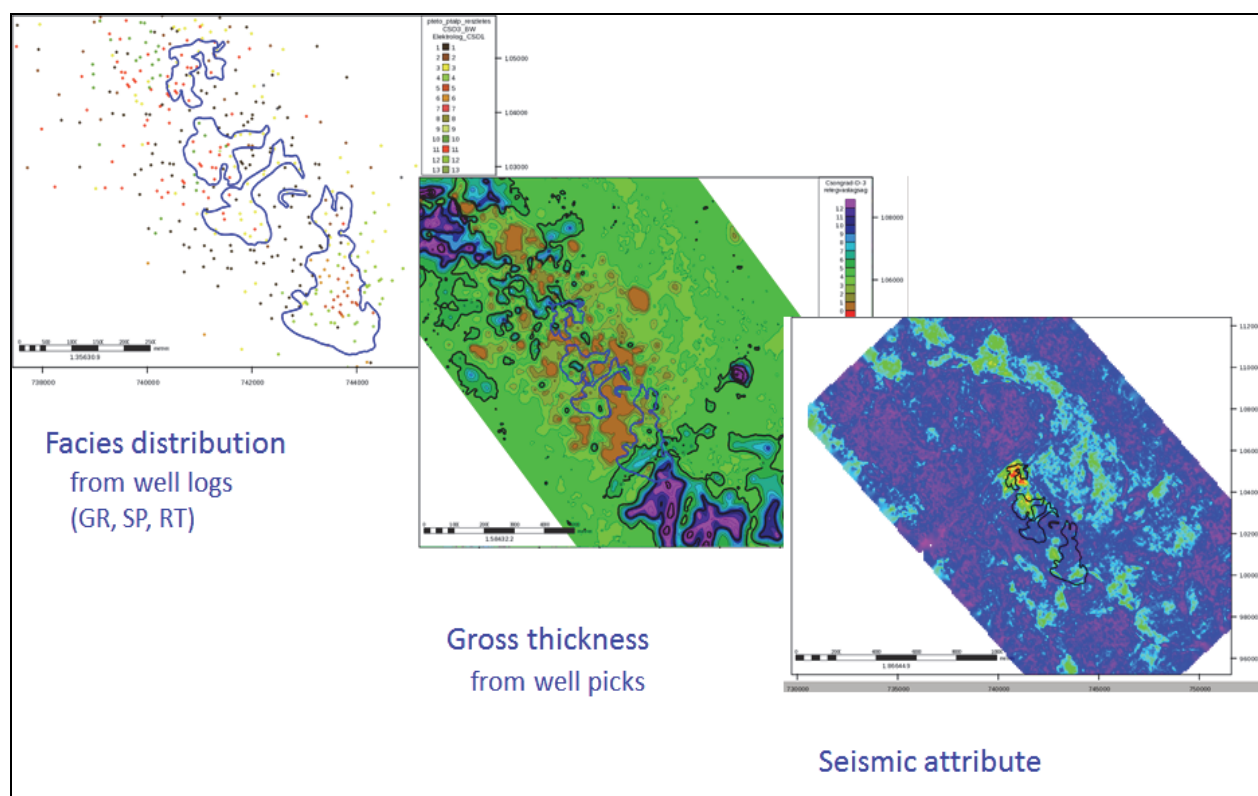


Figure 1: Facies distribution map; gross thickness map; seismic attribute map (Csongrád-Dél-3)

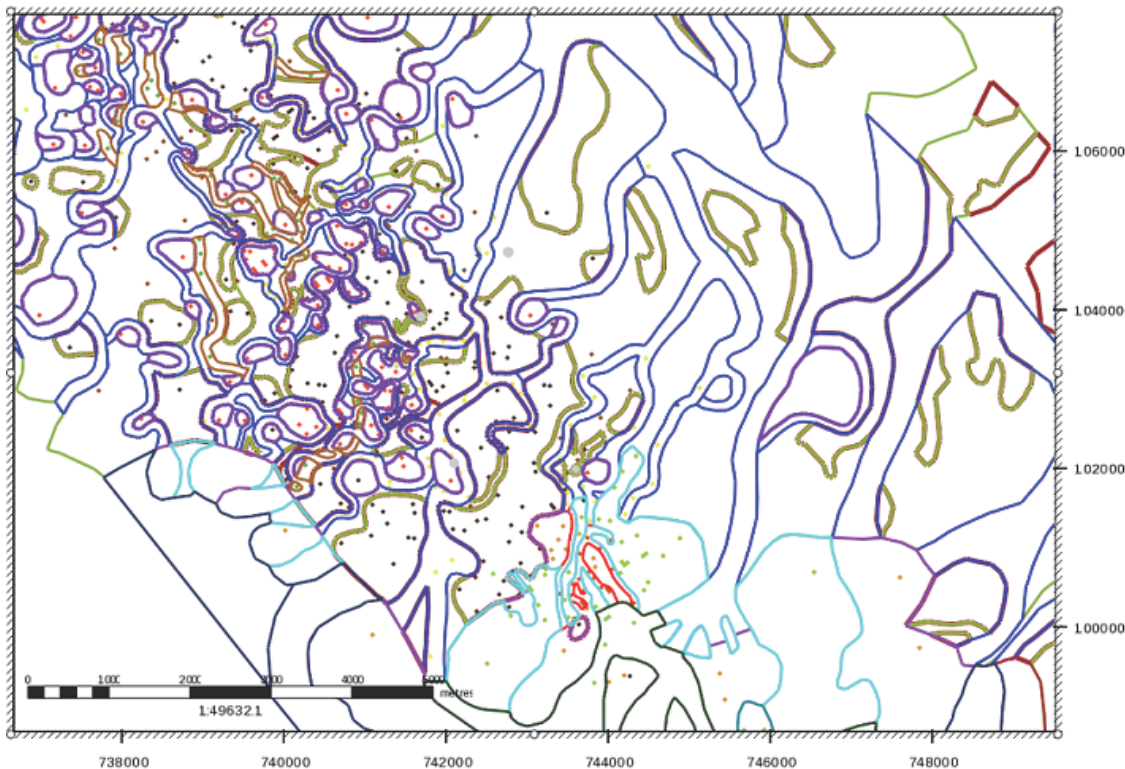


Figure 2: *Contours of facies in the area (Csongrád-Dél-3) after well log response interpretation*

3. THE RESERVOIR

The reservoir consists of siliciclastic sediments (unconsolidated sand) with interbedded silt and/or coal layers. The hydrocarbons accumulated in a structural trap (Compaction Anticline) Its geometry and position are also influenced by the development of delta system and related synsedimentary growth faults.

4. WHY WE HAD TO RECONSIDER THE FACIES MODEL?

In the phase of exploration it is enough to know the textural and lithological description of reservoir rocks (sand or silt system). However at the end of the production it is necessary to deal with the heterogeneity of the reservoir and the interconnection of the sand layers/bodies controlled predominantly by the depositional events. Furthermore they influence layering, structural, textural and petrophysical properties as well.

5. RESULTS

Our aim has been to know better the heterogeneity of the reservoirs furthermore to investigate the connectivity between the sand bodies. With facies maps indicating this (**Figure 3**) we can get information about the distribution of the potential reservoir rocks including but not limited to those with by-passed oil.

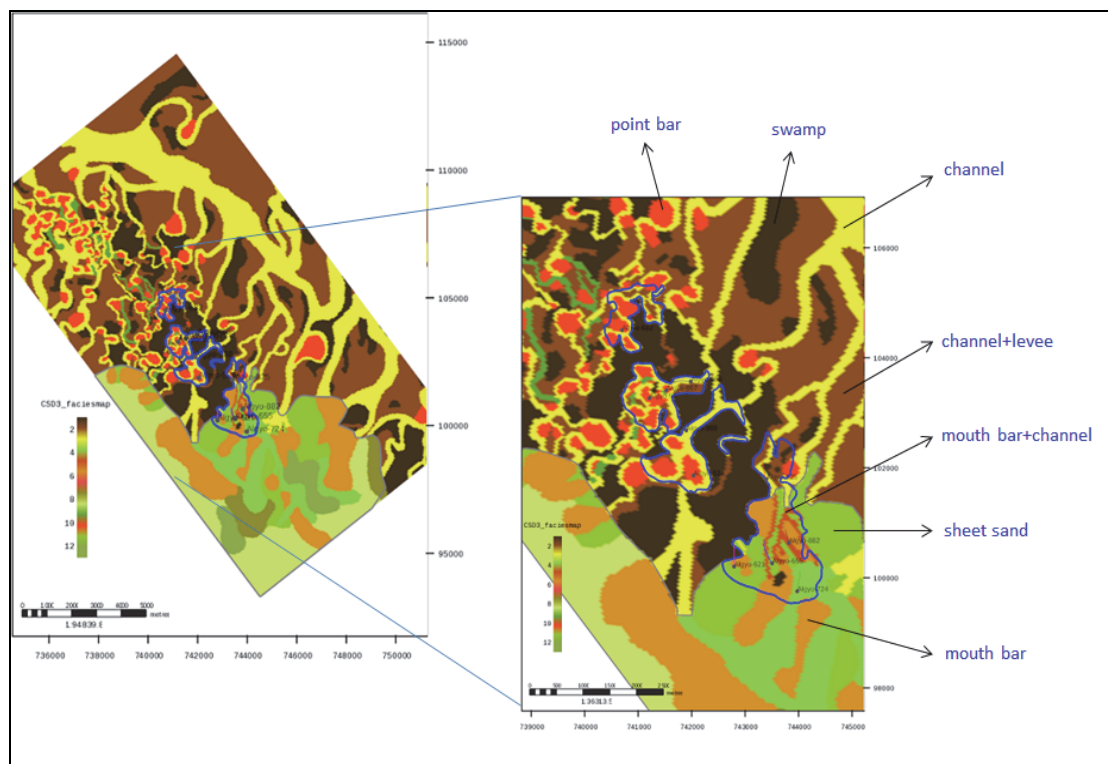


Figure 3: Facies map of Csongrád-Dél-3 deposit

Vertically, if we look at **Figure 4** we can see a concise story of development of the delta system. The lower layer of Csonrád-Dél-1 is the oldest, whilst Csongrád-Dél-3 the youngest one. According to these facies maps we can notice that the quality of the reservoirs is getting poorer and poorer worse upwards. If we check this tendency against the production rates the best reservoir rocks belong to mouth bars and related sediments. Good example for it the well 724 (mouth bar category) which was perforated with success in the level of Csongrád-Dél-3 deposit.

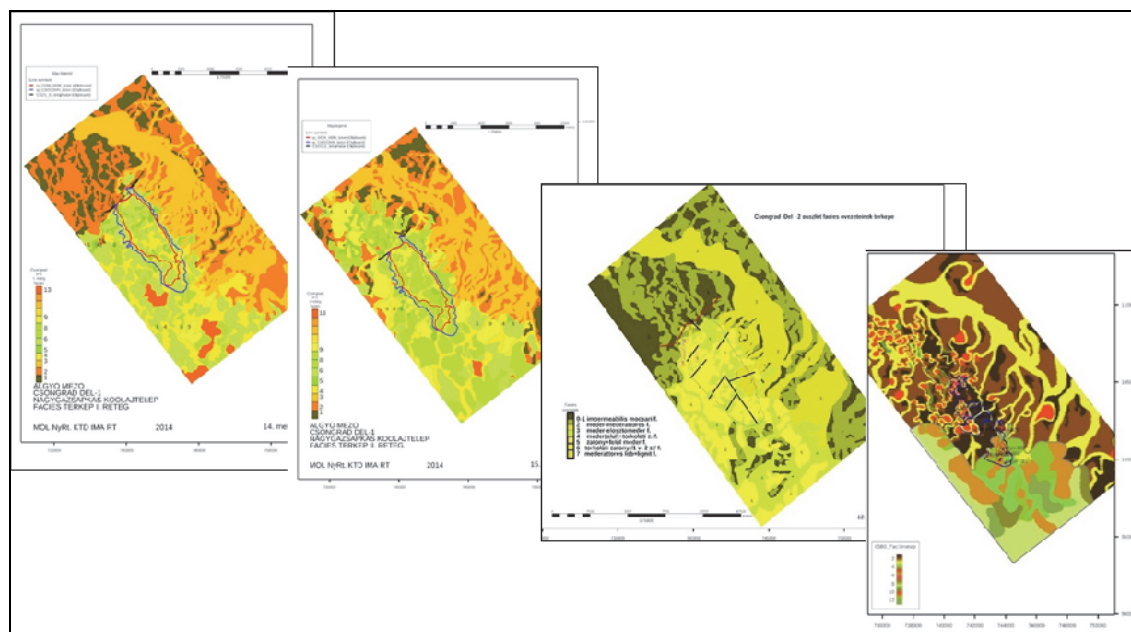


Figure 4: *Facies maps in Csongrád-Dél series*

These reconsidered facies model can help us to find by-passed oil bodies in the reservoirs but the real results will be given by practice; with other words, if we perforate a given layer with success as in case well 724 or 621.

6. REFERENCES

- KRUEGER, W. C. (1968): Depositional environments of sandstones as interpreted from electrical measurements. *Trans. Gulf Coast Geol. Soc.*, 18: 226-241
- RÉVÉSZ, I. (1980): Az Algyó-2 telep földtani felépítése, üledékföldtani heterogenitása és ősföldrajzi viszonyai. *Földtani közlöny*, vol. 110, No. 3-4., pp. 512-539.
- SERRA, O. (1985): Sedimentary environments from wireline logs. *Services Techniques Schlumberger*.

ROAD FROM USING SEISMIC ATTRIBUTE TO INVENTING SPECIAL APPROACH OF FACIES MODELLING

János BLAHÓ

MOL Plc. H-1117 Budapest, Októberhuszonharmadika u. 18.

jblaho@mol.hu

The use of seismic attributes may raise some difficulties in the facies modelling. We needed to invent a special approach of facies modelling. Seismic attributes do reflect well the facies distribution, but we cannot control their statistics in context of the facies incompatibility. The very first step of our special approach to define facies types is based on the analysing of log motifs of sedimentary facies of different environments. Next step is the creation of facies maps. Then comes the 3D parameter model, which used to come from the trend model of the actual parameter. These results are merged with a traditional sand-shale facies parameter. The facies types harmonize logs with cores, well tests, and production data. That is why facies categories serve real practical needs. Our aim is to build detailed genetic model for simulation and finally to make oil production more effective.

Keywords: *facies, facies modelling, environments*

1. INTRODUCTION

In an earlier presentation (Blahó, 2013.) it was been shown how seismic attributes could be used in mapping facies distribution and depositional environments in case of the Csongrád series, Algyő Field, SE-Hungary. However, repeated applications of this method revealed its weak points. This recognition initiated to develop an upgraded version of the seismic attribute based facies modelling of this reservoir.

2. PRINCIPLES AND IDEAS OF THE NEW APPROACH

Before the interpretation of any seismic attribute, two basic questions should be answered:

- how accurate is attribute image and why;
- what is the attribute shown in the picture;

Seismic attributes can be calculated by using different algorithms. They can result in similar patterns with different details. In this study the RMS Amplitude (**Figure 1**) and its thickness weighted form is used for demonstration (**Figure 1 and Figure 2** accordingly).

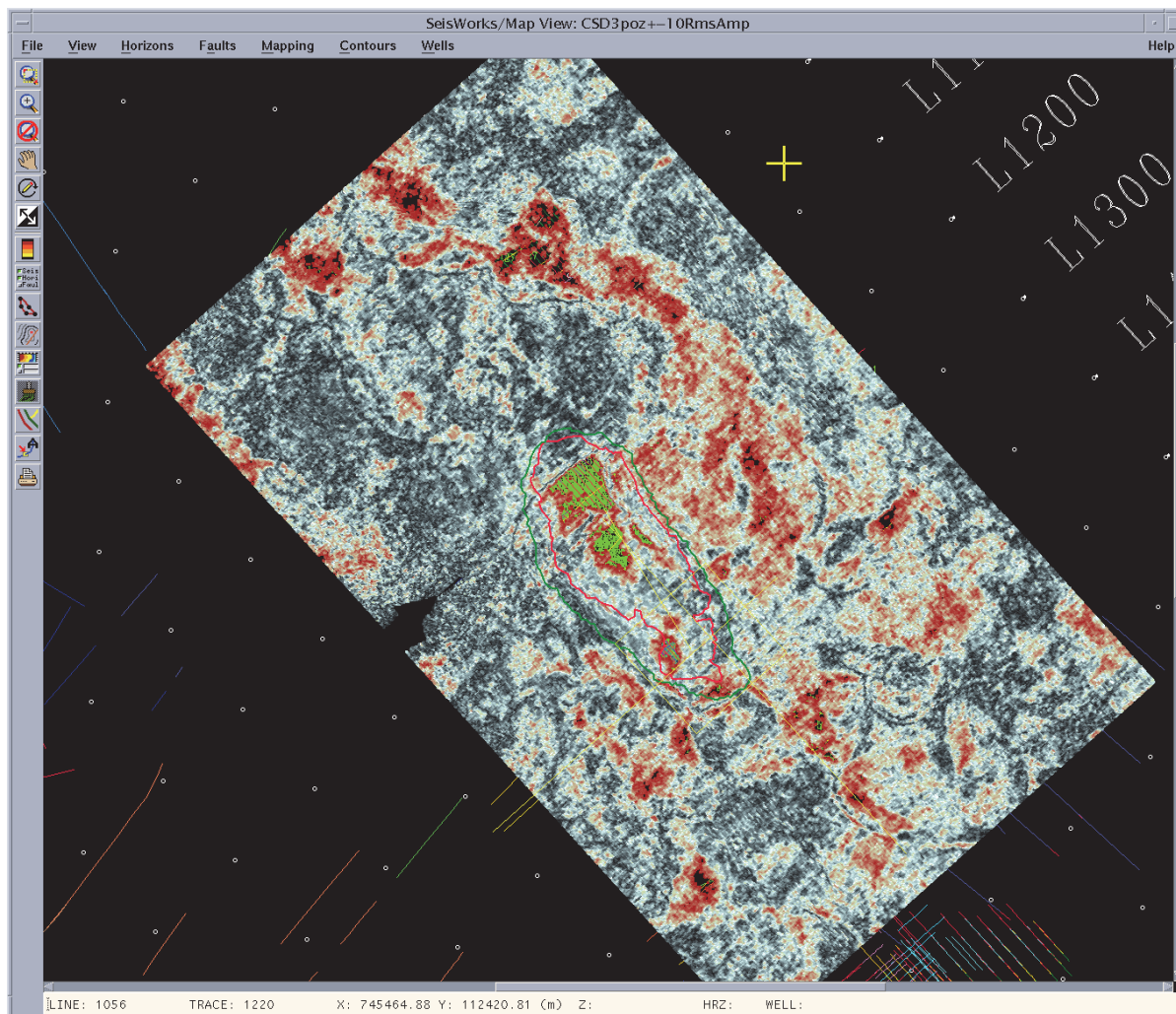


Figure1 RMS Amplitude of the Csongrád-Dél-2 series

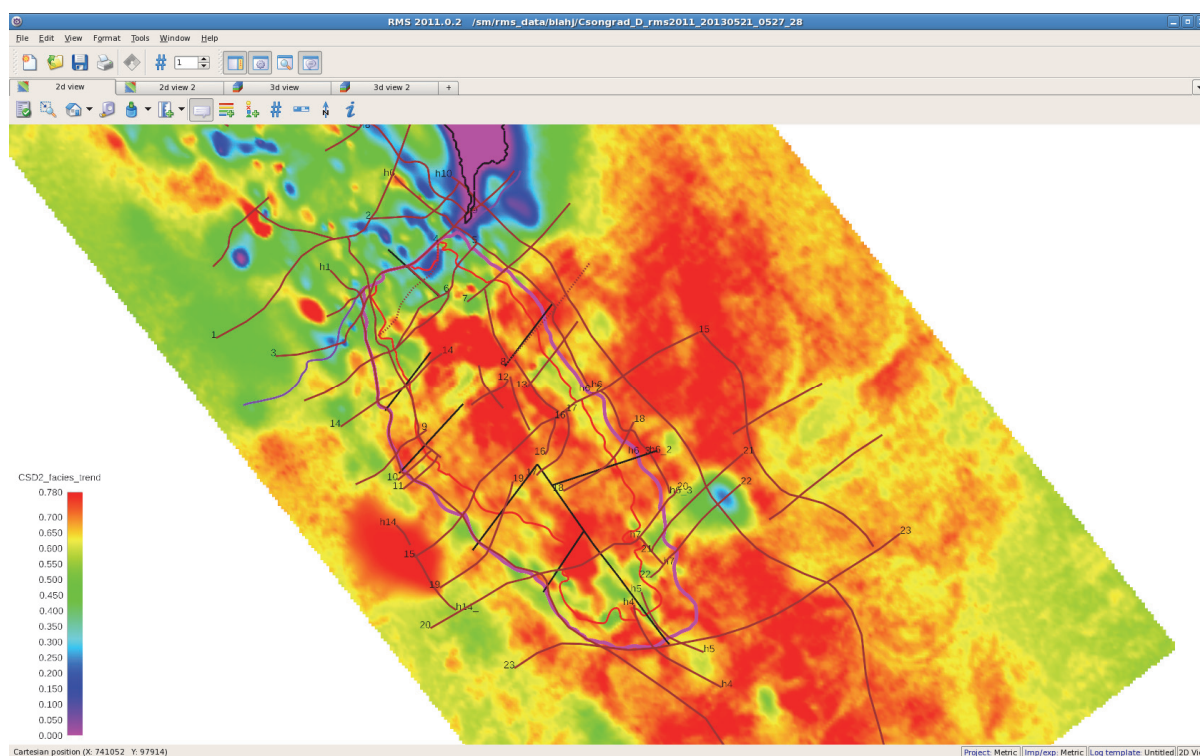


Figure 2: RMS Amplitude weighted by thickness, Csongrád-Dél-2 series

In **Figure 1**, the seismic attributes were generated as a combined effect of gas content and sand content. Note, the latter one is the indicator of the facies/depositional environment. These two factors together gave the actual value of the attribute at grid points. However, if there is relatively high gas content in the pore space, then it may appear as high as virtual sand content. This bias may result in misinterpretation of the 'true' situation, since an originally As a consequence a relatively poor reservoir with low sand content may appear as a good one with high sand content. In a former study, an apparently suitable method was used to eliminate this so called gas effect. This approach was able to produce quite fair values in the gas cap. But unfortunately, it did not work in the zones of oil and gas legs failed in the oil leg and water leg equally, due to the low gas saturation.

The high variability in reservoir thickness is another factor which may cause misinterpretation. It is, since the width of the selected window is proportional to the thickness of the reservoir. However, in case of high variable multiple layers, the definition of adequate cut-off values is almost impossible. Indeed, depending on the actual position relating to the reservoir body, different attribute values or different sand content may belong to the same facies. In addition, highly different values may represent the same facies.

Another problem can arise if seismic attributes do reflect well the facies distribution, but their statistics cannot be controlled in the context of facies incompatibility. If a given facies portion has been defined from facies logs, the

software lay great stress on them in generation of a facies model regardless of whether these facies units are adjacent or not. This uncertainty may be reduced by a dense well grid, if all the wells have good enough log-survey to identify the facies categories. However, when wells are located sparsely, and their logs are in poor quality, this uncertainty can be quite large. In building a facies model, the facies incompatibility between adjacent or successive layers as indicator parameter also occur (except where only 0, 1 are used). It can happen when co-simulation is used with original and manipulated seismic attribute as secondary variables. If we want to build a detailed facies model the process is more complicated. In the case of multi-facies model one has to be able to define the facies and to separate well data by facies types. In the case of good separation, the distribution is characteristic of the existing facies. In this case the calculation semi-variograms describing the spatial continuity of the specific facies is straightforward.

This paper would like to take a step toward the more reliable genetic models by introducing a new approach of facies modelling

3. DEFINING AND MAPPING FACIES

Seismic attributes reflect the facies distribution fairly well but usually do not assign some specific values to the right place on maps. In this approach the first step is to define the facies types on the basis of well logs and core description studies. This analysis relies on those ancient analogies which were presented by several text-books (e.g. Coleman & Prior, 1982, Serra, 1985). In this paper there are different sedimentary environments and the well log responses are shown in different positions of the specific environment.

Unfortunately, in the case of Algyó delta complex, the using of these analogies are not straightforward, since these 'theoretical' facies do not appear clearly. What is the worst, since the large lateral heterogeneity, the variability is very high.

For the Csongrád-D-2 series as the following facies types were assumed: marshy impermeable facies, channel-levee facies type, meandering point bar facies type, channel facies type, and two types of mouth bars. In some wells, the results of gravity flows were also recognized. In some cases the key of the correct interpretation was the structural model with the sedimentary faults and slumps resulting in changes of the appearance of the layers.

Next step was to generate facies maps. To define the adequate resolution for facies description, areas showing clearly the connections of the aforementioned facies were selected. Blocked well log was prepared for displaying the facies distribution. Then the regional extension of facies was approached by using map of seismic attribute. The facies geometry was defined by polygons (**Figure 3**).

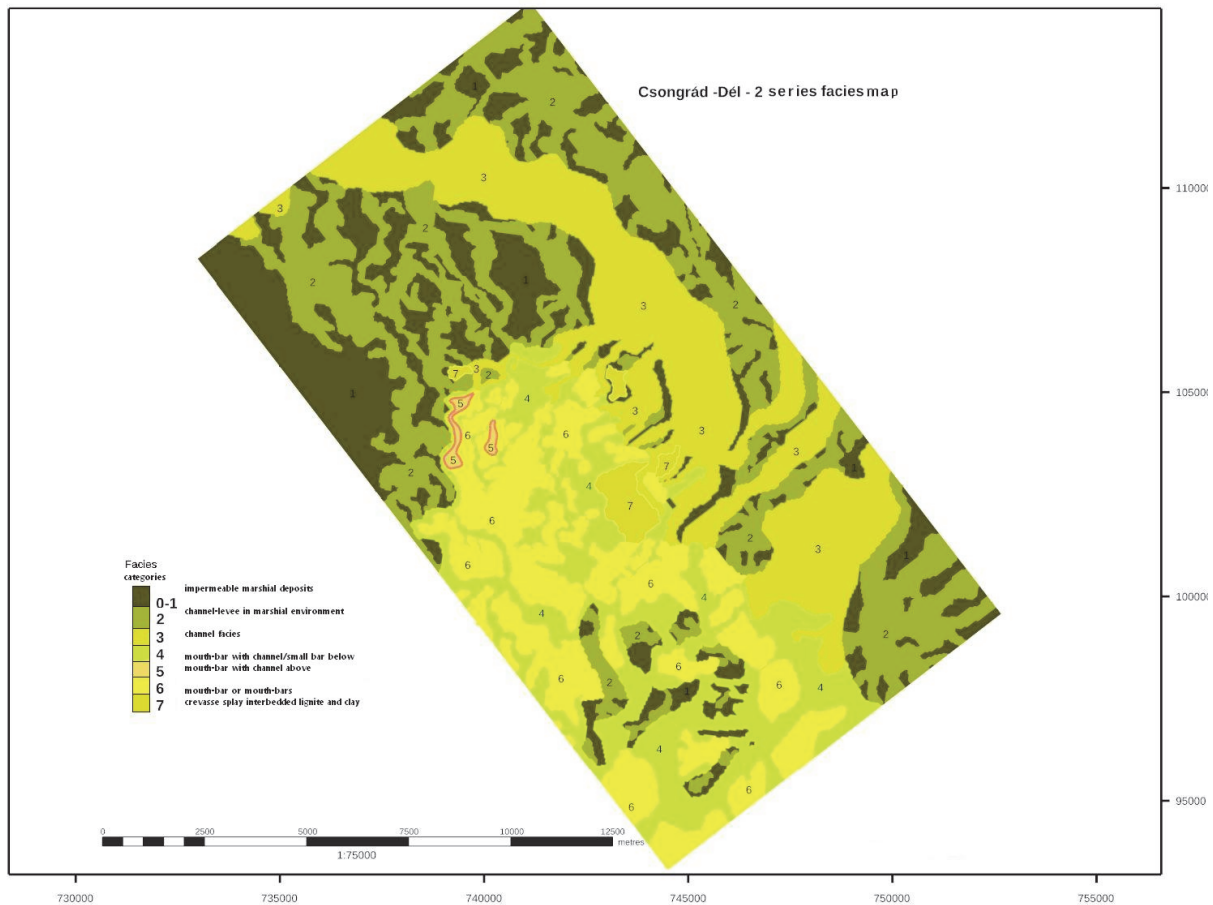


Figure 3: *Facies map of the Csongrád-2 series*

4. MODELLING

In the frame of 3D modelling, the approach of 3D trend model of the facies was used. The resulting quasi 3D parameter model was homogeneous. To improve its quality, this facies parameter model was merged with a traditional sand-shale (1/0) facies parameter generated by indicator modelling. Finally the petrophysical modelling was derived from the combined facies parameter. **Figure 4** shows how good matching could be achieved between the facies petrophysical models.

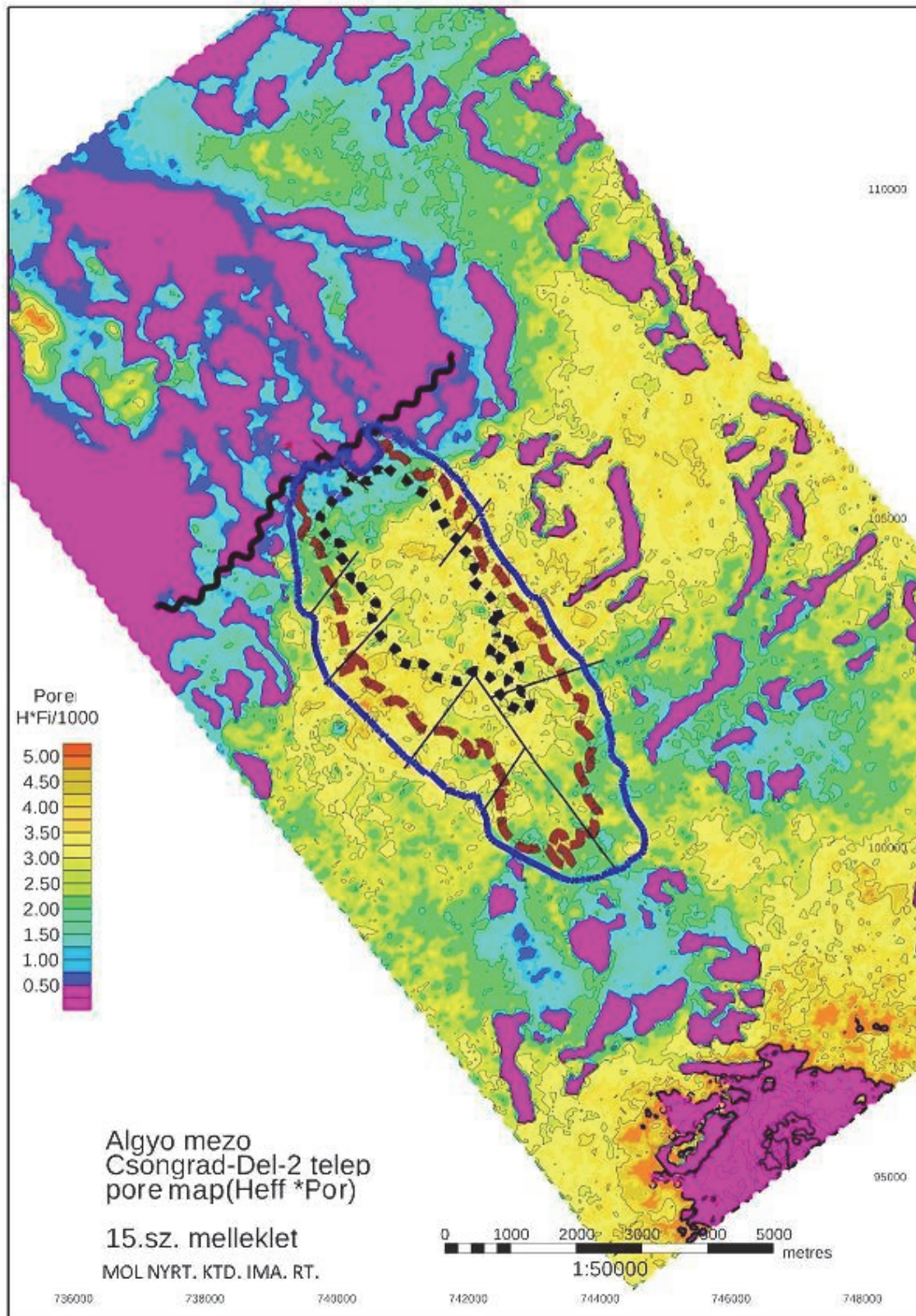


Figure 3: Pore volume map of the Csongrád-2 series

6. CONCLUSIONS

This modelling approach harmonized three different sources of information: (1) logs with cores, (2) well tests, and (3) production data. That is why the defined facies categories could serve real practical needs. As a result, the dynamical simulation of the Csongrád-Dél-2 reservoir was easier and more accurate, with significantly less problems than it used to be.

7. REFERENCES

OPTIMIZATION OF SAMPLING CONFIGURATION BY SPATIAL SIMULATED ANNEALING FOR MAPPING SOIL VARIABLES

Gábor SZATMÁRI

University of Szeged Department of Physical Geography and Geoinformatics, Egyetem u. 2-6.
Szeged H-6722 Hungary
szatmari.gabor.88@gmail.com

Sampling concerns selection of a subset of individuals from a population to estimate characteristics of the whole population. The characteristics could be the total or mean parameter value for a random field, values at unsampled sites or location of target(s). In this study, an SSA algorithm was used to optimize a completely new sampling design for two soil related variables in a Hungarian study area. This algorithm endeavours to optimize the sampling configuration both in geographic and feature space. The requisites of the algorithm were come from a legacy soil data set. In the algorithm suggested, a combined form of regression models and spatial structures of the residuals were used. The results showed that (1) the optimized sampling configuration represents well the feature space; (2) cover well the geographic space; (3) the median of the nearest neighbour distances is lower than the range of the semivariograms and (4) there is an inhibition (i.e. competition) between the points, which causes a (quasi) regular point pattern.

Key words: *soil sampling, optimization, spatial simulated annealing, regression kriging estimation variance.*

1. INTRODUCTION

Sampling concerns selection of a subset of individuals from a population to estimate characteristics of the whole population. The characteristics could be the total or mean parameter value for a random field, values at unsampled sites or location of target(s) (Wang et al., 2012). In digital soil mapping (DSM) the main aim is to estimate values of pedological variable(s) at unvisited locations. Direct observations of the soil are important for two main reasons: (1) they are used to characterize the relationship between the soil properties of interest and the auxiliary information and (2) they are used to improve the predictions based on the auxiliary information (Heuvelink et al., 2007). Hence,

there is a strong necessity to elaborate a well-established soil sampling strategy based on geostatistical tools, prior knowledge and available resources before the samples are actually collected.

Numerous sampling design optimization techniques have been developed in the past decades. One of these optimization techniques is spatial simulated annealing (SSA) (van Groenigen and Stein, 1998) that has been frequently used in soil survey to minimize the kriging variance. In general terms, the kriging variance is not a suitable measure to quantify the (local) accuracy of the prediction, but it is appropriate to compare alternative sampling configurations (Geiger, 2006). A great property of the kriging variance as optimization criterion is that, it can be calculated before the actual sampling takes place. One of the main drawbacks of SSA algorithm is that, it is able to optimize the sampling design for just one (soil) variable. However, in a soil survey the usually aim is to describe the spatial distribution of not just one but several pedological variables (Vašát et al., 2010).

In this paper a SSA procedure will be presented to optimize a completely new sampling design for two pedological variables using spatially averaged regression kriging (RK) estimation variance as optimization criterion in a Hungarian study site. The requisites of the algorithm were come from a legacy soil data set.

2. MATERIALS AND METHODS

2.1. STUDY SITE, LEGACY SOIL DATA AND AUXILIARY INFORMATION

The study site - its area is approximately 17 km² - is located in the central part of Hungary (**Figure 1**). The area of interest can be characterized by Calcic Endofluvic Chernozem soils. The site consists mainly of arable lands affected by various degree of water erosion, providing evidence of the high erosion rate.

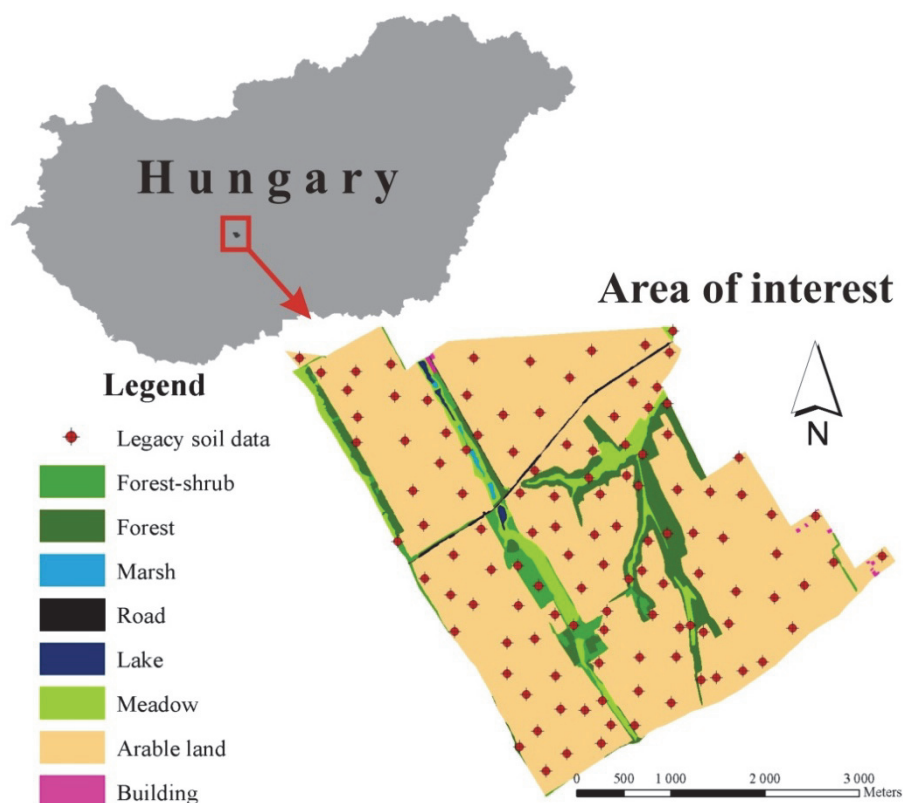


Figure 1: Location and land-use types of the study site and distribution of the legacy soil data points

A legacy soil data set (**Figure 1**) from the 1980s was used to satisfy the requirements of SSA using RK estimation variance as optimization criterion. These requirements are: (1) the known structure of the regression model and (2) the spatial structure of the residuals of the model (Heuvelink et al., 2007). In this study the soil organic matter (SOM) content and the rooting depth (RD) were chosen for the optimization procedure.

The auxiliary information was derived from the digital elevation model and from the land-use-map of the study area. Multiple linear regression (MLR) analysis was performed to characterize the relationship between the soil variables of interest and the auxiliary information. The stepwise selection method was used to select the explanatory variables in the regression models. Furthermore, the experimental semivariograms of the regression residuals were calculated to model their spatial structures.

2.2. OPTIMIZATION BY SSA

SSA is an iterative, combinatorial, model-based sampling optimization algorithm in which a sequence of combinations is generated by deriving a new combination from slightly and randomly changing the previous combination (van Groenigen et al., 1999). As mentioned, the spatially averaged RK

estimation variance was used as optimization criterion in SSA algorithm. RK estimation variance at an unvisited location is commonly written as:

$$\sigma_{RK}^2(s_0) = c(0) - \mathbf{c}_0^T \mathbf{C}^{-1} \mathbf{c}_0 + (\mathbf{q}_0 - \mathbf{q}^T \mathbf{C}^{-1} \mathbf{c}_0)^T (\mathbf{q}^T \mathbf{C}^{-1} \mathbf{q})^{-1} (\mathbf{q}_0 - \mathbf{q}^T \mathbf{C}^{-1} \mathbf{c}_0)$$

where $c(0)$ is the variance of the process, \mathbf{c}_0 is the vector of covariances between the residuals at the sampling and unvisited locations, \mathbf{C} is the covariance matrix of the residuals, \mathbf{q}_0 is the vector of auxiliary information at the unvisited location and \mathbf{q} is the matrix of auxiliary information at the sampling locations. RK variance incorporates both the kriging variance of the residuals and the estimation error variance of the trend, so SSA endeavours to optimize the sampling configuration both in geographic and feature space (Heuvelink et al., 2007).

A combined structure of regression models and spatial structures of the residuals were used in SSA algorithm. The “initial temperature” was chosen such that the average increase acceptance probability was 0.8 and the “cooling” was exponentially. Furthermore, a stopping criterion was defined to rein up the simulation when the quality measure did not improve in many tries. In this study, the stopping criterion value was 200. The optimization procedure was carried out in R (R Development Core Team, 2012). The resulted sampling design was evaluated by statistical and spatial statistical tools.

3. DISCUSSION OF RESULTS

The resulted models of MLR analyses explained 41% and 51% of the total variations of SOM and RD, respectively. The number of the selected explanatory variables in the SOM model is 5, whilst this number in the case of RD is 9. In the SOM model, three from the five explanatory variables also can be found in the RD regression model and only the two remaining explanatory variables were different.

Table 1: Parameters of the fitted isotropic semivariogram models for the residuals of the soil organic matter (SOM) and of the rooting depth (RD)

Variable	Model type	Nugget	Partial sill	Sill	Nugget/Sill ratio (%)	Range (meter)
Residuals of SOM	Spherical	0.04	0.12	0.16	25.0	1420
Residuals of RD	Spherical	70.0	105.0	175.0	40.0	970

The residuals were derived from the regression models and their experimental semivariograms were calculated to model the spatial structures, respectively.

Table 1 summarizes the parameters of the fitted isotropic semivariogram

models. As we see, the range of the fitted model for RD residuals is lower than in the case of SOM residuals, which means that the RD residual is the dominant parameter (Füst and Geiger, 2010; Füst, 2012) because its spatial continuity is the shortest (i.e. it is the most variable) across the area of interest. In SSA algorithm, the combined structure of the regression models (with 11 explanatory variables) and the fitted semivariogram model for RD residuals were used. The optimized sampling design for the pedological variables of interest (SOM and RD) is presented in **Figure 2.A**.

Kolmogorov-Smirnov test was used to examine for a given explanatory variable that, the distribution from the optimized sampling points is equal to the distribution from the complete area of interest. Through the tests 5% significance level was used. The results of the tests showed for every explanatory variable that, the distributions from the sampling points are equal to the distributions from the complete area of interest at 5% significance level. We can conclude that, the optimized sampling design represents well the feature space.

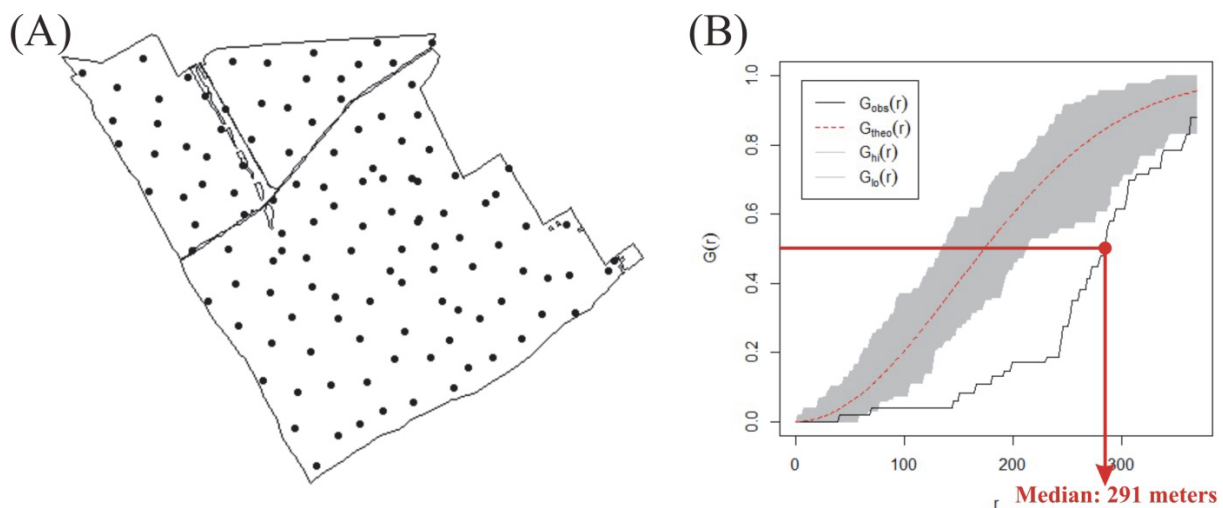


Figure 2: (A) Optimized sampling configuration by spatial simulated annealing for soil organic matter content and rooting depth and (B) cumulative distribution function of the nearest neighbour distances

The nearest neighbour distances were derived to examine how the sampling points cover the geographic space and to explore the type of interaction between the points. **Figure 2.B** presents the cumulative distribution function of the nearest neighbour distances. We can see that, there is an inhibition (i.e. competition) between the sampling points, which causes a (quasi) regular point pattern. On the other hand, the median of the distribution is 291 meters, which is lower than the range of the fitted semivariogram model for the RD residuals (which is 970 meters). We can conclude that, the optimized sampling

configuration covers well the geographic space and there is no any area which has left blank (i.e. each has an impact from least one sampling point).

4. CONCLUSIONS

The case study presented in this paper showed that, SSA algorithm (using RK estimation variance as optimization criterion) is a suitable technique to optimize sampling design for two soil variables, if a combined structure of the regression models and spatial structures of the residuals are used. We can conclude that based on the results of the performed statistical and spatial statistical tests, the optimized sampling configuration covers well the feature and geographic space and there is an inhibition between the points, which causes a (quasi) regular point pattern.

In the near future, we want to extend the methodology for more than two pedological variables.

5. ACKNOWLEDGEMENTS

I would like to thank my supervisors Károly BARTA and László PÁSZTOR for their assistance, useful comments and suggestions.

6. REFERENCES

FÜST, A. (2012): Calibration of monitoring systems. –In: GEIGER, J., PÁL-MOLNÁR, E. & MALVIĆ, T. (eds.): New Horizons in Central European Geomathematics, Geostatistics and Geoinformatics, GeoLitera, Szeged, 11-15.

FÜST, A. & GEIGER, J. (2010): Monitoringtervezés és –értékelés geostatisztikai módszerekkel I. Szakértői véleményen alapuló “igazoló” mintázás geostatisztikai támogatása [Setting up monitoring networks using geostatistics I. Geostatistical support for a judgmental sampling strategy - in Hungarian]. Földtani Közlöny, 140/3, 303-312.

GEIGER, J. (2006): Geostatisztika [Geostatistics - in Hungarian]. Department of Geology and Paleontology, University of Szeged, Szeged, 77 p.

HEUVELINK, G.B.M., BRUS, D.J. & de GRUIJTER, J.J. (2007): Optimization of sample configurations for digital mapping of soil properties with universal kriging. –In: LAGACHERIE, P., McBRATNEY, A.B. & VOLTZ, M. (eds.): Developments in Soil Science (Vol.31), Elsevier, Amsterdam, 137-151.

R Development Core Team (2012): R: A language and environment for statistical computing. R Foundation for Statistical Computing, Vienna, Austria.

van GROENIGEN, J.W., SIDERIUS, W. & STEIN, A. (1999): Constrained optimisation of soil sampling for minimisation of the kriging variance. *Geoderma*, 87, 239-259.

van GROENIGEN, J.W. & STEIN, A. (1998): Constrained optimization of spatial sampling using continuous simulated annealing. *Journal of Environmental Quality*, 27, 1078-1086.

Vašát, R., HEUVELINK, G.B.M. & BORŮVKA, L. (2010): Sampling design optimization for multivariate soil mapping. *Geoderma*, 155, 147-153.

WANG, J.-F., STEIN, A., GAO, B.-B. & GE, Y. (2012): A review of spatial sampling. *Spatial Statistics*, 2, 1-14.

SPATIOTEMPORAL PATTERNS OF ANTARCTIC STABLE WATER ISOTOPE RECORDS

István GÁBOR HATVANI^{a,*}, Zoltán KERN^a

^aInstitute for Geological and Geochemical Research, Research Center for Astronomy and Earth Sciences, Hungarian Academy of Sciences, H-1112 Budapest, Budaörsi út 45.,

[*hatvaniig@gmail.com](mailto:hatvaniig@gmail.com),

The stable isotope characteristics of ice cores hold vital information about the precipitation they were formed from. Such as: (i) the origin of water vapor; (ii) the circumstances during the condensation; and (iii) the conditions during precipitation. Ice cores serve as archives for precipitation. The aim of this study is to present a numerical example on pre-processing of stable isotope records for the subsequent analysis of spatiotemporal variability of the water isotope signal in an Antarctic region for the second half of the 20th century. Stochastic modeling, e.g. cross correlation was conducted, and dynamic factor analysis and principal component analysis were planned on a set of $\delta^{18}\text{O}$ & $\delta^2\text{H}$ records derived from numerous ice cores. It is supposed, that the results would further clarify the origin of precipitation fallen on the different regions of Antarctica and have a significant impact on the methodological aspect of the pre-processing and exploration techniques of ice core records.

Keywords: *cross correlation, $\delta^{18}\text{O}$ & $\delta^2\text{H}$ records, data filtering, factor analysis, ice core*

1. INTRODUCTION

The stable isotope characteristics of ice cores serve as archives for precipitation they were formed from; more specifically, (i) the origin of water vapor, (ii) the circumstances during the condensation, and (iii) the conditions during precipitation (Dansgaard, 1964).

The polar precipitation stored for millennia in ice sheets and recovered as ice cores since the mid-20th century, is being studied in a deeper-and-deeper extent (Jouzel, 2013) with Antarctica in the focus of attention. By dating the water isotope records derived from ice core arrays, the spatiotemporal pattern of paleoclimate can be assessed. However, as stated by David et al. (1988): “To make satisfactory statistical comparisons between year-to-year changes in

temperature and stable-isotope records from ice cores, dating should achieve a 1 year precision”. Therefore, the aim was to “correct” the dating as much as possible to form a coherent basis for subsequent analysis of spatiotemporal variability of the water isotope signals.

2. MATERIALS AND METHODS

The Antarctic study area (LAT: 64°S, 84°S; LON: 71°W, 12°E; **Figure 1**) was chosen due to the relatively high abundance of available ice core derived water isotope records and due to the fact that numerous deep ice cores were delivered from this region playing an important role in paleoclimatology.

Altogether an array of 70 stable water isotope records ($\delta^{18}\text{O}$ & $\delta^2\text{H}$) were gathered from ice cores spanning various time intervals. Taking into consideration all the crucial data input requirements of the planned geostatistical analyses a compromise had to be made to maximize both the time-span and the available number of records. As a result the chosen period covered 1970 – 1988 with 44 $\delta^{18}\text{O}$ and 1967-1989 with 21 $\delta^2\text{H}$ records before pre-processing and filtering (**Figure 1**). The data used was acquired from the corresponding research groups (Divine et al. 2009; Mulvaney et al. 2010; Naik et al. 2010; PANGAEA, 2014).

It is well known that the dating of ice cores is usually endured by a certain degree of uncertainty (**Table 1**). Thus, it became inevitable (David et al., 1988) to find a means to correct the possibly miss-dated time series before conducting geostatistical analyses.

Cross correlation analysis (CCA; Rhudy et al., 2009) was chosen to improve the synchronicity of the records within the bounds of the dating uncertainty. Three main characteristics of the cross correlation function (CCF) were used: (i) the time lag where the major peak can be found, (ii) the direction of the peak (positive or negative lag) and (iii) the value of the correlation coefficient at that certain peak. The principle was to synchronize the time series in such a way, that the major peak of the CCFs would be located at the zero year lag; based on the assumption/experience that in an optimal setting stable isotope records from the same annual layer should correlate to the highest extent at the zero year lag. The work was conducted on both stable isotope records in parallel; due to size restriction only $\delta^2\text{H}$ examples are given.

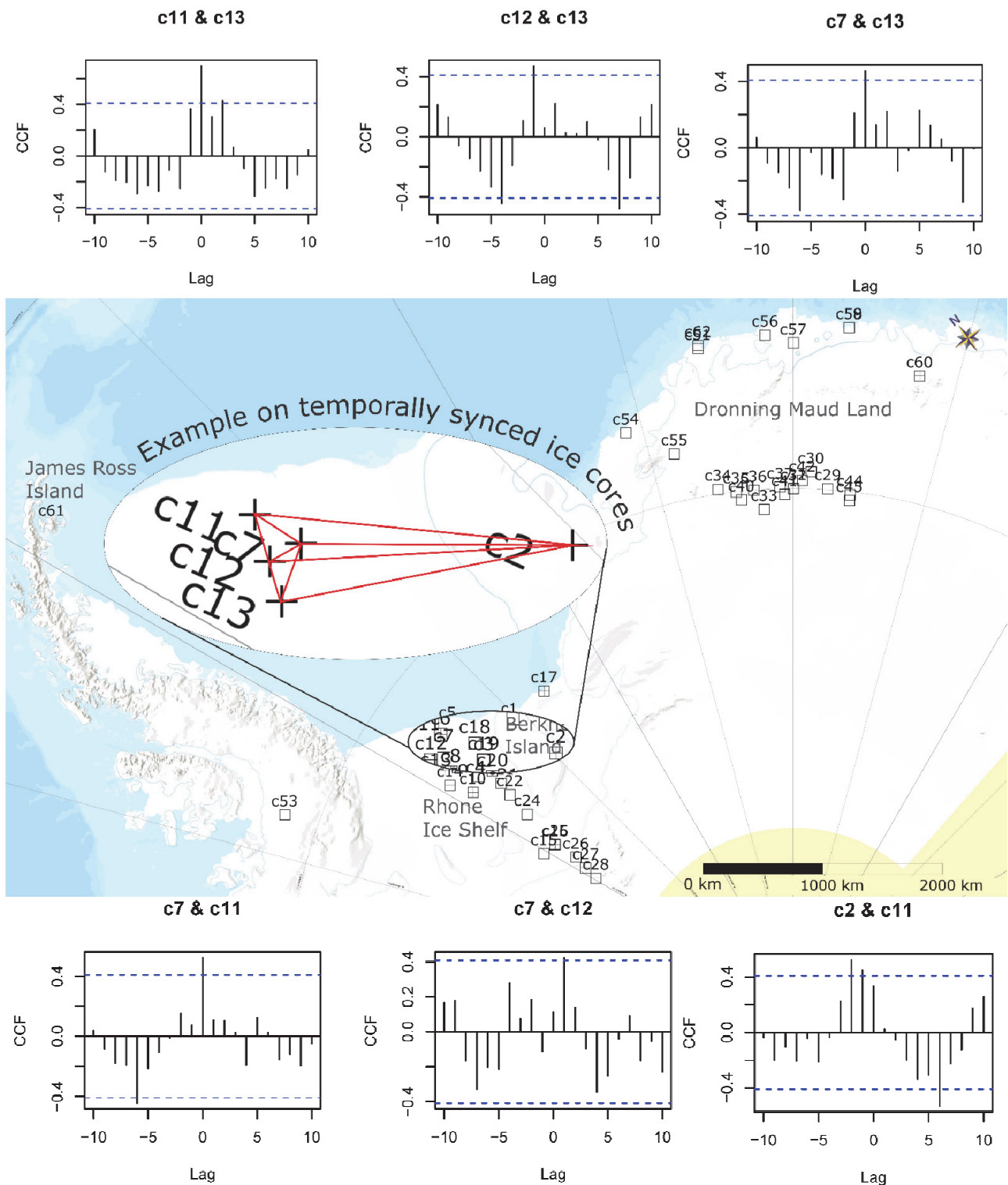


Figure 1: Spatial distribution of the studied ice core records and characteristic CCFs of the enlarged area (above and below the map). Open square $\delta^{18}O$ only; cross δ^2H only; square with cross both isotopes; red line connecting clearly synchronizable records. On the plots the blue broken line indicates the $\alpha=0.05$ confidence interval.

Table 1: *Reported dating uncertainties of studied ice cores*

Core code in the study	Core name in the reference	Geographic location	Dating uncertainty (yr)	Reference
c1 & 2	Berkner N & S	Berkner Island	NA	Wagenbach et al., 1994
c15 & 16	BAS 5 & 6	Rhone Ice Shelf - Henry Ice Rise	±2 - 3	Graf et al., 1994
c32 & 33	DML05 & 07	Dronning Maud Land highlands	±2	Oerter et al., 2000
c58	S100	coastal Dronning Maud Land	±3	Kaczmarska et al., 2004
c60	IND-25/B5	central Dronning Maud Land	±2	Naik et al., 2010
c61	JRI	James Ross Island	±1	Mulvaney et al., 2010

3. RESULTS AND DISCUSSIONS

The first step in the analysis was to synchronize the neighboring cores. Therefore, CCFs were plotted for all the ice core pairs in a range of 300 km, for each parameter separately. Note here, the longest distance between two cores with $\delta^{18}\text{O}$ records is 2570 km (c60 & c53), while the shortest is 2.5 km (c16 & c25). Hence, the search radius was $\sim 1/10$ the maximum and $\sim 10\times$ the minimum inter-core distance.

The obtained CCFs could be categorized into two classes: (i) there was a clear peak in the function and (ii) there was no evaluable signal obtained. In the case of the previous (i), if the peak of the CCF was not located at the zero year lag, the time series were shifted (for an example see **Figure 1** upper and lower graphs). In the case of the latter (ii), however, the record was (a) either compared to its neighbors outside the 300 km range and shifted, or (b) left unchanged, or as a final solution (c) discarded. Remark here that most of the cases where patterns were found in the water isotope records were those ones, where unresolvable chronological uncertainty have already been reported in the corresponding original studies (e.g. c15; c58; **Table 1**). These dating errors could be related to numerous reasons. From a technical point of view e.g. differences between various dating methods: layer counting, identification of volcanic peaks etc.; while from an environmental aspect it could have happened because of the meteorological/wind conditions causing disturbance in the signal. This effect is more pronounced in areas inside the continent with low accumulation.

The analyses for the two parameters in question were prepared in parallel. The patterns obtained were matched together based on the results derived from the 30 cores which had measurements for both $\delta^{18}\text{O}$ & $\delta^2\text{H}$ records.

The obtained overall temporal structure of the records (**Figure 2**) showed a much closer resemblance to well dated and organized dataset with the number of peaks cumulating at-, and the negative correlation coefficients fully

disappearing from the zero year lag. It is true, however, that it was impossible to synchronize all the cores to a full extent.

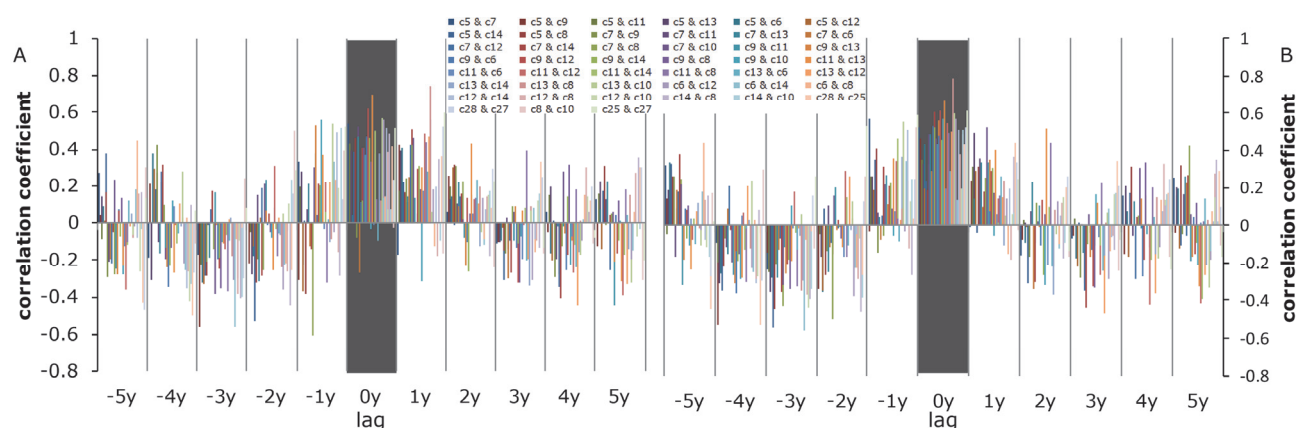


Figure 2: Cross correlation functions for $\delta^2\text{H}$ records within a 300 km search radius at lags between ± 5 years before (left; A) and after (right; B) synchronization with the zero year lag highlighted in grey

4. CONCLUSIONS AND OUTLOOK

The steps taken were obligatory if any further analysis is planned which takes into account the temporal characteristic of the records for multiple cores at once, in other words their temporal interrelationships. In fact, this was indeed the case; since the prime motivations are:

- (i) to estimate the relationship of factors/common trends with hemispheric climate fields as explanatory variables, where the factors are obtained from dimension reduction methods such as principal component analysis (PCA; Divine et al. 2009; Kovács et al., 2012a) or dynamic factor analysis (DFA; Kovács et al., 2004),
- (ii) to determine the spatial range of the two parameters (using Variography; Füst & Geiger, 2010; Kovács et al., 2012b) before and after the synchronization of the records and,
- (iii) to derive a space-time interpolated water isotope landscape for the region (Kern et al., 2012; Kohán & Kern, 2012).

On the one hand, although it is known that DFA is capable of taking into account the lagged correlation structure, authors were convinced that without sufficient synchronization, the dating errors seen in the present data set would presumably lead to biased results. On the other hand however, PCA is very sensitive to the correlation structure of the input dataset i.e. requires the highest correlation coefficients to be at the zero year lag. In addition, to obtain a representative spatial range the records should again be synchronized temporarily. It is suspected that the variogram analysis of the original records

would give either nugget effect type of semivariograms, or ones with much smaller ranges, than the semivariograms obtained after synchronization. In the present paper a universal example was given on pre-processing similar archived sedimentological (e.g. ice cores, varves etc.) records. A set of possible and/or necessary steps were discussed to successfully ameliorate the dating of stable water isotope records to form a coherent basis for subsequent analyses of spatiotemporal variability of water isotope signals.

5. ACKNOWLEDGMENTS

The work of I.G. Hatvani was supported was realized in the frames of TÁMOP 4.2.4. A/1-11-1-2012-0001 „National Excellence Program – Elaborating and operating an inland student and researcher personal support system”. The project was subsidized by the European Union and co-financed by the European Social Fund. Special thanks to R. Mulvaney, D. Divine, C.M. Laluraj providing access to their data and researchers who archived their Antarctic ice core derived stable isotope data in PANGAEA. Thanks for the support of the MTA “Lendület” program (LP2012-27/2012). This is contribution No. 07 of 2ka Palæoclimatology Research Group.

6. REFERENCES

- DANSGAARD, W. (1964): Stable isotopes in precipitation. *Tellus*, 16, 436-468.
- DAVID, A.P., MULVANEY, R., DAVISON, B. (1988): Stable-isotope/air-temperature relationships in ice cores from Dolleman Island and the Palmer Lad Plateau, Antarctic Peninsula *Ann. Glac.*, 10, 130-136.
- DIVINE, D. V., E. ISAKSSON, M. KACZMARSKA, F. GODTLIEBSEN, H. OERTER, E. SCHLOSSER, S. J. JOHNSEN, M. VAN DEN BROEKE, AND R. S. W. VAN DE WAL (2009), Tropical Pacific–High Latitude South Atlantic Teleconnections As Seen In $\delta^{18}\text{O}$ Variability In Antarctic Coastal Ice Cores, *J. Geophys. Res.*, 114, D11112.
- FÜST, A., GEIGER, J. (2010): Monitoringtervezés és -értékelés geostatistikai módszerekkel I. *Földtani Közlöny*, 140, 303-312.
- GRAF, W., MOSER, H., REINWARTH, O., KIPFSTUHL, J., OERTER, H., MINIKIN, A., WAGENBACH, D. (1994): Analysis of long Snow-accumulation rates and isotopic content (2H, 3H) of near-surface firn from the Filchner-Ronne Ice Shelf, Antarctica. *Ann. Glac.*, 20, 121-128.
- JOUZEL, J. (2013): A brief history of ice core science over the last 50 yr. *Clim. Past.*, 9, 2525-2547.
- KACZMARSKA, M., ISAKSSON, E., KARLÖF, L., WINTHER, J-G., KOHLER, J., GODTLIEBSEN, F., RINGSTADT OLSEN, L., HOFSTEDE, C.M., VAN DEN BROEKE, M.R., VAN DE WAS, R.S.W., GUNDESTRUP, N. (2004).

ACCUMULATION VARIABILITY DERIVED FROM AN ICE CORE FROM COASTAL Dronning Maud Land, Antarctica. *Ann. Glac.*, 39, 339-345.

KERN, Z., LEUENBERGER, M., KOHÁN, B. (2012): Mapping of stable isotope composition of precipitation over Switzerland. The water cycle in a changing climate: Observations, scenarios, impacts, 11th International NCCR Climate Summer School, 9-14 September 2012, Ascona, Switzerland pp.69-70.

KOHÁN, B., KERN, Z. (2012): A felszíni csapadék stabil oxigénizotóp összetételének becslése Magyarországon térinformatikai módszerekkel - előzetes eredmények. In: Lóki J. (ed.): Az elmélet és gyakorlat találkozása a térinformatikában III., Debrecen University Press, Debrecen, pp.189-196.

KOVÁCS, J., KORPONAI, J., KOVÁCS, I.SZ., HATVANI, I.G. (2012b) Introducing sampling frequency estimation using variograms in water research with the example of nutrient loads in the Kis-Balaton Water Protection System (W Hungary). *Ecol. Eng.* 42, 237-243

KOVÁCS, J., MÁRKUS, L., HALUPKA, G. (2004): Dynamic Factor Analysis for Quantifying Aquifer Vulnerability. *Act. Geol. Hung.*, 47, 1-17.

KOVÁCS, J., TANOS, P., KORPONAI, J., KOVÁCSNÉ, SZ. I., GONDÁR, K., GONDÁR-SŐREGI, K. & HATVANI, I. G. (2012a): Analysis of Water Quality Data for Scientist. -In: VOUDOURIS, K., VOUTSA, D. (eds.): Water Quality Monitoring and Assessment, InTech Open Access Publisher, Rijeka, pp. 65-94.

MULVANEY, R., ABRAHAM, N.J., HINGMARSH, R.C.A., ARROWSMITH, C., FLEET, L., TRIEST, J., SIME, L.C., ALEMANY, O., FOORD, S. (2010): Recent Antarctic Peninsula warming relative to Holocene climate and ice shelf history. *Nature*, 489, 141-144.

NAIK, S.S., THAMBAN, M., LALURAJ, C.M., REDKAR, B.L., CHATURVEDI, A. (2010): A century of climate variability in central Dronning Maud Land, East Antarctica, and its relation to Southern Annular Mode and El Niño-Southern Oscillation. *J. Geophys. Res.*, 115, D16102.

OERTER, H., WILHELMS, F., JUNG-ROTHENHÄUSLER, F., GÖKTAS, F., MILLER, H., GRAF, W., SOMMER, S. (2000): Accumulation rates in Dronning Maud Land, Antarctica, as revealed by dielectric-profiling measurements of shallow firn cores. *Ann. Glac.*, 30, 27-34.

PANGAEA (2014): DOI:10.1594/PANGAEA.548638-548652 & 548504-548514; 10.1594/PANGAEA.264593; last accessed 05.04.2014.

RHUDY, M., BUCCI, B., VIPPERMAN, J., ALLANACH, J., ABRAHAM, B. (2009): Microphone array analysis methods using cross-correlations. *Proceedings of IMECE2009 (D RAFT-| M EC E2009-1 0798)*, 8p.

WAGENBACH, D., GRAF, W., MINIKIN, A., TREFZER, U., KIPFSTUHL, J., OERTER, H., BLINDOW, N. (1994): Reconnaissance of chemical and isotopic firn properties on top of Berkner Island, Antarctica. *Ann. Glac.*, 20, 307-312.

3D FACIES ANALYSIS BASED ON WELL DATA WITH DIFFERENT GEOSTATISTICAL AND SEDIMENTOLOGICAL APPROACHE

Viktor VOLFORD

University of Szeged, H-6722, Szeged, Egyetem u. 2-6. Hungary;
viktor.volford2@gmail.com

The main aim of this work is to determine the depositional environment of a potential reservoir body, which has been developed in a Late Miocene (Lower Pannonian) turbidite system, through the lateral extension of facies in macro-scale. According to the actual stage of this work, the area can be identified as a Mud/Sand-Rich Ramps. The input database was built from measured and interpreted well data such as corrected spontaneous potential (SPC), gamma-ray (GR), porosity (PHI) and shale content (VSH). The first step was the identification of the well-log-shapes in the target reservoir for using the indicator kriging to reveal the possible lateral connections between wells in each categorical variable. The indicator kriging was chosen because it could be show the probability for all categories. The second stride was the variography of the predefined well shapes as indicator variables. For the appropriate interpretation, a widely accepted additional workflow was used that contains the spatial distribution of the lithology ratios. The ratio of the sandstone/non-sandstone lithology was able to reveal (1) the presence or absence of channels which had taken an important role in the depositional history, and (2) the lateral movement of the depositional system.

Key words: *variography, indicator kriging, uncertainty, spatial distribution, well logs*

1. THE STUDIED AREA

The field is located in the centre of the eastern region in Hungary. The target reservoir is a member of a bigger reservoir group in the Late Miocene (Lower Pannonian) turbidite system.

2. DATA AND METHODS

In the study area 28 wells were drilled (**Figure 1**). Two wells (5.;11. in **Figure 1**) were ignored since they were too far from the others. In each well spontaneous potential (SPC), gamma-ray (GR), porosity (PHI) and shale content (VSH) were available for well log response analyses.

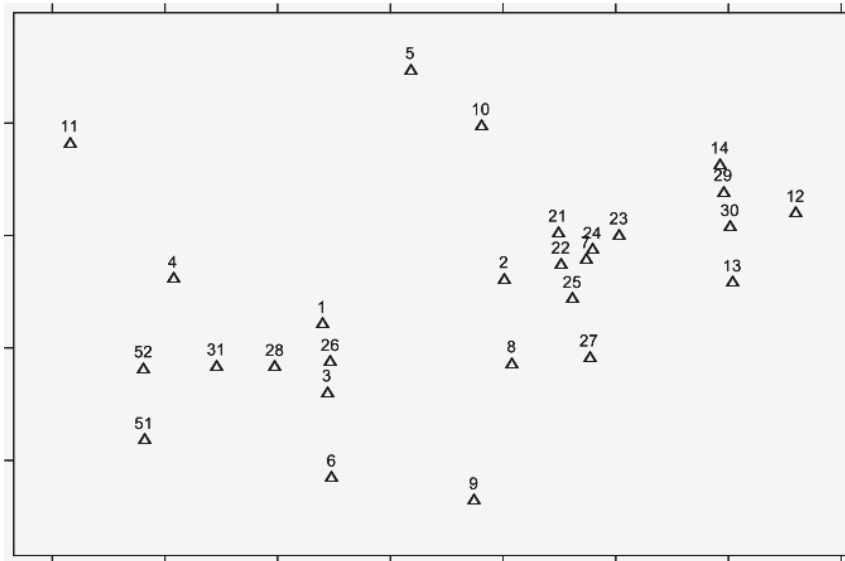


Figure 1: Location map

Figure 2 shows the spatial distribution of the reservoir thickness. As the map illustrates the thickness was continuously increased towards from the West and northwest part to the South and southeast region. The thinner parts, with less than 12 meters of thickness, were connected to higher relief of the basin.

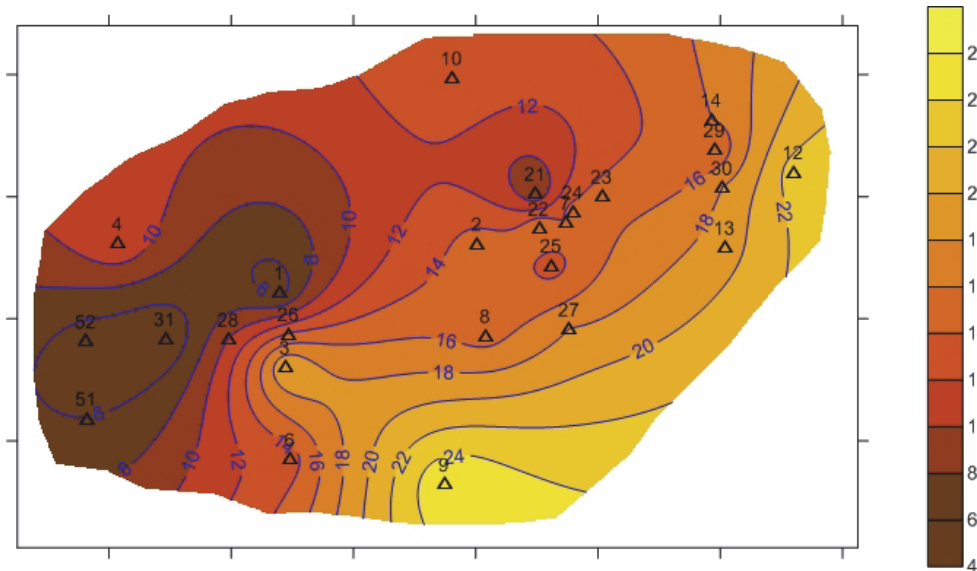


Figure 2: Gross thickness of the reservoir

3. LOG-SHAPE ANALYSES

Two different interpretations of well-log shapes were applied. One of them, I#1, captured the general vertical trend of the whole reservoir thickness, the

second one, I#2, concentrated only to the sandy intervals. In **Figure 3** the interpretations of log-shapes carried out to describe the grain size tendency of the whole thickness. The identified shapes were as follows: bell (green spots), serrated (red spots), funnel (blue spots), and symmetrical (purple spots).

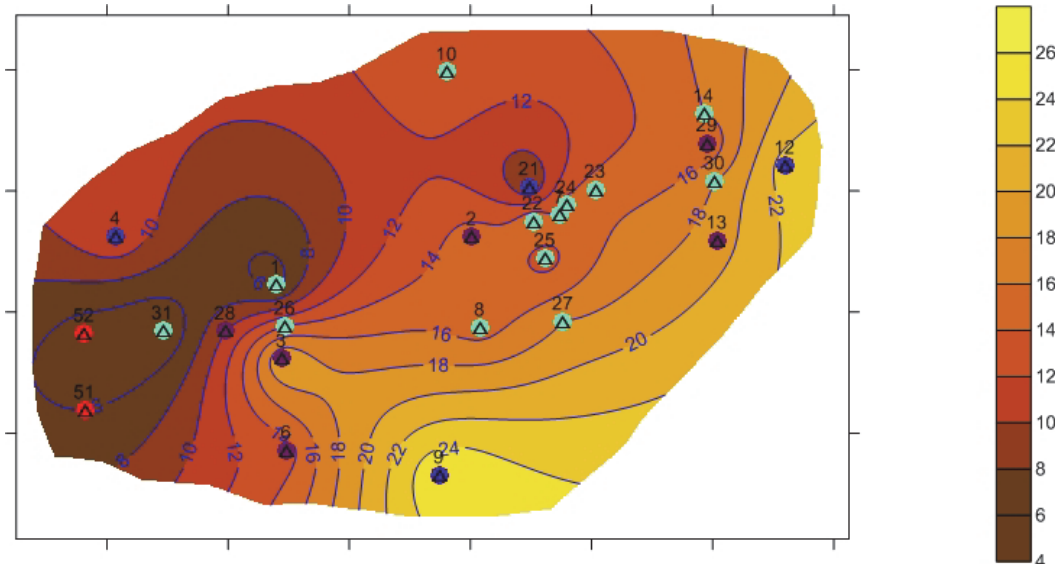


Figure 3: Map of the identified log shapes in the case of I#1 (Contours are thickness)

In **Figure 4** the interpretation focused on the shapes of the log curves only in sandy intervals. In this case the following types could be recognized: bell (green spots), serrated (red spots), and funnel (blue spots).

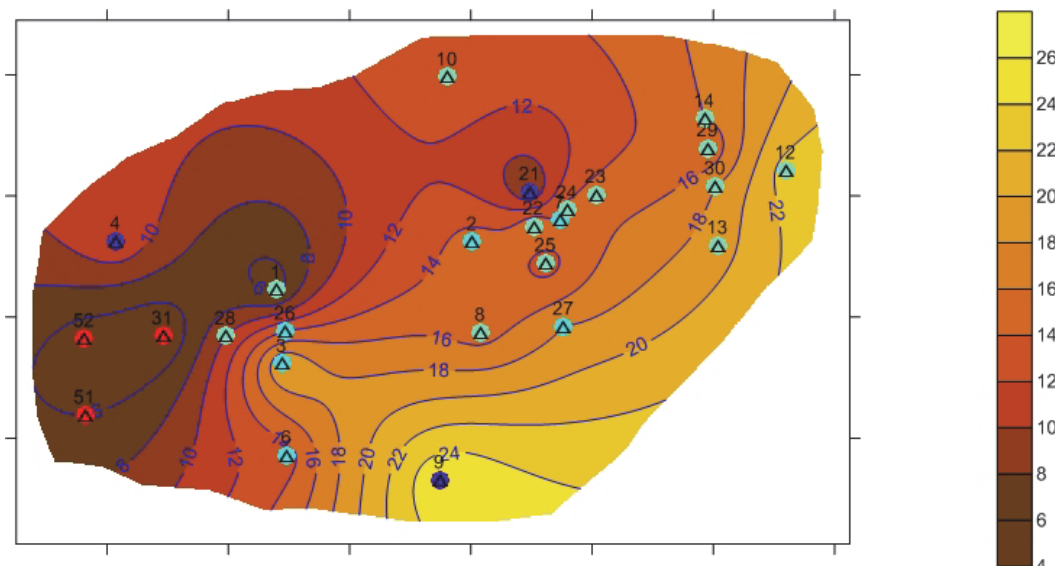


Figure 4: Map of the identified log shapes in the case of I#2 (Contours are thickness)

The symmetrical and bell-shapes were merged together. It is worth noting, that the classification was not changed significantly in the eastern part and it almost only concentrated to West side of the rock body. The consequence was

that the IK of the log shapes could be expected to give similar results for the eastern part and more different maps for the western part when processing I#1 and I#2.

The bell-shapes appeared within the medium thickness part of the reservoir and their presence was noticeable where the thickness started to increase abruptly. Their thickness varied between 14 and 18 m. The serrated-shapes were detected only three wells which were connected to the thinnest part on the West side of the area. The funnel-shapes appeared randomly through the reservoir (**Figure 4**).

On the basis of turbidity genetics of this rock body, the bell shapes showing fining upward sequence could be incorporated with channels on the fan. Funnel shapes representing coarsening upward sequences could be connected belonged to fan lobes. The serrated shapes without any trends were associated with the aggradations of the shale and silt in abyssal and sea-floor plain.

4. INDICATOR KRIGING

Indicator kriging is a non-parametric method of interpolation to estimate the local conditional probability distributions by using some pre-defined threshold value. In this case this method was used the three categorical variables representing the three log-shapes. That is why the result showed the probability of appearing each shapes at grid points. The purpose of this step was to reveal the possible lateral connection of each variable.

In the IK process, the first step was the definition of three indicator variable one for each log-shape. Then the experimental indicator variograms were modelled using some permissible theoretical functions. The final estimation of multi-variable indicator function occurred by full IK within the frame of WinGSLIB (Deutsch and Journel, 1997).

5. RESULTS AND INTERPRETATIONS

IK was applied for both well log-shape analysis approaches (I#1 and I#2). In the interpretation of the results the main emphasize was given to the lateral distribution of bell-shapes since: (1) the geometry of the isolines could be evidenced the presence of channels; (2) only a few points were belonged to funnels and serrated-shapes which did not show any significant spatial relation. **Figure 5-6** showed the results for both I#1 and I#2 analysis.

The shapes of contours belonging to $p > 0.8$ probabilities are very similar in the eastern side on both maps. **Figure 5** shows a possible distributary channel geometry that can also be recognized on **Figure 6** with the same probability, but with a bit different geometry. The negligible difference was probably caused by the different ranges of the two indicator semivariograms. It was resulted in the disappearing of the typical channel geometry in **Figure 6**.

In **Figure 7** the lithology ratio (blue isolines) is shown along with the lithology number (red isolines). This map points out where the channels and lobes approximately can be expected. The lithology ratio expresses how many percent was occupied by sand from the total thickness. The high ratio could be incorporated with channels and lobes.

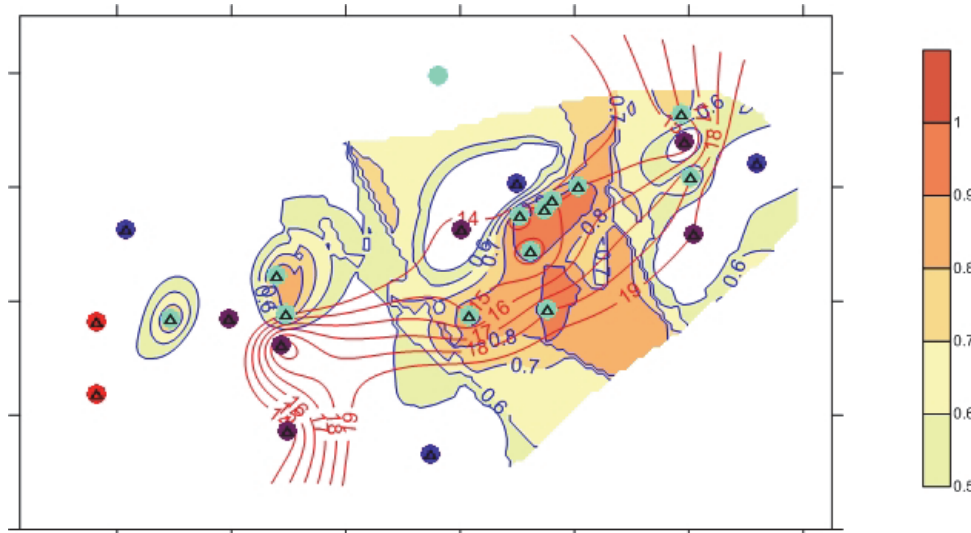


Figure 5: IK map of the first well-log shape analysis (I#1). For explanation see the text.

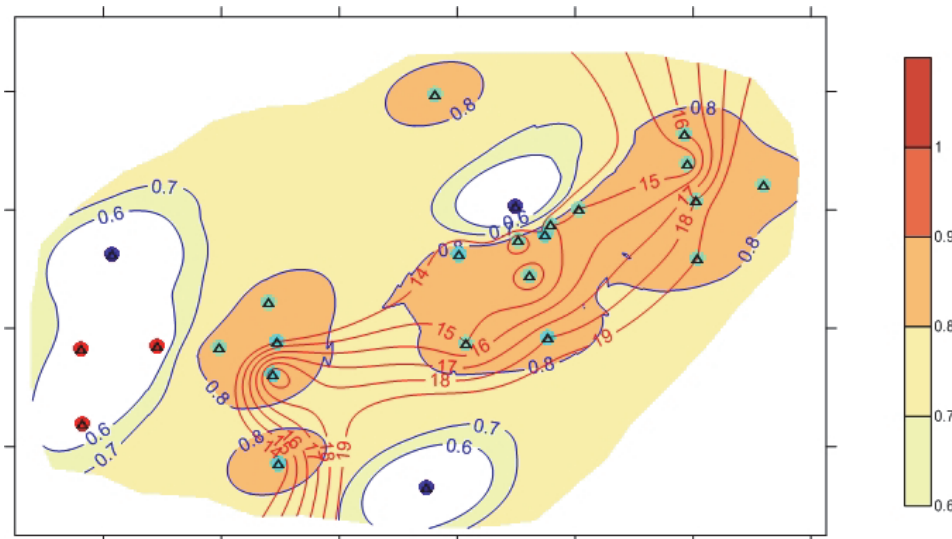


Figure 6: IK map of the second well-log shape analysis (I#2). For explanation see the text.

In theory the lithology number gradually increases from the proximal side toward the distal side of the lobe (in downstream direction). **Figure 7** suggests those regions where the lithology ratio decreases and the simultaneously the lithology number increases toward the South and Southeast directions.

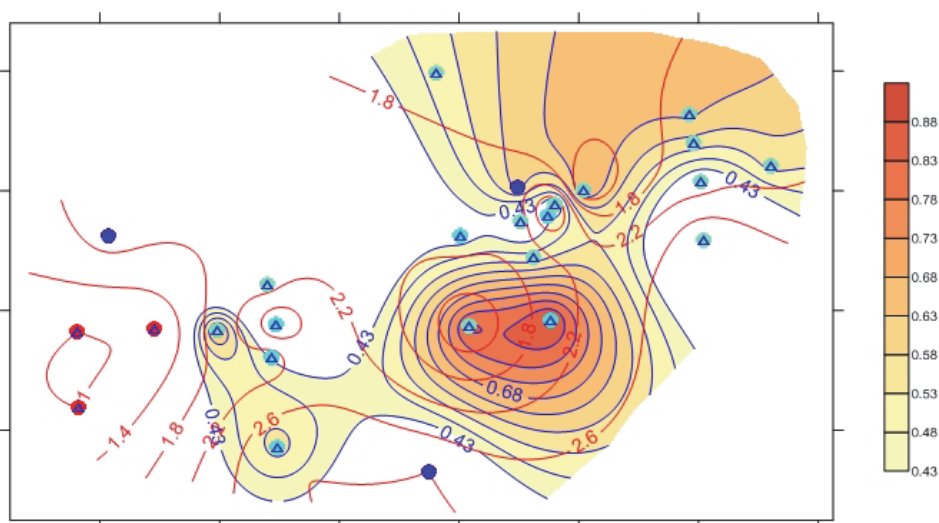


Figure 7: *Lithology ratios and lithology numbers*

Finally, **Figure 5-7** have proved that lob-channels could be connected to the center of the studied are, while lobe could be expected withing the South and Southeast side of the rock body. The lateral distributions of the available wells do not allow to extend this result to the North and Northeast.

6. DISCUSSION

In the analysis of this rock body many evidences suggested that the depositional environment could be identified as a Mud/Sand-Rich Ramps (**Figure 8**). They were as follows: (1) deformation structures caused by slumping in Well 14; (2) sedimentary structures of channel successions in Well 25; (3) a possible distributary channel geometry around Well 25; in the IK map of **Figure 5** (4) the IK of the second interpretation (**Figure 6**) indicated the same channels location on the eastern side with the same probability; (5) the lithology ratio did not exceed 0.7 which could be achieved in Sand-Rich Ramp setting (Richards, 1994); (6) the thickness was increased abruptly from 12 meters and it could be identified as proximal or medial ramp.

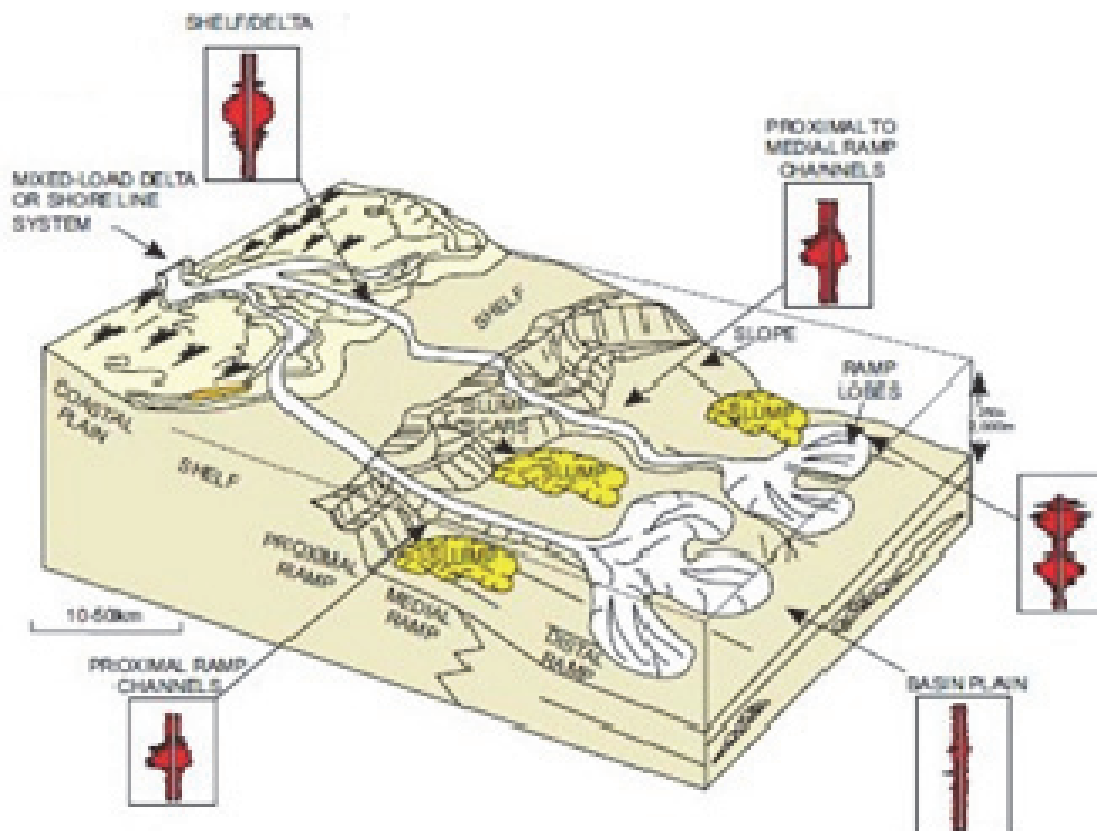


Figure 8: *Mud/Sand-Rich Ramps (after Harold; Richards 1994)*

7. ANKNOWLEDGEMENT

I would like to express my gratitude to János Geiger (Dep. of Geology and Paleontology, University of Szeged, Hungary) and Janina Horváth (Dep. of Geology and Paleontology, University of Szeged, Hungary) for their useful suggestions.

8. REFERENCES

- DEUTSCH, C.V. & JOURNEL, A.G. (1998): GSLIB Geostatistical Software Library and User's Guide. Oxford University Press. 63-116.
- RICHARDS, M. & READING, G. H.(1994): Turbidite Systems in Deep-Water Basin Margins Classified by Grain Size and Feeder System, AAPG Bulletin, 78, 5 (May 1994), 792-882

ANALYSIS OF AN EARTHQUAKE BASED ON EXTENSOMETRIC AND SEISMOLOGICAL MEASUREMENTS OF HAS AND MFGI OBSERVATORIES

Márta KIS¹, Katalin GRIBOVSZKI², Márta KISZELY², András KOPPÁN¹

¹Geological and Geophysical Institute of Hungary (MFGI), 14 Stefania St., H-1143 Budapest,
Hungary

²Geodetic and Geophysical Institute, Research Centre for Astronomy and Earth Sciences,
Hungarian Academy of Sciences, 6-8 Csatkai Endre St., H-9400 Sopron, Hungary

E-mail: kis.marta@mfgi.hu

t

The rock-deformation data series collected by extensometers provide an opportunity for studying various changes in the geological, rock-physical environment, caused by earthquakes (e.g., displacement, deformation of rock mass). Hereby further information can be achieved about the nature of these effects, complementing the analysis of seismograms (as e.g. the frequency range embraced by extensometers can record changes with much higher time of periods). In order to investigate the appearance of effects of earthquakes in extensometric data, authors chose a registratum which was collected in the Matyashegy Gravity and Geodynamical Observatory in Budapest in the time of a significant M7.2 earthquake occurred in Turkey, and started its spectral analysis. Results of the examinations were compared to the spectrum of records of a typical, undisturbed lapse of time, as well as to the spectrum calculated from seismograms of Kövesligethy Radó Seismological Observatory in Budapest, nearby the gravity observatory.

Keywords: extensometer, deformation, seismogram, earthquake.

1. THE M7.1 EASTERN TURKEY REGION EARTHQUAKE

The investigated M7.1 earthquake occurred near the city Van (**Figure 1**), close to the Iranian border, in a broad region of convergence beyond the eastern extent of Anatolian strike-slip tectonics. The intensity in Van has reached IX in Mercalli-scale. At least 534 people killed, 2,300 injured and 14,618 buildings and homes destroyed or damaged in the Ercis-Tabanlı-Van area. Several M>5 aftershock events followed. Telecommunications, electricity and water services disrupted. It was felt throughout eastern Turkey, Armenia, Georgia, Azerbaijan and northwestern Iran and parts of Iraq, Syria, Lebanon, Jordan and Israel.

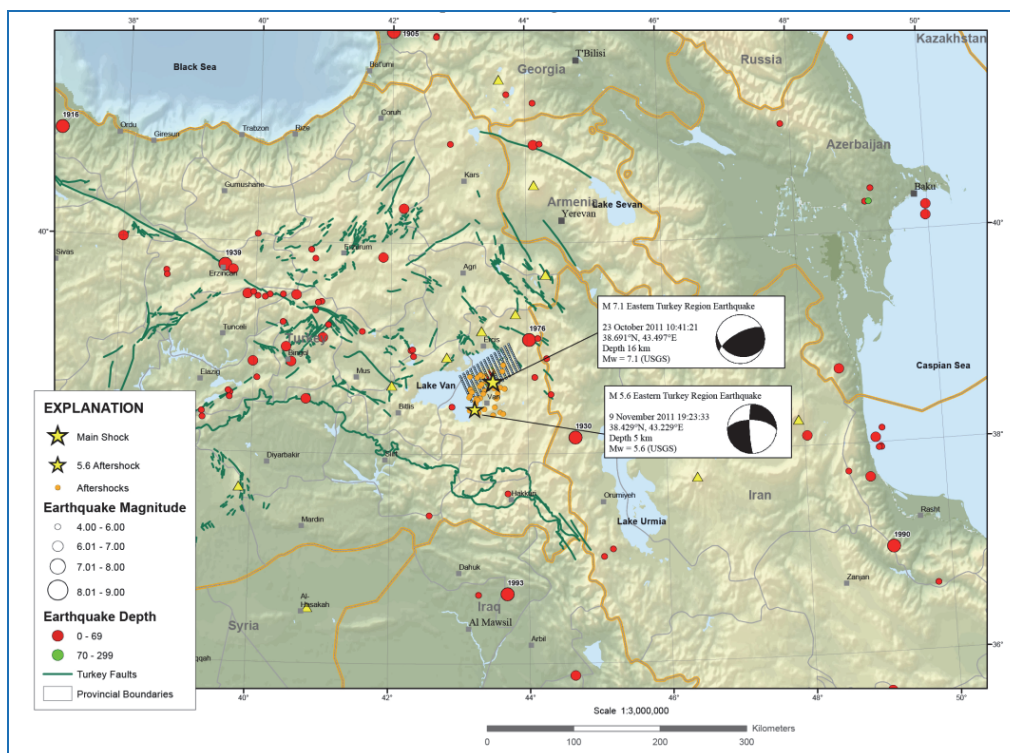


Figure 1: Location and tectonic settings (USGS)

Observations of the nm-scale accuracy extensometer at Budapest Mathias Hill Gravity and Geodynamical Observatory and that of a three component STS-2 Streckeisen broad band seismometer at the Kövesligethy Radó Seismological Observatory can be seen on **Figure 2**. The distance between the gravity and seismological stations is less than 6 km.

2. METHOD OF INVESTIGATION

In order to compare the time series of teleseismic waves recorded by extensometer (located in the Mathyas-Hill) and that of horizontal components of seismograms recorded at BUD seismological station, the North and East seismogram components were rotated with a certain angle to align with the azimuth of the extensometer (**Figure 3**). The rotated component quantities R and T can be expressed by (**Eq. 1**)

$$\begin{bmatrix} R \\ T \end{bmatrix} = \mathbf{A} \begin{bmatrix} N \\ E \end{bmatrix} \quad (1)$$

where **N** and **E** are the horizontal North and East components of the seismogram, respectively, and **A** (**Eq. 2**) denotes the “rotation matrix”

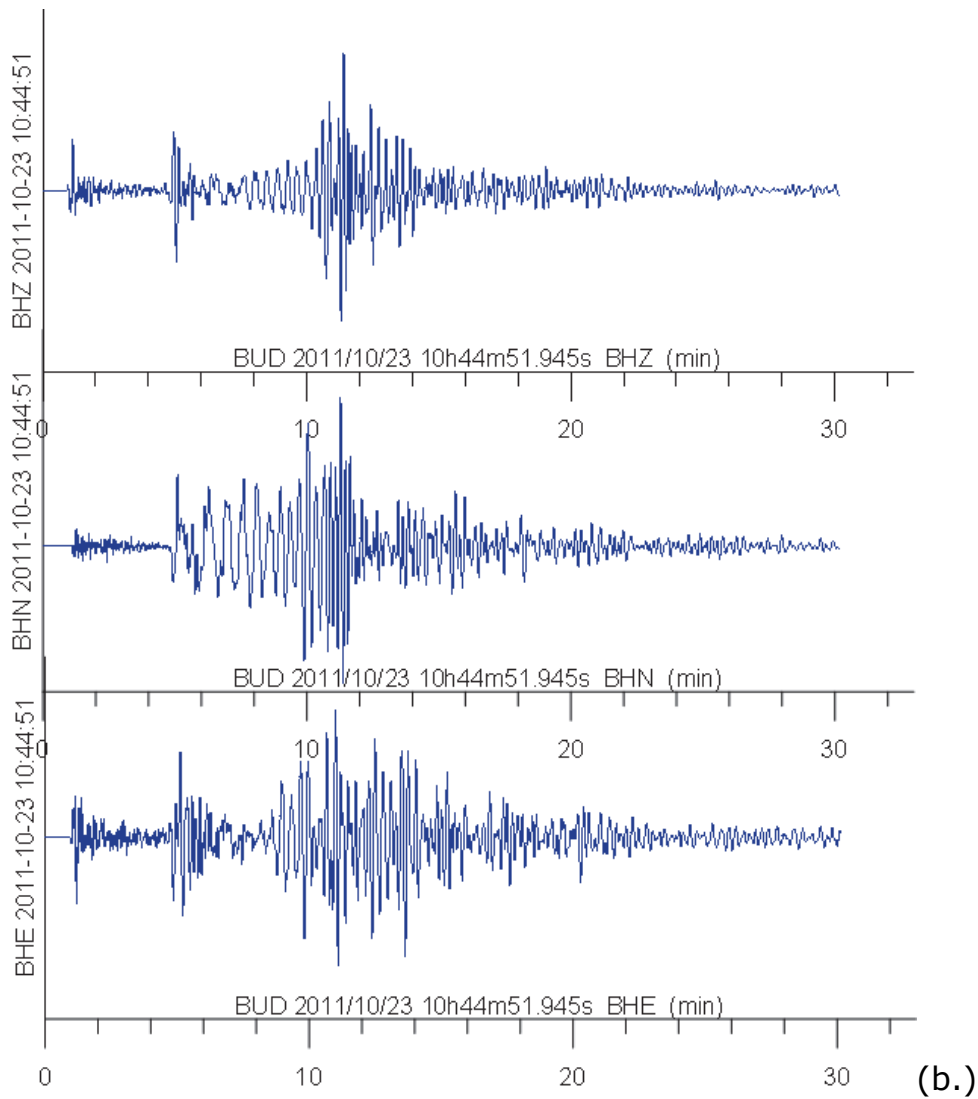
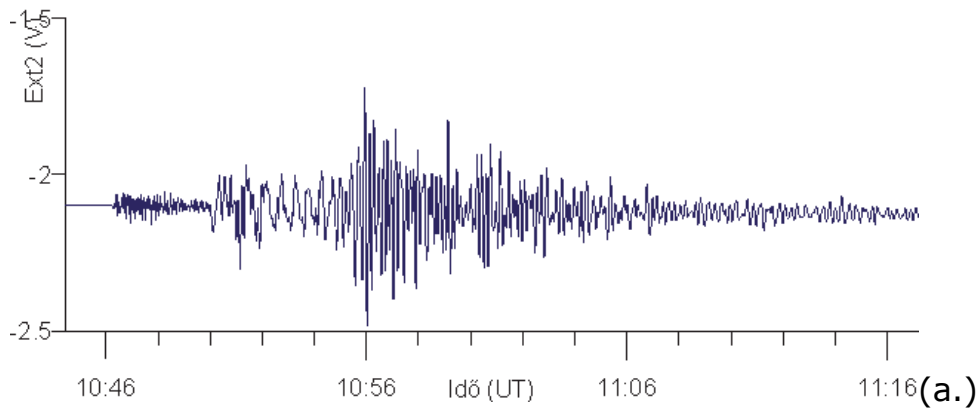


Figure 2: Observations by extensometer (a.) and seismometer (b.)

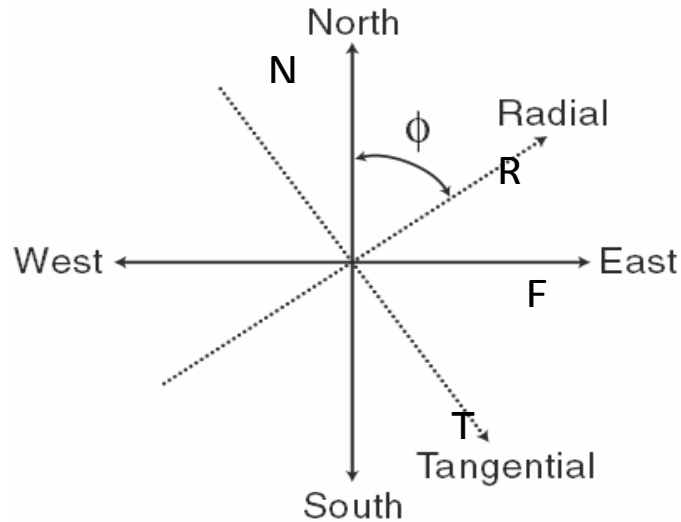


Figure 3: Original and rotated components

$$A = \begin{bmatrix} \cos \Phi & \sin \Phi \\ -\sin \Phi & \cos \Phi \end{bmatrix} \cdot \quad (2)$$

3. SPECTRAL ANALYSIS

The registrations of BUD seismological station were rotated with certain angles, and FFT were performed to analyse the spectral content (extensometer: Fig. 4, seismometer /e.g. $\Phi=218^\circ$ /: Fig. 5).

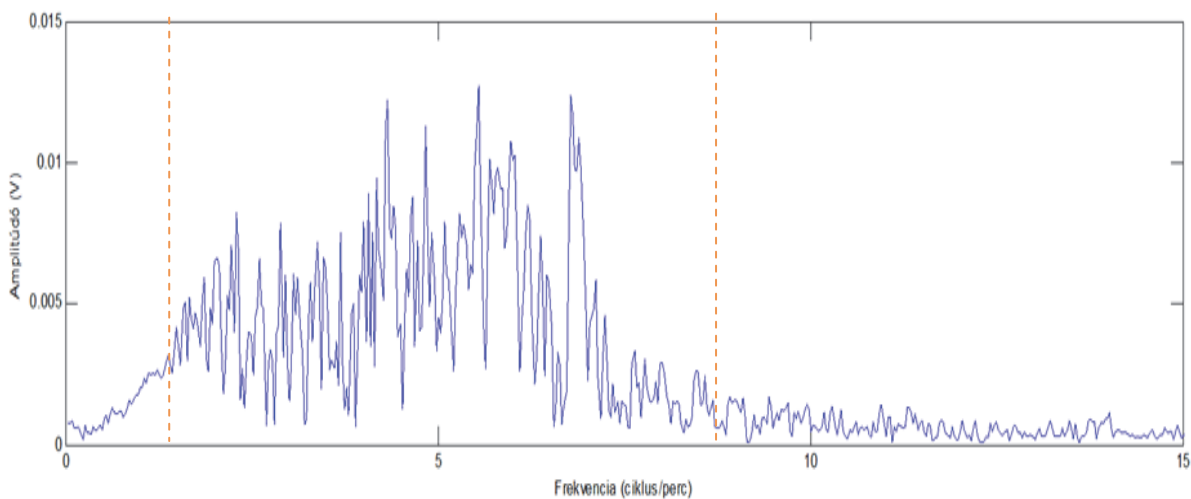


Figure 4: Extensometric FFT spectrum of the Turkey earthquake (UT2011.10.23 10:45-11:20), azimuth of the extensometer: N 218°

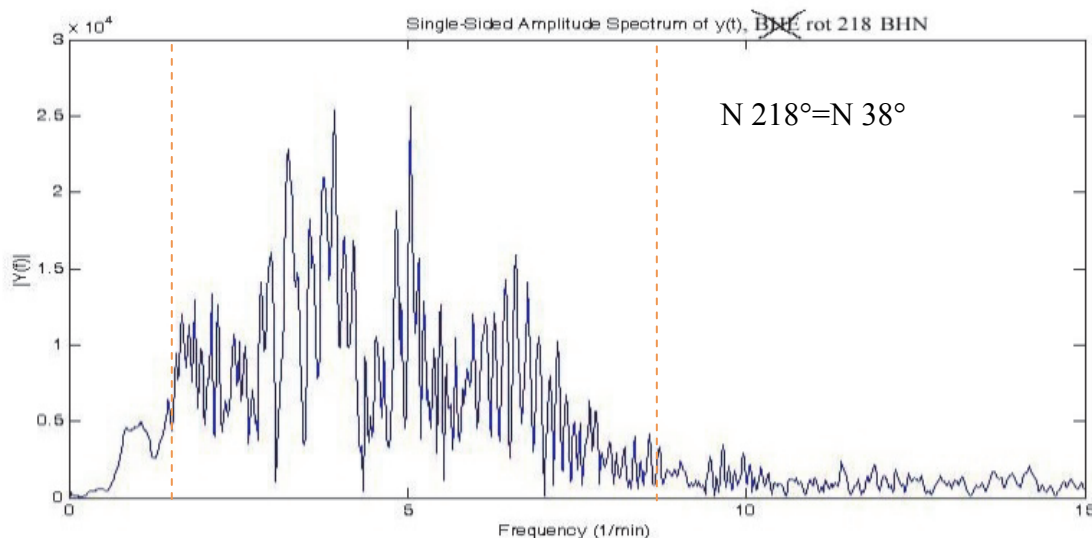


Figure 5: FFT spectra of rotated ($\Phi=218^\circ$) radial components of seismogram calculated from BHE (horizontal East) and BHN (horizontal North) components (UT2011.10.23 10:38 -11:08, 20 Hz sample rate).

4. CONCLUSION

Different types of rock-deformation measurements (seismogram and extensometric data) were compared in the analysis of a significant earthquake. It was concluded that there were some similarities between the time series and spectra registered by the different methods. The complementary analysis of extensometric data gives a chance for investigating various earthquake-originated changes in the rock-physical environment (deformation fields).

5. ACKNOWLEDGEMENT

Authors wish to express their thanks to OTKA (Hungarian Scientific Research Fund) for their support (OTKA K101603, OTKA K109060).

6. REFERENCES

GEOFON PROGRAM GFZ POTSDAM- Global Seismic Network, Earthquake Information Service.

<http://geofon.gfz-potsdam.de/eqinfo/event.php?id=gfz2011utuo>

KÖVESLIGETHY-RADÓ SEISMOLOGICAL OBSERVATORY BUD: Earthquakes in the past 30 days. <http://www.seismology.hu/>

KÖVESLIGETHY-RADÓ SEISMOLOGICAL OBSERVATORY BUD: Significant earthquake in Turkey (in Hungarian).

<http://www.seismology.hu/index.php/hu/component/content/article/74-reports/90-significant-earthquake-in-turkey>

ANALYSIS OF LONG-TERM EXTENSOMETRIC DATA OF SOPRON AND BUDAPEST GEODYNAMICAL OBSERVATORIES

Gyula MENTES¹, Ildikó EPER-PÁPAI¹, Márta KIS², András KOPPÁN²

¹Geodetic and Geophysical Institute, Research Centre for Astronomy and Earth Sciences,
Hungarian Academy of Sciences, Csatkai Endre út 6-8, H-9400 Sopron, Hungary

²Geological and Geophysical Institute of Hungary (MFGI), 14 Stefania St., H-1143 Budapest,
Hungary

E-mail: kis.marta@mfgi.hu

Long quartz-tube extensometric measurement systems are monitoring rock deformations in two geodynamical observatories in Hungary. The Sopronbánfalva Geodynamical Observatory (SGO) is situated in Sopron, at the border of the Alps, in metamorphic (gneiss) environment. The Mátyáshegy Gravity and Geodynamical Observatory (MGGO) is created in the karstic environment of Mátyás-Hill in W-Budapest. The 8 year-long time series of continuous measurements are processed and examined, attending to geologic and topographic features of the measurement sites. Tidal and coherence analysis were performed to determine the tidal deformation parameters as well as to study the sensitivity at both locations. The stability of the geodynamical measurement places was investigated by means of signal to noise values derived from the processing of higher frequency variations in both observatories. The long-term deformation rates measured by the extensometers are compared with the strain rates inferred from GPS measurements of the Hungarian GPS Geodynamic Reference Network (HGRN).

Keywords: extensometer, tidal analysis, long-term data processing

1. EXTENSOMETRIC MEASUREMENT SYSTEMS

Monitoring of long period deformations of the upper Earth crust is mostly performed by extensometry using equipments with different principles, capable for observing variations in 10^{-11} order (nm-scale displacements). The observations are used to study tidal and non-tidal rock deformations, as well as to monitor recent geodynamic processes. Application possibilities are to analyse the natural (wide spectrum of the Earth's physical processes, e.g. tides, self-oscillation of solid Earth, pole motion, variation of Earth's rotation, mass rearrangements, tectonics, climatic changes) and man-made (e.g. mining, water accumulation, industrial activity) deformations. In order to characterise global processes in continental range, datasets earned from network of observatories should be used.

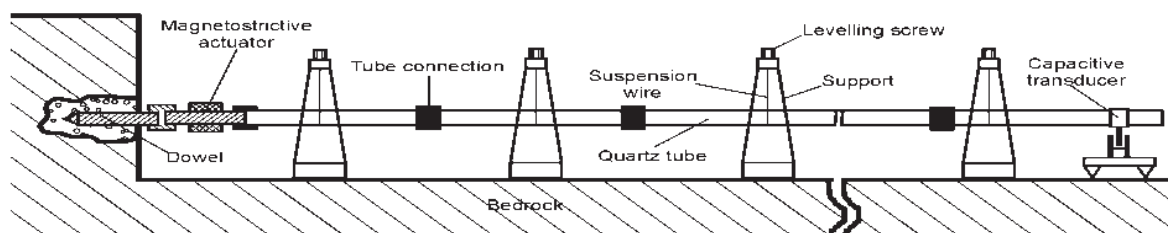


Figure 1: Scheme of suspended long tube extensometers

2. APPLIED INVESTIGATIONS

Properties and signal transfer characteristics of the local deformation field were examined by means of tidal analysis in the short wavelength band of variations. Tidal calculations were carried out by ETERNA 3.40 'Earth Tide Data Processing Package' (Wenzel, 1996), applying Wahr-Dehant model and HW95 tidal potential catalogue. For tidal investigations data were high-pass filtered with a cut-off frequency 0.8 cycles per day. Spectral analysis was carried out by FFT (Fast Fourier Transformation). The signal transfer characteristics and tidal parameters of the two stations were examined by tidal and coherence analysis. Long term variations (with geodynamical contents) and admittances of strain and outer temperature variations were also studied. Strain rates measured in the Hungarian GPS Geodynamic Reference Network (HGRN) (Grenerczy et al., 2000), and in the Central European GPS Reference Network (CEGRN) (Caporali et al., 2008) were compared to the measured rates at both sites.

3. CONCLUSION

Tidal analysis results show that the extensometer in MGGO has better transfer mechanism concerning the horizontal higher frequency deformations. The measured tidal amplitudes are near to the theoretical model values in MGGO, however they are 44-60% lower in the SGO (diurnal and semi-diurnal band). Based on signal transfer characteristics it was also concluded that higher stability for tidal measurements can be achieved at the MGGO (due to low attenuation of tidal waves), and the stability of the SGO is very good for long wavelength geodynamical/tectonic deformation measurements. The measured strain rates in both observatories are in a good agreement with the strain rates determined by means of the GPS networks.

4. ACKNOWLEDGEMENT

Authors wish to express their thanks to OTKA (Hungarian Scientific Research Fund) for their support (OTKA K109060).

5. REFERENCES

CAPORALI, A, AICHHORN, C., BECKER, M., FEJES, I., GERHATOVA, L., GHITAU, D., GRENERCZY, G., HEFTY, J., KRAUSS, S., MEDAK, D., MILEV, G., MOJZES, M., MULIC, M., NARDO ,A., PESEC, P., RUS, T., SIMEK, J., SLEDZINSKI, J., SOLARIC, M., STANGL, G., VESPE, F., VIRAG, G., VODOPIVEC, F., ZABLOTSKYI, F., (2008): Geokinematics of Central Europe: New insights from the CERGOP-2/Environment Project. *Journal of Geodynamics*, 45, 246–256

EPER-PÁPAI, I., MENTES, GY., KIS, M., KOPPÁN, A. (2014): Comparison of two extensometric stations in Hungary. *Journal of Geodynamics* (in print).

GRENERCZY, GY., KENYERES, A., FEJES, I. (2000): Present crustal movement and strain distribution in Central Europe inferred from GPS measurements. *J. Geophys. Res.* 105 (B9), 21835–21846

WENZEL, H. G. (1996):The nanogal software: Earth tide data processing package ETERNA 3.30. *Bulletin D’Inf. Marées Terrestres* 124, 9425-9439

SATELLITE-BASED INLAND EXCESS WATER FLOOD DETECTION

Zalán TOBAK *, Boudewijn VAN LEEUWEN, László HENITS, József SZATMÁRI

Department of Physical Geography and Geoinformatics, University of Szeged, H-6722
Szeged, Egyetem u. 2-6.

* tobak@geo.u-szeged.hu

Inland excess water (IEW) is the phenomenon where water remains temporary in local depressions on flat terrain. This type of flooding is a common problem in the Carpathian Basin. Nearly every year large areas are covered by water due to lack of natural run off of superfluous water. IEW damages crops, obstructs agricultural activities and local transportation, leads to soil and groundwater contamination and deterioration of the soil quality in the long term. To study the development of this phenomenon, it is necessary to determine where these inundations occur. Different methods were evaluated to locate and classify inland excess water occurrences on a study area covering south-eastern Hungary and northern Serbia. Three separate methods are used to determine their applicability to the problem. The methods use the same input data set but differ in approach and complexity. The input data set consists of a mosaic of RapidEye medium resolution multispectral satellite images. This study uses (semi-)automatic classification methods to determine the occurrences of inland excess water based on satellite images. The results of the classifications show that all three methods can be applied to the problem and provide high quality satellite based inland excess water maps over a large area.

Key words: *inland excess water, multispectral satellite image, (semi-) automatic classification*

1. INTRODUCTION

1.1. INLAND EXCESS WATER

On the relatively flat terrain of our study area covering south-eastern Hungary and northern Serbia, large areas are temporary flooded, which is caused by different physical and anthropogenic factors. In local depressions water can remain due to lack of runoff, insufficient evaporation and/or low infiltration capacity of the soil. Not only precipitation, but also upwelling groundwater can accumulate in these depressions. Beside the natural factors, the anthropogenic influences, such as the construction of roads and railroads, or the agricultural activity, can have a significant impact. With the maintenance of hydrological structures like channels and pumping stations, humans try to mitigate the damage of inland excess water (IEW) (Kozák, 2006).

1.2. CLIMATE CHANGE

Long-term climate models forecast for the Carpathian basin a warming trend, but no significant change in precipitation. It is very likely, that the amount of precipitation will increase in winter (and to a smaller extent in spring), while it is expected to decrease in summer. The intensity of the precipitation will increase, because the same amount of precipitation will fall in a shorter period. This will likely increase the risk for IEW, since a larger amount of water needs to evaporate or find its way to channels and rivers gravitationally (Bartholy et al. 2007).

2. STUDY AREA

As the IEW is basically a physical phenomenon, we are working in a Hungarian-Serbian cross border study area (**Figure 1**). The area was formed predominantly by fluvial processes.

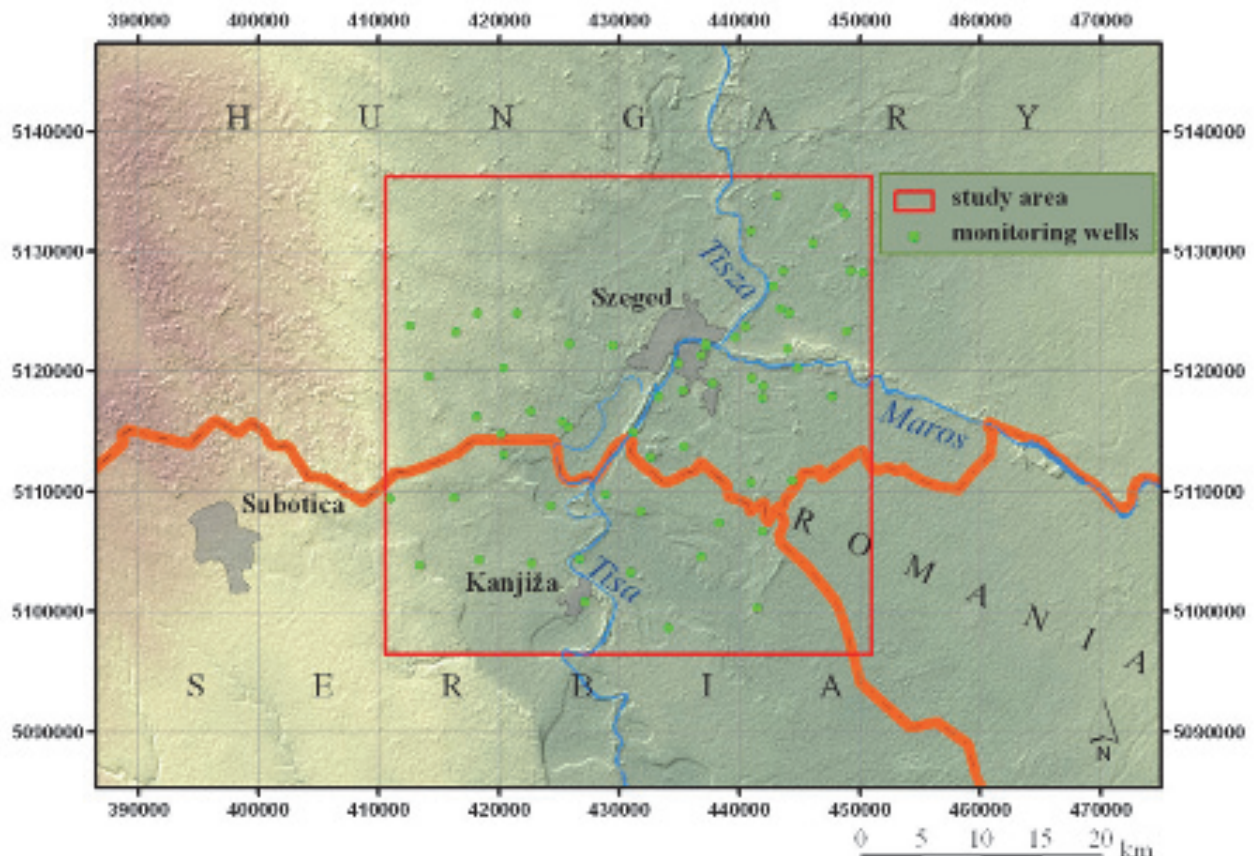


Figure 1: Cross-border study area

The main aim of this study is to map and delineate inland excess water inundations using satellite imagery and image classification methods. The

expected results are more precise and up-to-date, than the traditional field mapping campaigns.

3. DATA AND METHODS

The efficiency of passive sensors, which were used in this study, depends on good weather condition, and IEW often occurs during cloudy periods with lots of precipitation. Pixel and sub-pixel based classification techniques are needed to extract the IEW areas from the images.

3.1. RAPIDEYE SATELLITE IMAGERY

The main advantage of RapidEye over other earth observation satellites is the combination of high temporal (daily) and relative good (5 m) spatial resolution with a reasonable price. In IEW research, it is necessary that images are acquired from the phenomenon when it happens. For this study, RapidEye satellite images covering an area of 9,000 km² were processed for the winter/early spring IEW period of 2010-2011.

3.2. CLASSIFICATION

The RapidEye mosaic was classified using 2 commonly used and 2 advanced classification methods. Beside pixel-based unsupervised Isodata clustering and supervised Maximum Likelihood (ML) (Lillesand et al., 1998) algorithm, a subpixel-based Spectral Mixture Analysis (SMA) (Roberts et al., 1998) was applied. The fourth approach used an artificial neural network (ANN) to sort the pixels into different classes (Dawson and Wilby, 2001). In the supervised methods 3 vegetation, 1 water, 1 soil and a class with high albedo were defined.

4. RESULTS

4.1. ISODATA CLASSIFICATION

IEW mapping for operative purposes would benefit a lot from a fully automatic identification method. In potential, the Isodata methods could provide this capability. **Figure 2** shows the Isodata results for 6 and 8 classes. Clearly, the result with 6 classes shows too much water, while the classification with 8 classes is slightly better to interpret visually, but still mixes soil and water in many areas.

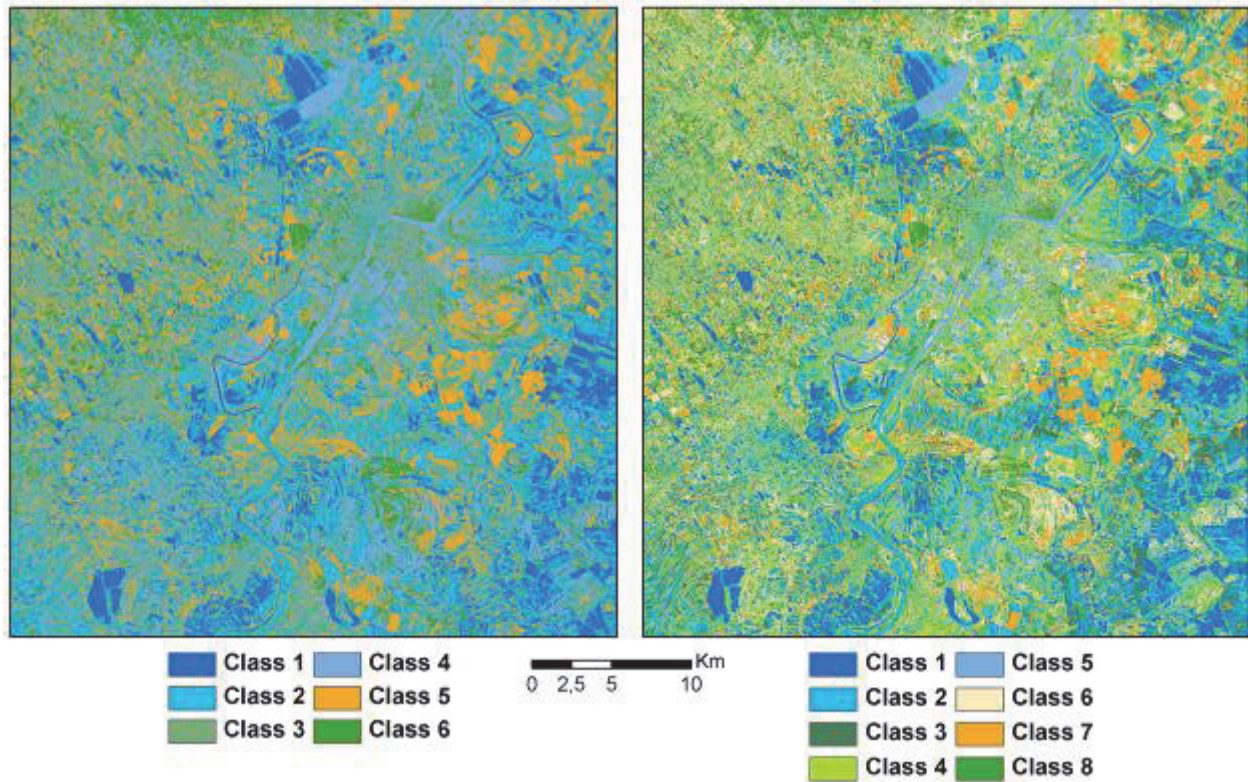


Figure 2: Results of Isodata clustering with 6 (left) and 8 (right) classes

4.2. MAXIMUM LIKELIHOOD (ML)

Visual inspection of the ML result reveals large areas covered with water in the East and South East (**Figure 3**). If the type of water is not relevant, all water classes can be combined, which results for the combined water classes of 0.99. Other classes show very little misclassification.

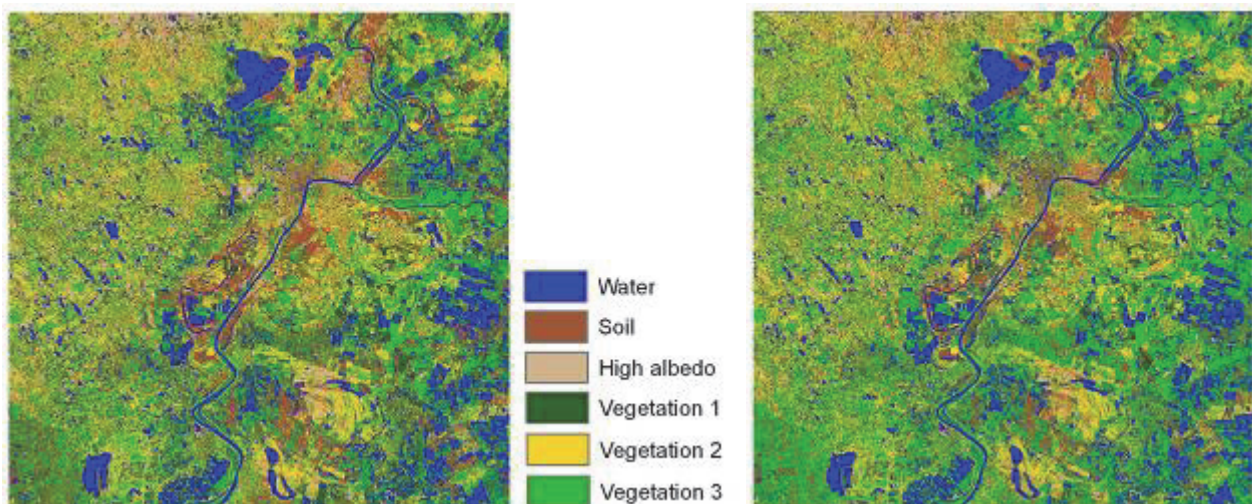


Figure 3: Results of Maximum Likelihood (left) and Artificial Neural Network classification (right)

4.3. SPECTRAL MIXTURE ANALYSIS (SMA)

The SMA method results in two maps (**Figure 4**). The first result is a color composite of the three fraction maps that give the ratio for each endmember soil, vegetation and water. The final result is a thematic map that is created by applying a ML classification to the endmember composite. The overall accuracy of this method is 0.75. This is because ‘Deep water’ and the ‘High albedo’ class are often misclassified as ‘Soil’. The accuracy of the ‘IEW’ and ‘Shallow water’ classes are about 0.8 though.

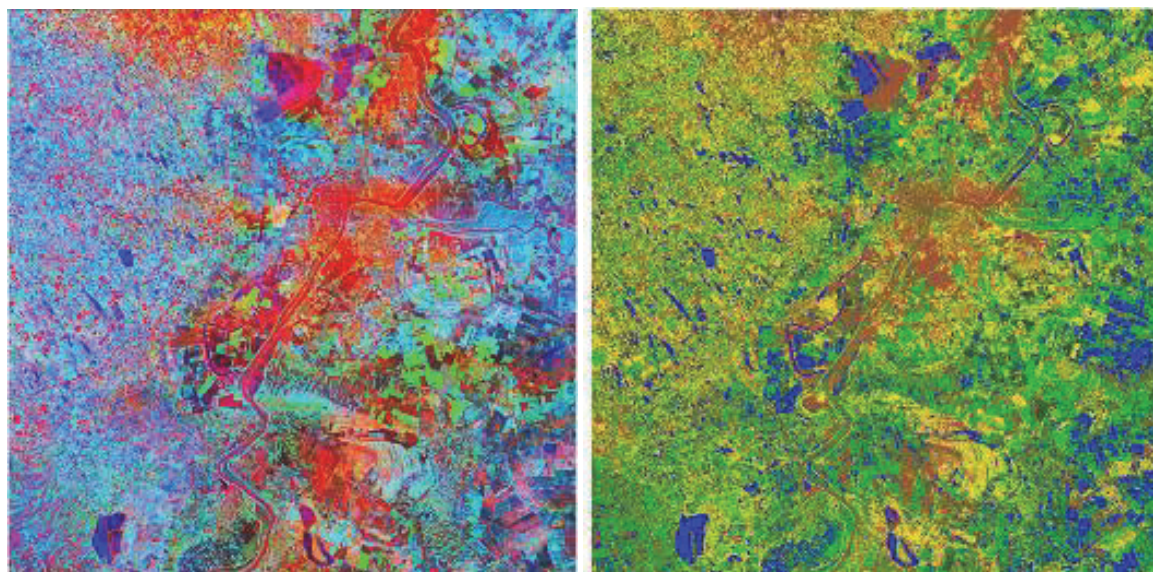


Figure 4: SMA fraction (left) and result (right) map

4.4. ARTIFICIAL NEURAL NETWORK (ANN)

The thematic map of the ANN method (**Figure 3**) is similar to the ML result. Although, the different water classes are sometimes mixed, the overall accuracy of the ANN method is 0.96, because the ‘Vegetation’, ‘Soil’ and ‘High albedo’ classes are rarely misclassified.

5. CONCLUSIONS

According to our experiences, all applied methods have their own advantages and/or disadvantages. The result of *Isodata clustering* does not provide an IEW map of sufficient quality. The quality of the 3 supervised classification methods can be compared to each other (**Table 1**).

Table 1: Accuracy measurements of the three supervised classification methods

	Overall accuracy	Cohen's Kappa
Maximum Likelihood (ML)	0.95	0.94
Spectral mixture analysis (SMA)	0.75	0.71
Artificial neural network (ANN)	0.96	0.96

The SMA classification has the lowest overall accuracy and Kappa value, while ML and ANN methods perform similarly. The Maximum Likelihood classification method is relatively simple and requires the least user input. Therefore, in operational circumstances this method is most suitable. The ANN method requires more user interaction because the network needs to be defined and trained. RapidEye satellite data can be useful for the generation of IEW maps. They can be (semi-)automatically classified to generate thematic maps that show areas where land is covered with water. The generation of these maps can be more efficient and accurate than with the traditional fieldwork.

6. ACKNOWLEDGEMENTS

This research was supported by the IPA Cross-border Cooperation Programme of the European Union under the project WAHASTRAT (HUSRB/1203/121/130).

7. REFERENCES

- BARTHOLY, J., PONGRÁCZ, R., GELYBÓ, GY. (2007): Regional climate change expected in Hungary for 2071-2100. *Applied ecology and environmental research*, 5, 1, 1-17.
- DAWSON, C.W. & WILBY, R.L. (2001): Hydrological modelling using artificial neural networks. *Progress in Physical Geography*, 25, 1, 80-108.
- KOZÁK, P. (2006): A belvízjárás összefüggései az Alföld délkeleti részén, különös tekintettel a vízkárelhárítás európai igényeire [*The evaluation of the excess surface waters on the Hungarian lowland's south-east part, in the expectation of the water management in Europe*]. - PhD Thesis, SZTE Földtudományi Doktori Iskola, Szeged, 86 p.
- LILLESAND, T.M., KIEFER, R.W., CHIPMAN, J.W. (2004): *Remote Sensing and Image Interpretation*. Wiley, 784 p.
- ROBERTS, D.A., GARDNER, M., CHURCH, R., USTIN, S., SCHEER, G., GREEN, R.O. (1998): Mapping chaparral in the Santa Monica mountains using multiple endmember spectral mixture models. *Remote Sensing of Environment*, 65, 267-279.

OBSERVATORY GRAVIMETER CALIBRATION RESULTS WITH MAGNETIC CORRECTION

András KOPPÁN, Márta KIS, Péter KOVÁCS, László MERÉNYI, Gergely VADÁSZ
Geological and Geophysical Institute of Hungary (MFGI), 14 Stefania St., H-1143 Budapest,
Hungary
E-mail: kis.marta@mfgi.hu

A gravimeter calibration facility exists in the Mátyáshegy Gravity and Geodynamical Observatory of Geological and Geophysical Institute in Hungary. During the calibration a cylindrical ring of 3100 kg mass is moving vertically around the equipment, generating ~ 110 microGal gravity variations, so it provides excellent possibility for the fine calibration of gravimeters in the tidal range. The instrument was out of order for many years and in 2013 it was renovated and automatized. The calibration process is aided by a PLC-based control unit. As it is well known that variations of the magnetic field can influence the measurements of metal-spring gravimeters, authors carried out magnetic experiments on the pillar of the calibration device as well, in order to analyze the magnetic effect of the moving stainless steel-mass. In this presentation authors show the facility in details and the numerical results of tests carried out by applying LCR-G gravimeters.

Keywords: metal-spring gravimeter, calibration, magnetic effect

1. THE MOVING-MASS GRAVIMETER CALIBRATION DEVICE

A calibration device (**Figure 1**) was developed for Lacoste-Romberg gravimeters in the Mátyáshegy Gravimetric and Geodynamical Observatory in 1990 (Varga et al., 1995). The main target of the calibration device was to reach a relative accuracy of 0.1-0.2% for the calibration of Earth tide registering gravimeters. The total mass of the cylinder is 3103.765 ± 0.021 kg, and its material is stainless steel. The total height of the cylinder is 1030 mm, its inner diameter is 320 mm, and the outer diameter is 770 mm (Csapó and Szatmári, 1995). The maximum theoretical gravity variation (**Figure 2**) produced by the vertical movement of the mass is 109.98 μ Gal (calculated by G. Csapó, based on the numerical integration method of Hajósy (1988)).

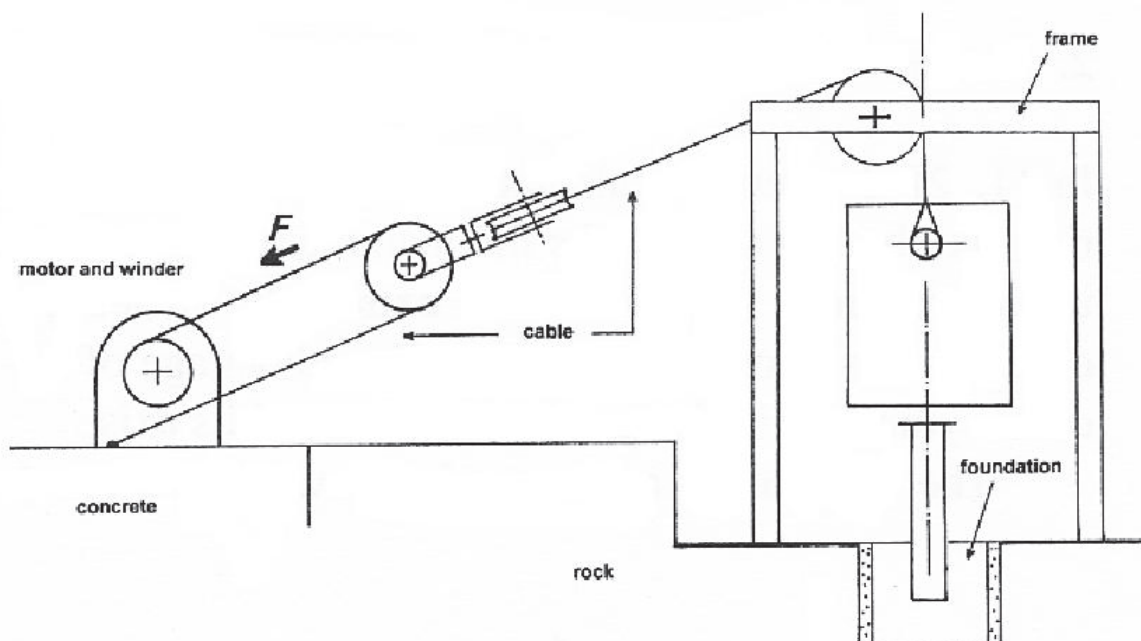


Figure 1: The scheme of the moving-mass calibration device

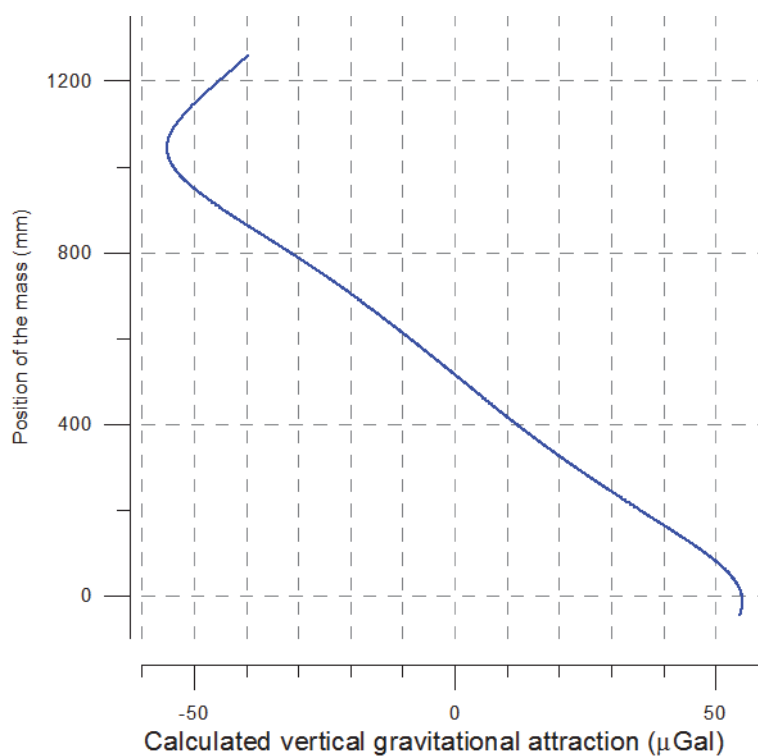


Figure 2: The theoretical gravity effect

A new PLC-based system has been developed to allow easy control of the movement of the calibrating mass and to measure the mass position. The system can be programmed for different measurement scenarios: speed of the mass moving, one or more (up to 15) waiting positions and waiting times can be set. The accuracy of positioning is 0.1 mm. All parameters (position of the

mass, gravity data, X/Y levelling positions) are recorded with 1/sec. sampling rate. The whole system can be controlled remotely through the Internet.

2. METAL-SPRING GRAVIMETER CALIBRATION

The full renovation of the mass moving calibration device was completed in March 2013. The first test calibration measurements were carried out on 9 April 2013, by using the LCR-G 1919 gravimeter. During the test 3 full up-down cycles were measured (**Figure 3**) with 1300 mm maximal mass elevation. 2 minutes long resting periods were used at the lowest and highest positions. After the tidal and barometric corrections and drift removal, all g_{min} and g_{max} values were determined for every cycle (**Table 1**). The mean Δg is 111.232 μGal .

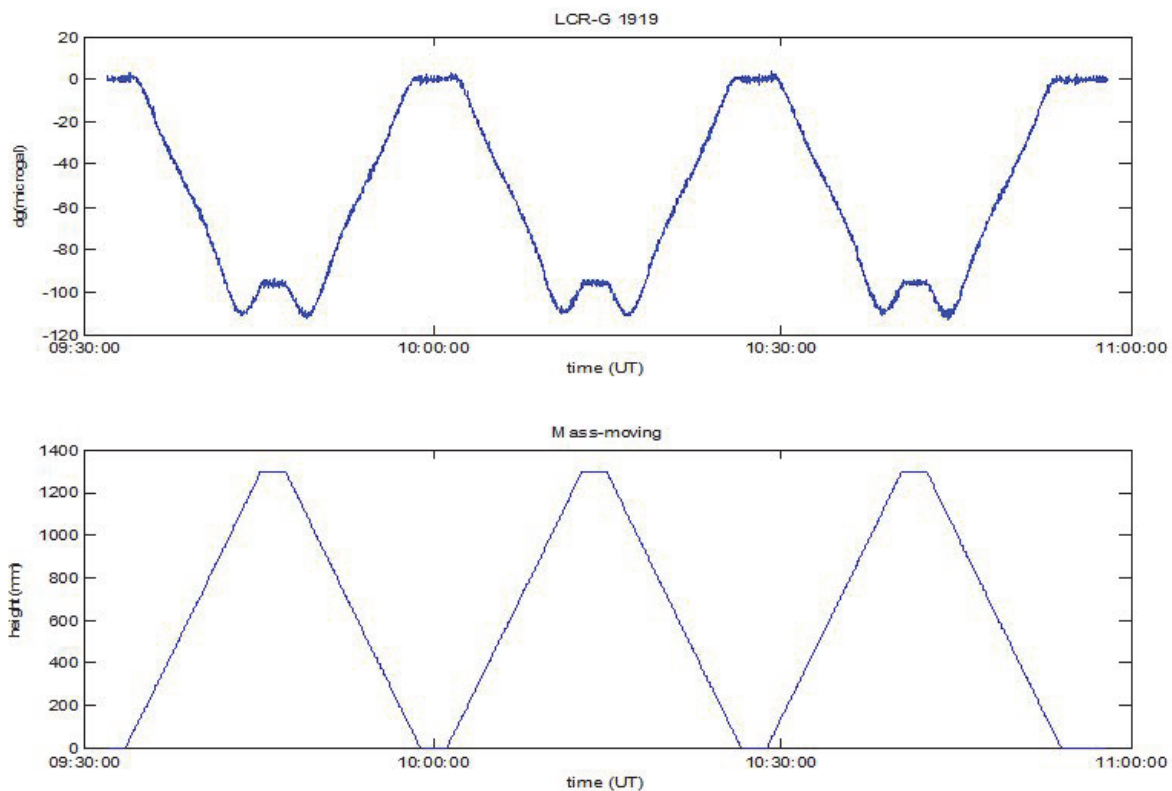


Figure 3: Test calibration of LCR-G 1919 (09 April 2013)

It is well known from the literature and earlier experiments that the magnetic field can influence the results of measurements of metal-spring gravimeters (Torge, 1989). Therefore a question arises whether the stainless steel mass and the frames have any magnetic effect. As the sensitivity of LCR-G gravimeters for the magnetic field is diverse in different directions, 3-component magnetic measurements were carried out.

Table 1: The results of the test calibration (without magnetic effect corrections)

	gmin	gmax	Δg
1. up	-109.7936	1.7145	111.508
1. down	-110.7692	0.8453	111.615
2. up	-109.2446	1.7513	110.996
2. down	-110.3946	0.8640	111.259
3. up	-109.2497	1.7118	110.962
3. down	-110.3488	0.7057	111.054
mean	-109.967	1.265	111.232
σ	0.639	0.508	0.277

As the measuring range of the magnetometers generally used in the geomagnetic observatories are limited to achieve an increased precision (few hundred or thousand nT), a brand-new FluxSet magnetometer was used for the experiment with wider measurement range (**Figure 4**). This magnetometer is developed by the Central Research Institute for Physics of Hungarian Academy of Sciences (MTA KFKI) and the Aviatronic Ltd. (for more information: <http://alag3.mfa.kfki.hu/magnet/fluxset/index.htm>).

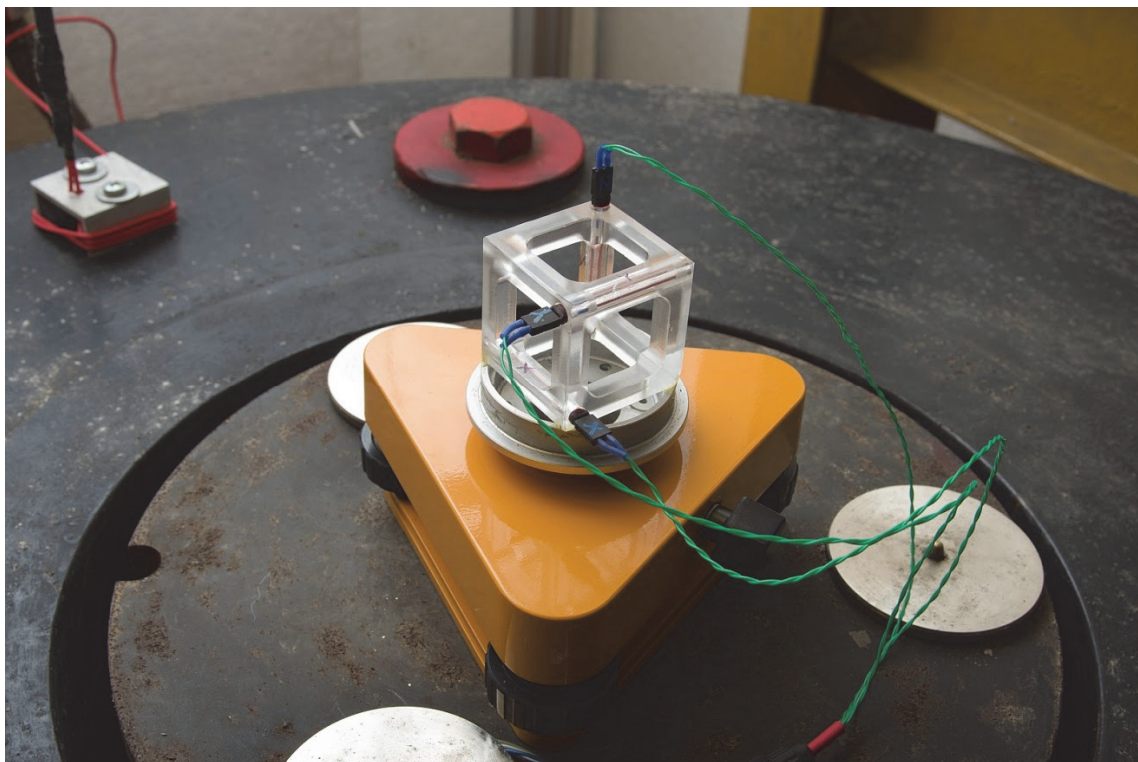


Figure 4: The FluxSet magnetometer sensor

The sensor was positioned on the pillar of the calibration device in direction „N” (geomagnetic X). During the up and down movements of the mass (dH=1300 mm), the observed magnetic field has been changed significantly: in X

direction varied from -1000 to +17000 nT, in Y direction from -1100 to +900 nT and in the Z direction between 3000 and 45000 nT.

Based on results of the experiment it can be concluded that the change of the magnetic field is theoretically large enough to influence the gravimetric measurements during the calibration (max. 2-3 μ Gal). The magnetic sensitivity of LCR-G 1919 in the main directions gravimeter were determined earlier by using Helmholtz coils.

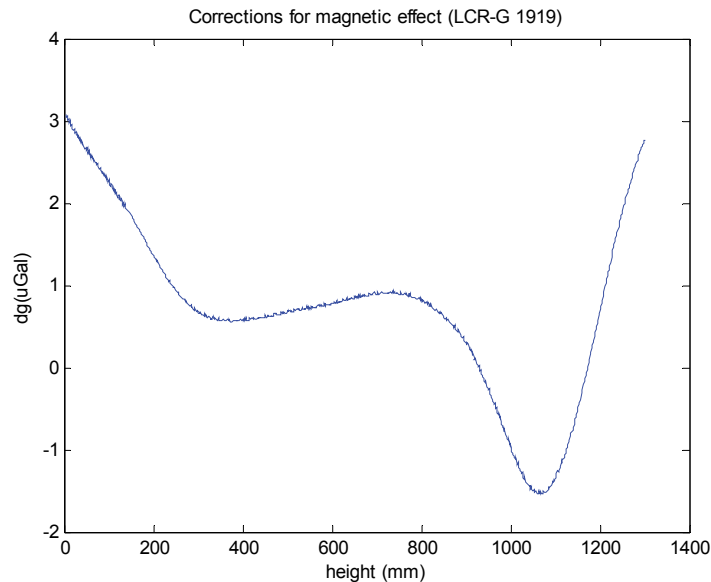


Figure 5: The calculated corrections for the magnetic effect in the case of LCR-G 1919

According to the mentioned magnetic measurements, a correction for the magnetic effect was applied on the measured data series (**Figure 5**). The **Table 2** contains the altered values after this correction. The mean Δg is 107.358 μ Gal. The calibration factors calculated by the two methods are 0.988743 and 0.965168, respectively.

Table 2: The results of the test calibration (after magnetic effect corrections)

	gmin(mc)	gmax(mc)	Δg(mc)
1. up	-108.9225	-1.0806	107.842
1. down	-109.5769	-2.0419	107.535
2. up	-108.3774	-1.0353	107.342
2. down	-109.1938	-2.0206	107.173
3. up	-108.3745	-1.0822	107.292
3. down	-109.1469	-2.1849	106.962
mean	-108.932	-1.574	107.358
σ	0.479	0.560	0.304

3. CONCLUSION

The moving-mass calibrating device is able to generate fine variations in the gravity field in a significantly narrower (typical tidal) range compared to the usual gravimeter calibration lines characterizable with several hundred mGal variations. In case of tidal monitoring gravimeters it is expedient to apply this high-accuracy calibration method, furthermore, it can be used for checking the time stability of the scale factor of gravimeters.

4. ACKNOWLEDGEMENTS

Authors wish to express their thanks to OTKA (Hungarian Scientific Research Fund) for their support (OTKA K101603, OTKA K109060).

5. REFERENCES

- CSAPÓ G., SZATMÁRI G. (1995): Apparatus for moving mass calibration of LaCoste-Romberg feedback gravimeters. *Metrologia* 32, 225-230.
- HAJÓSY, A. (1988): Numerical integration with linear combination of Chebyshev-Gauss quadratures. *Annales Univ. Sci. Budapest Sec. Comp.* 9, 139-148.
- TORGE, W. (1989): *Gravimetry*. Walter de Gruyter, Berlin, New York, 211 p.
- VARGA P., HAJÓSY A., CSAPÓ G. (1995): Laboratory calibration of Lacoste-Romberg type gravimeters by using a heavy cylindrical ring. *Geophys. J. Int.* 120, 745-757.

CARBON CAPTURE AND STORAGE POSSIBILITY, CASE STUDY IVANIĆ FIELD

Karolina NOVAK¹, Ivan ZELENKA²

¹ PhD student on the Faculty of Mining, Geology and Petroleum Engineering, Pierottijeva 6, 10000 Zagreb, Croatia; E-mail: mirime79@gmail.com

² Miramarska 15B, Zagreb, Croatia, PhD student on the Faculty of Mining, Geology and Petroleum Engineering, Pierottijeva 6, 10000 Zagreb, Croatia
E-mail: krk2367@gmail.com

The EOR (Enhanced Oil Recovery) project on the Ivanić and Žutica Fields, located in the Sava Depression, considers injection of 600000 m³/day of carbon dioxide (CO₂) into the reservoirs. Beside additional oil production, the project will significantly contribute in reducing CO₂ emission. The CO₂ source will be the gas processing facilities Molve. During the next 25 years more than 5 billion m³ of CO₂ could be injected. About 50 % of that volume would remain permanently stored in the subsurface.

Since 2014, Croatia has been a part of the EU Emission Trading Scheme (ETS). Although current CO₂ market price is unexpectedly low, expected future trends will justify investment in technologies for reducing climate change including Carbon capture and storage technology recognized by the European Commission. The volume of CO₂, which can be permanently stored in the Ivanić field after termination of the EOR project, is calculated using a software program (MBAL).

Key words: carbon dioxide, sequestration, enhanced oil recovery, sandstones.

1. POSSIBILITY AND PRACTICE OF CO₂ INJECTION INTO CROATIAN OIL FIELDS

Carbon dioxide capture and storage methods (abbr. CCS) play an increasingly important role in reducing CO₂ emissions from human activities. Although the enhanced oil recovery methods (abbr. EOR) are not common representatives of the CCS methods since additional hydrocarbons and a part of injected CO₂ are produced, nevertheless, by the EOR projects significant CO₂ quantities can be successfully removed from the atmosphere.

Based on detailed laboratory studies done for Croatian oil fields in the '70s and the '80s of the last century, the candidates for tertiary oil recovery method have been identified. Survey results singled out the Ivanić oil Field as one of the most suitable candidate for enhanced oil recovery method application and confirmed EOR project feasibility. Characteristics of the Ivanić Field are: porosity between 21.5 and 23.6%, permeability between 14 and 80 x 10⁻¹⁵ m² and initial water saturation between 28 and 38.5% (Malvić, 2008; Perić and Kovač, 2003). The tests (Goričnik and Domitrović, 2003; Perić and Kovač,

2003) determined solubility of CO₂, oil swelling due to CO₂, viscosity reduction and volume expansion, and efficiency of oil displacement by using CO₂ at varying reservoir conditions, including pressure, temperature, and fluids saturation. Minimum miscible pressure, between 190 and 200 bars was determined by the lim-tube tests.

Since the market oil price proves feasibility of tertiary hydrocarbon recovery projects, depleted hydrocarbon reservoirs can be considered as possible storage only in case of permanent abandonment decision. The quantities of CO₂ that can be stored into main reservoirs of depleted Ivanić Field after termination of the EOR project will be calculated by material balance method.

2. GEOLOGICAL SETTINGS OF THE ANALYSED RESERVOIRS

The Ivanić Field is located in the Sava Depression which takes a part of the Pannonian Basin System (**Figure 1**). The most important hydrocarbons reservoirs of the Sava Depression belong to the Upper Miocene sandstone lithostratigraphic members. The most important hydrocarbon reservoirs in the Ivanić Field are informally called the “Gamma series”. The “Gamma series” refers to particular sandstone bodies (in the rank of bed) deposited as single depositional events during the Upper Pannonian in lacustrine environments with consequent activity of turbiditic currents. Lithologically it is about fine-grained quartz and mica sandstones in alternation with marls and calcitic marls (e.g. Velić et al., 2011; Malvić, 2012; Novak Zelenika, 2012; Novak et al., 2014).



Figure 1: Location map of the Ivanić Field (from Novak et al., 2014)

3. EXPLOITATION STAGES OF THE IVANIĆ FIELD

Exploitation of economically significant hydrocarbon reservoirs of the Ivanić Field started on five wells in 1963. The solution gas drive production had led to highest oil production rate achieved already in 1966, with low recovery of 9.2 %. Water flooding started in 1972 and maximum oil production was reached in

1977 (Novosel, 2010). In the late phase had been tested the tertiary pilot project of alternating water and CO₂ injection, performed in part of reservoirs between 2003 and 2006. It has proved feasibility of the EOR project (Vrbošić et al., 2003; Perić & Kovač, 2003; Novosel, 2010). Numerical results indicated about additionally 3.9 mil m³ of hydrocarbons. As a CO₂ source the Gas Processing Facilities Molve will be used (CPS MOLVE III), where CO₂ is released into the atmosphere. The EOR project involves dehydration, compression and transportation of 600,000 m³/day of CO₂ via 20" pipeline in length of 88 km to the location of the fractionation facilities Ivanić Grad, where after compression and liquefaction CO₂ would be transported to the injection wells of the Ivanić (400000 m³/day) and Žutica (200000 m³/day) Fields. During 25 years of the EOR project more than 5 billion m³ of CO₂ could be injected. About 50 % of injected CO₂ will remain permanently stored in the reservoirs, and the rest will be re-produced with hydrocarbons.

CO₂ injection in the Ivanić Field will increased oil recovery by 4% of OOIP, what means an annual oil production increasing by 60000 m³ on average during the next 25 years (Novosel 2005, 2009). By carrying out the EOR project lifetime of selected fields is going to prolong for more than 20 years, and the total emission of CO₂ on CPS MOLVE will be reduced to about 400000 t/year.

4. IVANIĆ RESERVOIR MAPPING AND CO₂ INJECTION MODELLING

Modelling of the “Gamma 3” and the “Gamma 4” sandstone reservoirs of the Ivanić Field is done by using the Ordinary Kriging technique. It covered variogram analyses of reservoir variables (porosity, depth and reservoir thickness) and calculation the Upper Pannonian reservoir volumes (**Table 1**, Novak et al, 2014). Ordinary Kriging maps for porosity, thickness and depth for the „Gama 3” and the „Gama 4” reservoirs are shown on the **Figures 2 and 3**.

Table 1 Summary statistics of input data (from Novak et al, 2014)

	The Gamma 3			The Gamma 4		
	Thickness	Porosity	Depth	Thickness	Porosity	Depth
Min	8.00	14.32	-1628.75	2.13	0.81	-1613.81
Max	21.21	24.21	-1545.81	20.74	23.76	-1532.98
Avarage	13.69	20.37	-1565.86	7.80	12.50	-1557.00
Median	14.00	20.99	-1564.42	5.70	12.07	-1551.48
Number of data	16.00	16.00	16.00	16.00	16.00	16.00

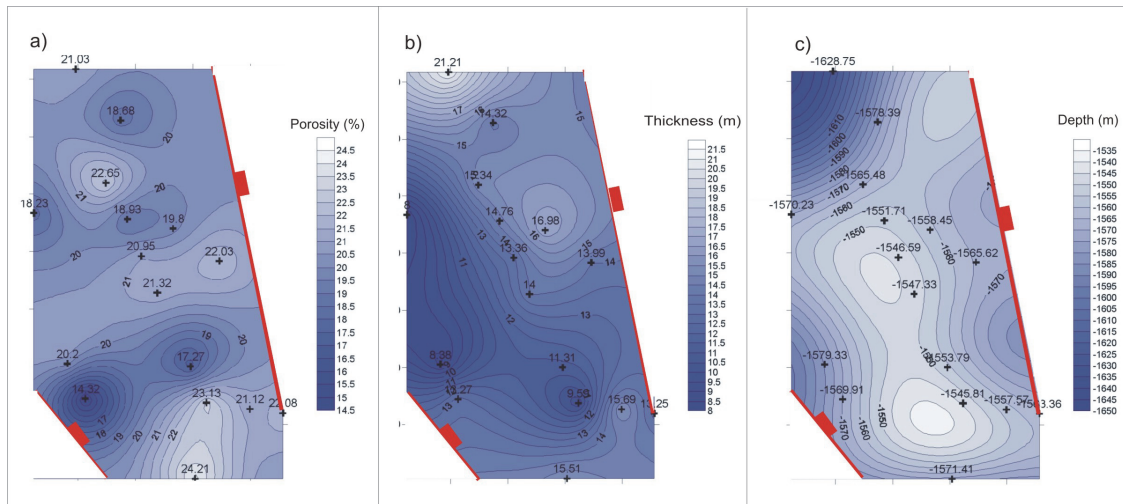


Figure 2: Kriging map for: a) „porosity“, b) „thickness“, c) „depth“ for the „Gama 3“ reservoir, the Ivanić Field (from Novak et al., 2014)

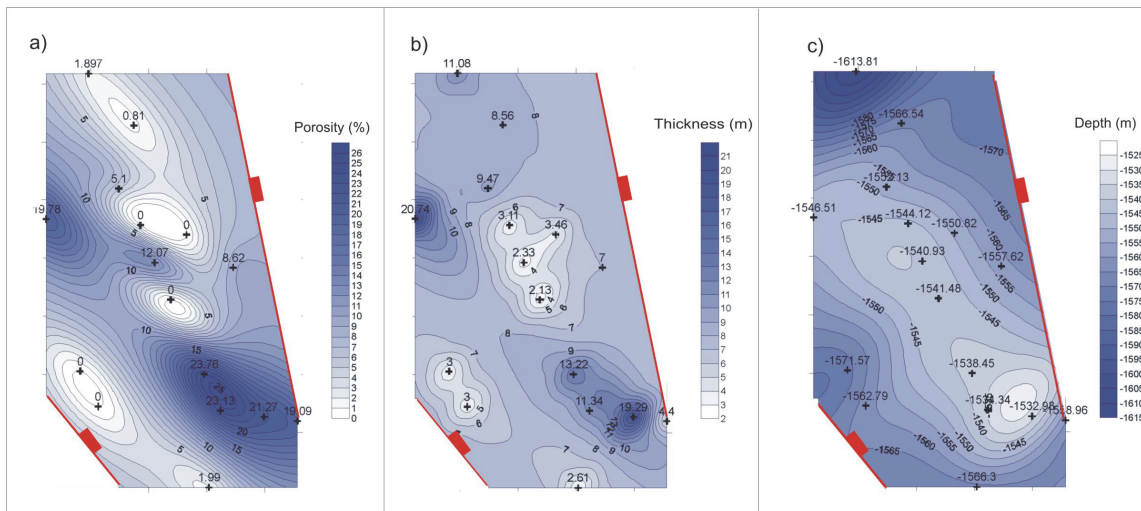


Figure 3: Kriging map for: a) „porosity“, b) „thickness“, c) „depth“ for the „Gama 4“ reservoir, the Ivanić Field (from Novak et al, 2014)

Based on data on thickness and porosity of two largest reservoir of the „Gamma series“, and considering data on water saturation, total and pore volume are calculated (**Table 2**).

Table 2: Calculated reservoir and pore volume for the „Gamma 3“ and the „Gamma 4“ reservoirs (from Novak et al, 2014)

Reservoir:	The „Gamma 3“	The „Gamma 4“
Volume of reservoir (m ³)	107,224,438.20	62,132,698.42
Pore volume above oil-water contact (m ³)	20,223,642.35	5,524,923.63
Pore volume under oil-water contact (m ³)	1,531,357.30	42,984.34
Volume saturated by water above oil-water contact (m ³)	5,339,041.58	1,442,005.10
Volume saturated by oil above oil-water contact (m ³)	14,884,600.77	4,082,918.53

Consequently, the volume of CO₂ expressed at standard condition, which can be injected in the “Gamma 3” and the “Gamma 4” reservoirs is simulated by using the MBAL softwer.

Cumulative of CO₂ injected into the „Gamma 3” reservoir was calculated using material balance using variable PVT composition option in MBAL softwer PVTP model and equation of state for characterization both reservoir and injected fluid. Starting point of calculation procedure was final reservoir condition from previous reservoir studies done on Ivanic Field. Results of MBAL model are presented on **Figures 5** and **6**. Cumulative injected volume of CO₂ was calculated from 134 barg reservoir pressure up to initial reservoir condition of 184 barg with reservoir temeperature of 97.7 °C.

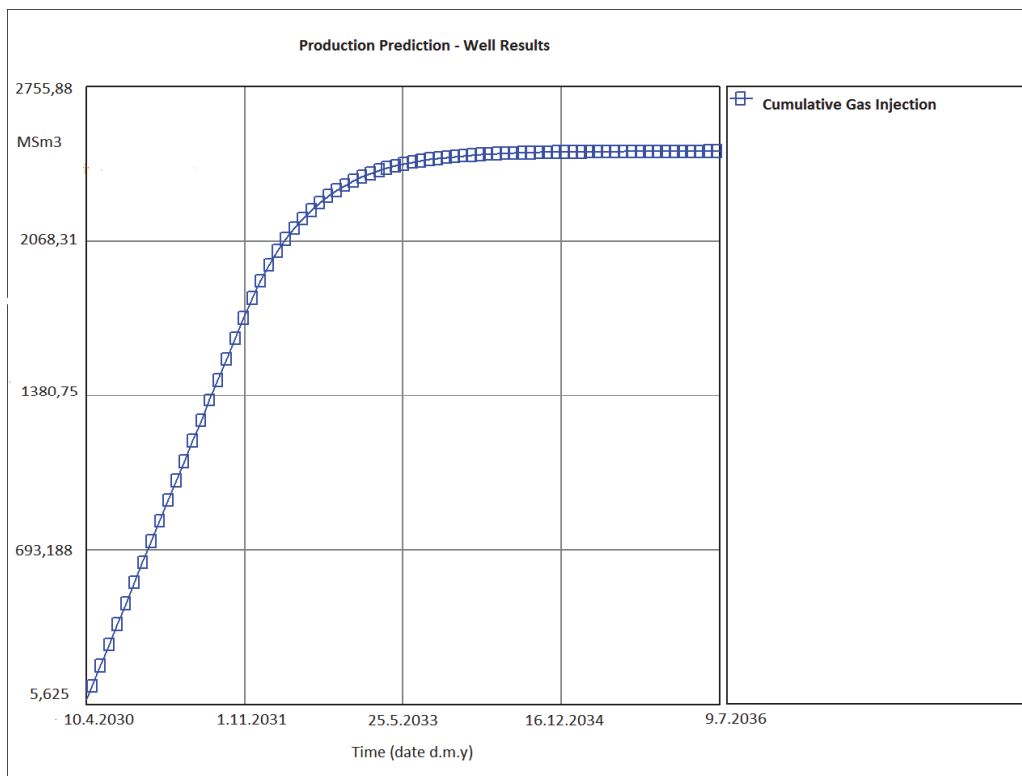


Figure 5: Cumulative of CO₂ injection versus reservoir pressure

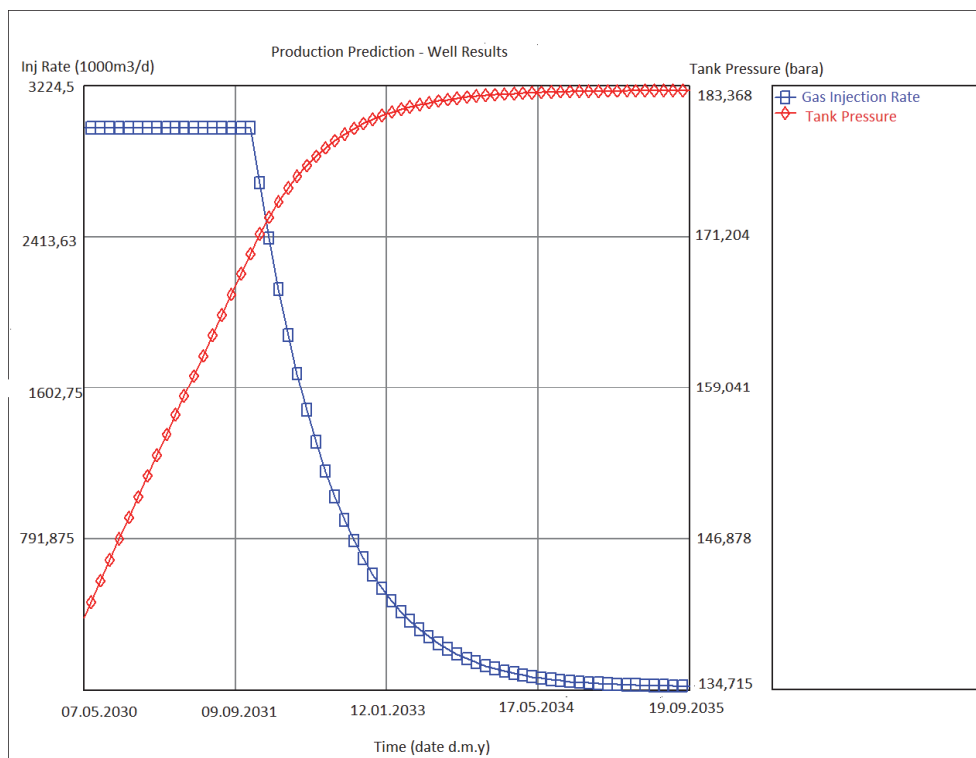


Figure 6 Tank pressure versus time during CO₂ injection phase.

5. DISCUSSION AND CONCLUSIONS

Considering EU target emission reduction targets and the fact that Croatia is a part of EU ETS, geological sequestration of CO₂ represents a perspective method for removal of CO₂ from atmosphere and local environmental protection.

The CO₂ injection within deplete oil fields (Ivanić and Žutica) would include CO₂ sequestration and additional fossil fuel production. About 3.5 billion t of CO₂ is planned to be injected into the Ivanić Field, but 50% of injected CO₂ will be recovered within hydrocarbons. Considering reservoir conditions at time of project termination, volume of CO₂ which can be potentially stored within the reservoirs of the Ivanić field amounting about 2.5 billion Sm³ is calculated, representing significant potential capacity for CO₂ storage.

6. REFERENCES

- GORIČNIK, B. & DOMITROVIĆ, D. (2003): Laboratorijska istraživanja primjenjivosti CO₂ procesa na naftnim poljima u Hrvatskoj [Laboratory Research of CO₂ EOR Potential in the Mature Oilfields in the Republic of Croatia – *In Croatian*]. Naftaplin, 1, 5–12.
- MALVIĆ, T. (2008): Production of Porosity Map by Kriging in Sandstone Reservoirs, Case Study from the Sava Depression. Kartografija i Geoinformacije, 9, 12–19.

- MALVIĆ, T. (2012): Review of Miocene shallow marine and lacustrine depositional environments in Northern Croatia. *Geological Quarterly*, 56/3, 493–504.
- NOVAK, K., MALVIĆ, T., VELIĆ, J. & SIMON, K. (2014): Increased hydrocarbon recovery and CO₂ storage in Neogene sandstones, a Croatian example: part II. *Environmental Earth Sciences*, 71, 3641–3653. doi: 10.1007/s12665-013-2756-6
- NOVAK ZELENKA, K. (2012): Deterministički i stohastičkigeološki modeli gornjomiocenskih pješčenjačkih ležišta u naftno-plinskom polju Kloštar [Deterministic and stochastic geological models of Upper Miocene sandstones reservoirs at the Kloštar oil and gas field – *in Croatian*]. –PhD Thesis, University of Zagreb, Faculty of Mining, Geology and Petroleum Engineering, Zagreb, 190p.
- NOVOSEL, D. (2005): Results of Testing Oil Displacement by Carbon Dioxide Injection into the Ivanić Oil Field [Rezultati projekta pokusnog istiskivanja nafte utiskivanjem ugljičnog dioksida na naftnom polju Ivanić– *In Croatian*]. *Naftaplin*, 1, 51-60.
- NOVOSEL, D. (2009): Impact of Carbon Dioxide on Ivanić Oilfield in Tertiary Oil Recovery Phase [Učinak ugljičnog dioksida u tercijarnoj fazi iskorištavanja naftnih ležišta polja Ivanić]. –PhD Thesis, University of Zagreb, Faculty of Mining, Geology and Petroleum Engineering, Zagreb, 162p.
- NOVOSEL, D. (2010): Učinak ugljičnog dioksida u tercijarnoj fazi iskorištavanja naftnih ležišta polja Ivanić [The effect of the carbon dioxide on the tertiary exploration phase at the Ivanić oil field – *In Croatian*]. *Nafta*, 61, 300–307.
- PERIĆ, M. & KOVAČ, S. (2003): Simulacijska studija procesa povećanja iscrpka nafte (EOR-procesa) istiskivanjem ugljik-dioksidom primjenom višekomponentnog modela COMP III [Simulation Study of Enhanced Oil Recovery Process by CO₂ injection Applying a Multi-component COMP II – *In Croatian*]. *Naftaplin*, 13–25.
- VELIĆ, J., MALVIĆ, T. & CVETKOVIĆ, M. (2011): Palinspastic reconstruction of synsedimentary tectonics of Neogene and Quaternary sediments in the Kloštar Field (Sava depression, Pannonian Basin, Croatia). *Zeitschrift der Deutsche Gesellschaft für Geowissenschaften*, 162, 193-201.
- VRBOŠIĆ, A., ŠKRLEC, M., NOVOSEL, D. & IVANOVIĆ, K. (2003): Naftno polje Ivanić 1963.-2003. [The Ivanić Oil Field 1963–2003 – *In Croatian*]. *Naftaplin*, 1, 1–4.

THE IMPACT OF SEDIMENTARY FACIES CHARACTERISTICS ON THE PETROPHYSICAL RESERVOIR PROPERTIES: LOWER CRETACEOUS NUBIAN FORMATION, SOUTH EAST SIRT BASIN, LIBYA

Omar SLIMAN,

Libyan Petroleum Institute, P.O.BOX 6431, Tripoli, Libya,

E-mail: oharaba59@hotmail.com

The purpose of this work was to study the reservoir rock characteristics and petrophysical properties in the Lower Cretaceous Nubian sandstone reservoirs. For this study, an important oil well of the SE of Sirt Basin, Libya was selected. In this well, the cored intervals of the Upper, Middle and Lower Nubian reservoirs were analysed. The relationships between facies characteristics and petrophysical reservoir properties were determined by analysing the effects of facies characteristics (sorting, grain size) on porosity, permeability, shale and sand fractions. The petrophysical data set including porosity and permeability came from laboratory. Analysis of 273 plugs of a 420 feet cored section was carried out. The volumetric shale and sand fractions originate from well log analysis. The processed cored intervals exhibit strong depositional facies controls (primary and secondary) on their porosity - permeability properties. The sandstones of meandering deposits showed the largest porosity and permeability values. Braided stream deposits showed moderate porosity and permeability values. The lacustrine deposits recorded the relatively low porosity and permeability values. The deposits of alluvial fan deposit sandstones were characterized by the worst properties.

Keywords: Reservoir characterisation, depositional facies, Lower Cretaceous, Nubian sandstone, Libya

1. INTRODUCTION

This study were conducted on the sedimentary rocks belonging to the Nubian Formation (Lower Cretaceous), penetrated in a well situated in South East Sirti Basin. The studied section was divided into three members as upper, middle and lower Nubian. The following paragraphs describe the sedimentary setting of each member briefly.

1.1. The Upper Nubian (UNS)

This member is divided into two environments. (1) First is the braided environment with thickness of 82 feet. It contains channel deposit with thickness ranging from 10 to 19 ft and overbank deposit with thickness ranging from 1 to 2 ft;(2) The second environment represents the meandering environments with thickness of 66.5 ft. It is described by four facies point bar deposit (from 5 to 12.5 ft), channel deposit (from 1.5 to 5 ft), crevasse splay deposit (from 2 to 14.5 ft) and levee deposit (from 1.5 to 4 ft).

1.2. The Middle Nubian (NM)

This consists of two environments. (1) First is the meandering environment with thickness of 110 ft. It contains five facies crevasse splay (from 6 to 10.5 ft),levee deposits (from 3 to 11.5 ft), point bar deposits (from 3 to 18.5 ft), flood plain deposits (from 3.5 to 6 ft), channel deposits (from 2 to 3.5 ft);(2) the second one is the lacustrine environment which is 34 ft thick.

1.3. The Lower Nubian (LNS)

The lower part is divided into meandering, braided, alluvial fan environments. The meandering group is 8 ft thick and contains two facies as the point bar deposit (7 ft) and flood plain deposit (1 ft). The braided environment consists of channel deposit (2.5-25.5 ft), over bank deposit (1-3.5ft), abandoned deposit (3ft). The whole thickness of this environment is 72.5 ft. The last environment of Lower Nubian part appears in 42.5 ft thickness and contains two facies. The sheet flood deposit changes between 1 and 10 ft thick and the thickness of deposit of stream channel changes between 1 and 6.5 ft.

2. METHODOLOGY

The goal of this study is to establish relationships between the deposited sandstones and petrophysical rock properties. The Porosity-permeability relationships of the routine core analyses (namely porosity and horizontal permeability measurements) come from 273 plugs. The processed intervals revealed 16 facies. The impact of the facies characteristics(primary and

secondary) on this relationship were examined by facies texture (grain size, sorting) and facies lithology (shale volume).

The shale volume computed from the following formula:

$$GR_{meas} = GR_{shale} * V_{shale} + GR_{clean\ sand} * (1 - V_{shale}),$$

where:

V_{shale} is the shale volume;

GR_{meas} is the gamma ray response in the zone of interest;

$GR_{clean\ sand}$ is the gamma ray response in a shale-free zone of the same zone;

GR_{shale} is the gamma ray response in 100 percent shale.

The correlation of porosity and permeability were presented by scatter-plot. These correlations were analysed in each case of sedimentary facies of all reservoir units separately. The scatter-plots showed that the cloud of points arranged in a two-dimensional plane. The correlation of the porosity and permeability was coded by facies attribute which is suitable for investigating the reservoir quality. The quality of this correlation is determined by the correlation coefficient value given by the scatter-plot.

3. RESULTS

The porosity-permeability relationships were interpreted according to the applied methodology which were analysed by scatter plots. The sediment grain size classes of the processed interval, from the Nubian formation were described on the bottom borehole cores and could be categorized into grain sizes. The shale volume (vsh) from the quantitative interpretation of the gamma ray log was classified according to the obtained values into four classes. These classes are the follows:

Class1 when vsh (0.0;0.1) interval, class2 when vsh (0.1;0.15), class3 when vsh (0.15;0.20), class4 when vsh (0.2;0.25).

The deposit of *levee facies* is characterized by mainly of mudstones variably silty and the average porosity is 0.095; the average permeability is 2.341mD.

In the *channel facies* the sandstones showed high reservoir qualities. It means 0.118 averages porosity and 2.529 mD averages permeability. This good quality can be explained with the generally better sorting. This deposit is described by fine average grain size and lack of muddy laminations.

The sandstones in the *over bank facies* show also high reservoir qualities. The porosity average is 0.12 and the average value of permeability is 3.060 mD. These sandstones are fine grained, moderately sorted and altered with mud lamination sporadically.

The *point bar facies* consists of medium to fine grained sediment with 0.1 average porosity and 2.033 mD average permeability. This deposit contains locally scattered pebble grains and mudclasts and it is slightly argillaceous. *Channel meandering deposits* comprises medium grained scattered pebbles but only locally, slightly argillaceous and mud clasts are often in the sediment. This deposit is characterized by 0.121 porosity values and 4.405 mD permeability.

The *facies of crevasse splay* deposit is generally sandstone with very fine to medium grain size and with relatively high content of argillaceous. The character of this facies is described by 0.0713 average porosity values and 1.814 mD permeability.

The *facies of flood plain deposit* is generally mudstone which alternate with silt. The main porosity is similar than in the facies of crevasse splay, so it is 0.0792 but with lower permeability. The average permeability is 1.461 mD.

In the *lacustrine deposits* the silt and mudstone alternate. These deposits are characterized by 0.109 main porosity and 0.729 mD permeability.

The *stream channel facies* was characterized by normal graded sandstone with small to larger pebble grain size. It contains locally argillaceous medium to coarse sand matrix, mud clasts. The sorting is not uniform, the poor and moderate sorting varies. This sorting and relatively large grain size implies that the average porosity is very low, only 0.05 generally and the average permeability is 1.311 mD.

The facies of sheet flood deposit consists of sandstones. The grain size of this deposit is mostly very fine but locally reaches the medium grain size. These sandstones contain sporadically granules and it is also slightly to highly

argillaceous and micaceous. The porosity in this deposit is also very low, only 0.053 average but the permeability relative large, 2.048 mD.

4. DISCUSSION

All facies were characterized by their texture and petrophysical properties. The characteristics of these facies could be revealed and conclusion was drawn about the quality of each facies for being a potential reservoir rock or not. **Table 1** summarizes the most important petrophysical properties of each facies in all reservoir units.

Table 2: *Petrophysical properties of facieses*

Reservoir unit	Facies	Thickness (ft)	Average porosity	Average permeability(mD)
Upper Nubian	Channel braided deposit	74	0.126	2.66
	Over bank deposit	8	0.131	4.44
	Point bar deposit	30.5	0.109	2.47
	Channel meandering deposit	10.5	0.121	4.40
	Crevasse splay deposit	16.5	0.076	4.51
	Levee deposit	9	0.109	4.21
Middle Nubian	Point bar deposit	41	0.087	1.64
	Crevasse splay deposit	34.5	0.076	0.86
	Levee deposit	20.5	0.072	0.88
	Flood plain deposit	8.5	0.076	1.31
	Lacustrine deposit	34	0.109	0.73
Lower Nubian	Stream channel deposit	18	0.050	1.31
	Sheet flood deposit	24.5	0.053	2.05
	Channel braided deposit	61	0.106	2.34
	Over bank deposit	8.5	0.106	1.86
	Abandoned Channeldeposit	3	0.085	5.58
	Point bar deposit	7	0.127	2.64
	Flood plain deposit	1	0.093	2.24

The permeability and porosity correlation showed that this relationship is strongly controlled by the facies characteristics. It was analysed by several cross-plots which constructed for permeability versus porosity and coded by grain size classes and shale volume categories. This relationship cloud be clustered into several levels depending on the value of the correlation

coefficient. The regression model was also performed. The location of each point on the cross-plot was related to the regression line. The distance of scattering can be explained by the sediment grain size and the shale content of the subject point. Tables 2-4 summarize the controls on the permeability-porosity relationship for each recognized facies.

Table 3: *Facies characterization in the the Upper Nubian deposits*

Reservoir unit	Facies	Facies characteristics
Upper Nubian	Channel braided deposit	The sandstone is mostly fine to very coarse, slightly silty, moderately sorted, and locally slightly argillaceous.
	Over bank deposit	The sandstone is mostly fine to very coarse sandstone slightly silty, well sorted, highly argillaceous.
	Point bar deposit	Medium sandstone is mostly fine to very fine sandstone, moderately sorted, clean sandstone to slightly argillaceous.
	Channel meandering deposit	It consists of well sorted medium grained sandstone, clean to slightly argillaceous.
	Crevasse splay deposit	The sandstone is mostly fine to medium, locally medium to coarse, slightly silty and moderately sorted highly argillaceous
	Levee deposit	This facies consists of sandstone mostly fine to very fine, locally medium slightly silt, well sorted, clean to slightly argillaceous

Table 4: *Facies characterization in the the Middle Nubian deposits*

Reservoir unit	Facies	Facies characteristics
Middle Nubian	Point bar deposit	This facies consists of, medium to very fine sandstone with coarse silt, moderately sorted, clean to argillaceous
	Crevasse splay deposit	Consists of sandstone mostly medium to very fine slightly medium to coarse silt, poorly sorted, highly argillaceous
	Levee deposit	Very fine sandstone with medium to coarse silt, poorly sorted, highly argillaceous
	Flood plain deposit	Fine to medium silt, poorly sorted, highly argillaceous
	Lacustrine deposit	Medium sandstone with medium to fine silt, poorly sorted, highly argillaceous

Table 5: *Facies characterization in the the Lower Nubian deposits*

Reservoir unit	Facies	Facies characteristics
Lower Nubian	stream channel deposit	Mostly medium to coarse sandstone, locally medium size pebbles, poorly sorted, highly argillaceous
	Sheet flood deposit	Fine to very fine sandstone locally medium size pebbles, with medium to coarse silt, moderately sorted, highly argillaceous
	Channel braided deposit	Mostly fine to medium sandstone, slightly coarse to very coarse sandstone, locally granular, slightly silty, moderately sorted, clean to slightly argillaceous
	Over bank deposit	Medium to coarse silt with very fine sandstone, poorly sorted, highly argillaceous
	Point bar deposit	Fine to very fine sandstone, locally fine silt, poorly sorted, clean.

5. CONCLUSION

Regarding the texture and petrophysical characteristics of all the studied facies from the upper, middle and lower Nubian sandstones we can conclude that the Upper and lower Nubian intervals are composed the most favorable facies to be considered as good potential reservoir rocks. Those facies are namely channel braided deposits, point bar deposits, channel meandering deposits and stream channel deposits.

Porosity-permeability relationships are strongly related to the primary and the secondary sedimentary process which are represented by grain size grading(primary controls) and the dispersed clay minerals precipitated in the pores network(secondary controls).

6. REFERENCES

- NELSON, P.H. (1994): Permeability-Porosity Relationships in Sedimentary Rocks, The Log Analyst, pp.38-62.
- MORSE, D.G. (1994): Siliciclastic Reservoir Rocks, AAPG Memoir 60, pp. 121-139.
- BEARD, D. AND WEYL, P. (1973): Influence of texture on porosity and permeability of unconsolidated sands, AAPG Bulletin. 57, pp. 349-369.
- HOOK, J., R., (2003): An Introduction to Porosity, PETROPHYSICS, VOL. 44, NO.3, PP.205-212.
- PATTERSON, D. and PRENSKY, S. (2007): Petroleum Engineering and Petrophysics, Volume V (a), Chapter 3C, from the Petroleum Engineering Handbook, Editor, Edward Holstein.
- SHOUXIANG, M. and MORROW, N. R. (1996): Relationships between Porosity and Permeability for Porous Rocks, International Symposium of the Society of Core Analysts, Paper Number 9610.
- KATZ, A.J. And THOMPSON, A.H. (1986): Quantitative Prediction of Permeability in Porous Rock, *Physical Review B*, v.34, 8179-81.
- MONICARD, R. P. (1980): Properties of Reservoir Rocks: Core Analysis. Gulf Publishing Co., Houston, TX.
- BLOCH, S. (1991): Empirical prediction of porosity and permeability in sandstones, American association of petroleum geologists, AAPG Bulletin. Vol.75 No.7, pp. 1145-1160.

PETROPHYSICAL AND HYDRODYNAMICAL INVESTIGATION OF UNCONSOLIDATED ROCKS - MEASUREMENT VS. EMPIRICAL ESTIMATION

Judit HORVÁTH^{1*}, Péter KORONCZ¹, Ferenc FEDOR¹

¹GEOCHEM Ltd. 55/1 Viola str. Kozármisleny, H-7761

*horvath.judit@geochem-ltd.eu

Regarding sustainable geothermal energy utilization, the knowledge of texture and petrophysical features of unconsolidated, Upper Pannonian aquifers is fundamental in planning well completion and injection technology. In a complex petrophysical analysis, among others grain size distribution, porosity, permeability and acoustic velocity were measured to characterize and estimate in situ features of Upper Pannonian formations. In case of unconsolidated rocks, it is problematic to form and measure rock plugs, thus the estimation of porosity and permeability values are often done by empirical formulae. Certain measurements can only be performed in dry or air dry state due to the stability of rocks, so parameter recalculation is needed to the saturated state. Besides presenting the results, this article deals especially with revealing the correspondence among physical parameters and their estimation potential, as well as with the applicability and limits of empirical connections used in hydrogeology.

Keywords: unconsolidated, sandstone, porosity, permeability, acoustic velocity

1. INTRODUCTION

One of the goals of a running project entitled “Well completion technology development of sustainable geothermal energy utilization I.” is the petrophysical and rock mechanical qualification of Upper Pannonian unconsolidated sandstones affecting well completion and water reinjection. Related to the project, several complex petrophysical measurements were performed despite of the following problems:

(1) The small amount of cement minerals in the formation caused several problems concerning plug drilling and the measurement of porosity, permeability and rock mechanical properties. The estimation of these parameters, especially of permeability, based on known empirical equations is questionable. (2) The most adequate information on petrophysical properties came from the measurement of saturated core plugs. However, in most cases flooding destroyed the plugs. (3) In order to make the acoustic parameters measured on dry plugs comparable with well log data (in situ), the modifying

effect of the saturation fluid on wave velocity has to be taken into consideration. The reference on the saturated state during the acoustic measurements was produced by the Gassmann static correlation (Gassmann 1951). (4) Since the well-logging survey did not produce any porosity logging, there was a need to estimate porosity from the available logs (SP, Resistivity and Natural Gamma (NG)).

2. DESCRIPTION OF THE FORMATION, SAMPLING

The unconsolidated cores came from well Bánk-2, NE Hungary. The laboratory samples were taken dominantly from the lower section of the drilled formation (1190-1270 m below sea level). Hence, the results are representative only of the well-location (Horváth et al., 2013).

In the studied interval, the gamma log suggested a definite upward coarsening and thickening sequence. From this interval, core plugs with 1" and 1,5" diameter were formed. Residual debris was disaggregated for grain size analysis with distilled water, without added chemicals.

3. METHODS

Grain size analysis was carried out by using CILAS 1180 with laser diffraction method. For the numerical interpretation the Fraunhofer equation was applied (Cilas, 2004). The samples were exposed to 240 s before the measurement, and during it they were affected by ultrasound. For the sake of representativity, 3-5 measurements were made per sample. Obscuration level was maximized at 35% (Mingard et al, 2009).

Matrix volume was measured with Quantachrome Pentapyc 5200e He-pycnometer at 25°C. For measuring gas permeability Coreval 700 was used, working on the basis of the pressure fall-off method (API, 1998). In case of radial samples and axial samples, the applied confining pressure was 30 and 50 bar, respectively. The self-developed RS-PPD permeameter served for water permeability measurements.

An AVS 700 instrument, working on the basis of pulse transmission method measured acoustic wave velocity. The applied confining pressure was the same than in the case of permeability measurements. For the determination of time of flights AIC program was used with both P- and S-waves (Akaike, 1973; Nagy et al, 2013). Rock mechanical parameters were calculated from P- and S-wave velocities.

Altogether 84 grain size analyses were performed. Porosity was measured on 68 plugs, gas permeability on 65 dried plugs, acoustic measurements on 50 dry plugs. In addition, attempts were made to measure the saturated state.

3.1 Applicability of the possibilities of permeability estimation

According to grain size analysis, 19 clayey silt, 16 silt, 21 sandy silt, 27 silty sand and 1 sand samples were classified, i.e. mud formations were sampled as well. The statistical indicators of parameters considered below are shown in **Table 1**. Regarding classification according to rock type, the majority of parameters show several modes.

Table 6 The statistical parameters of the main properties

	Mean	Min	Max	Standard Deviation	Modus 1	Modus 2
d20 (mm)	15.19	1.6	64.2	15.3	6-7	4-5
d50 (mm)	65.427	4.3	281.19	69.249	4-5	2-3
d90 (mm)	148.02	12.48	451.26	140.98	4-5	1-2
clay (%)	13.497	3.575	47.06	9.043	5-10	-
fine silt (%)	21.553	5.189	50.21	12.373	5-10	15-20; 25-30
coarse silt (%)	34.591	4.411	62.977	16.322	10-15	35-40; 50-55
very fine sand (%)	12.824	0	44.043	12.739	0-5	40-45
fine sand and coarser (%)	17.534	0	73.062	26.081	0-5	60-65
sorting	64.857	5.132	196.77	64.223	0-25	175-200
measured porosity (%)	28.63	12.03	38.23	6.59	30-35	15-20
calculated porosity (%)	28.3164	25.52	34.59	1.95416	25-30	-
permeability mD	574.59	0.18	2005.72	668.5	0-500	1000-1500

For the sake of comparison, porosity was also calculated from grain size data by using the method introduced by Vukovic and Soro (1992). The range of calculated porosity was 25-35% that coincided with the mode of the measured porosity set (**Figure 1**). The core (measured) porosity showed a bimodal, while a calculated one exhibited an unimodal distribution. (**Figure 1**). There was a negative relation between the measured and calculated porosity values (**Figure 2**). This resulted from the fact that there was not the suspected negative exponential relationship between the uniformity coefficient and porosity. Instead, a weak, positive correlation ($r=0.688$) was found between them.

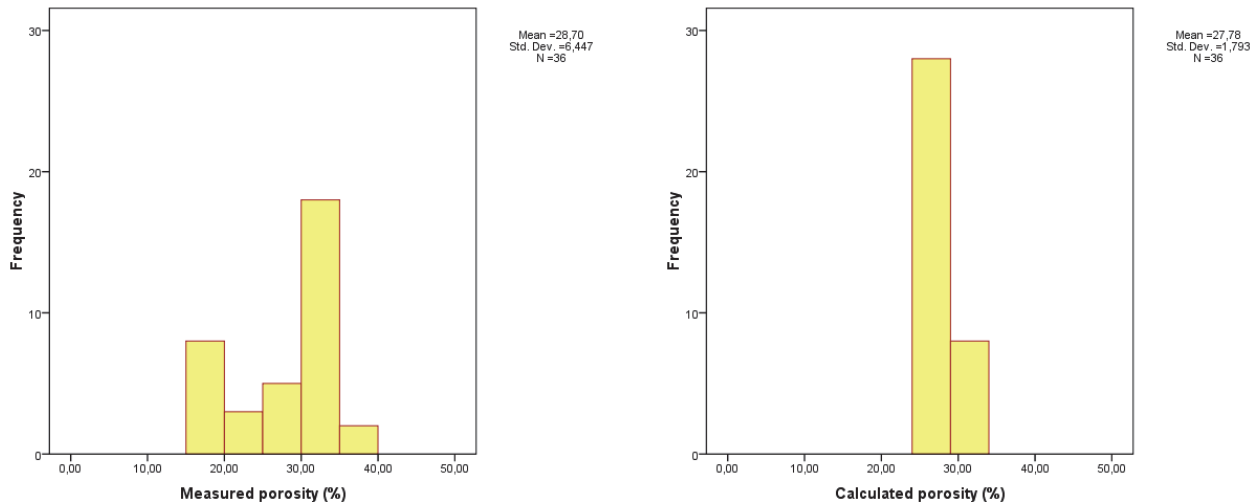


Figure 8 Histogram of measured (left) and predicted porosity (right)

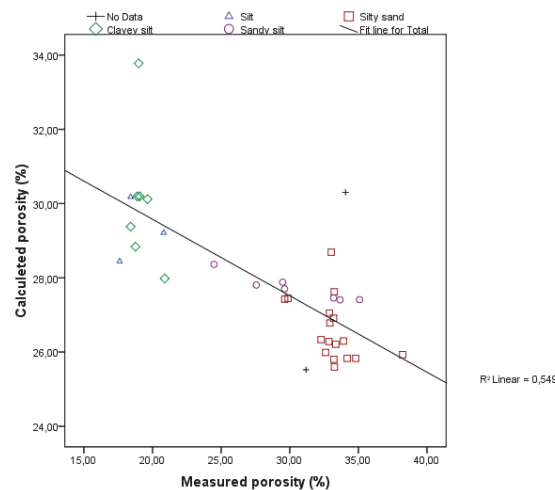


Figure 9 Crossplot of predicted and measured porosity
 ($r=-0,741$, $p < 0,05$)

In general, permeability decreases with grain size (**Table 2**). The observed negative correlation arises from the definition of the phi unit ($\phi = -\log 2d$). Although the most common fraction was coarse silt (**Table 1**), clay and fine silt content have much more influence on permeability. Linear correlation increased when the natural logarithm of values was taken into account (**Table 2, Figure 3**). Theoretically, there is a strong relationship between permeability and the fine and coarser sand fractions. Unfortunately, some samples lacked this grain size interval, thus it was not considered in further calculations.

Table 7 Correlation coefficients between the logarithm of permeability ($\ln(k)$) and grain size parameters

N=35	clay	Inclay	fine silt	Infsilt	coarse silt	very fine sand	fine sand and coarser	d ₅₀	d ₂₀
$\ln(k)$	-0.789	-0.895	-0.885	-0.938	-0.603	0.334	0.878	-0.938	-0.922
	0.00	0.00	0.00	0.00	0.00	0.05	0.00	0.00	0.00

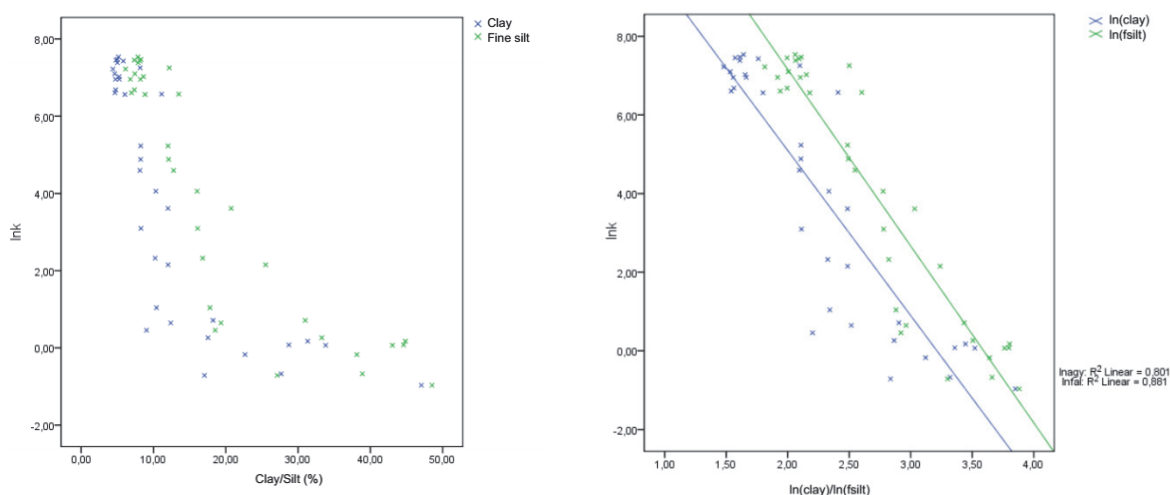


Figure 10 Relationships of permeability with clay and silt content and their common logarithms ($\ln(k)$: logarithm of permeability; $\ln(\text{clay})$ logarithm of clay; $\ln(\text{fsilt})$: logarithm of fine silt)

Measured and calculated permeability values were available for several samples. The calculations were carried out by using the general equation introduced by Vukovic and Soro (1992). In fact, there were several orders of difference (underestimation) between them. The standardized residuals did not show the desired random distribution. Moreover, in certain equations, they had negative relationship with the standardized permeability values. For this situation there is a general view to make correction using regression analysis. When applying this approach, we found that the estimated and measured values became the same order of magnitude, whereas the residuals showed bimodal distribution (**Figure 4**). Consequently, in our experience, the error cannot be estimated.

In the multi-variable approximation of permeability the natural logarithm of following variables were taken into consideration: Zunker porosity ($\ln zunker$), sorting ($\ln sort$), fine silt ($\ln fsilt$), clay fraction ($\ln clay$) and the square of porosity value and d_{20} grain diameter given in phi unit. The results are shown in **Table 3**. The permeability values calculated this way were usually higher than the measured ones, and in nearly half of the cases the residuals showed

bimodal distribution. The best approach seemed to be the equation E' with respect to R² and p-p plots.

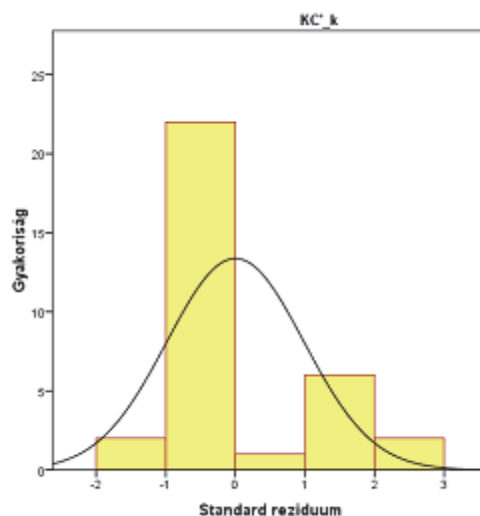


Figure 11 Histogram of the standard residual after regression in case of Kozeny-Carmen equation

Table 8 The results of multiple regression analysis for estimating permeability of Upper Pannonian Unconsolidated Sandstone

Model	lnk	k (mD)
A'	$2.56 \ln zunker + 2.012 \ln sort$	$zunker^{2.56} \times sort^{2.012}$
B'	$15.591 + 2.361 \ln zunker - 3.4 \ln fsilt$	$e^{15.591} \times zunker^{2.361} \times fsilt^{-3.4}$
C'	$13.632 + 3.305 \ln zunker - 2.784 \ln clay$	$e^{13.632} \times zunker^{3.305} \times clay^{-2.784}$
D'	$15.623 + 2.912 \ln zunker - 1.374 d_{20}$	$e^{15.623 - 1.374 d_{20}} \times zunker^{2.912}$
E'	$1.646 \ln sort - 0.805 d_{20}$	$e^{-0.805 d_{20}} \times oszt^{1.646}$
F'	$-6.134 + 2.160 \ln sort$	$e^{-6.134} \times oszt^{2.160}$
G'	$11.932 + 20.937 \varphi^2 - 3.531 \ln fsilt$	$e^{11.932 + 20.937 \varphi^2} \times fsilt^{-3.531}$
H'	$8.381 + 29.534 \varphi^2 - 2.953 \ln clay$	$e^{8.381 + 29.534 \varphi^2} \times clay^{-2.953}$
I'	$11.126 + 25.768 \varphi^2 - 1.445 d_{20}$	$e^{11.126 + 25.768 \varphi^2 - 1.445 d_{20}}$

3.2 Acoustic velocity measurements

Acoustic velocities measured on dry plugs under laboratory conditions were lower than in situ log results. The greatest difference was in case of high porosity samples. For the comparison of data with geophysical measurement results, the results measured in dry state have to be corrected with the effect of saturation.

Figure 5 shows the comparison of compression and shear wave velocity values measured on dry samples and modified by the Gassmann equation with

the geophysical well logs. The compressibility velocities deduced from the Gassmann equation are closer to the log interpretation.

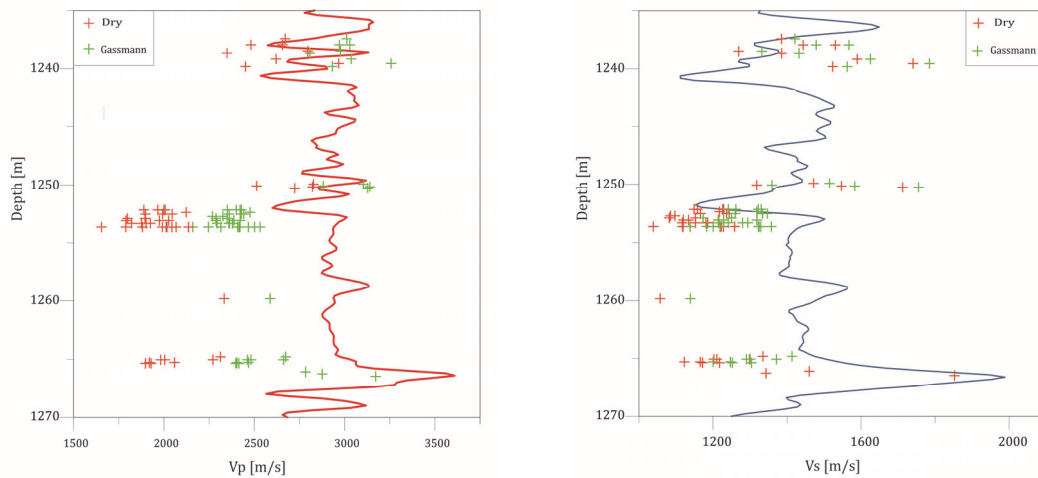


Figure 12 Compression and shear wave velocities measured on dry plugs and corrected by the Gassmann formula

Saturation had a smaller effect on shear wave velocity. The experience was that after recalculation to the saturated state, the V_p/V_s ratio showed smaller difference with well log data. (**Figure 5**)

3.3 Log measurement results

In those samples, where the textures were less affected by formation damage, a strong correlation could be observed between the porosity values calculated from NG and corrected density log ($r = 0,905$). The corresponding linear regression was $\varphi = 33,316 - 22,304 \cdot IGR$, where IGR is the normalized form of the natural gamma log.

The lower and upper 'bounding' function of the above equation ($p=0.05$) is as follows: (1) $\varphi = 32,934 - 23,041 \cdot IGR$, and (2) $\varphi = 33,698 - 21,566 \cdot IGR$. Based on the regression equation, in the same depth interval there may arise a possibility for the approximate estimation of porosity in case of wells, where there is no information available about porosity.

4. SUMMARY

Summarizing the results, following observations and suggestions can be made: While estimating the permeability value with empirical formulae, several orders of magnitude difference was detected. Correction with regression analysis decreased this difference, but the error could not be estimated due to the bimodal distribution of residuals. Several attempts were made to create a more exact empirical formula, but the too strong correlation relationships between independent variables constitute a problem when applying multivariable

regression. Also, errors showed multimodal distribution in that case as well. Increasing the number of samples would provide a possibility for measurement according to rock type, but further analysis of texture parameters is needed. Comparing the acoustic features measured in the laboratory and on the field, the results derived from the Gassmann formula from dried samples in saturated state approximated the geophysical results.

Strong correlation could be observed between natural gamma and corrected density log, except the damaged zones. With empirical equation based on regression analysis between the two variables, it is possible to estimate porosity from the GR log in drillings of the well site, when no porosity log is available.

5. ACKNOWLEDGEMENT

The presented studies were parts of GOP-1.1.1-11-2012-0033 project. The authors would like to thank József Csicsák for his support related to the project, Miklós Hlatki and János Geiger for the professional advices, Alexandra Nagy for developing the programs assisting the interpretation of acoustic and grain size distribution measurements and Tímea Streicher for her valuable assistance.

6. REFERENCES

- AKAIKE, H. (1973): Information theory and an extension of the maximum likelihood principle. –In B. N. Petrov and F. Csaki (Eds.), Second international symposium on information theory. Akademiai Kiado, Budapest, 267-281
- AMERICAN PETROLEUM INSTITUTE, (1998): Permeability determination in Recommended Practice for Core Analysis, API Publishing Services, Washington D.C, 2005
- Blott, S. J., Pye, K., (2001): Gradistat: A Grain Size Distribution and Statistics Package for the Analysis of Unconsolidated sediments, Earth Surf. Process. Landforms 26, 1237-1248
- CILAS S.A., (2004): Particle Size Analyser, User manual, www.particle-size-analyzer.com
- HORVÁTH, J., KORONCZ, P., FEDOR, F., HLAKTKI, M. (2013): Felső-pannon konszolidálatlan homokkövek kőzetfizikai, kőzetmechanikai vizsgálata. – In: Mérnökgeológiai-Kőzetmechanika 2013, 229-240.
- MINGARD K., MORELL R., JACKSON P., LAWSON, S., PATEL, S., BUXTON, R., (2009): Measurement Good Practice Guide No. 111: Good Practice Guide for Improving the Consistency of Particle Size Measurement, National Physical Laboratory, 66
- NAGY A., FEDOR F., FEURER V., (2013): Purpose and Limits of Automation in Laboratory Practice, 5th HR-HU and 16th HU Geomathematical Congress „Geomathematics as Geoscience”, Mórahalom
- VUKOVIC, M., SORO, A., (1992): Determination of Hydraulic Conductivity of Porous Media from Grain-Size Composition. Water Resources Publications, Littleton, Colorado

SATELLITE BASED SOIL MOISTURE ESTIMATES FOR AGRICULTURAL DROUGHT PREDICTION

Van LEEUWEN Boudewijn^{1*}, TOBAK Zalán¹, LADÁNYI Zsuzsana¹, BLANKA Viktoria¹,

¹Department of Physical Geography and Geoinformatics University of Szeged
Egyetem utca 2-6, 6721 Szeged, Hungary, *leeuwen@geo.u-szeged.hu

The combined trend of higher average temperatures and less summer precipitation predicted by climate models makes the Great Hungarian Plain susceptible to future droughts. The continuous estimation of soil moisture at regional scale allows for monitoring of the development of the water content in the soil. The trend and direction can be used as early warning for future droughts. In this study, a method is presented for the estimation of soil moisture based on MODIS satellite data. Point clouds are generated showing the relationship between vegetation cover and land surface temperature (LST). The point clouds are classified based on vegetation cover intervals and a linear relationship between LST and soil moisture is determined. The relative SMI values are compared to absolute local soil moisture measurements. Continuous calculation of the SMI provides trend information on the development of soil moisture, which can help to predict future periods of drought.

Key words: *soil moisture, land surface temperature, NDVI, MODIS*

1. INTRODUCTION

Soil moisture plays a key role in the global energy and water cycle (Patel et al., 2009; Wang, 2008). The continuous estimation of soil moisture allows for dynamic monitoring of the development of the water content in the soil. The trend and direction can be used as early warning for future droughts or inland excess water. Even though soil moisture is an important parameter in many applications, widespread and/or continuous measurements of soil moisture are rare (Patel et al., 2009). Another problem is the limited possibility for upscaling of point measurements to larger areas. These problems can be solved using remotely sensed data. Remote sensing observations cover large areas and can be executed with a high temporal resolution.

Largely, two groups of remote sensing based techniques for soil moisture estimation exist. The first uses data from passive microwave instruments. The method is based on the large difference in the dielectric properties of liquid water (~ 80) and dry soil (< 4). The dielectric constant is inversely proportional to the soil emissivity. The soil emissivity can be derived from the microwave satellite data (Owe et al., 1992; Schmugge et al., 2002; Wang, 2008). The advantage of the method is that it has a solid physical basis and that the data

can be collected in all-weather circumstances. Drawbacks are the low resolution of the current passive microwave sensors and the strong disturbance of vegetation to the method (Wang, 2008; Vicente – Serrano et al., 2004).

The other group of techniques uses a combination of data collected in the visible, near-infrared and thermal infrared part of the electro-magnetic spectrum. The visible and near-infrared bands are used to derive the relative amount of vegetation, which is often expressed by the Normalized Difference Vegetation Index (NDVI) or the fractional vegetation cover (F_r). The thermal data is used to calculate the land surface temperature (LST). The basic assumption of these methods is that thermal differences in areas with similar vegetation cover are the result of changes in their soil moisture (Vicente-Serrano et al., 2004). Many authors have successfully derived soil moisture estimates based on this principle. For example, Patel et al. (2009) found a strong and significant relationship when comparing surface moisture based on the vegetation-surface temperature space and in-situ measured soil moisture, and Mallick et al. (2009) used ASTER and MODIS data to create LST-NDVI spaces and to evaluate their usefulness for soil moisture estimates. They found a fair correlation with microwave sounding measurements from AMSR-A for areas with less vegetation. Advantages of these methods are that they are relatively simple and that the base data is available at global level and at medium spatial and high temporal resolutions.

There are several limitations to the LST-NDVI space based soil moisture estimates. A study area may not cover the full range of vegetation classes (from bare soil to well-developed dense vegetation), and therefore the LST-NDVI space may not be fully determined. Furthermore, since the method is based on remotely sensed LST data only the top few millimetres to 1 cm of soil moisture are “measured”, although via the vegetation indirectly also the root moisture is taken into consideration. Also LST and NDVI values derived from satellite imagery may include errors which can propagate into the SMI calculation (Carlson, 2007; Mallick et al. 2009).

The aim of this study is to develop a workflow for the dynamic estimation of soil moisture to analyse the water balance at medium scale on the Great Hungarian Plain using MODIS satellite data. Therefore, a fully automatic procedure was developed based on ArcGIS geoprocessing functionality and several Python programs to process MODIS vegetation and land surface temperature satellite data to soil moisture index maps. This article describes the workflow and presents the first results.

The Moderate Resolution Imaging Spectroradiometer (MODIS) has 36 bands covering the visible to thermal parts of the electromagnetic spectrum with spatial resolutions ranging from 250 to 1,000 meter. Many different products

have been derived from the raw data and are made available free of charge. For this study, three Vegetation indices (MOD13) and 36 Land surface temperature and emissivity (MOD11) images were used, covering the period from 1 March 2014 until 6 April 2014. Every image covers an area of about 1,100 x 1,100 kilometre.

2. STUDY AREA

The study area is a cross border area covering the South of the Great Hungarian Plain and Vojvodina, Serbia (**Figure 1**). It mainly consists of agricultural areas but there are also several urban centres in the area, namely Szeged and Novi Sad. The Tisza and Danube are the main rivers crossing the area. In the North-East part of the study area mostly sandy soils can be found, while in the rest of the area a complex mixture of alluvial meadow soils and chernozems occur. The climate is moderate continental, with cold winters and hot and humid summers with a large range of extreme temperatures and non-equal distribution of rainfall (Péczely, 1998; Jovanović et al. 2013).

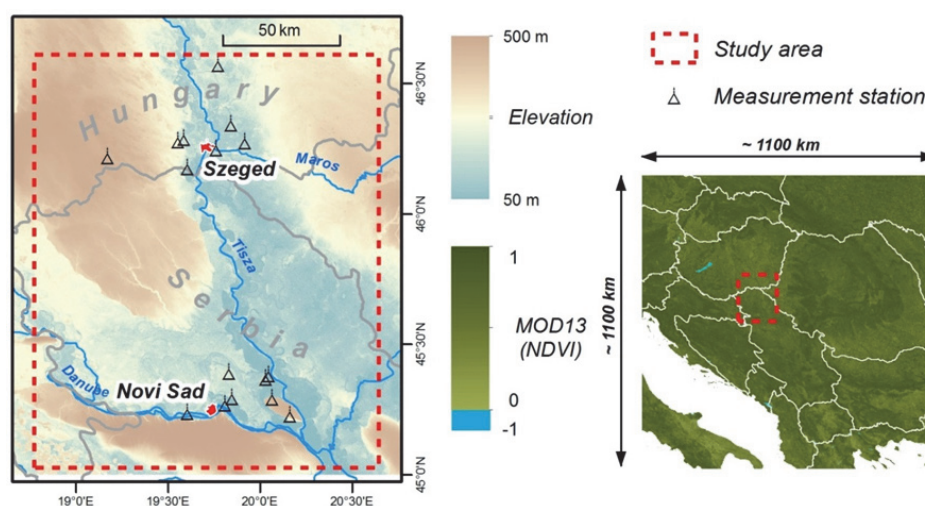


Figure 1: A MODIS NDVI image (right) and the study area (left)

3. METHOD

The base data for the soil moisture index estimate (SMI) workflow are Vegetation indices (MOD13) and Land surface temperature and emissivity (MOD11) products. After registration, these can be downloaded free of charge from the USGS Earth Explorer website. For this study, the MOD13A1 product is used which consists of – among others – a Normalized Difference Vegetation Index (NDVI), an Enhanced Vegetation Index (EVI) and a data quality (QA) layer. These data sets are composed of 16 days of measurements in the blue, red and near infrared spectral bands and have a spatial resolution of 500 meter. Both indices are computed from atmospherically corrected bi-directional surface reflectances that have been masked for water, clouds, heavy aerosols,

and cloud shadows. The QA layer is a binary coded file where for every pixel information is provided about the pixel reliability. The second input data set is the MOD11A1 product, which contains – among others – a layer with daily land surface temperatures (LST) at 1 kilometre resolution. The temperatures are retrieved by the split-window algorithm. This product also comes with a QA layer.

The first step of the SMI workflow is importing the NDVI and QA layers from the MOD13A1 product. From the QA layer, all pixels with codes 2112, 2116 or 2120 are extracted and converted to a mask map. Using the mask, only those NDVI pixels are extracted that are of “good quality”. The original NDVI data is stored in 16 bits ranging from -2,000 to 10,000, and therefore all masked pixels are multiplied by a scale factor to get the values back to the -1 to 1 range. Finally, a spatial subset of the data set is extracted to match the research area.

In the next step, the NDVI data is normalized to eliminating negative values and create an index between 0 and 1:

$$N = \frac{NDVI - NDVI_{min}}{NDVI_{max} - NDVI_{min}} \quad (1)$$

Gilles et al. (1997) established the relationship $F_r \approx N^2$, where F_r is the so-called fractional vegetation cover. The LST and F_r form a theoretical triangular shaped space, where the wet areas form the lower boundary of the space and the dry areas the upper diagonal (Vicente – Serrano et al., 2004; Carlson, 2007; Mallick et al., 2009; Patel et al., 2009) (**Figure 2**).

In the next step, the N map is transformed to a F_r map and – by reclassifying the F_r values into equal intervals – 10 sub maps with increasing vegetation thicknesses are created.

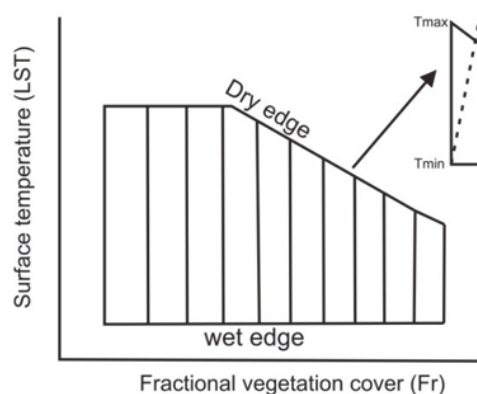


Figure 2: Theoretical triangular LST- F_r space (based on Vicente – Serrano et al., 2004)

In the next part of the workflow, the LST map is preprocessed. The original day time land surface temperature values are imported from the MOD11A1 data set and masked based on the QA layer, where all pixels with a value of 0, indicating nominal data are selected as useful data. In many LST files, large

areas are excluded, because LST values were not produced due to clouds. The masked LST values are multiplied with the scale factor to receive temperatures in degrees Kelvin. Then, the LST data with a spatial resolution of 1,000 meter is resampled to match the 500 meter resolution and geometry of the NDVI data. Finally, a spatial subset covering the research area is created from the LST data.

The presented method assumes a linear relationship between the LST and the soil moisture within one F_r class, therefore for every F_r map the pixel with the lowest and highest values are extracted from the LST map. The pixel with the lowest LST value in a particular F_r class gets a soil moisture value of 1 and the pixel with the highest LST gets a soil moisture value of 0. The soil moisture value SMI for F_r map i for the intermediate pixels was calculated by:

$$SMI_i = \frac{LST_{min} - LST}{LST_{max} - LST_{min}} + 1 \quad (2)$$

This results in a SMI map for each of the 10 F_r maps. In the final step, all SMI_i maps are combined to form the SMI map for the total study area (**Figure 3**). This map shows the spatial distribution of soil moisture in the area at a particular moment in time, where the 0 indicates the lowest soil moisture and 1 the highest soil moisture.

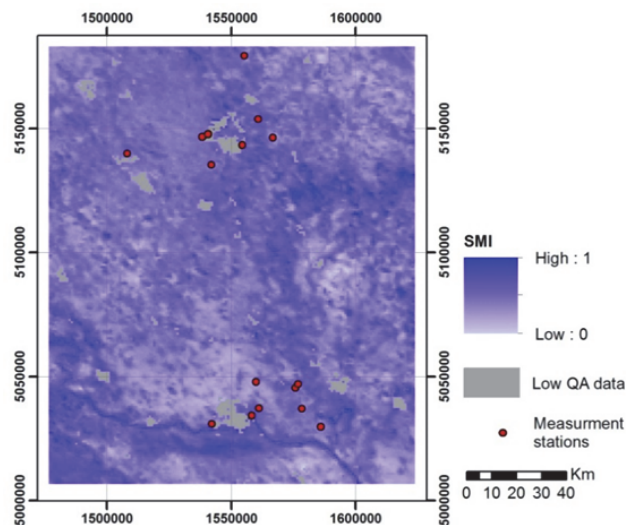


Figure 3: Soil moisture index map of 13th March 2014

4. RESULTS

SMI maps were calculated for a period from 1st March 2014 to 13th April 2014 to determine the change in the spatial distribution of soil moisture in the area. The resulting maps for four days are shown in **Figure 4**. In this picture, the rivers in the South and the forested areas are clearly visible in the images. Also, the total study area shows a larger variation in soil moisture on the first and last day than during the intermediate days. LST data can only be collected from cloud free areas. Therefore on 31st March, and especially on 3rd April, in

many areas data is missing and the SMI cannot be calculated at those locations.

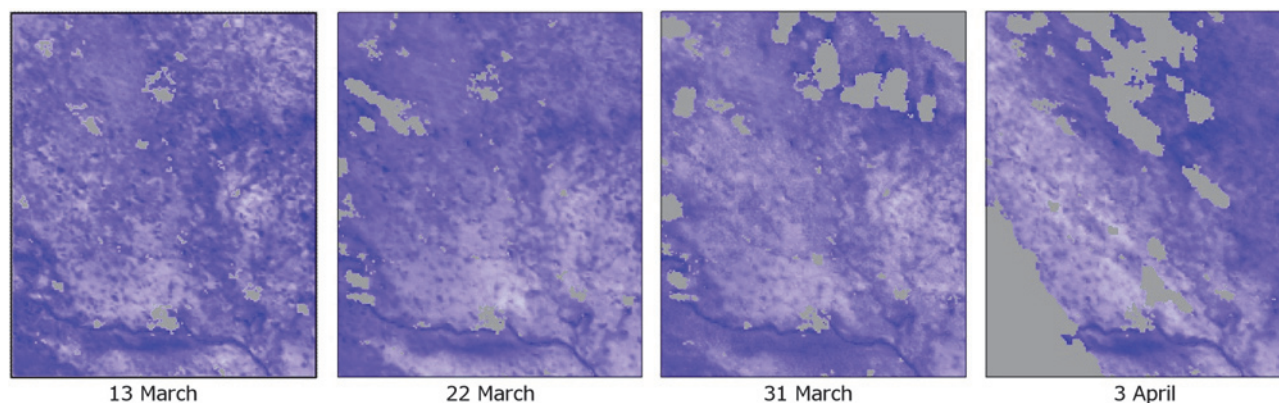


Figure 4: SMI maps for 6 days (13 March – 3 April)

Following similar approaches by Wang (2008) and Mallick et al. (2009), satellite based SMI values were compared to ground soil moisture (SM) measurements. At both sides of the border, eight stations were established and since end of January 2014, soil moisture data is collected in every hour from 6 different depths (from -10 to -75 cm), by using Decagon EC 5 volumetric water content sensors (Jovanović et al., 2013).

At the locations of the measurement stations, soil moisture index values were extracted from the satellite based maps. Data from two stations were omitted because they were not representative for the neighbouring 1 km zone (the spatial distribution of SMI mapping). **Figure 5** shows scatterplots of SM ground measurements and the satellite derived SMI values for two different days. The relationship between the two data sets during the period when ground measurements are available is not very strong. The main reason for this is the large difference in scale between the data sets. The spatial representativeness of the point measurements is limited to maximum several hundreds of square meters around the measurement stations, while the satellite data is an integrated measurement of a 1 km² area. Furthermore, the ground data is measured at depths of 10 cm (Hungary) and 20 cm (in Serbia) while the satellite acquires only surface temperature. **Figure 6** shows the precipitation and SM in the observed period at two Hungarian stations. The first part of March (before the 13th March SMI map) was a long dry period, and higher correlation ($R^2=0.57$) between satellite based SMI and ground station based SM is observed on 13th March. Hardly any connection between parameters was detected ($R^2=0.14$) on the 22nd March (after minor precipitation), which can be due to different water holding capacity of the soils and due to infiltration. Again, higher correlation ($R^2=0.54$) was detected on 31st March which was after a rainfall event.

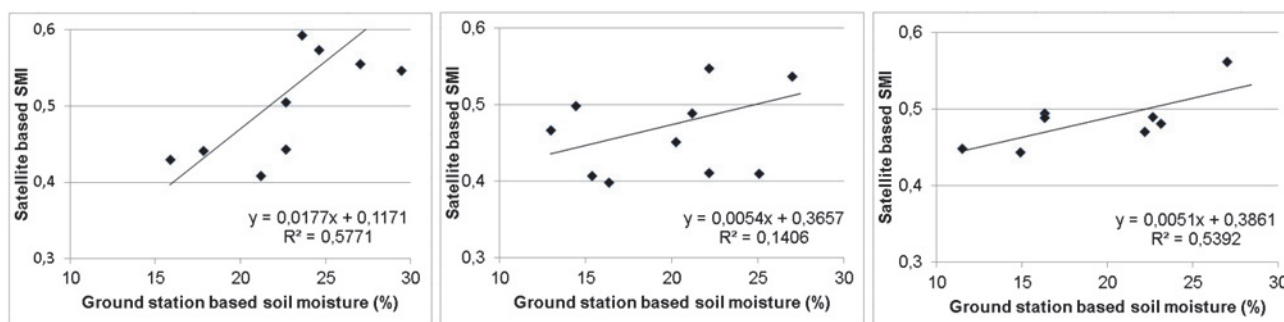


Figure 5: Scatterplots of three days of satellite derived soil moisture and ground measurements (a, 13 March; b, 22 March; c, 31 March)

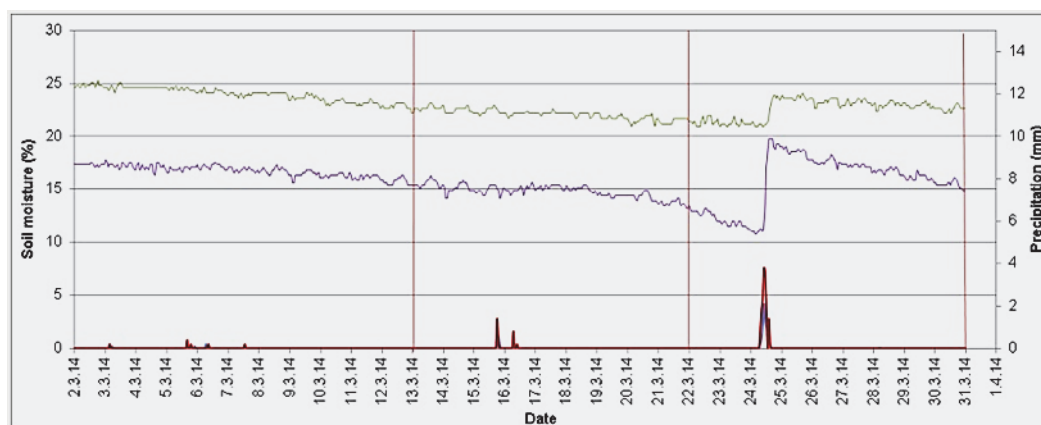


Figure 6: Precipitation (red) and station soil moisture data (blue) on 2 Hungarian stations, vertical lines show the date of satellite images

5. CONCLUSIONS AND DISCUSSION

SMI maps based on MOD11 and MOD13 products can be created automatically with the presented workflow. These maps provide a good impression of the spatial distribution of SM at a specific moment in time. The fractional vegetation maps can be enhanced by incorporation soil type information in the bare soil class.

The relationship with the local point measurements is not very strong, and therefore absolute calibration of the relative SMI maps is not feasible. Using longer data series can improve calibration and the effects of rainfall events on correlation can be investigated. Many possible improvements to the method exist. Among others, absolute calibration of the SMI values can improve the relationship with the point measurements. Also, additional information on the soil type may improve the creation of the LST – F_r space. The use EVI or LAI instead of NDVI may result in better F_r data and therefore improving the LST – F_r space, as well.

6. ACKNOWLEDGEMENTS

This research was supported by the IPA Cross-border Cooperation Programme of the European Union under the project WAHASTRAT (HUSRB/1203/121/130).

7. REFERENCES

CARLOS, T. (2007): An Overview of the “Triangle Method” for Estimating Surface Evapotranspiration and Soil Moisture from Satellite Imagery. *Sensors*, 7, 8, 1012-1029.

GILLIES, R.R., CARLSON, T.N., CUI, J., KUSTAS, W.P., HUMES, K.S. (1997): A verification of the ‘triangle’ method for obtaining surface soil water content and energy fluxes from remote measurements of the Normalized Difference Vegetation Index (NDVI) and surface radiant temperature. *Int. J. of Remote Sensing*, 18, 3145–3166.

JOVANOVIĆ, M., PAVIĆ, D., MESAROŠ, M., STANKOV, U., PANTELIĆ, M., ARMENSKI, T., DOLINAJ, D., POPOV, S., ĆOSIĆ, Đ., POPOVIĆ, L., FRANK, A., CRNOJEVIĆ, V. (2013): Water shortage and drought monitoring in Bačka region (Vojvodina, North Serbia) – setting-up measurement stations network. *Geographica Pannonica*, 17, 4, 114-124.

MALLICK, K., BHATTACHARYA, B.K., PATEL, N.K. (2009): Estimating volumetric surface moisture content for cropped soils using a soil wetness index based on surface temperature and NDVI. *Agricultural and Forest Meteorology*, 149, 8, 1327 - 1342.

OWE, M., VAN DE GRIEND, A. A., CHANG, A.T.C. (1992): Surface moisture and satellite microwave observations in semiarid southern Africa. *Water resources research*, 28, 3, 829-839.

PATEL, N.R., ANAPASHSHA, R., KUMAR, S., SAHA, S.K., DADHWAL, V.K. (2009): Assessing potential of MODIS derived temperature/vegetation condition index (TVDI) to infer soil moisture status. *Int. J. of Remote Sensing*, 30, 1, 23 – 39.

PÉCZELY GY. (1998): *Éghajlattan (Climatology)*. Nemzeti Tankönykiadó, Budapest, 258-285.

SCHMUGGE, T., FRENCH, A., RITCHIE, J.C., RANGO, A., PELGRUM, H. (2002): Temperature and emissivity separation from multispectral thermal infrared observations. *Remote Sensing of Environment*, 79, 189-198.

VINCENTE – SERRANO, S.M., PONS-FERNANDEZ, X., CUADRAT-PRATS, J.M. (2004): Mapping soil moisture in the central Ebro river valley (northeast Spain) with Landsat and NOAA satellite imagery: a comparison with meteorological data. *Int. J. of Remote Sensing*, 25, 20, 4325-4350.

WANG, L. (2008): *Remote Sensing Techniques for Soil Moisture and Agricultural Drought Monitoring*. PhD Thesis, George Mason University, 151 p.

DECLUSTERING OF FIELD'S DATA LOCATED ON NORTHERN MARGIN OF THE BJELOVAR SUBDEPRESSION

Ivana MESIĆ^{1,2}, Gordana MEDUNIĆ³

¹Kralja Tomislava Elementary School, Matice hrvatske 1, 31500 Našice, Croatia, e-mail: ivy.mesic@gmail.com

²Geology PhD student at University of Zagreb, Faculty of Science, Horvatovac 102a, 10000 Zagreb, Croatia

³University of Zagreb, Faculty of Science, Horvatovac 95, 10000 Zagreb, Croatia, e-mail: gpavlovi@inet.hr

The Bjelovar Subdepression is located in the Croatian part of the Pannonian Basin System, within the south-western part of the Drava Depression. The following fields on northern margin of the Bjelovar Subdepression were analyzed: Lepavina, Jagnjedovac, Mosti, Šandrovac and Letičani. As input data, structural map of e-log depth marker Z', i.e. the Pannonian and Pontian chronostratigraphic boundary, was used directly for well coordinates and relative depth values. Explored fields had small number of wells. Only the Šandrovac Field contained 18 well data. The analysis was based on Thiessen polygons. This approach is one of the most popular declustering methods of geomathematics. The mapping process was performed by using zonal assessment and Ordinary Kriging. It was concluded that the depth maps should be constructed in both ways, using Thiessen polygons and Kriging maps simultaneously, later compared and mutually interpreted. It is special valid approach in case of small input data.

Key words: Bjelovar Subdepression, declustering, Ordinary kriging, Thiessen polygons.

1. INTRODUCTION

Declustering methods generally used in geostatistics are, namely: the polygonal method and the cell-declustering method. In the polygonal method, polygon of influence (known as Thiessen or Voronoi polygon, e.g. Boots, 1987) is constructed in such a way that its geometry will include all data points that are closer to the sample compared to any other measurements. As a result, the estimated global mean, $F(x)$, of a data set is defined by (**Equation 1**):

$$F(x) = \frac{\sum_{i=1}^n w_i x_i}{\sum_{i=1}^n w_i} \quad (\text{Eq. 1})$$

where the weights w_i are defined by the surfaces of the polygons (Isaaks & Srivastava, 1989). Accordingly, the number of cells covering the investigated area defines the sum of the weights in Equation 1.

In areas known to be oversampled, cell size is also a factor in the calculation of weighted mean of the data. Such an example is processed using data from the

Bjelovar Subdepression, specifically the following fields: Lepavina, Jagnjedovac, Mosti, Letičani and Šandrovac.

2. GEOGRAPHICAL AND GEOLOGICAL SETTING

The Bjelovar Subdepression is located in the northern part of Croatia (**Figure 1**). It represents a separate regional geotectonic unit in the Croatian part of the Pannonian Basin System (CPBS). Due to uplift of Bilogora Mt. in the Pliocene and Quaternary, this area is geologically and geographically separated from the Drava Depression (Malvić, 2011).

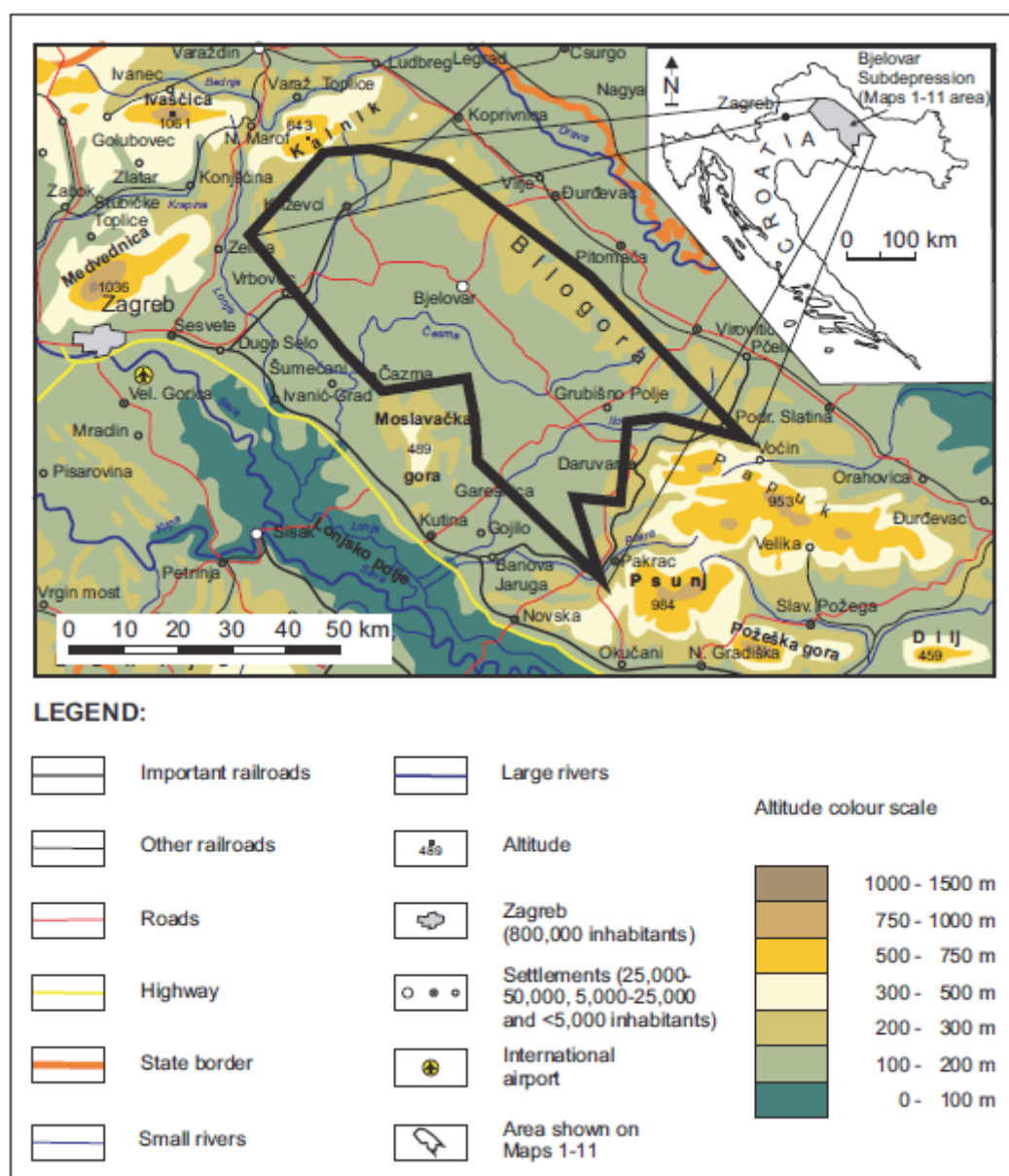


Figure 1: Geographic map of Bjelovar Subdepression (Malvić, 2011)

Fields discussed in this paper, namely Mosti, Lepavina, Jagnjedovac, Letičani and Šandrovac; are located on the northern margin of the Bjelovar Subdepression (**Figure 2**).

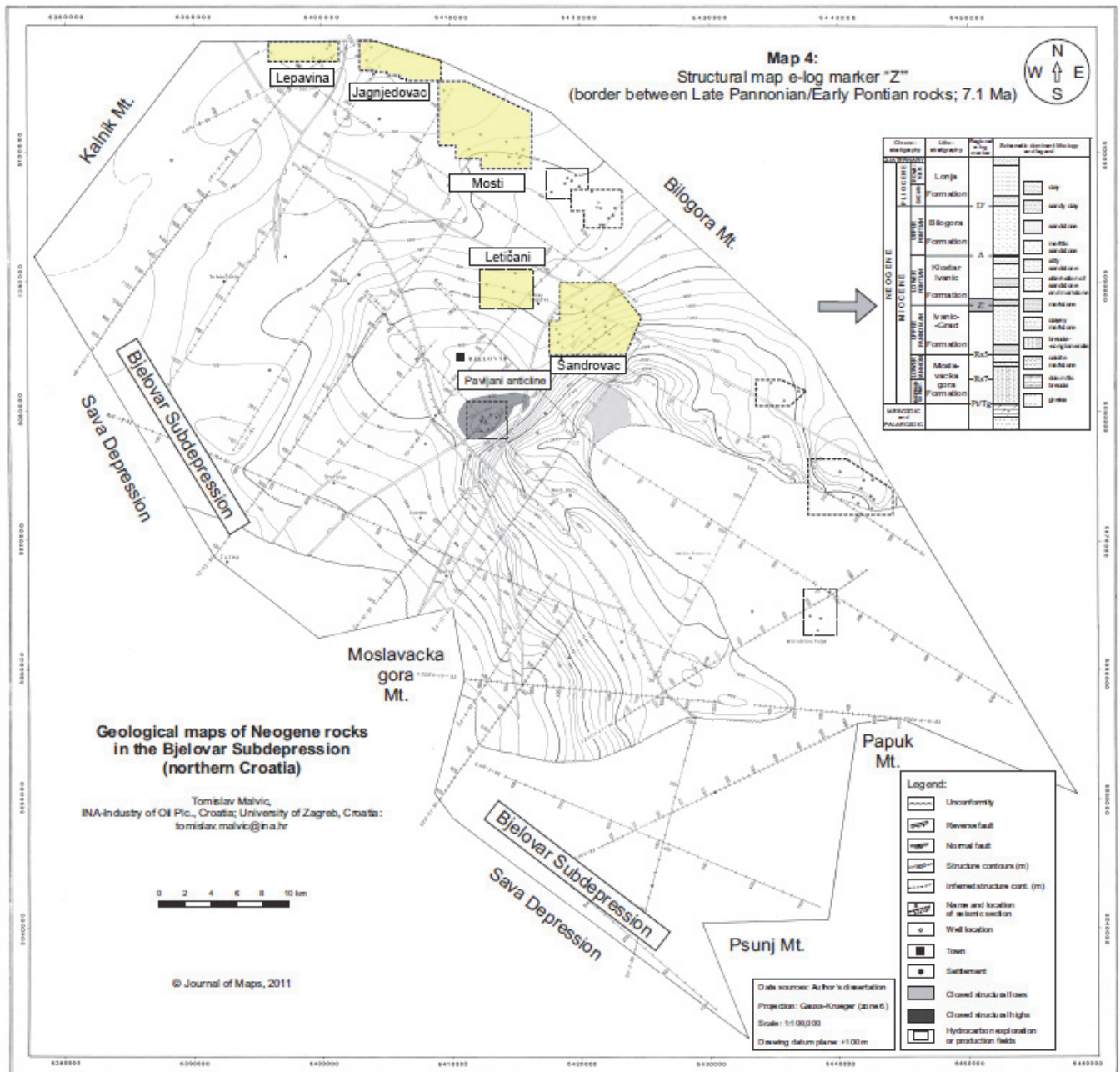


Figure 2: Structural map of e-log marker Z' (Malvić, 2011)

Structural map of e-log depth marker Z' (7.1 Ma) was used as an input data (Malvić, 2011). It is characterised by an unconformity that reached maximum extension, especially on the east of the investigated area and around Pavljani anticline. In analysis, field's and well's coordinates, as well as relative depths were read directly for given structural map, interpolated regarding datum plane at +100 m.

3. DATA DECLUSTERING USING THIESSEN'S POLYGONS

Thiessen's polygons (Boots, 1987) are areas (geometric figures) created around the point objects that make up each overlapping neighbourhood facilities. The entire content of one Thiessen polygon defines an area around a point, where every location is nearer to this point than to all the others.

Thiessen diagram (also known as a Voronoi diagram, Wigner-Seitz cells, or Dirichlet tessellation) represents the net of all Thiessen polygons defined by the point set. Proximal polygons are constructed by computing the perpendicular bisectors among all neighbouring points of the set. The points are connected with a line and the radius is greater than one half of their distance. The intersection of the circle represents the perpendicular bisectors, which are ultimately the edge of the polygon (**Figure 3**).

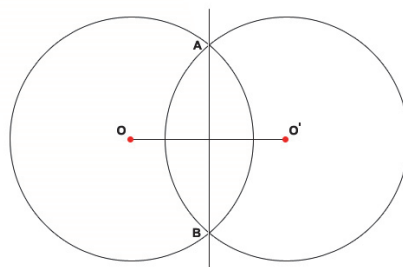


Figure 3: Construction of the perpendicular bisectors between two adjacent points

A set N of n labelled points in the plane are called *centroids* (**Figure 4**). A *Thiessen* polygon is defined as the locus of all points closer to a centroid $C \in N$ than to any other centroid which implies that Thiessen polygons are convex. The convex hull of the set N of centroids is defined as the smallest convex polygon enclosing all centroids. All centroids of the boundary of the convex hull have open Thiessen polygons, and all interior centroids have closed polygons (Brassel & Reif, 1979). A centroid B is called a Thiessen neighbour of a centroid C if the Thiessen polygons around the two centroids have an edge in common (**Figure 4**).

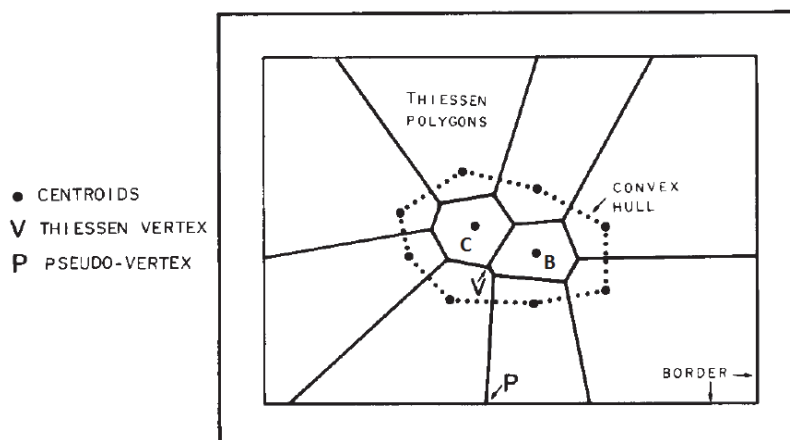


Figure 4: Definition of terms used for the Thiessen polygon computation (modified from Brassel & Reif, 1979)

3.1. Thiessen polygons derived from structural map of e-log marker Z'

Thiessen polygons are made in SAGA GIS 2.1.0. software. If polygons were to be constructed, the frame field coordinates read from the map position of fields and exploration wells from which the data was recovered were required (**Figure 2**). The order of connecting the points must be entered properly, otherwise all the points would be connected to each other.

Once polygons have been made, the next step is entering the coordinates of the points that are inside a polygon by means of which the Thiessen polygons are made. If we look at the structural map of e-log marker Z' as the point data, then there are 5 points within the polygon of the Lepavina Field, 4 points within the Jagnjedovac Field, 12 points within the Mosti Filed, 5 points within the Letičani Filed and 18 points within the polygon of the Šandrovac Field.

Each polygon is represented with colour that belongs to the specified depth class. The presentation of the depth value of each belonging polygon within these fields can be seen in **Figure 5**, where the prominent zonal evaluation of this method is shown.

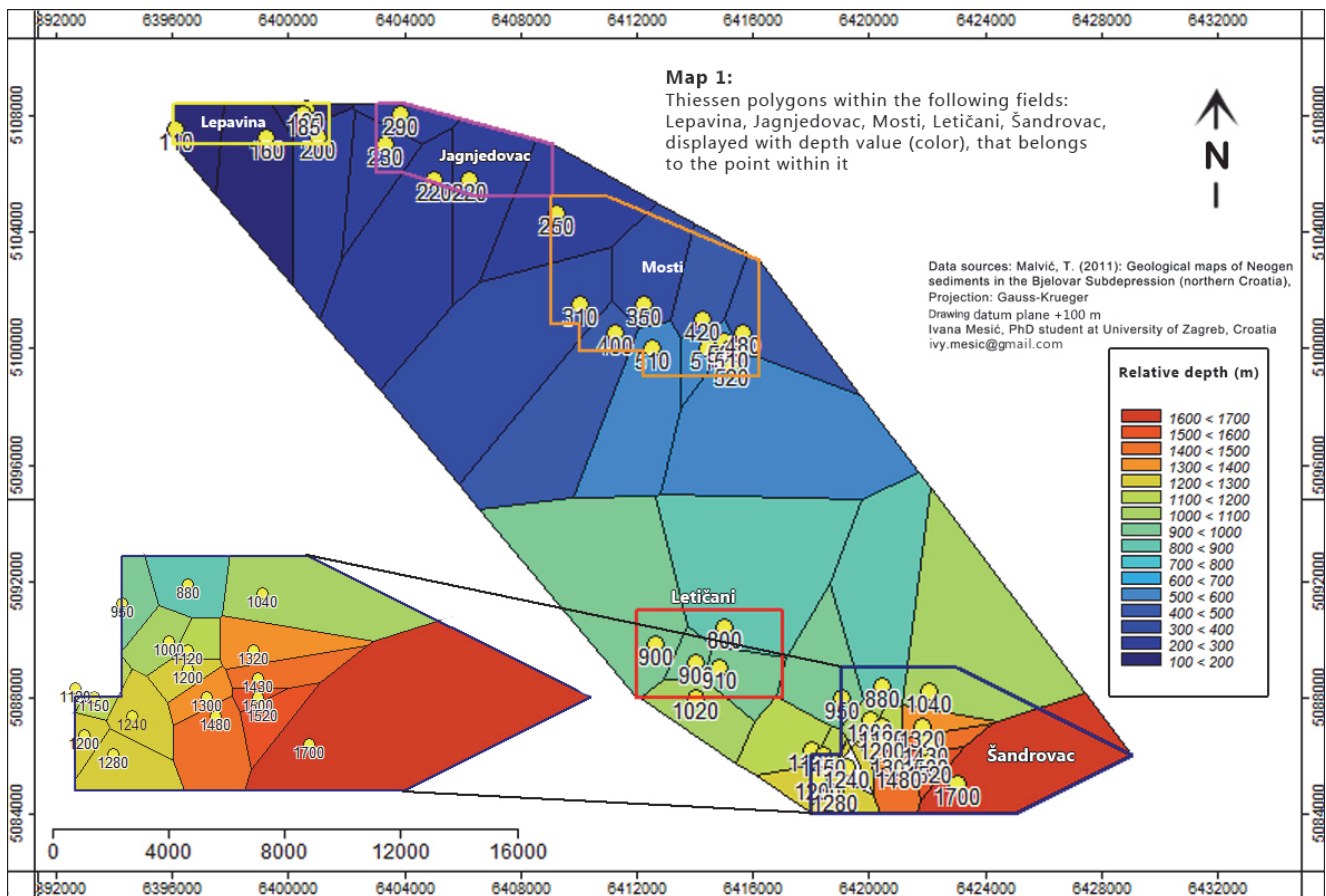


Figure 5: Thiessen's polygons displayed with the depth value (colour) that belongs to the point within it

3.2. Kriging map from the well data

E-log marker Z' (Pannonian/Pontian border) relative depths had been interpolated by Ordinary Kriging, using "default" variogram model. The map was created by using SAGA GIS software, and covering only the northern part of the Bjelovar Subdepression (**Figure 6**) where the data are available.

There are 43 points within the evaluated fields, which is sufficient for the map interpolation using Kriging. Only the Šandrovac field exceeds 15 points, which is considered as a minimum data set for calculation reliable variograms, so it is why they were "replaced" with such auto-defined model in SAGA. Therefore, if the fields were to be analysed separately by comparison of Thiessen and Kriging results, this problem of non-possibility for variogram model would be much more emphasised and make interpretation impossible.

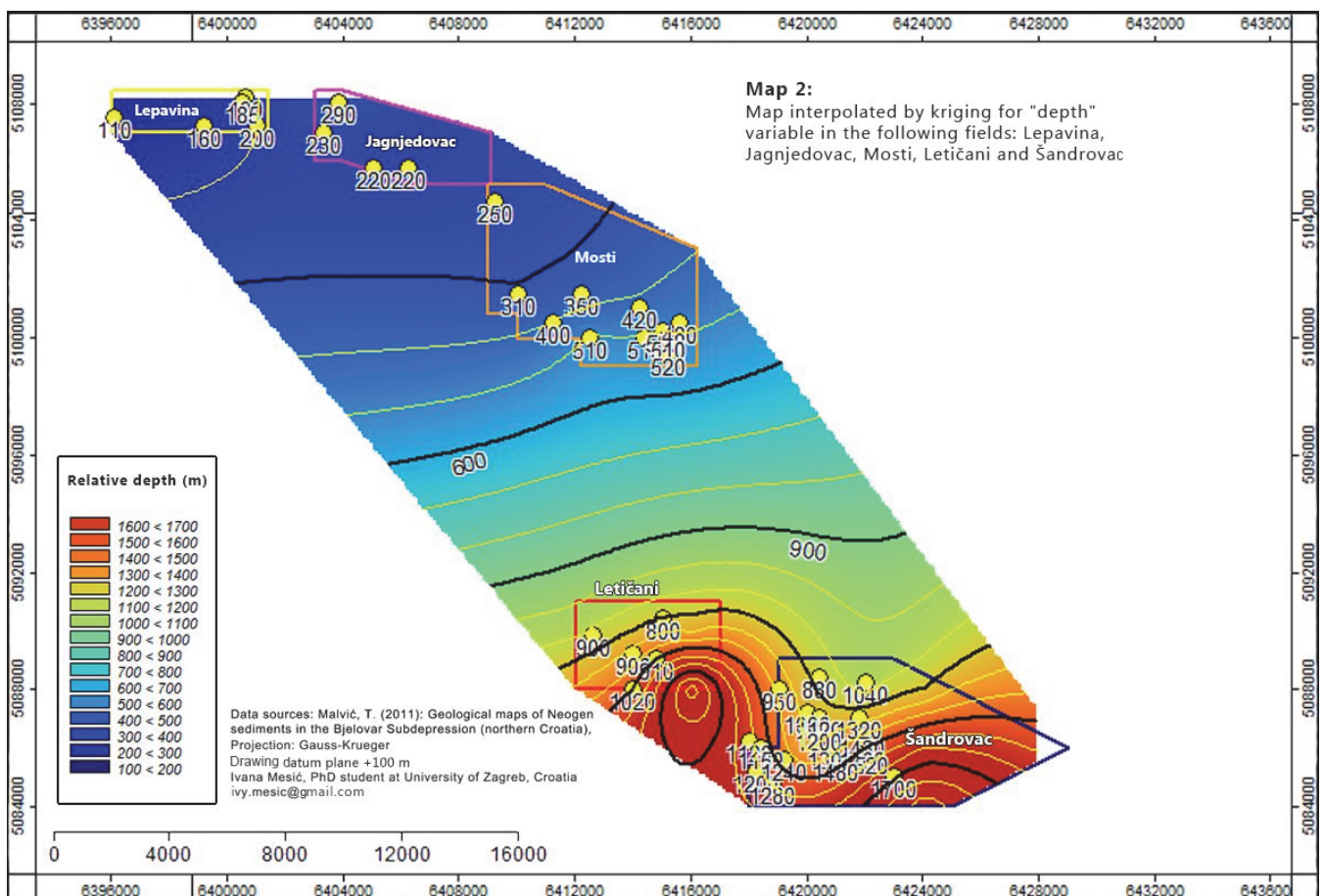


Figure 6: Map interpolated by kriging for „depth“ variable

4. RESULTS OBTAINED BY COMPARISON OF METHODS

By comparison of the maps interpolated by Kriging and by the Thiessen's polygons of the evaluated fields, there appears an obvious approximation, especially on the north. Thiessen polygons map allowed a quick assessment of depth values, even in unsampled area between Mosti and Letičani, and interestingly more detail view on trends of depth changes along the field' structures. Oppositely, the Kriging regionally showed only large monocline.

Kriging as a basic geostatistical estimation technique provides a number of advantages over the other interpolation methods. It is certain that the Kriging method generally provides a better spatial depth value estimate rather than Thiessen polygon method (that we called a zonal assessment and not an interpolation method).

However, deterministical interpolation methods such as Inverse Distance, Weighting Average, Kriging, etc. include large uncertainties in the cases with the small number of input data. The Kriging is special sensitive due to need to determine spatial dependence. In such a case, the zonal assessment has its advantages, at least in fast obtaining the “maximums” and “minimums” over the analysed area or volume. For better insight in main structural features and subareas where extremes are located, and number of data per area is low, here is recommended that in structural mapping of subsurface in the CPBS are used both, the zonal estimation and deterministical interpolation by simultaneously comparing their outputs.

5. REFERENCES

BOOTS, B.N. (1987): Modifying Thiessen Polygons. *The Canadian Geographer*, 31, 2, 160-169.

BRASSEL, K.E. & REIF D. (1979): A Procedure to Generate Thiessen Polygons. *Geographical Analysis*, 11, 3, 289-303.

ISAAKS, E. & SRIVASTAVA, R. (1989): *An Introduction to Applied Geostatistics*, Oxford University Press Inc., New York, 592 p.

MALVIĆ, T. (2011): Geological maps of Neogene sediments in the Bjelovar Subdepression (northern Croatia). *Journal of Maps*, 7, 1, 304-317.